

**Spontaneously Adsorbed Monolayers: Anthraquinones
and Osmium Polypyridyl Complexes as Molecular
“Building Blocks”**

By

Dominic P. O’Hanlon B.Sc. (Hons)

**A Thesis presented at Dublin City University for the degree of
Doctor of Philosophy**

Supervisor Dr. Robert J. Forster.

School of Chemical Sciences

Dublin City University

September 1999

This Thesis is dedicated to my family.

“I may not have gone where I intended to go, but I think I have ended up where I intended to be.”

-Douglas Adams

I hereby certify that the material, which I now submit for assessment on the programme of study leading to the award of Doctor of Philosophy is entirely of my own work and has not been taken from the work of others save and to the extent that such works has been cited and acknowledged within the text of my work.

Signed:  ID No.: 95970720

Date: 20/7/1999

Acknowledgements

First and foremost I would like to express my sincere and deepest gratitude to my supervisor Dr. Robert Forster for his constant support, advice, encouragement and his friendship over the last few years. Thank you. To the technical staff at DCU, Mick, Maurice, Damien, Veronica, Ann, Vinny and Ambrose, thank you for all your help during my stay. It was gratefully appreciated.

To past members of the RFG, Joe, Aoife, Tim, Nick, Johan and Egbert and the present, Conor, Richard, Jenni and Edna, you're a great bunch. A special thanks to Conor and Aoife and the original of the species Joe.

Also, to those who have moved on to bigger and brighter things, Teresa, Frances and Rachel, cheers.

To all the chemistry postgrads and postdocs of DCU, thanks, especially, Dee, Christine, Bronagh, Luke (Munster squash champion !!!!!), Karen, Darren, Mike, Scott, Mairéad, Carol, Damien O'Brien (biology), Mary Farrell, Anthea, Stefano, Siobhán and of course the musical maestro Paddy Kane.

A special thanks to Dr. William Breen for all the chats, before and during my time at DCU.

I would like to thank the following whom I met over the last four years and who were instrumental in helping me enjoy my social time outside of DCU. Aileen and Paul Harmon, Mark Redican, Vincent Savage (two of the best), Sean McCarthy, James McIntyre (roll on Paris), Caesar Guinto, all those in GSD and of course Wendy (Ted) and Paul (Ted) Burns (thanks for plying me with drink!!).

Also thanks to David Gray, Lauren Hill, Stereophonics, Counting Crows and Paul Weller for the hip tunes during the writing of this Thesis.

Finally, to those I love the most, Mum, Dad, Aileen and Paul.

Abstract

Spontaneously Adsorbed Monolayers: Anthraquinones and Osmium Polypyridyl Complexes as Molecular "Building Blocks"

The synthesis and characterisation of a series of osmium polypyridyl complexes and the characterisation of a variety of anthraquinones is described, along with the fabrication and of gold, platinum and mercury microelectrodes. The methods of characterisation include HPLC, UV-Visible spectroscopy, ^1H -NMR and Cyclic voltammetry and Chronoamperometry.

Monolayers of osmium polypyridyl complexes and anthraquinones were found to adsorb from micromolar solutions of the respective compounds dissolved in their appropriate solvent. In respect to the osmium complexes adsorption occurred through the free pendant nitrogen present on the ligand while adsorption for the anthraquinone was by means of a π interaction with the electrode surface. The microenvironments of the osmium polypyridyl complexes were found to be sensitive to both the type and concentration of electrolytic species in solution with perchlorate ions being the most strongly ion-paired. Osmium polypyridyl monolayers also proved to be highly solvated at saturation coverages with the double layer setting up within the immobilised film.

Spontaneous adsorption of single and binary anthraquinone monolayers of anthraquinone-2,7-disulphonic acid (2,7-AQDS) and 1-chloro-4-hydroxy-anthraquinone (1,4-AQCIOH) revealed that the adsorbates interact laterally within both single- and two-component monolayers with the concentration dependence of the surface coverage being adequately described by the Frumkin adsorption isotherm over the concentration range 1 – 30 μM . The formal potentials, saturation surface coverages, free energies of adsorption and Frumkin interaction parameters are all affected by co-adsorption of the second quinone suggesting that dissimilar adsorbates interact laterally, most likely through intermolecular hydrogen bonding. Analysis of anthraquinone monolayers of 1-amino-2-sulphonic-4-hydroxy-anthraquinone [AQNHSO_3H] revealed that at coverages were the inter-site separation of the adsorbates was at a minimum and during electrochemical switching of the redox state of the adsorbed film, the voltammetry altered from the ideal response resulting in the presence of a sharp spike. Analysis of this anomaly illustrated extensive lateral adsorbate interaction resulting in the formation of an intermolecular hydrogen bonded network at saturation coverages.

TABLE OF CONTENTS

Acknowledgements	I
Table of Contents	II
<u>Chapter 1</u>	
Introduction, Review of Osmium Polypyridyl complexes, Anthraquinones and Microelectrodes	1
Section 1 Introduction	2
1.1 Electrical Double Layer	5
1.2 Adsorption of Redox-Active Molecules	7
1.3 Review of Electrode Surfaces Modified with Monolayers	9
1.3.1 Alkane / Ferrocene Alkanethiol Monolayers	9
1.3.2 Osmium and Ruthenium Polypyridyl Monolayers	13
1.3.3 Adsorption of Quinones	19
1.3.3.1 Hydrogen Bonding Effects within Adsorbed Quinone Monolayers	22
1.4 Microelectrodes	23
1.4.1 Introduction	23
1.4.2 Microelectrode Geometries	24
1.4.3 Mass Transport	26
1.4.3.1 Short Times	26
1.4.3.2 Long Times	27
1.4.4 Microelectrode Characteristics	28
1.4.4.1 RC Time Constant	28
1.4.4.2 Ohmic Drop	29
1.4.5 Applications of Microelectrodes	29
1.5 Electrochemical Techniques	30
1.5.1 Cyclic Voltammetry	30
1.5.1.1 Solution Phase Electrochemistry	32
1.5.1.2 Surface Confined Electrochemistry	35
1.5.2 Conclusion	37
1.6 References	38

Chapter 2	Synthesis and Characterisation of Redox-Active Complexes for Self-Assembly	43
Section 2	Introduction	44
2.1	Osmium Polypyridyl Complexes	44
2.2	Synthesis of Osmium Complexes	46
2.2.1	Materials and Instrumentation	46
2.2.1.1	Chromatographic Techniques	46
2.2.1.2	Adsorption Spectroscopy	46
2.2.1.3	Electrochemistry	46
2.2.1.4	Nuclear Magnetic Resonance Spectroscopy	47
2.2.1.5	Elemental Analysis	47
2.3	Characterisation of Osmium Complexes	48
2.3.1	Synthesis of Metal Complexes	48
2.3.1.1	Synthesis of $[\text{Os}(\text{bpy})_2\text{Cl}_2]\text{Cl}$	48
2.3.1.2	Synthesis of $[\text{Os}(\text{bpy})_2\text{Cl}_2]\cdot 2\text{H}_2\text{O}$	48
2.3.2	HPLC	49
2.3.3	UV-Vis	51
2.3.4	Electrochemistry	52
2.3.5	NMR	53
2.4	$\text{N}_5\text{-Cl}$ Osmium Complexes	55
2.5	$\text{N}_6\text{-Cl}$ Osmium Complexes	56
2.5.1	HPLC	57
2.5.2	UV-Vis	58
2.5.3	Electrochemistry	60
2.5.4	NMR	62
2.6	Anthraquinones	65
2.7	Characterisation of Anthraquinones	64
2.7.1	HPLC	66
2.7.2	UV-Vis	68
2.7.3	Electrochemistry	68
2.7.4	NMR	70
2.8	Conclusion	73
2.9	References	74

<u>Chapter 3</u>	Fabrication and Characterisation of Microelectrodes	76
3	Introduction	77
3.1	Construction of Gold and Platinum Microelectrodes	79
3.1.1	5 μm Gold and Platinum Electrodes	79
3.1.2	25 μm Gold Electrodes	82
3.1.3	Exposing the Metal Electrode	83
3.2	Construction of Mercury Microelectrodes	84
3.3	Characterisation of Microelectrodes	89
3.3.1	Polishing Technique	89
3.3.2	Electrochemical Cleaning of Microelectrodes	91
3.4	Surface Area Measurements	94
3.4.1	Electrochemical Technique for the Determination of Surface Area	94
3.4.1.1	Gold: Oxygen Adsorption from Solution	94
3.4.1.2	Platinum: Hydrogen Adsorption from Solution	99
3.4.1.3	Mercury: Drop Weight Method	101
3.5	Resistance and Capacitance Effects on Gold Microelectrodes	103
3.6	Conclusion	112
3.7	References	113
<u>Chapter 4</u>	Ion-Pairing, Capacitance and Temperature effects on $\text{N}_5\text{-Cl}$ Osmium Monolayers	116
Section 4	Introduction	117
4.1	Experimental Equipment	118
4.1.1	Apparatus	118
4.1.2	Materials	118
4.2	Discussion	119
4.2.1	Electrochemical Properties of Osmium Compounds	119
4.2.2	Electrolyte Studies	128
4.2.3	Capacitance Effects	137
4.2.4	Temperature Dependence of $\text{N}_5\text{-Cl}$ Osmium Complexes	142
4.3	Conclusion	145
4.4	References	146

<u>Chapter 5</u>	Hydrogen bonding in 2-Dimensions:	
	Single component Anthraquinones as Model Systems	148
Section 5	Introduction	149
5.1	Apparatus and Materials	150
5.1.1	Apparatus	150
5.1.2	Materials	150
5.2	Discussion	152
5.2.1	General Electrochemical Properties of [AQNH ₂ SOH]	152
5.2.2	Effect of Concentration on Monolayers of [AQNH ₂ SOH]	157
5.2.3	Adsorption Isotherms	162
5.2.3.1	The Langmuir Isotherm	162
5.2.3.2	The Frumkin Isotherm	168
5.2.4	Origin of the Non-ideal Voltammetric Response	174
5.2.5	Molecular Modelling on [AQNH ₂ SOH]	175
5.2.6	Orientational Layout of Structure	182
5.2.7	Proton Dependence of Surface Confined [AQNH ₂ SOH]	183
5.2.8	Temperature Dependence of the Formal Potential	188
5.3	Conclusion	193
5.6	References	195
<u>Chapter 6</u>	Intermolecular Hydrogen Bonding:	
	Two-Component Anthraquinone Monolayers	197
Section 6	Introduction	198
6.1	Apparatus	201
6.2	Materials and Procedures	201
6.3	Results and Discussion	203
6.3.1	Electrochemical Properties of Single-Component Monolayers	203
6.3.2	Adsorption Isotherms	206
6.3.3	Mixed monolayer systems	214
6.3.4	Relationship between solution concentration and surface coverage	218
6.3.5	Competitive Adsorption	219
6.3.6	Adsorption Dynamics	223
6.4	Conclusion	232
6.5	References	233

<u>Chapter 7</u>	Conclusions	235
7	Conclusion	236

Appendix 1

Major Symbols

Standard Abbreviations

HPLC N₅-Cl Osmium Complexes

HPLC N₆-Cl Osmium Complexes

NMR of Osmium Complexes

Determination of the pK_a of [AQNH₂SOH]

CHAPTER 1

Introduction, Review of Osmium Polypyridyl Complexes, Anthraquinones and Microelectrodes

1 Introduction

The electrode / solution interface has been an area of intense interest for electrochemists, surface scientists and materials chemists for many decades^{1-6, 8-15}. Interesting processes which occur at the interface include electron transfer,^{1, 2, 3, 4} corrosion of metals,⁵ and analyte detection.^{6, 7} Of the most recent advances in modern electrochemistry, the one that stands out has been the deliberate modification of the electrode surface. Interest stems in part because these coatings allow the properties of the interface to be rationally designed and indept studies of structure-function relationships at electrode surfaces to be performed.

The Langmuir-Blodgett approach (LB)⁸ was the first technique to provide the chemist with the ability of constructing ordered molecular assemblies. This process entailed compressing the molecules on the air-water interface and subsequently transferring them onto a solid substrate. The second technique involves self assembly (SA). Self-assembly is the formation of orientated monolayer films on a surface by the spontaneous adsorption of molecules from a solution directly onto a solid substrate. Molecular self-assembly is an excellent approach for constructing stable, structurally and compositionally well-defined films on electrode surfaces. The technique works well for molecules that bond strongly to a surface and have shapes that pack well in two dimensions so as to favour lateral interactions. Types of SA include organosilicon on hydroxylated surfaces (SiO₂ on Si, Al₂O₃ on Al, glass, etc.), polymer films^{9, 10} and alkanethiols^{11, 12, 13} on transition metal complexes such as gold, glassy carbon and platinum. Attachment of these monolayers depends on either the electrostatic attraction of the complex with the electrode or covalent attachment from a functional group such as sulphur or nitrogen with the substrate.

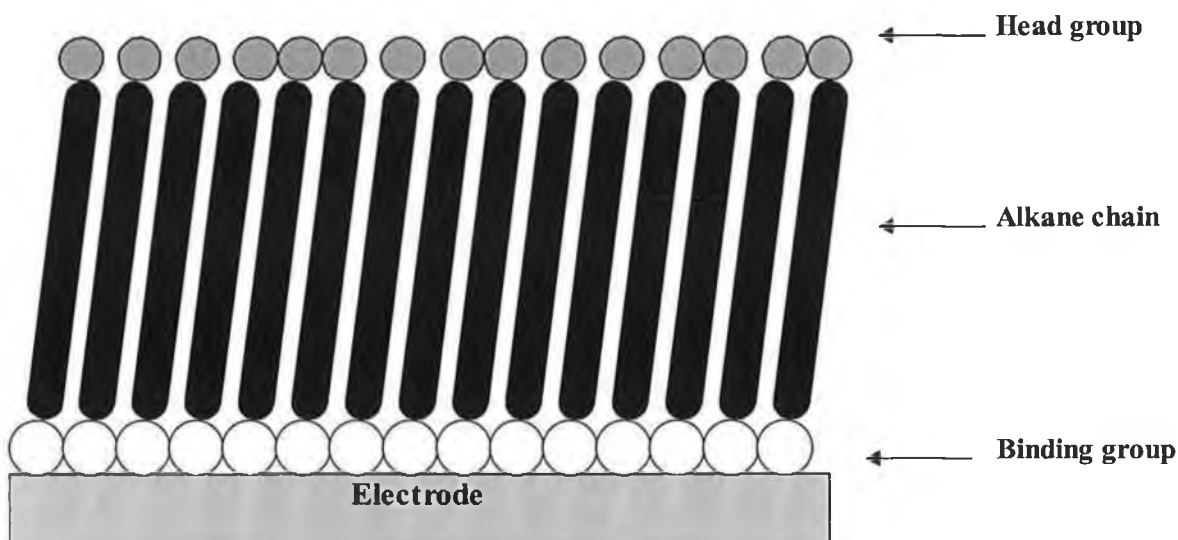


Figure 1 Illustration of a SAM adsorbed onto an electrode surface.

Modification of electrodes using SA has enabled electrochemists to probe not only influences from external forces including temperature,¹⁴ electrolyte,¹⁵ and pH¹⁶ on the structure of the monolayer, but they may also gain an insight into the corresponding effects on the electrical double layer residing between the electrode and molecular film. The ability to modify electrodes has also enabled electrochemists study the effects of interactions occurring in two-dimensions on electrode surfaces¹⁷. The magnitude of these lateral interactions gives important information regarding the stability of the redox-active assemblies. The type of interaction, i.e., destabilising or stabilising for example, arising from processes such as inter- and intramolecular hydrogen bonding and even the orientation of the complexes on the electrode surface all impact not only the stability of the assembly but also the electrochemical properties.

This thesis spans the synthesis and characterisation of transition metal complexes, the formation of monolayers and the elucidation of intra- and intermolecular interactions. Chapter 2 considers the synthesis of osmium polypyridyl complexes and the characterisation of the osmium complexes and anthraquinones used in successive chapters. Chapter 3 examines the fabrication and cleaning of microelectrodes and their electrochemical characterisation. Chapter 4 examines interactions occurring in osmium

polypyridyl complexes and single component anthraquinone monolayers. In particular, it deals with the effects of temperature and electrolytes on the monolayer structure and electrochemical properties. Intermolecular hydrogen bonding is the topic examined in chapter 5. The electrochemistry of 1-amino-2-sulphonic-4-hydroxy-anthraquinone [AQNH₂SOH] probes the possibility of triggering structural changes within the monolayers by switching their redox state. Chapter 6 deals with the electrochemistry of two-component anthraquinone monolayers. Using cyclic voltammetry we consider the presence of a second component on lateral interactions, surface coverages, free energies of adsorption and formal potentials. This chapter also examines the kinetics of adsorbate exchange between both quinone adsorbates.

This chapter (chapter 1) reviews the past literature, dedicated to the analyses of surface confined redox active monolayers focusing especially on alkane thiol, osmium polypyridyl and anthraquinone monolayers. The theory and characteristics of microelectrodes are also examined in this chapter along with an insight into the electrochemical techniques employed in this work.

1.1 Electrical double layer

In order to understand the process of adsorption of redox active compounds onto electrode surfaces, it is desirable to understand all the parameters that can influence the energetics and dynamics of adsorption including the electrode, electrolyte, solvent and the redox active species itself. Potential dependent adsorption is one of the focuses of this thesis. Therefore, it is important to have an understanding of the electrical double layer and the distribution of ions and molecules at the electrode/electrolyte interface.

All electrochemical reactions take place at the interface between an electronic conductor, the *electrode* and an ionic conductor, the *electrolyte*. The course of these electrochemical reactions and their variation with the electrode potential depend on the distribution of the particles and the charges in this interfacial region. Therefore, interfacial structure is of paramount importance for electrochemistry and has been a topic of intensive research since the time of Lippmann¹⁸ and Helmholtz.¹⁹ It was Helmholtz who pointed out that the high capacity of the interface between a metal and a concentrated electrolyte solution could be explained by the existence of two layers of charge of equal magnitude and opposite sign. A layer of charge on the metal surface, which is balanced by an ionic excess charge in the adjacent solution. This distribution of charges became known as the *electric double layer*.

The development of microscopic models for the double layer began with the works of Guoy and Chapmann who proposed a space charge theory for the solution part of the double layer.^{20, 21} Their results show a diffuse layer of charge in which the concentration of ions is greatest next to the electrode surface and decreases progressively until the bulk concentration is realised far from the electrode surface. However, their theory neglects the finite size of the ions and it was Stern who postulated that ions could not approach the electrode beyond a plane of closest approach. Stern's approach was a combination of the Helmholtz and Guoy-Chapmann approaches. Recently Grahame,²² aided by earlier works on the topic^{20, 21, 23} realised that the full interpretation of the thermodynamic data required two planes of closest approach. One for specifically adsorbed ions and one for non-specifically adsorbed ions, and a diffuse layer region extending to the bulk electrolyte phase, represented by Figure 1.

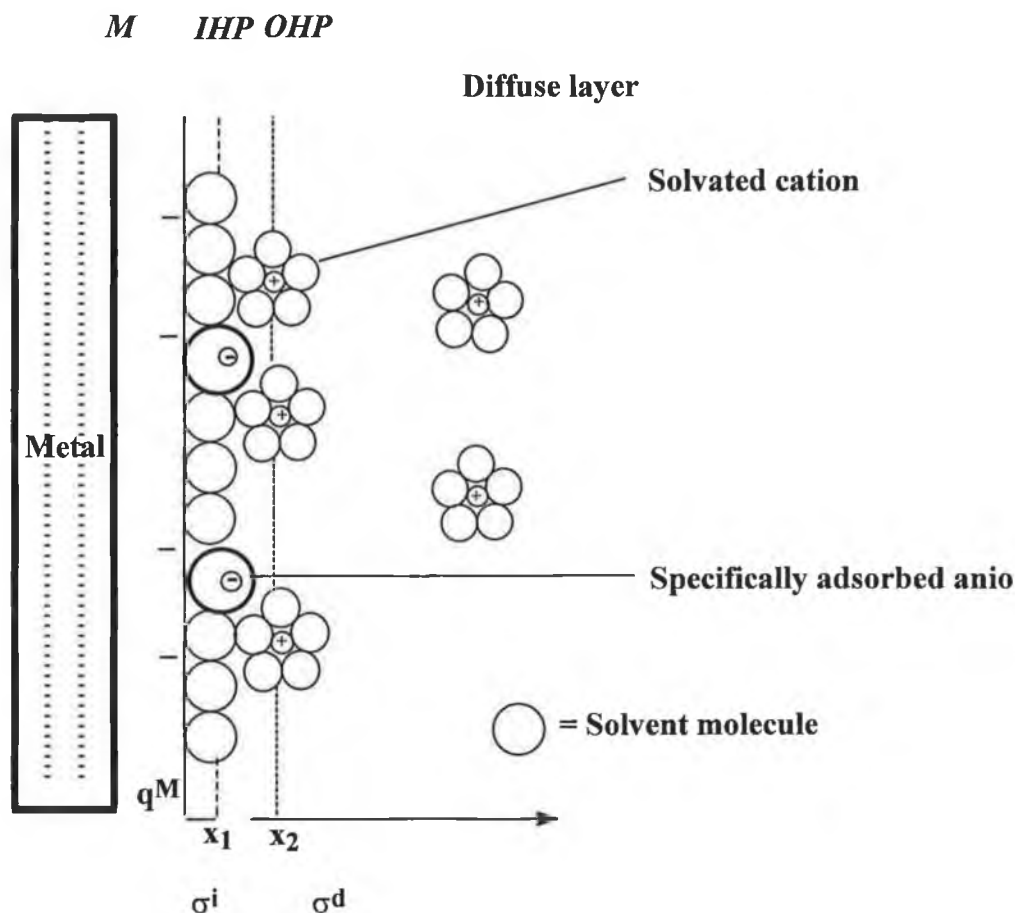


Figure 2 Proposed model for the double layer region of the electrode-solution interface.

The interface is split into three regions: the metal layer, the diffuse layer and the inner layer. The metal layer is homogeneous and the charge on the solution side of the metal resides in a thin two-dimensional layer adjacent to the solution. The layer closest to the electrode, the inner layer contains solvent molecules and sometimes, ions or molecules, said to be specifically adsorbed. The inner layer, also known as the compact, Helmholtz or Stern layer is only one or two molecular diameters in thickness. The inner Helmholtz plane, IHP, is situated at the position where the locus of the specifically adsorbed ion centres lie, at a distance x_1 . The outer Helmholtz plane, OHP, is situated at a position where the locus of the solvated ion centres lie, at a distance x_2 . The interaction of the specifically and solvated ions (non-specifically adsorbed) with the electrode surface are

short and long range respectively. The diffuse layer is the region between the bulk and the outer Helmholtz plane (OHP) which is recognised as the plane of closest approach for non-specifically adsorbed species. The total charge density from specifically adsorbed ions in the inner layer is σ^i while for the diffuse layer is σ^d . The total charge density for the solution side of the double layer being equal to the sum of the charges, σ^s .

$$\sigma^s = \sigma^i + \sigma^d = -\sigma^M$$

where σ^M is the charge density on the electrode side of the double layer.

1.2 Adsorption of redox active molecules

Adsorption involves the formation of some type of bond between the adsorbate and the electrode surface. The interaction may be merely electrostatic (e.g., the adsorption of cations or anions on a surface of opposite charge) or charge dipole in nature (e.g., the adsorption of amines, thiourea, or benzene) or due to the formation of a covalent bond. Specific adsorption of an electroactive species can dramatically alter the electrochemical response, for example, by forming a blocking layer on the electrode surface.²⁴ The reactivity of a species may also be increased, for example, by causing dissociation of a material that is non reactive prior to adsorption into reactive fragments, such as in the adsorption of aliphatic hydrocarbons on a platinum electrode. Molecules may stick to surfaces in two ways, namely *physisorption* and *chemisorption*. Physisorption is a long range but weak interaction due to van der Waals interactions between the electrode surface and the adsorbed molecule. In chemisorption, the molecules are immobilised on to the electrode surface as a result of the formation of a chemical, and usually a covalent bond, as in the case of alkane-thiols.

The extent of adsorption is usually expressed as a surface coverage, Γ , i.e., the number of moles of the adsorbate per cm^2 . Adsorption must be considered as a competition between all species in the system for sites on the electrode surface. Hence, Γ will depend on the nature of the electrode material, solvent, electrolyte composition, adsorbate structure and

concentration. The coverage of an adsorbate is related to its concentration in solution by an isotherm. There are several isotherms, which differ in the extent and method of taking into account lateral interactions between adjacent adsorbed species. The adsorption isotherm, a plot of surface coverage, Γ vs concentration C , describes the relationship at constant temperature, pressure, and electrical variable between the surface concentration, Γ , and bulk concentration of an adsorbed species. The isotherm is an attempt to separate the electrode-adsorbate interaction, β , which is related to the standard free energy of adsorption, from the lateral adsorbate-adsorbate interactions. The main adsorption isotherms are the Langmuir, Frumkin, and Temkin isotherms. The former does not include interactions occurring between adsorbates on the electrode while the latter two isotherms contains a parameter describing adsorbate interactions. The Langmuir²⁵ and Frumkin^{26,27} isotherms are the two predominately used in this work and shall be discussed in Chapters 5 and 6.

Adsorption is also affected by the potential at which the electrode is poised. This effect manifests itself through the incorporation of ions through the monolayer structure and changes in the surface coverage may become apparent. The charge present on adsorbed ions may depend on the charge on the electrode surface. As would be expected, anions adsorb when the electrode is positively charged, albeit weakly, cations adsorb to a negatively charged electrode and neutral molecules adsorb when no charge is present on the electrode surface, i.e., at the potential of zero charge, PZC.

When most organic molecules adsorb on electrode surfaces, they align themselves in order to attain the most negative free energy of adsorption. However, these orientations depend on certain conditions, such as pH, concentration and temperature. This ability to control the topology of electrode surfaces enables the determination of many interesting facts occurring at the interfacial layer.

1.3 Review of electrode surfaces modified with monolayers

1.3.1 Alkanethiol / Ferrocene alkanethiol monolayers

The formation of ordered monolayer films on a surface by the spontaneous adsorption of molecules from solution in which the adsorbate interacts strongly with both the surface and with itself has become known as self assembly. One of the main types of self assembled monolayer systems, capable of controlling the chemical structure of organic structures has been the adsorption of organosulphur compounds on noble metals such as gold.^{4, 8, 28, 29, 30, 31, 32, 33} Many variations including the effects of chain length,¹² differing linkages,^{34, 35} organic solvents,³⁶ temperature^{37, 38} have been investigated as well as their use in biological systems.^{39, 40}

Silver,^{28, 41, 42, 43, 44} copper²⁸ and ITO^{45, 46} have also been used as substrates for the formation of alkane and ferrocene tagged alkane-thiols. The oxides that form on silver and copper substrates adsorb polar contaminants resulting in a higher surface roughness of the electrode and disruption of the monolayer structures. Mercury electrodes are atomically smooth and have been shown to rapidly adsorb dodecanethiol.⁴⁷ Using a hanging mercury drop electrode, Madja⁴⁷ has shown that the electrode area of modified mercury electrodes can be increased by 30% without generating pin-hole defects. This has enabled the analysis of the observed tunnelling current in terms of two different pathways; through-bond and chain-to-chain coupling.

Monolayers of alkane-thiols and ferrocene alkane-thiols are typically formed by immersion of the substrate into a milli-molar solution of the thiol in question ranging from hours^{48, 49} to a period of days⁵⁰ and sometimes weeks⁵¹ from ethanol, hexane and hexadecane solutions. When the interaction and attachment occurs between the substrate and the thiol the hydrogen from the thiol is thought to be lost⁴².

Analysis of thiols adsorbed onto gold substrates provides an understanding of the kinetics and thermodynamics of these systems at the metal/monolayer interface. They were one of the first to be used for this type of investigation. Analysis was achieved using techniques

ranging from optical ellipsometry²⁸, x-ray photoelectron spectroscopy^{52, 53, 54} to cyclic voltammetry.²⁸⁻³³ Initial observations by Whiteside *et al*^{28, 52, 53, 54} on the characterisation of alkane-thiols suggest that preference occurs in adsorption for long chain thiols over short chain thiols. The strength of binding to the gold surface was found to be decreased for thiols with functional groups such as CH₃, COOH, OH and CN. Alkane-thiol monolayers when adsorbed were found to pack tightly with adsorbates being tilted with respect to the surface normal between 20 and 30°.

Adsorption and desorption of alkane-thiols evoked much early interest. Schneider and Buttry,⁵⁵ using EQCM, studied adsorption behaviour of long chain alkane-thiols on gold adsorbed from non-aqueous solutions by monitoring the mass change of the electrode surface caused by the formation of the self assembled monolayer (SAM). Multi-layer formation was found to occur for monolayer adsorbed from ACN while no such multi-layer formed from DMF. They also found the time-scale for the reductive desorption of the thiols proceeded at a quicker rate in DMF than ACN.

Chidsey and co-workers⁵⁶ studied the co-adsorption of ferrocene-terminated and unsubstituted alkane-thiols on gold. Figure 3 illustrates this system of co-adsorption. They noticed that the addition of the diluent thiol resulted in a marked improvement in the ideality of the ferrocene electrochemical responses. Without dilution voltammetric peak widths were broadened indicating interactions among the ferrocene groups or possibly inhomogeneous sites. Collard and Fox⁵⁷ continued this trend by examining the effect on adsorbed mixed monolayers by placing them in alkane-thiol solutions. They found the diluent thiol replaced the electroactive thiol by one-third of the original surface coverage. Their results are consistent with exchange of thiols at defect sites. Creager and Rowe,^{31, 49} in a series of papers found that increasing the alkane chain length relative to the ferrocene-terminated thiol resulted in the reduction in the amount of ferrocene thiol adsorbed and a positive shift in the formal potential. They explain this shift in terms of the progressively more alkane like environment created by the co-adsorbed alkane-thiols, which stabilises ferricinium relative to ferrocene.

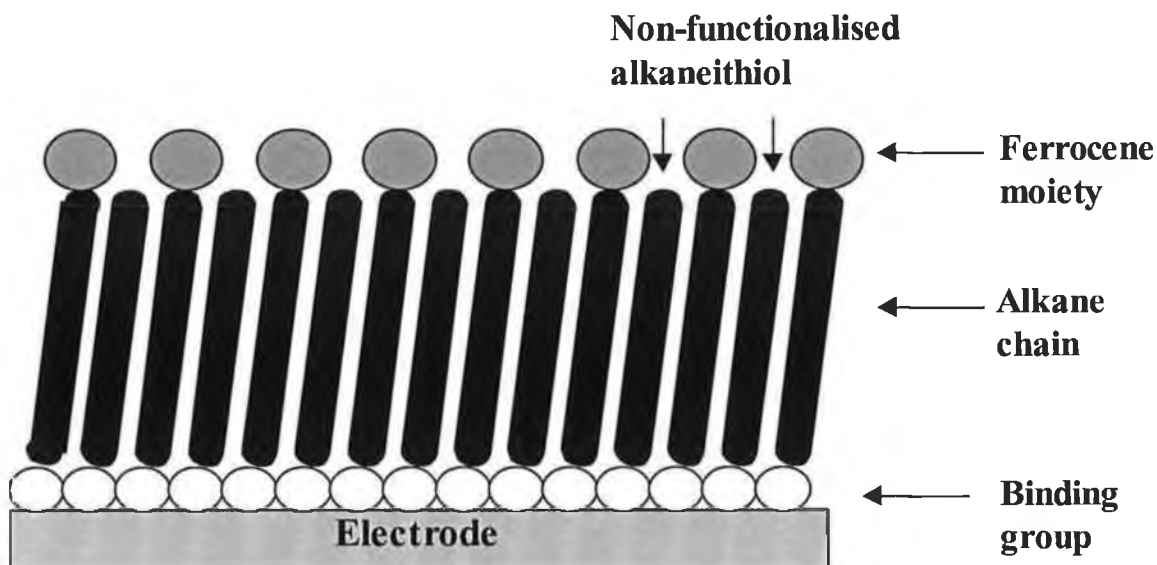


Figure 3 Representation of an electroactive complex adsorbed onto an electrode separated by a diluent alkane chain.

The ability of thiols to co-adsorb onto metal substrates in an ordered, close packed fashion, exhibiting near ideal electrochemistry has enabled the analysis of the thermodynamics and kinetics of electron transfer. Bunding Lee³⁰ who studied electron transfer in alkane-thiol monolayers, found that for non-conjugated hydrocarbon films electron transfer depended on the distance of the electroactive group from the electrode surface. An important paper published by Chidsey⁴ examined the free energy and temperature dependence of electron transfer for gold electrodes adsorbed with ferrocene-terminated alkane thiols. This was a comprehensive piece of research in which he demonstrated that electron transfer follows a tunnelling mechanism, where the dependence of the electron transfer rate on the electrode potential was independent of the length of the alkane bridge. He also gave an insight into the dependence of electron transfer on temperature. Katz⁵⁸ studied both ordered and non-ordered monolayers and the effect this has on electron transfer. Non-ordered monolayers revealed electron transfer rates which were independent of chain length whereas ordered monolayers showed a dependence of the electron transfer rate on chain length. In a series of publications Miller and co-workers^{50, 59, 60, 61} synthesised alkane-thiols with hydroxy tail groups. Dense monolayers were formed which had reduced defect sites and pin holes,

resulting in films which act as effective barriers to redox active species in solution. Electron transfer rates were measured for the solution phase species and found to decrease as the number of methylene spacers increased. Probing the defects within these thiol monolayers by electrochemical measurements indicated that defects do not significantly perturb the kinetic measurements.

Finklea *et al*^{14, 62, 63, 64} examined the thermodynamics and kinetics of electron transfer using self assembled monolayers containing a pendant $\text{Ru}(\text{NH}_3)_5$ redox centre. Semi-log chronoamperometric plots ($\ln i$ vs t) exhibited a deviation from linearity at short times for all overpotentials and electrolytes examined. Finklea attributed this deviation to a population of “fast” redox centres. He suggests that some of the electroactive thiols are attached to defect sites therefore reducing the distance from the electrode to the redox centres resulting in enhanced electron transfer. Consistent with Chidsey’s conclusions⁴ he also notes that one reorganisation energy adequately describes the slope of the Tafel plots at all temperatures. Recently Finklea⁶⁵ examined similar systems, this time forming monolayers where the electroactive thiol is outside, level and inside the diluent thiol. Reorganisation energies obtained from Tafel plots show no systematic trend with chain length. Standard rate constants were found to decrease exponentially with chain length at a rate consistent with a through bond electron tunnelling pathway. A large β for the exposed case and a small β for the buried case is interpreted in terms of multiple paths of electronic coupling between the redox centre and the electrode. Coupling via the diluent thiol, with one through-space step is believed to be the dominant path in the exposed case.

The effects of electrolytes have been extensively investigated for alkane-thiol monolayers. Creager and Rowe^{49, 66} examined interfacial electron transfer and ion-pairing dynamics for such monolayers. The redox potential was dependent on the electrolyte concentration shifting in a negative potential direction with increasing electrolyte concentration. Specific ion pairs were formed between ferricinium and several ions. The propensity of ClO_4^- to ion-pair increased as the local medium around ferrocene became more alkane like, a result found by Shimazu and co-workers³³ and Leech.¹³ DeLong and Buttry¹⁵ also found an association of anions with ferrocene following oxidation to the ferricinium state.

In a subsequent paper⁶⁷ alkane-thiols were adsorbed where viologen groups were present within the alkane-thiol. Results suggested the degree of solvation of the viologen moiety depends on the proximity to the monolayer/solution interface. Also the formal potential in this case was found to be more negative in ClO_4^- electrolyte over Cl^- , an expected result based on the hydrophobicity of ClO_4^- relative to Cl^- . A theoretical approach was adopted by Andreu *et al* when examining ion-pairing and double layer effects⁶⁸. They discovered a strong coupling between both that may lead in some situations to the same variation of the peak potential with decreasing concentration.

1.3.2 Osmium and ruthenium polypyridyl monolayers

The majority of research groups devoted to understanding heterogeneous electron transfer, adsorption/desorption and interfacial processes have focused on the ability of ferrocene alkanethiols to adsorb on metal substrates as organic films as discussed in section 2.1. However, a few groups, namely those of Abruña and Forster have synthesised and used new osmium and ruthenium polypyridyl complexes to investigate the above phenomena. Osmium polypyridyl complexes were preferred over ruthenium analogues due to their lower oxidation potentials. This lower oxidation is of great importance as it reduces interference from the effects of electrode oxidation which may hamper electrochemical analysis of ruthenium polypyridyl complexes.

In an early publication, Acevedo and Abruña¹ investigated how changing the solvent affects the formal potential of the redox-active self assembling system $[\text{Os}(\text{bpy})_2(\text{dipy})\text{Cl}]^{1+}$ (bpy, 2,2'-bipyridine; dipy, 4,4'-trimethylenedipyridine) in various organic solvents and aqueous solutions. The complex was found to adsorb from organic solvents to a much lesser extent than in aqueous solution presumably because of higher solubility. There was little or no dependence of the surface coverage on ionic strength but a strong dependence on pH was observed. Interestingly, they observed an increase ($\sim 30\%$) in the double-layer capacitance when the monolayer was switched from a reduced to an oxidised form which may reflect a higher degree of ionic charge within the monolayer for the 2^+ form. They conclude that the variation of the formal potential with coverage indicated the formation of a spread submonolayer as the coverage decreases as opposed to island formation. Ion-pair

formation with the perchlorate anions and the cationic head groups strongly influences the energetics of the redox system. Heterogeneous electron transfer rate constants were of the order of 10^5 s^{-1} .

Abruña⁶⁹ presented a comprehensive study of the adsorption kinetics for an analogous compound where the ligand length was altered in each case. He investigated the effects of deposition potential, pH and ionic strength on the adsorption energetics. The coverage was found to be lower for both non-aqueous solvents and when the pH of the deposition was reduced. The pH dependence arises because protonation of the pendant nitrogen which chemisorbs onto the electrode surface blocks the adsorption of the complex. At low concentrations they believe that an induction period takes place until a variation in local concentration achieves a critical value after which adsorption is induced. Also, the ionic strength did not effect the adsorption isotherms.

An important paper was published by Hudson and Abruña⁷⁰ on osmium polypyridyl based complexes, which studied the formation and structure of the self assembling osmium complexes using scanning tunnelling microscopy (STM) and electrochemical scanning tunnelling microscopy (ECSTM). Using cyclic voltammetry, they monitored the coverage of the adsorbing monolayer in real time while employing ECSTM to study the structure of the submonolayer. Their results suggest the spread of a submonolayer uniformly across the sample surface due to electrostatic repulsions between adsorbate molecules and the apparent high mobility of the osmium complex molecules on the sample surface. At higher coverages, regions of the adsorbate layer lose part of their solvation to accommodate further adsorption and closer packing of the monolayer. Ex-situ STM showed that fully formed monolayers appear to be crystalline forming tightly packed two dimensional crystals on the sample surface, with unit cell dimensions of 9.3 ± 0.3 by $12.4 \pm 0.4 \text{ \AA}$.

Abruña⁷¹, in conjunction with Bretz continued this research into osmium containing complexes, this time synthesising a new series of compounds $[\text{Os}(\text{bpy})_2\text{Cl}(\text{Py}-(\text{CH}_2)_n\text{-SH})](\text{PF}_6)$, with $n = 4, 6$, and 9 ; $\text{py} = \text{pyridine}$. They investigated the effect of the applied potential on the adsorption of these new complexes on gold, platinum and silver. They state that by controlling the potential applied to the working electrode during deposition to

values both positive and negative of the potential of zero charge, E_{pzc} , that the effect of electrostatic forces between the electrode and the redox active osmium involved in the adsorption process may be studied. In the reduced form the Os^{2+} complexes studied have a net +1 charge and in the oxidised form Os^{3+} , a net +2 charge is present, i.e., in the oxidised form the repulsive forces exhibited will be stronger than those in the reduced form due to the increase in the charge on the complex with oxidation. Results show that at potentials positive of the E_{pzc} , the amount deposited was much smaller and virtually independent of the applied potential, than the amount deposited at potentials negative of the E_{pzc} . At values positive of the E_{pzc} , a sharp decrease in coverage was observed for all complexes with varying chain length. The only difference being the position of the sharp decrease in coverage, which they showed was due to the electrode material. The discontinuity occurred at the E_{pzc} of each electrode. Attractive forces seem to play a role in the amount of osmium complex adsorbed. However, at potentials positive of the E_{pzc} repulsive forces do not play a dominant role in the amount of material adsorbed.

Abruña⁷² and Bretz also examined the adsorption and desorption of these redox-active osmium thiol monolayers. For these complexes they found no influence on the amount adsorbed from solution pH and ionic strength. This finding is interesting since for the osmium pyridine complexes pH plays a key role in the amount of adsorbate adsorbed.¹⁶ Multilayer formation of these monolayers was also prevalent for the osmium thiol systems a property also noticed by Chidsey⁴ for pure ferrocene thiol complexes. Abruña found their results consistent with the Freundlich model, a model which does not require a saturation coverage. The desorption kinetics of the complexes were found to follow an exponential expression with an increase in the rate at elevated temperatures. We have also examined the desorption of adsorbed species. However, for our system we examined multi-component monolayers and found that while one component desorbed by first order kinetics, the surface coverage of the second component increased without effecting the desorption of the former.

Abruña⁷³ has also studied the exchange dynamics between adsorbed osmium and ruthenium complexes. The exchange appears to be controlled by a dissociative mechanism whereby the desorption of one molecule occurs before adsorption into the vacant site. They found

increased broadening in the ruthenium wave over the osmium wave, which was probably due to an enhanced degree of electrostatic repulsion. Chapter 6 of this thesis deals with investigations into the exchange dynamics between adsorbed species without the complication of electrostatics by using quinone species where proton and electron transfer is coupled.

Forster and Faulkner^{2, 3} published two papers in which they examined the ability of existing electron transfer models to accurately predict the potential and temperature dependence of electrode kinetics. Their first paper² reported on ionic interactions and heterogeneous electron transfer kinetics within a family of spontaneously adsorbed monolayers of $[\text{Os}(\text{bpy})_2\text{Cl}(\text{pNp})]^+$, where bpy was 2,2'-bipyridyl, and pNp was 4,4'-bipyridyl, 1,2-bis(4-pyridyl)ethane, or 4,4'-trimethylenedipyridine. They investigated the electrochemical response of the spontaneously adsorbed monolayers as a function of electrolyte, solvent, temperature and electron transfer distance. They determined the interfacial capacitance as a function of potential and found that the interfacial capacitance depended on the redox composition of the monolayer. An increase in interfacial capacitance was noted as the films became increasingly oxidised. It was also noted that hydrophilic anions gave a higher interfacial capacitance than lipophilic anions, suggesting that the extent of ion pairing and solvent penetration across the monolayer/electrolyte interface was dependent on the anion in solution. Ion pairing was probed and they suggest a single extra anion becomes paired with the redox centre upon oxidation and the extent of ion pairing to be solvent dependent. The temperature dependence of the formal potential over the range -5 to 40 °C showed that the reaction entropy ($\Delta S_{\text{rc}}^\circ$) was positive indicating increased solvent ordering in the higher oxidation state. A correlation was observed between the experimentally determined $\Delta S_{\text{rc}}^\circ$ and that predicated by the Born dielectric continuum theory model compound with a slope of near unity being observed. Tafel plots of the dependence of $\ln k$ (heterogeneous electron transfer rate constant) on overpotential showed curvature (non-linear response), indicating that the transfer coefficient was potential dependant. The Tafel plots were consistent with the Butler-Volmer formulation of the potential dependence of electrochemical reaction rates. They observed a higher cathodic than anodic rate constant for a given overpotential (η), which an existing electron transfer model predicts for a through-space tunnelling

mechanism. η may be defined as the deviation of the potential from the equilibrium value, ($\eta = E - E_{eq}$).

In the subsequent paper,³ Forster and Faulkner explored the effects of solvent, potential and temperature on the kinetics and thermodynamics of heterogeneous electron transfer. Initially, they constructed Arrhenius plots of $\ln k$ vs temperature as a function of overpotential (η). The plots were linear over a temperature range of -5 to 40 °C. From the slopes the ideal electrochemical enthalpy (ΔH_1^\ddagger) was calculated and the potential dependence of the ideal electrochemical enthalpy measured. They observed that the transfer coefficient's for the osmium monolayers are at best very weakly temperature dependent, consistent with their assumption they were probing the elementary electron transfer event in a simple outer-sphere electron transfer. They also found evidence from the temperature derivatives of the transfer coefficients that they are too small to explain the relative insensitivity of ΔH_1^\ddagger to changes in η . The results showed that the entropy of activation depended markedly on potential. They calculated the potential dependence of ΔH_1^\ddagger using an overlap integral model. The results predicted that ΔH_1^\ddagger was less sensitive to changes in potential than was predicted by the Butler-Volmer formulation. The model was also used to calculate the potential dependence of the pre-exponential factor and found it to predict both the sign and the approximate magnitude of the slope for a plot of $\ln [A_{et} \exp(\Delta S^\ddagger)]$ vs η . On the basis of the above observations they concluded that the Butler-Volmer approach was not useful for understanding the activation parameters of electrode kinetics. They examined the effect of solvent reorganisation on the rate of electron transfer and found solvent relaxation dynamics strongly influence the electron transfer rates. The adiabaticity of the reaction was analysed by calculating the electronic transmission coefficient k_{el} from the pre-exponential factor. The transmission factor obtained was less than unity, indicating a low probability of electron transfer from the metal to the redox centre and therefore suggesting a nonadiabatic reaction. However, existing models of electron transfer did not predict an apparently nonadiabatic reaction.

Forster and Faulkner⁷⁴ also investigated the kinetic separation of mixed monolayers of osmium and ruthenium polypyridyl complexes using chronoamperometry. First, using

complexes where the metal centres were different cyclic voltammetry was used to determine the surface coverages as their formal potentials were separated by approximately 380 mV. Then using the intercept from the first order plots from their chronoamperometric responses, a second estimate of the surface coverage was determined. An excellent correlation was achieved. With this in mind Forster analysed mixed monolayers of osmium complexes with identical formal potentials where the only difference was the length of the bridging ligand. This was achieved by forming a partial monolayer of one monolayer and backfilling with the second component. The difference in bridging ligand length lead to differences in their rate constants. Again using chronoamperometry, the current response revealed three decays, one for double layer charging and the other two for the osmium complexes. Forster calculated the surface coverages of both osmium complexes to be identical for both methods used. The complexes were found to adsorb according to the Langmuir isotherm with no alteration in behaviour during the backfilling procedure. This analysis indicates that lateral interactions are not significant.

Forster,⁷⁵ using an analogous system to his previous reports, investigated heterogeneous kinetics of both metal and ligand based redox reactions within adsorbed monolayers of $[\text{Os}(\text{bpy})_2\text{py}(\text{p3p})]^{2+}$, where py is pyridine, bpy is 2,2'-bipyridyl and P_3P is 4,4'-trimethylenedipyridine. Using chronoamperometry, rate constants corresponding to osmium and bipyridyl based redox reactions were obtained. As predicted by Marcus theory,⁷⁶ Tafel plots showed curvature at high overpotential (η) for all three redox reactions. Probing the temperature dependence of the formal potential Forster found that the reaction entropy ($\Delta S_{\text{rc}}^\circ$) depends on the state of charge on the monolayer. The electronic transmission coefficient (k_{el}) was also found to be larger for the bipyridyl based reactions compared with the metal based reaction.

More recently Forster and O'Kelly¹⁶ have investigated the factors that influence heterogeneous electron transfer. They formed dense monolayers by spontaneously adsorbing $[\text{Os}(\text{bpy})_2(\text{P}_3\text{P})_2]^{2+}$ complexes, where bpy was 2,2'-bipyridyl and P_3P was 4,4'-trimethylenedipyridine, onto clean platinum microelectrodes. They found that cyclic voltammetry of these adsorbed monolayers in aqueous perchlorate solutions was nearly

ideal over a wide pH and temperature range. In this instance, adsorption occurs through the pendant nitrogen from one of the P3P ligands. It appears that the bite angle imposed by having the pyridine moieties of both P3P ligands adsorb results in weak interaction of the pyridine lone pair with the surface causing adsorption to occur through only one P3P ligand. It is the free ligand which allows pH effects be studied. The ideal behaviour allowed them to probe both thermodynamic and kinetic aspects of heterogeneous electron transfer across metal/monolayer interfaces. They concluded that the reaction entropy ΔS_{rc}° was unaffected by protonating the adsorbed complex. In addition, monolayer protonation effects the electron transfer dynamics by changing both the free energy of activation ΔG^{\ddagger} and the degree of electronic coupling, k_{el} .

A recent publication by Campbell and Anson⁷⁷ focused on the unusually strong adsorption of osmium polypyridyl and other related complexes onto gold and pyrolytic graphite electrodes. Strong adsorption of all complexes occurred on graphite electrodes and all with the exception of pyridine, as Ligand, onto gold. They conclude that adsorption appears to be driven by hydrophobic interactions of the organic ligands with the electrode surface and with each other, as well as specific surface-ligand bond formation when a pendant pyridine group is present. Although the concentration dependence of the surface coverages could be modelled by a Langmuir isotherm, they conclude that the dynamics of the adsorption and desorption reactions were not consistent with Langmuirian adsorption. Their main conclusion was that the unusual stability of the adsorbed layers arises because intermolecular reactions among the aromatic rings of the ligands coordinated to the metal centre, produce a surface phase that equilibrates only slowly with aqueous solutions to which it is exposed.

1.3.3 Adsorption of quinones

As they often exhibit well behaved electrochemistry, quinone/hydroquinone (Q/H₂Q) couples have been widely used in electrochemical studies.^{78, 79, 80} Interest in these complexes has increased since Gill and Stonehill⁸¹ investigated the redox behaviour of certain hydroxy- and sulphonic acid derivatives of anthraquinone.

Soriaga and Hubbard carried out some pioneering research on aromatic compounds adsorbed onto platinum electrodes. Their initial investigations⁸² centred on the determination of the orientation of some 40 aromatic compounds including phenols, halogenated diphenols, polycyclic quinones and hydroquinone mercaptans. They determined the limiting coverage of these interesting compounds and used the coverages to calculate the area occupied per molecule on the electrode surface. They compared their results with values calculated for various orientations. Most of the 40 compounds adopted the flat orientation, i.e., benzene ring parallel to the electrode surface. Aromatic compounds containing side chains such as amines predominately adsorbed in a flat orientation with a percentage of the complex adopting the position where the amine is attached to the electrode surface. The quinones examined by Soriaga which are of relevance to this thesis, anthraquinone-1,5-disulphonic acid and anthraquinone-2,6-disulphonic acid, were found to adopt a flat orientation on the electrode surface.

Their following paper examined the effect of exposure of adsorbed aromatic compounds to the surface active anion, iodide⁸³. Twenty eight compounds were analysed with respect to changes in their surface coverage, mode of orientation and change in the position of attachment. Results indicated that displacement by iodide solutions was greatest in acid media. Thiol aromatic complexes were unaffected. Alkyl substituents present on aromatic compound were found to stabilise displacement. While monocyclic complexes re-orientated with exposure, polycyclic complexes such as anthraquinone-2,6-disulphonic acid were found only to desorb. In general, re-orientations induced by iodide convert structures making inefficient use of surface area into orientations occupying smaller surface area.

They next examined the effect of solute concentration on a series of similar compounds using thin layer cells⁸⁴. Plots of coverage versus concentration showed that most of the compounds displayed multiple plateaus separated by abrupt transitions to higher densities at higher concentrations. The values of the coverage at the plateaus were compared to a model calculation and a series of orientations were found to be adopted as the solute concentration increased. Each individual orientation was stable over an appreciable range of concentrations. In all 26 compounds examined, those analogous to the ones used in this thesis showed no change in orientation with increasing concentration. They attribute this

resistance to orientation to an entropy effect: in the flat orientation, the three fused rings can each interact with the platinum surface, whereas the edgewise orientations would permit only limited interaction.

In keeping with the concept of the orientation of aromatic compounds, Soriaga and Hubbard as well as White⁸⁵ investigated the effect of temperature on a limited number of aromatic compounds. Anthraquinone-1,5-disulphonic acid and analogous polycyclic compounds of which are relevant here were found to be independent of temperature for orientation. Compounds such as anthraquinones, whose orientation changed with increasing concentration as previously discussed were effected resulting, they say, in an increased packing density at low concentration with more sharply defined transitions.

Forster also contributed to the area of analysis of quinones adsorbed onto mercury electrodes in a number of papers.^{86, 87, 88, 89} The first pair of these papers dealt with the adsorption and elucidation of the kinetic parameters of mixed monolayers.⁸⁶ Anthraquinone-2,6-disulphonic acid and anthraquinone-1,5-disulphonic with identical formal potentials were adsorbed onto mercury microelectrodes, initially as single component monolayers and then as mixed systems. Using chronoamperometry and the fact that both quinones exhibit different heterogeneous electron transfer rate constants their individual surface coverages in mixed monolayer systems could be determined. One of the reasons this was possible was the similarity in the free energies of adsorption (β) of both complexes determined in their pure state, although this is not necessarily a precondition. Forster's second mixed quinone monolayer paper was similar to the previous paper, this time elucidating surface coverages using adriamycin and quinizarin as the quinone couples with identical formal potentials.⁸⁹

The effect of potential on the adsorption thermodynamics of quinone monolayers was also probed by Forster and co workers in three separate papers. In the first paper, monolayers of 2-hydroxyanthraquinone (2OH-AQ) were found to adsorb onto mercury microelectrodes in an ideal manner and adsorption followed the Langmuir isotherm. The potential dependence of the free energy of adsorption was examined by analysing capacitance data determined using potential step chronoamperometry. Forster concluded that a change in the free

energy of adsorption occurs when the redox state of the monolayer is changed. This appears to be due to differences in hydrogen bonding within the reduced and oxidised forms of the monolayer.

The electrochemical behaviour of anthraquinone-2-carboxylic acid (2-AQCA) monolayers was also analysed.⁸⁷ As well as investigating the adsorption characteristics of 2-AQCA as previously discussed,⁸⁸ he examined the potential dependence of the electron transfer rate constant as a function of pH. Tafel plots suggested that pH was influencing the rate constants indicating a coupled proton/electron process taking place. Together with O'Kelly,⁹⁰ Forster investigated the electrochemistry of anthraquinone-2,7-disulphonic acid (2,7-AQDS). This analysis was in keeping with the previous two papers in so much as it investigated the potential dependent adsorption of 2,7-AQDS.

1.3.3.1 Hydrogen bonding effects within adsorbed quinone monolayers.

Adsorbed quinones often exhibit near ideal electrochemical responses. However, some authors have investigated systems which show anomalously sharp spikes in their voltammetric responses.

A careful study was presented by Faulkner and co-workers dealing with the adsorption of a series of sulphonated quinones (1,5- and 2,6-AQDS) adsorbed onto mercury.⁹¹ Using chronocoulometry and cyclic voltammetry they evaluated the effect of quinone concentration on the surface coverage. Adsorption followed the Langmuir isotherm up to concentrations of 5×10^{-5} M. An interesting result was obtained in concentrations above 2×10^{-5} M. An extremely sharp reversible pair of spikes developed in the cyclic voltammogram for the adsorbed 2,6-AQDS redox couple. It was proposed that intermolecular hydrogen bonds were the source of the attractive interactions. Examples of these types of interactions may be found in Chapter 5, Section 5.2.3.2. A slight elaboration of this model could involve a $-\text{CO}---\text{HO}_3\text{S}-$ grouping in the oxidised reactant at pH values low enough to produce significant protonation of the sulphonated groups and an $-\text{OH}---\text{O}_3\text{S}-$ grouping in the reduced reactant.

Graphite electrodes were used by Zhang and Anson when investigating the voltammetry of anthraquinone disulphonates.⁹² They investigated the pH dependence of the spike and found that the behaviour is strongly pH dependent. The presence of the spike diminished and ultimately was eliminated at pH 3.7. This behaviour suggests, that protonation of the sulphonate groups diminishes electrostatic repulsions which may be important in facilitating intermolecular attractions which are responsible for the narrow spikes.

McDermott *et al*⁹³ also discovered the presence of the spike for 2,6-AQDS on ordered graphite electrodes. They presume the spike is due to significant intermolecular interactions and used STM and SFM to aid their investigation. They found 2,6-AQDS adsorbed in an extremely ordered fashion that the formation of this ordered state was important for observing the spike response. The disappearance of the spike correlated with the disassembly of the linear domains found in STM images.

The spike is observed when 2,6-AQDS has been adsorbed on graphite and mercury electrodes. This appearance on various electrode substrates adds weight to the suggestion of intermolecular hydrogen bonding as the source of the development of the spike and not interaction between the substrate and electrode surface.

The above-cited papers, which are relevant to the scope of this thesis, do not impart all knowledge of these fascinating compounds. Therefore, the interested reader should consult insightful reviews such as Chambers^{94, 95} and Hubbard⁹⁶ for quinoid compounds and Swallen for a review on molecular monolayers and films.⁸

1.4 Microelectrodes

1.4.1 Introduction

It is clear from the above review that heterogeneous electron transfer across the electrode / monolayer interface can be a very rapid process e.g., 10^5 s⁻¹ in the case of osmium polypyridyl systems. Therefore, an important objective is the development of fast electrochemical methods. To achieve microsecond and shorter timescales it is vital to

shrink the size of the working electrode to micrometer dimensions. The ability to routinely fabricate electrodes with radii smaller than one hundredth of the thickness of a human hair has profoundly changed the way one goes about doing electrochemistry. For this thesis, microelectrodes have been fabricated in order to extend the timescale in which to perform electrochemical experiments. Complexes, which have standard rate constants in the order of 10^5 s^{-1} cannot be determined by cyclic voltammetry unless scan rates up to 1000 Vs^{-1} may be performed with no interference from ohmic drop.

A microelectrode, or ultramicroelectrode (UME) as they are also known, is an electrode whose smallest dimension is in the micrometer range. The importance of microelectrodes is widely recognised and interest in their construction^{97, 98, 99, 100} and application in diverse areas of research has been increasing over the past 15 years.^{101, 102, 103, 104, 105} There has been an explosion of interest in the properties of microelectrodes because of their potential use in areas where conventional electrodes cannot be used or expensive alternative instrumentation is needed. Microelectrodes have made both a fundamental and applied impact on electrochemistry unequalled by almost any other electrochemical approach in recent times. The increase in recent years of the number of papers published, dealing with the theory and applications of microelectrodes, serves to increase our understanding of their properties and has revealed many new applications.^{101, 102, 103, 104, 105} By using microelectrodes the reduction in experimental timescale presents new opportunities for applications of voltammetry in the characterisation of solution redox behaviour as well as chemical analysis.¹⁰⁶ Voltammetry using microelectrodes has many advantages in the measurement of heterogeneous-electron transfer rates compared to macroelectrodes. These advantages include: First, the ability of microelectrodes to respond rapidly to changes in the applied potential. Second, their immunity to 'ohmic drop' phenomena, which allows experiments to be performed in non-polar solvents, supercritical fluids and solids. Third, diffusional mass transport is made extremely efficient using microelectrodes, and capacitance is reduced.¹⁰¹ The special features of mass transport to microelectrodes, including their distinctive behaviour at long times, are important advantages of microelectrodes which shall be discussed below.

1.4.2 Microelectrode geometries

The critical dimensions of microelectrodes generally fall in the range of 0.1 - 50 μm . However, researchers have also fabricated microelectrodes with dimensions as small as 10 \AA .¹⁰⁷ The geometries of microelectrodes range from discs and bands to integrated arrays. Figure 4 lists the most commonly used microelectrodes.

Microdisk electrodes are the most commonly employed and 50% of all investigations use them. Cylinders and arrays make up 20% each and the remaining 10% comprise of spheres and hemispheres etc. The materials used in their manufacture vary from iridium to superconducting ceramics. However, the most commonly employed materials are gold, platinum and carbon fibre. The reason microdisks predominate is because they are readily constructed by sealing very fine wires into an insulating material, e.g., glass, cutting perpendicular to the axis of the wire and polishing the front face of the disc which is created, leading to a reproducible surface. The construction of gold microdisk electrodes is discussed in considerably more detail in chapter 3.

1.4.3 Mass transport

Microelectrodes have very important properties, one of which is the mass transport of species to the electrode surface. Although the scope of this thesis is in the electrochemical analysis of surface confined species it is important to consider diffusional processes at various electrode dimensions. This is because shrinking the radius of the electrode affects the diffusion process, which may be manifested in the experimental response, i.e., steady state responses may be observed when a smaller size electrode is used. There are two main limiting regimes depending on the experimental timescale, i.e., being long or short.

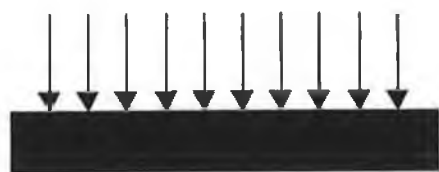
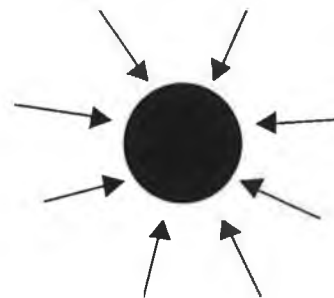
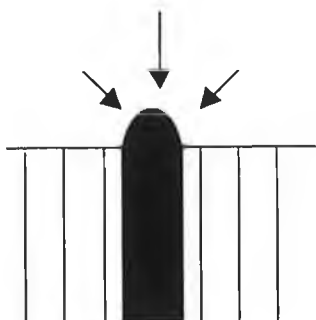
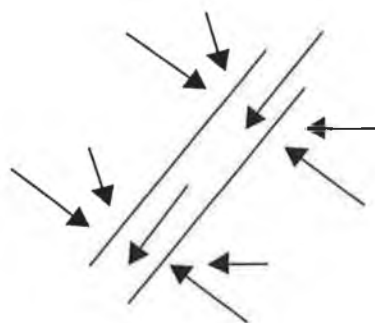
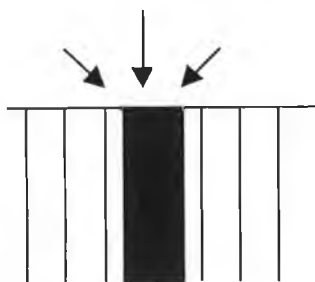
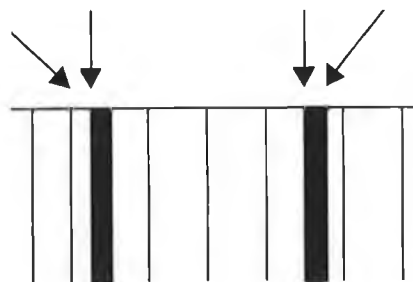
**Semi infinite planar electrode****Spherical electrode****Hemispherical electrode****Line electrode****Disk electrode****Ring electrode**

Figure 4 Illustration of the common types of microelectrode and their diffusion fields.

1.4.3.1 Short times

At short times a transient will be observed similar to one at a large electrode where linear diffusion to a plane electrode is the appropriate description of the mass transport regime, i_d is given by the Cottrell equation.

$$i(t) = \frac{nFAD^{1/2}C^\infty}{\pi^{1/2}t^{1/2}} \quad \text{Eq. 1}$$

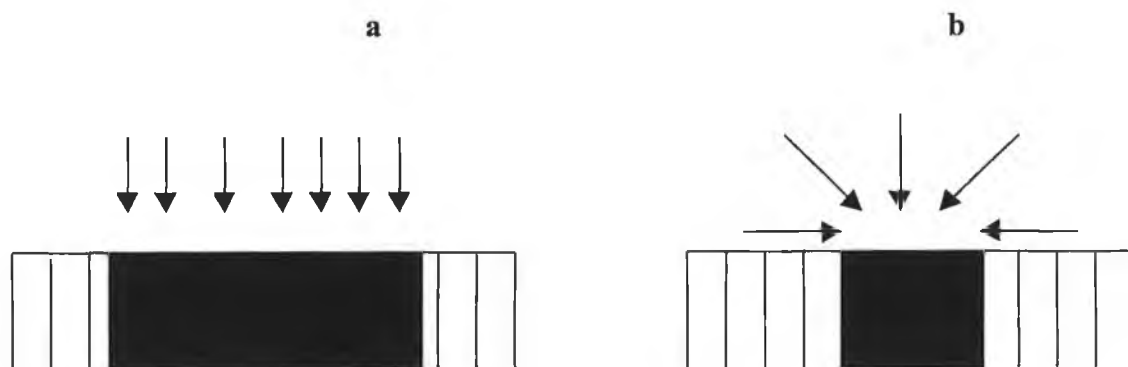


Figure 5 The time-dependence of the diffusion field at microelectrodes. (a) Linear diffusion at short times and (b) radial diffusion at long times.

1.4.3.2 Long times

When the timescale becomes sufficiently long, the transient current density will decrease to a negligible value and the current reaches a steady state value, as given by Equation 2:

$$i_{ss} = \frac{nFADC^\infty}{r_s} \quad \text{Eq. 2}$$

At these long times, the spherical character r_s of the electrode becomes important and mass transport is dominated by radial or spherical diffusion as illustrated in Figure 5 (b). The

steady state response (sigmoidal) arises because the electrolysis rate is equal to the rate at which molecules diffuse to the electrode surface. The experimental response of mass transport to microdisk electrodes is more complicated than spherical electrodes because a disk is not a uniformly accessible electrode. The flux of material reacting is unequal across the electrode surface.¹⁰⁸ This is because electrolysis that occurs at the outer circumference of the disk diminishes the flux of redox active material to the centre of the electrode. However, microdisk geometries share the advantage of spherical microelectrodes in that quasi-spherical diffusion fields are established within short lengths of time.

$$i_{ss} = 4nFDC^{\infty}r \quad \text{Eq. 3}$$

where r is the radius of the disk.

1.4.4 Microelectrode characteristics

1.4.4.1 RC time constant

When a potential is applied across the metal of an electrode, placed in an electrolytic medium, a double layer is formed in which the charge on the metal is compensated for by a layer of oppositely charged ions from the medium. This process is accompanied by the flow of a charging current, characterised by the RC time constant, where R is the solution resistance and C the double layer capacitance. Following a potential step experiment from $E_1 - E_2$ (ΔE) decreases exponentially in time at a rate determined by RC.

$$i_c = \frac{\Delta E}{R} \exp\left(\frac{-t}{RC}\right) \quad \text{Eq. 4}$$

RC cell time constants may be as short as 25 ns for a 5 μm gold microdisk electrode in 0.1 M LiClO_4 . Using higher concentrations of electrolyte may significantly decrease the RC values. This time constant defines the shortest time domain over which the cell will accept a significant perturbation. Microelectrodes reduce the amplitude of the charging current and the overall RC time constant making it possible for electrochemical measurements to

take place in a very short time regime, e.g., by rapid scan cyclic voltammetry and high-speed chronoamperometry. These short times make it possible to measure heterogeneous electron transfer rate constants for kinetically facile spontaneously adsorbed complexes on metal microelectrodes.

The resistance in an electrochemical cell depends on the specific conductance of the medium and the electrode radius (r_s);

$$R = \frac{1}{4\pi\kappa r_s} \quad \text{Eq. 5}$$

where κ is the specific conductivity of the electrolyte. Eq. 5 reveals that the resistance increases with decreasing electrode radius, which does not favour short response times. However, the RC time constant depends on both the resistance and capacitance. Since the electrode capacitance is proportional to the electrode area or r^2 , the product RC decreases with decreasing electrode radius. When dealing with spontaneously adsorbed monolayers on microelectrodes with fast heterogeneous electron transfer rates, the Faradaic and charging currents may be convolved. Useful analytical information may only be obtained when the Faradaic portion of the decay is at least 5-10 times longer than the non-Faradaic portion of the decay.

1.4.4.2 Ohmic drop

Ohmic effects occur when Faradaic and charging currents flow through a solution generating a potential that acts to weaken the applied potential by an amount iR , where i is the total current and R is the resistance of the cell. This iR drop can lead to distorted responses. It has been mentioned previously that resistance increases with decreasing electrode radius. However, since the currents observed at microelectrodes are typically six orders of magnitude less than conventional macroelectrodes, ohmic effects are significantly reduced or eliminated, even when working in organic compounds where resistances are quite high. Reducing the size of an electrode from a typical macroelectrode size of 2.5 mm to 5 μm decreases the ohmic drop observed at short times by a factor of 500. In contrast,

Eq. 2 shows that at long times and in steady state conditions i_{ss} is proportional to r_s and the iR drop is independent of the size of the electrode.

1.4.5 Applications of microelectrodes

The fact that the size of electrode material has been reduced over the years has led to a reduction in the diameter of electrodes. This in turn has increased the area's for analysis. Microelectrodes have been used to increase the sensitivity of anodic stripping voltammetry of heavy metals,^{109, 110} within an on-column electrochemical detector for open-tubular liquid chromatography for the detection of ascorbic acid and catechol.¹¹¹ More recently microelectrodes have been used in the *in-vivo* analysis of blood plasma.¹¹² These sample analyses have only been possible due to the reduced ohmic drop from microelectrodes as the samples are highly resistive. Analyses of other samples of high resistivity, which may be analysed, are resins, paints and solids to name a few. The uses of solvents of low dielectric constants such as hexane and toluene have been reported along with analyses in oils. The area, which has probably seen the largest increase in the use of microelectrodes, must be that of electron transfer.

1.5 Electrochemical techniques

1.5.1 Cyclic voltammetry

Voltammetry comprises of a group of electroanalytical techniques, of which cyclic voltammetry (CV) is one, in which information about the analyte is derived from the measurement of current as a function of applied potential. Although primarily a qualitative technique, quantitative measurements may be performed.¹¹³ Cyclic voltammetry is widely used by inorganic, physical and biological chemists for analytical and non-analytical purposes including fundamental studies of oxidation and reduction processes in various media, adsorption processes on surfaces and electron transfer mechanisms at chemically modified surfaces and gives an insight into the packing, order and orientation of surface confined species.

Cyclic voltammetry consists of cycling the potential of a stationary electrode immersed in a quiescent solution and measuring the resulting current. The excitation signal is a linear potential scan with a triangular waveform as seen in Figure 6.¹¹⁴ Symmetrical scan rates range from a few milli-volts per second to thousands of volts per second depending on the size of the electrode used. The potential signal sweeps the potential of the working electrode back and forth between two designated values called switching potentials. The potential cycling may be repeated several times. The scan direction may be altered depending on the initial conditions being the oxidation or reduction of the analyte.

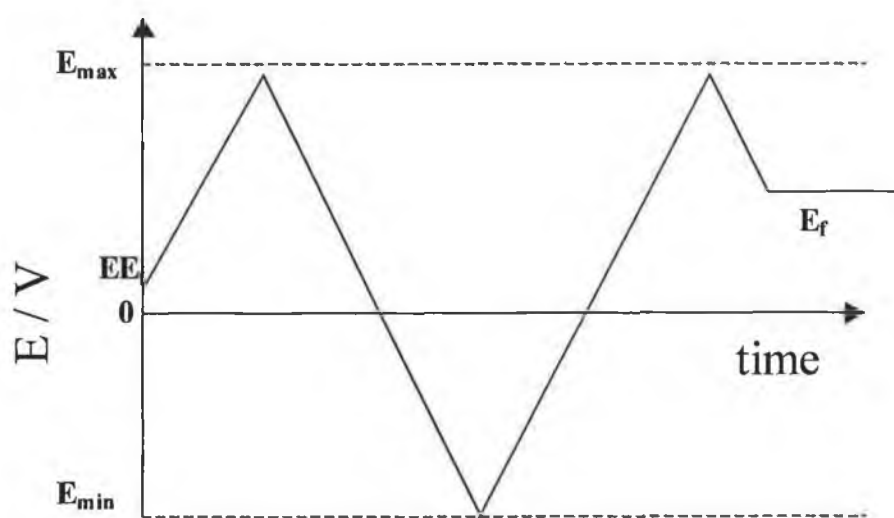


Figure 6 Potential waveform for cyclic voltammogram. E_i is the initial potential, E_f the final potential, E_{max} , the maximum and E_{min} the minimum potentials.

The voltammograms obtained using CV depend on varying factors including the electrode size, scan rate employed and whether the species being examined is in solution or adsorbed on the electrode surface. The following section deals with the differing types of voltammograms as both will be in evidence during the course of this thesis.

1.5.1.1 Solution phase electrochemistry

Figure 7 shows a typical current response for a solution containing $\text{Os}(\text{bpy})_3$ where bpy is 2,2'-bipyridine. Consider the situation where the redox species is being oxidised. At the initial potential of 0.2 V no current is observed as no oxidisable or reducible species is present in this potential range. When the potential approaches the point where oxidation of the species is observed an anodic current develops due to the oxidation of Os^{2+} to Os^{3+} . A rapid increase in current occurs as the concentration of Os^{2+} at the electrode surface becomes smaller. At the formal potential there exists 50% of Os^{2+} and 50% of Os^{3+} at the electrode surface. Past the peak potential the current decays as the diffusion layer is extended farther away from the surface. When the potential is switched the current remains anodic as the potentials are still positive enough to oxidise the Os^{2+} . Once the potential becomes sufficiently negative so oxidation can no longer occur, the current goes to zero and then becomes cathodic. The cathodic current results from the reduction of Os^{3+} that accumulates at the surface during the forward scan. The cathodic current peaks and then decreases as the Os^{3+} is used up by the reduction reaction.

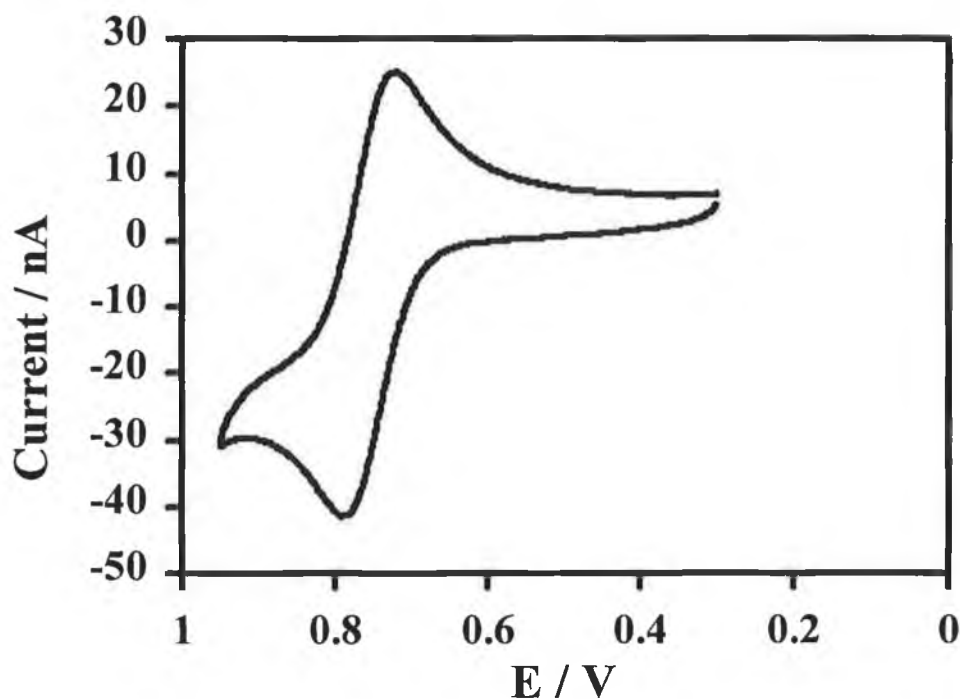


Figure 7 Solution phase CV response for a 1 mM solution of $\text{Os}(\text{bpy})_3$ in CH_3CN with 0.1 M TBABF_4 as the electrolyte. A 25 μm platinum electrode was used. The initial potential is 0.3 V. The scan rate is 0.5 Vs^{-1} .

Figure 7 shows the CV response for an electrode being scanned at high scan rates. The electrochemical response at slow scan rates (long experimental timescale) is markedly different. Figure 8 represents the CV response for a freely diffusing species at low scan rates. In this instance, the scan rate is sufficiently slow in order for a steady state response (sigmoidal) to be observed. A sigmoidal response indicates that the electrolysis rate is equal to the rate at which molecules diffuse to the electrode surface and therefore, the CV response from the anodic scan tracks directly the cathodic scan. A steady state response may also arise when solutions are being stirred, e.g., in rotating disk voltammetry, RDV.

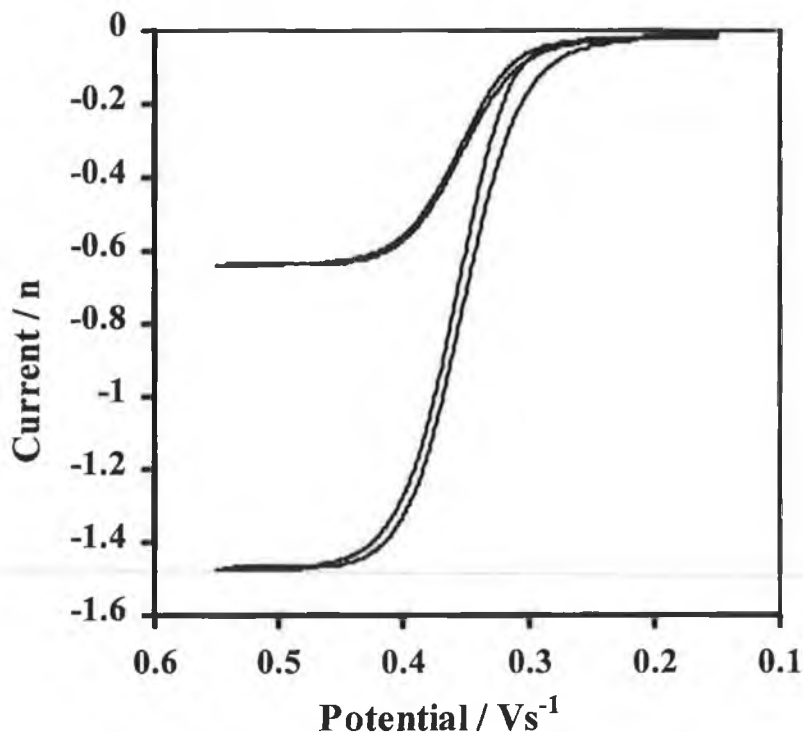


Figure 8 Slow scan rate steady state responses for $\text{Os}(\text{bpy})_2\text{P0PCl}$ (0.5 mM) in methanol where the electrolyte is 0.1 M LiClO_4 . The small steady state CV is the response from a 5 μM gold microelectrode and the large from a 12.5 μM gold electrode.

Theoretical analysis of the wave shape leads to the Randles-Sevcik equation for the determination of the peak current, i_p , in a high sweep rate, semi-infinite diffusion CV, according to;

$$i_p = 0.433nFAC\left(\frac{nF}{RT}\right)v^{1/2}D_0^{1/2} \quad \text{Eq. 6}$$

where n is the number of electrons, R the gas constant in $\text{J mol}^{-1} \text{K}^{-1}$, F the Faraday constant in C mol^{-1} , A the electrode area in cm^2 , D_0 the diffusion coefficient of the electroactive species in cm^2/sec , C the concentration of the electroactive species in mol/cm^3 and v the scan rate in V/sec .

The peak current, i_p in amperes, is given by;

$$i_p = (2.69 \times 10^5) n^{3/2} A D_O^{1/2} v^{1/2} C \quad \text{Eq. 7}$$

For a reversible wave, the potential, E_p , is independent of scan rate and i_p is proportional to $v^{1/2}$. Other features are;

$$E_p = E_{pa} - E_{pc} = 0.0592 / n \text{ V at } 25^\circ \text{C} \quad \text{Eq. 8}$$

and;

$$i_{pa} / i_{pc} = 1 \quad \text{Eq. 9}$$

where i_{pa} , i_{pc} , E_{pa} and E_{pc} are the anodic and cathodic peak currents and potentials respectively.

1.5.1.2 Electrochemistry of surface confined species

Figure 9 illustrates the typical theoretical response for a cyclic voltammogram of an electrochemically reversible couple that is confined on the electrode surface. Adsorption leads to changes in the shape of cyclic voltammograms since the redox active material does not have to diffuse to the electrode surface. The peaks for surface confined species are sharp and symmetrical unlike those for freely diffusing species. This behaviour is due to the presence of a fixed amount of redox active species at the electrode surface which is not hindered by the complications of mass transfer. When a potential is applied to a surface modified electrode the current rises from essentially zero to a peak value and then back to zero. For an ideal system no peak to peak separation is expected. The peak current for a surface confined reactant is given by;

$$i_p = \frac{n^2 F^2}{4RT} v A \Gamma \quad \text{Eq. 10}$$

where Γ is the surface coverage. The area under the voltammetric peak, corrected for any background current, represents the charge associated with the reduction or oxidation of the adsorbed species and can be used to calculate Γ according to:

$$\Gamma = \frac{Q}{nFA} \quad \text{Eq. 11}$$

where Q is the charge under either the anodic or cathodic peak in coulombs. For an ideal Nernstian reaction under Langmuir isotherm conditions, where no interaction occurs between adsorbates or at least they are concentration independent, a surface confined species will follow the following relationship;

$$\Delta E_{p1/2} = 3.53 \frac{RT}{nF} = \frac{90.6}{n} \text{mV}(25^\circ\text{C}) \quad \text{Eq. 12}$$

and;

$$E_{pa} = E_{pc} \quad \text{Eq. 13}$$

where $\Delta E_{p,1/2}$ is the total width at half-height of either the cathodic or anodic wave. The peak currents for surface confined species are also proportional to scan rate, v .

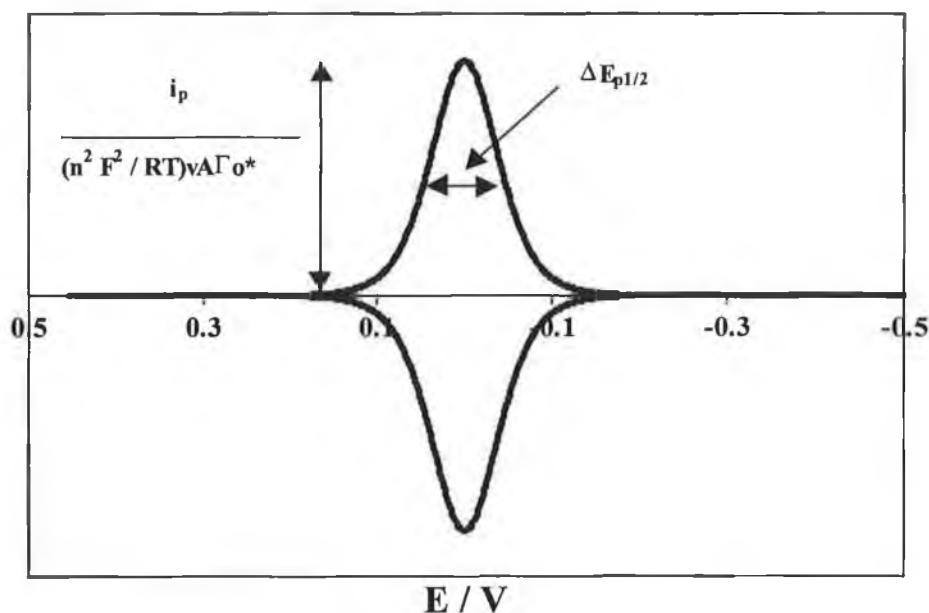


Figure 9 Current-potential curve for cyclic voltammetry for reduction of adsorbed O and sweep reversal. Current is given in normalised form and potential axis is shown for 25 °C.

1.5.2 Conclusion

This chapter has reviewed the electrochemistry of the various types of complexes, which adsorb on solid and liquid electrodes. The volume of research on modified electrodes is enormous and what is reviewed has considered only the most significant contributions in the areas of this thesis. The theory of microelectrodes has been discussed in order to show that microelectrodes exhibit considerable advantages over macroelectrodes in similar research areas and have also widened those areas to include supercritical fluids, solids and non-polar solvents.

1.6 References

1. Acevedo, D., Abruña, H. D. *J. Phys. Chem.*, **1991**, 95, 9590
2. Forster, R. J., Faulkner, L. R. *J. Am. Chem. Soc.*, **1994**, 116, 5444
3. Forster, R. J., Faulkner, L. R. *J. Am. Chem. Soc.*, **1994**, 116, 5453
4. Chidsey, C. E. D., *Science*, **1991**, 251, 919
5. Zezula, I., Galova, M., *J. Solid State Electrochem.*, **1999**, 3, 231
6. Pravda, M., Junger, C. M., Iwuoha, E. I., Smyth, M. R., Vytras, K., Ivaska, A., *Analytica Chimica Acta*, **1995**, 304, 127
7. Smyth, M. R., Park, T.-M., *Electroanalysis*, **1997**, 9, 1
8. Ulman, A. *An Introduction to Ultrathin Organic Films. From Langmuir-Blodgett to Self-Assembly.*; Academic Press, Inc.: San Diego, CA, 1991
9. Leech, D., Ju, H., *Analytica Chimica Acta*, **1997**, 345, 51
10. Foulds, N. C., Lowe, C. R., *Anal. Chem.*, **1988**, 60, 2473
11. Creager, S. E., Rowe, G. K., *J. Electroanal. Chem.*, **1997**, 420, 291
12. Balzer, F., Gerlach, R., Polanski, G., Rubahn, H. G., *Chem. Phys. Lett.*, **1997**, 274, 145
13. Ju, H. Leech, D., *Phys. Chem. Chem. Phys.*, **1999**, 1, 1549
14. Finklea, H. O., Ravenscroft, M. S., Snider, D. A., *Langmuir*, **1993**, 9, 223
15. De Long, H. C., Donohue, J. J., Buttry, D. A., *Langmuir*, **1991**, 7, 219
16. Forster, R. J., O'Kelly, J. P. *J. Phys. Chem.* **1996**, 100, 3695-3704
17. Forster, R. J., O'Hanlon, D., *Submitted for publication*
18. Lippmann, G., *Ann. Chim. Phys. (Paris)*, **1975**, 5, 494
19. von Helmholtz, H. L. *Wied. Ann.*, **1879**, 7, 337
20. Guoy, G., *J. Phys. Radium*, **1910**, 9, 457
21. Guoy, G., *Compt. Rend.*, **1910**, 149, 654
22. Grahame, D. C., *Chem. Rev.*, **1947**, 41, 441
23. Stern, O. Z., *Elektorchem.*, **1924**, 30, 508
24. Slowinski, K., Chamberlain, R. V., Miller, C. J., Majda, M., *J. Am. Chem Soc.*, **1997**, 119, 11910
25. Bard, A. J., Faulkner, L. R., *'Electrochemical methods'*, Wiley, New York, **1980**

26. Trassati, S., *Electroanalytical Chemistry and Interfacial Electrochemistry*, **1974**, 53, 335
27. Peng, W., Rusling, J. F., *J. Phys. Chem.*, **1995**, 99, 16436
28. Labinis, P. E., Whitesides, G. M., Allara, D. L., Tao, Yu-Tai, Parikah, A. N., Nuzzo, R., G., *J. Am. Chem. Soc.*, **1991**, 113, 7152
29. Porter, M. D., Bright, T. B., Allara, D. L., Chidsey, C. E. D., *J. Am. Chem. Soc.*, **1987**, 109, 3559
30. Bunding Lee, K. A., *Langmuir*, **1990**, 6, 709
31. Rowe, G. K., Creager, S. E., *Langmuir*, **1994**, 10, 1186
32. Delamarche, E., Michel, B., Biebuyck, H.A., Geber, C., *Adv. Mater.*, **1996**, 8, 719
33. Shimazu, K., Yagi, I., Sato, Y., Uosaki, K., *J. Electroanal. Chem.*, **1994**, 372, 117
34. Sabatani, E., Cohen-Boulakia, J., Bruening, M., Rubenstein, I., *Langmuir*, **1993**, 9, 2974
35. Tour, J. M., *et al*, *J. Am. Chem. Soc.*, **1995**, 117, 9529
36. Sinniah, K., Cheng, J., *et al*, *J. Phys. Chem.*, **1995**, 99, 14500
37. Yu, H., W, Y., Cai, S., Liu, Z., *Ber. Bunsenges. Phys. Chem.*, **1997**, 101, 257
38. Sabapathy, R. C., Bhattacharyya, S, Leavy, M. C., Cleland, W. E., Hussey, C. L., *Langmuir*, **1998**, 14, 124
39. Rickert, J., Göpel, W., Beck, W., Jung, G., Heiduschka, P., *Biosen. & Bioelec.*, **1996**, 11, 757
40. Linbland, M., Lestelius, M., Johansson, A., Tengvall, T., Thomsen, P., *Biomaterials*, **1997**, 18, 1059
41. Curtin, L. S., Peck, S. R., Tender, L.M., Murray, R. W., Rowe, G. K., Creager, S. E.; *Anal. Chem.* **1993**, 65, 386-392
42. Widrig, C.A.; Chung, C.; Porter, M.D., *J. Electroanal. Chem.* **1991**, 310, 335
43. Bryant, M.A.; Pemberton, J.E., *J. Am. Chem. Soc.* **1991**, 113, 8284
44. Widrig, C.A.; Chung, C.; Porter, M.D., *J. Electroanal. Chem.* **1991**, 310, 335
45. Kondo, T., Takechi, M., Sato, Y., Uosaki, K., *J. Electroanal. Chem.*, **1995**, 381, 203
46. Sato, Y., Uosaki, K., *Denki Kagaku*, **1994**, 62, 1269

47. Slowinski. K., Chamberlain. R. V., Miller. C. J., Majda. M., *J. Am. Chem Soc.*, **1996**, 118, 4709
48. Finklea, H.O., Snider, D.A., Fedyk, J., *Langmuir*, **1990**, 6, 371
49. Creager, S. E., Rowe, G. K., *Anal. Chim. Acta.*, **1991**, 246, 233
50. Cheng. J., Sàghi-Szabó. G., Tossell. J. A., Miller. C. J., *J. Am. Chem Soc.*, **1996**, 118, 680
51. Uosaki. K., Sato, Y., Kita, H., *Langmuir*, **1991**, 7, 1510
52. Bain. C. D., Barry Throughton. E., Tao. Yu-Tai., Evall. J., Whitesides. G. M., Nuzzo. R., G., *J. Am. Chem. Soc.*, **1989**, 111, 321
53. Bain. C. D., Evall. J., Whitesides. G. M., *J. Am. Chem Soc.*, **1989**, 111, 7155
54. Bain. C. D., Whitesides. G. M., *J. Am. Chem Soc.*, **1989**, 111, 7164
55. Schneider, T. W., Buttry, D. A., *J. Am. Chem. Soc.*, **1993**, 115, 12391
56. Chidsey, C. E. D., Bertozzi. C. R., Putvinski. T. M., Majsce. A. M., *J. Am. Chem Soc.*, **1990**, 112, 4301
57. Collard, D.M.; Fox, M.A., *Langmuir* ,**1991**, 7, 1192
58. Katz. E., Itzhak. N., Willner. I., *Langmuir*, **1993**, 9, 1392
59. Miller. C., Cuendet. P., Grätzel. M., *J. Phys. Chem.*, **1991**, 95, 877
60. Miller. C., Grätzel. M., *J. Phys. Chem.* **1991**, 95, 5225
61. Becka. A. M., Miller. C. J., *J. Phys. Chem.*, **1992**, 96, 2657
62. Finklea, H. O., Hanshew, D. D. *J. Am. Chem Soc.*, **1992**, 114, 3174
63. Finklea, H. O., Hanshew, D. D. *J. Electroanal. Chem.*, **1993**, 347, 327
64. Redepenning, J.; Tunison, H.M.; Finklea, H.O. *Langmuir* **1993**, 9, 1404
65. Finklea, H.O., Liu, L., Ravencroft, M.S., Punturi, S., *J. Phys. Chem.* **1996**, 100, 11852
66. Creager, S.E. Rowe, G.K., *Langmuir*, **1991**, 7, 2307
67. De Long. H. C., Buttry. D. A., *Langmuir*, **1992**, 8, 2491
68. Andreu, R. Calvente, J.J. Fawcett, W.R. Molero, M. *J. Phys. Chem.* **1997**, 101, 2884.
69. Acevedo, D., Bretz, R. L., Tirado, J. D., Abruña, H. D., *Langmuir*, **1994**, 10, 1300
70. Hudson, J. E., Abruña, H. D., *J Phys. Chem.* **1996**, 100, 1036
71. Bretz, R. L., Abruña, H. D. *J. Electroanal. Chem.*, **1995**, 388, 123

72. Bretz, R. L., Abruña, H. D. *J. Electroanal. Chem.*, **1996**, 408, 199
73. Tirado, J. D., Abruña, H. D., *J. Phys. Chem.*, **1996**, 100, 4556
74. Forster, R. J., Faulkner, L. R. *Anal. Chem.*, **1995**, 67, 1232
75. Forster, R. J., *Inorg. Chem.*, **1996**, 35, 3394
76. Marcus, R. A., *Chemical Physics*, **1965**, 43, 679
77. Campbell, J. L., Anson, F. C., *Langmuir*, **1996**, 12, 4008
78. Gordillo, G. J., Schriffrin, D. J., *J. Chem. Soc., Faraday Trans. I*, **1994**, 90, 1913
79. Port, S. N., Solomon, T., Schriffrin, D. J., *Langmuir*, **1995**, 11, 4577
80. Cheng, Y., Cunnane, V. J., Kontturi, A.-K., Kontturi, K., *J. Phys. Chem.*, **1996**, 100, 1547
81. Gill, R., Stonehill, H. I., *J. Electrochem. Soc.*, **1984**, 106, 1352
82. Soriaga, M.P., Hubbard, A.T., *J. Am. Chem. Soc.*, **1982**, 104, 2735
83. Soriaga, M.P., Hubbard, A.T., *J. Am. Chem. Soc.*, **1982**, 104, 2742
84. Soriaga, M.P., Hubbard, A.T., *J. Am. Chem. Soc.*, **1982**, 104, 3937
85. Soriaga, M.P., Hubbard, A.T., *J. Phys. Chem.*, **1983**, 87, 3048
86. Forster, R. J., *Langmuir* **1995**, 11, 2247
87. Forster, R.J., *J. Electrochem. Soc.*, **1997**, 144, 1165
88. Forster, R.J., *Anal. Chem.*, **1996**, 68, 3143
89. Forster, R.J., *Analyst*, **1996**, 121, 733
90. O'Kelly, J. P., Forster, R.J., *Analyst*, **1998**, 123, 1987
91. He, P., Crooks, R. M., Faulkner, L. R., *J. Phys. Chem.*, **1990**, 94, 1135
92. Zhang, J., Anson, F. C., *J. Electroanal. Chem.*, **1992**, 331, 945
93. Truong, C. Ta., Kanda, V., McDermott, M. T., *J. Phys. Chem.*, **1999**, 103, 1295
94. Chambers, J.Q. *The Chemistry of Quinonoid Compounds*, Vol II, Patai, S. Rappoport, Z. Eds., 1998, Ch 12, 1988 Wiley & Sons Ltd
95. Chambers, J.A. *Chemistry of the Quinoids*, Part 2; Patai, S. Ed.; Wiley: New York, 1974, Chapter 14
96. Hubbard, A. T., *et al.*, *J. Electroanal. Chem.*, **1984**, 168, 43
97. Malem, F., Mandler, D., *J. Electrochem. Soc.*, 139, No. 7, **1992**
98. Tschuncky, P., Heinze, J., *J. Anal. Chem.*, **1995**, 67, 4020
99. Pendley, B. D., Abruna, H. D.; *Anal. Chem.*, **1990**, 62, 782-784

100. Cheng, F., Schimpf, J. M.; Martin, C. R.; *J. Electroanal. Chem.*, **1990**, 284, 499
101. Forster, R. J. *Chem. Soc. Rev.*, **1994**, 289
102. Christensen, P. A.; Hamnett, A. *Techniques and Mechanisms in Electrochemistry*, **1994**
103. Chen, X., Zhuang, J., He, P., *J. Electroanal. Chem.*, **1989**, 271, 257
104. Duo, R., Pena, M. J., Celdran, R., *J. Electroanal. Chem.*, **1996**, 404, 99
105. Sabatani, E., Rubinstein, I., *J. Phys. Chem.* **1987**, 91, 6663
106. Montenegro, M. I.; Queirós, M. A.; Daschbach, J. L.; *Microelectrodes: Theory and Applications*, **1990**
107. Penner, R. M., Heben, M. J., Longin, T. L., Lewis, N. S., *Science*, **1990**, 250, 1118
108. Brett, C. M. A.; Brett, A. M. O. *Electrochemistry Principles, Methods, and Applications*; New York, **1993**
109. Baranski, A. S., Quon, H., *Anal. Chem.*, **1986**, 58, 407
110. Wightman, R. M., Wehmeyer, K. R., *Anal. Chem.*, **1985**, 57, 1989
111. Knecht, L. A., Guthrie, E. J., Jorgenson, J. W., *Anal. Chem.*, **1984**, 56, 479
112. Lindblad, M., Lestelius, M., Johansson, A., Tengvall, P., Thomsen, P., *Biomaterials*, **1997**, 18, 1059
113. Bard, A. J., Faulkner, L. R., *'Electrochemical methods'*, Wiley, New York, **1980**
114. Southampton electrochemistry Group *Instrumental Methods in Electrochemistry*; Ellis Harwood, England, **1985**

CHAPTER 2

Synthesis and Characterisation of Redox – Active Molecules as Building Blocks for Spontaneously Adsorbed Monolayers

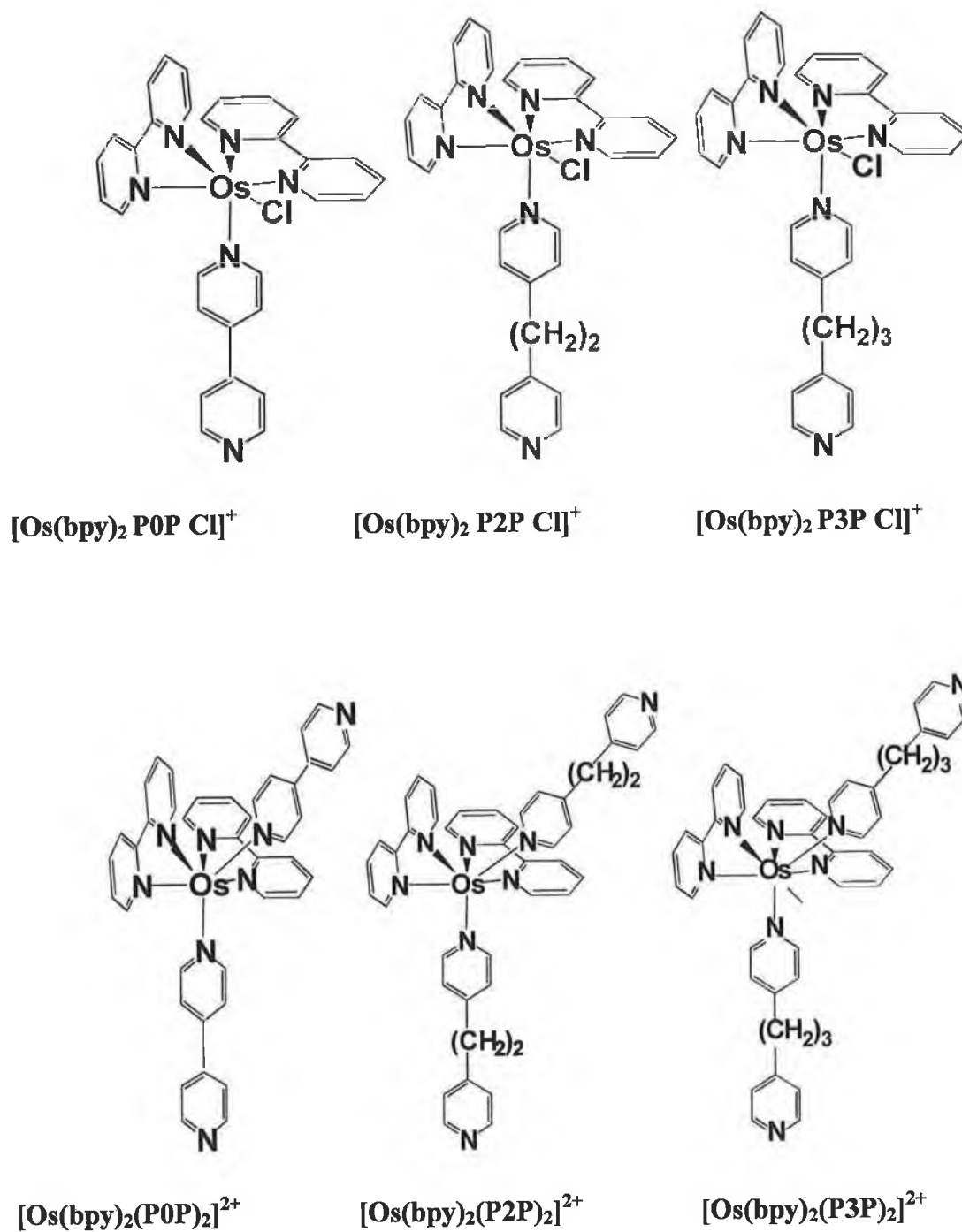
2 Introduction

2.1 Osmium polypyridyl complexes

Osmium and ruthenium complexes have been widely used in industrial applications including catalysis¹, electroplating² and for building electronic devices.³ Moreover, because they exhibit close to ideal reversible electrochemical properties, they make extremely useful model systems for probing the details of electron transfer. A surface active ligand means that highly ordered monolayers and multilayers can be formed on electrode surfaces. These ordered assemblies allow not only the interfacial reactivity to be controlled, but also provide time control over the electron transfer distance, tunnelling medium and local microenvironment of the complexes.^{4,5,6,7,8,9}

The metal complexes discussed here have been chosen for three distinct reasons. First, they adsorb rapidly from aqueous based solutions forming stable monomolecular films on gold and platinum electrodes. Second, the thin layers are ordered on the molecular length scale. Third, the rates of desorption are low and the films are photochemically stable. These properties make them attractive complexes for a wide variety of electrochemical studies. Although ferrocene alkanethiols have received a lot of attention,^{10, 11, 12, 13, 14} research using osmium containing complexes has been the recent focus of much attention by a small number of research groups due to their ideal electrochemical responses.^{15,16,17,18,19}

In this chapter, the synthesis and characterisation of a series of N₅ - Cl and N₆ - osmium polypyridyl complexes (Scheme 1) is reported along with the characterisation of various anthraquinones.

Scheme 1 N_5 -Cl and N_6 - osmium complexes

2.2 Synthesis of Osmium Complexes

2.2.1 Materials and Instrumentation

2.2.1.1 *Chromatographic Techniques*

High performance liquid chromatography (HPLC) was performed using a Waters 510 HPLC pump and a Waters 990 photodiode array detector connected to a NEC PAC III computer, with a 20 μ l injector loop and a partisil SCX radial PAK cartridge. The detection wavelength used was 280 nm. The mobile phase Acetonitrile: Water 80:20 (v/v) containing 0.08 M lithium perchlorate. The flow rate used was 2 ml min⁻¹ unless otherwise stated.

2.2.1.2 *Absorption Spectroscopy*

UV/Vis spectra were carried out on a Shimadzu UV-160A, spectrophotometer. The range used was 200 – 800 nm with 1 cm matched quartz cells.

2.2.1.3 *Electrochemistry*

Cyclic voltammetry (CV) was performed with a CH instruments Model 660 electrochemical workstation and a conventional three-electrode cell. A picoamp booster and Faraday cage were also used when microelectrodes were employed. Potentials were measured against a sodium chloride saturated silver/silver chloride (Ag/AgCl) reference electrode. The auxiliary electrode used was a platinum flag (1.2 cm square). The solvent employed for the solution phase voltammograms was acetonitrile with 0.1 M tetra-butyl-ammonium tetrafluoroborate (TBABF₄) as the supporting electrolyte. All solutions used in electrochemical experiments were thoroughly degassed using nitrogen gas and a blanket of nitrogen was maintained over the solution during the experiments. Gold electrodes were used in solution phase and adsorption studies unless stated otherwise.

2.2.1.4 Nuclear Magnetic Resonance Spectroscopy

Proton nuclear magnetic resonance (NMR) spectra were obtained using a Bruker ACF 400 MHz spectrometer. Measurements were carried out in d_4 -DMSO for the $\text{Os}(\text{bpy})_2\text{Cl}_2$ and d_8 -acetonitrile for the complexes, unless otherwise stated. NMR temperature studies were performed using the attached variable temperature unit.

2.2.1.5 Elemental analysis

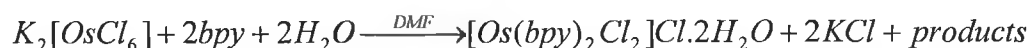
Elemental analysis on C, H and N were carried out at the Microanalytical Laboratory of the University College Dublin (UCD) in Dublin, Ireland.

2.3 Characterisation of Osmium Complexes

2.3.1 Synthesis of metal complexes

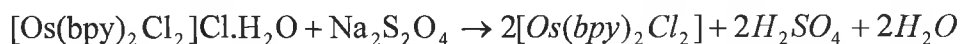
$\text{Os}(\text{bpy})_2\text{Cl}_2$ was synthesised following a procedure previously described²⁰ using K_2OsCl_6 as the starting material.

2.3.1.1 Synthesis of $[\text{Os}(\text{bpy})_2\text{Cl}_2]\text{Cl}$



Potassium hexachlorosmate (IV), $\text{K}_2[\text{OsCl}_6]$, (5.0 g, 9.6 mmol), was heated to 120°C in DMF, (40 cm³), in a round bottomed flask (100 cm³). 2,2'-bipyridine, (3.42 g, 2.2 mmol), dissolved in DMF, (15 cm³) was added in 1 cm³ samples and heated to reflux for approximately 1 hour, with continuous stirring. After 15 mins, crystals of KCl form, which were removed by filtration at the end of the reaction while the solution was still hot. After cooling the complex was precipitated by the slow addition of the complex solution to diethyl ether, while rapidly stirring. The precipitate was filtered, washed with copious volumes of diethyl ether, and air-dried.

2.3.1.2 Synthesis of $[\text{Os}(\text{bpy})_2\text{Cl}_2] \cdot 2\text{H}_2\text{O}$



Bis (2,2'-bpy) dichloro-osmium (III) chloride dihydrate, $[\text{Os}(\text{bpy})_2\text{Cl}_2]\text{Cl} \cdot \text{H}_2\text{O}$, (1.0 g, 1.55 mmol), was dissolved in a mixture of DMF (20 cm³) and methanol (10 cm³) in a 500 ml beaker. A dilute aqueous solution of sodium dithionite, $\text{Na}_2\text{S}_2\text{O}_4$, (2 g, 1.1 mmol in 200 cm³) was added slowly over the period of 30 mins with continuous stirring. Stirring was continued for an additional 15 mins after all the dithionite was added. The solution

containing the dark purple oily suspension of the complex was cooled on an ice bath and the walls scratched to encourage crystallisation. The solution was left to stand overnight at 4°C. The resulting precipitate was filtered, washed with water (2x10 cm³) and diethyl ether (2x10 cm³).

[Os(bpy)₂Cl₂] ¹H-n.m.r. (400 MHz) δ (DMSO): 6.75 (2H, t, H5), 7.25 (2H, t, H4), 7.3 (2H, d, H6), 7.5 (2H, t, H5'), 7.6 (2H, t, H4'), 8.3 (2H, d, H3), 8.5 (2H, d, H3'), 9.7 (2H, d, H6').

Calculated for [Os(bpy)₂Cl₂].2H₂O. C, 39.38; H, 3.31; N, 9.10 %. Found C, 40.89; H, 3.42; N, 9.13 %.

2.3.2 HPLC

HPLC of the product revealed a single peak at 1.72 min, shown in Figure 1, thus indicating the formation of a single product. The retention time of the dichloride depends on the concentration of electrolyte ions present in the mobile phase. In this elution the concentration of LiClO₄ is 0.08 M. The elution time is consistent with the complex being neutral.

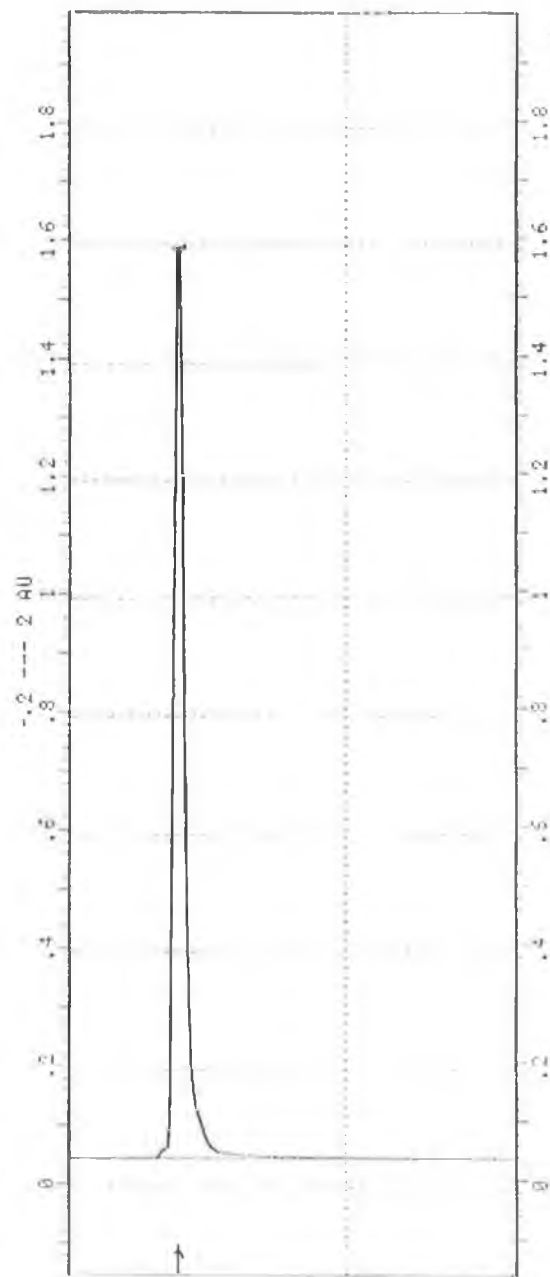


Figure 1 HPLC of $[\text{Os}(\text{bpy})_2\text{Cl}_2]$. The mobile phase is Acetonitrile: Water 80:20 (v/v) containing 0.08 M lithium perchlorate. The flow rate used was 2 ml min^{-1} .

2.3.3 UV-Vis

Figure 2 shows the UV-Visible absorbance spectrum for $[\text{Os}(\text{bpy})_2\text{Cl}_2]$. In the ultra-violet region of the spectrum a sharp absorption band is observed at approximately 290 nm. This band arises from a bpy based $\pi\text{-}\pi^*$ transition. In the visible region, broad bands exist between 350 and 550 nm. These bands are associated with metal-to-ligand-charge-transfer (MLCT) bands ($\text{d-}\pi^*$), indicated in the spectrum by the broad bands. Broadness is also due to the effect of spin orbit coupling. The metal-ligand interaction is stronger for osmium complexes over their corresponding ruthenium analogues, subsequently resulting in a larger ligand-field splitting for osmium complexes. The position of these intense bands is governed by both the position of the anti-bonding orbital (π^*) in respect to the d-orbital for the metal.

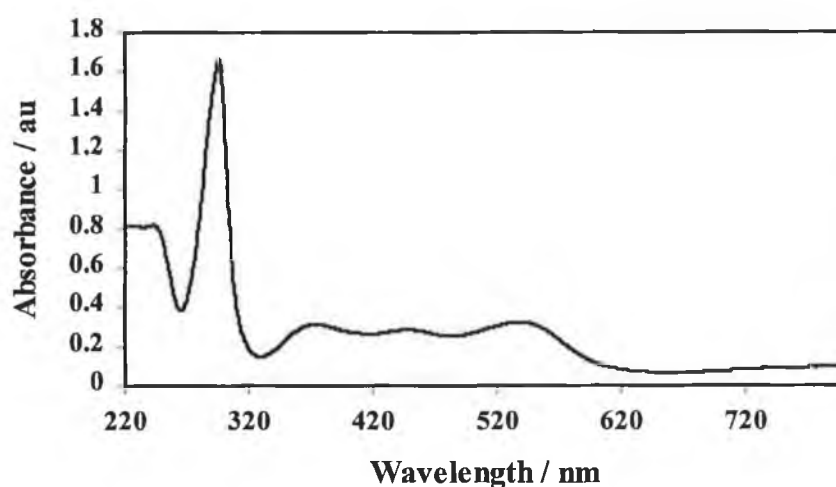


Figure 2 UV-Vis spectrum of $[\text{Os}(\text{bpy})_2\text{Cl}_2]$ in acetonitrile:water, 80:20.

2.3.4 Electrochemistry

Solution phase cyclic voltammetry for $[\text{Os}(\text{bpy})_2\text{Cl}_2]$ is represented by Figure 3. A single redox couple is observed at approximately 0.01 V. The typical response of this redox-active couple is characteristic of a one electron transfer involving a third row transition metal containing two neutral ligands and two electronegative atoms.

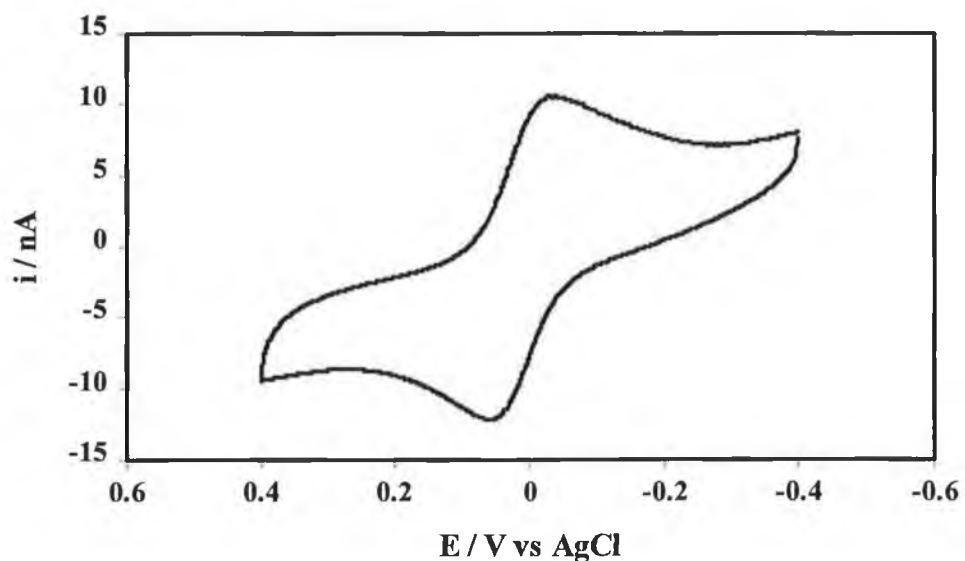


Figure 3 Cyclic voltammogram of $[\text{Os}(\text{bpy})_2\text{Cl}_2]$ in acetonitrile with 0.1 M TBABF_4 as electrolyte. The scan rate was 0.5 Vs^{-1} and a $25 \mu\text{m}$ radius gold microelectrode was used. The initial potential was -0.4 V , in a positive direction. The concentration of $[\text{Os}(\text{bpy})_2\text{Cl}_2]$ in solution was 1 mM.

2.3.5 NMR

[Os(bpy)₂Cl₂] was analysed by ¹H NMR using d-DMSO as a solvent. The initial spectrum (room temperature, 296 K) of [Os(bpy)₂Cl₂] (Figure 4) was insufficiently resolved to assign the chemical shifts of H₄, H₄', H₅ and H₆. Therefore, spectra at increased temperatures were recorded. Figure 5 shows an NMR spectra performed at 336 K. This figure shows that well defined peaks are observed at higher temperatures allowing chemical shifts to be assigned. The integration of the Os(bpy)₂Cl₂ complex gave a value of eight proton peaks, each peak integrating for two protons, corresponding to the protons from the bipyridyl ligands. The fact only 8 peaks are noticed indicates the equivalence of the bipyridyl molecules. Four doublets and four triplet peaks were observed. The doublets are attributable to the H₃, H₃', H₆ and H₆' protons on the pyridyl ring and the triplets attributable to the H₄, H₄', H₅ and H₅' protons. The doublet at approximately 9.7 ppm, which is the H₆ proton, is shifted downfield. This is due to the proton hanging over the pyridine ring on an adjacent bpy ligand resulting in a deshielding effect on the proton and the subsequent downfield shift.

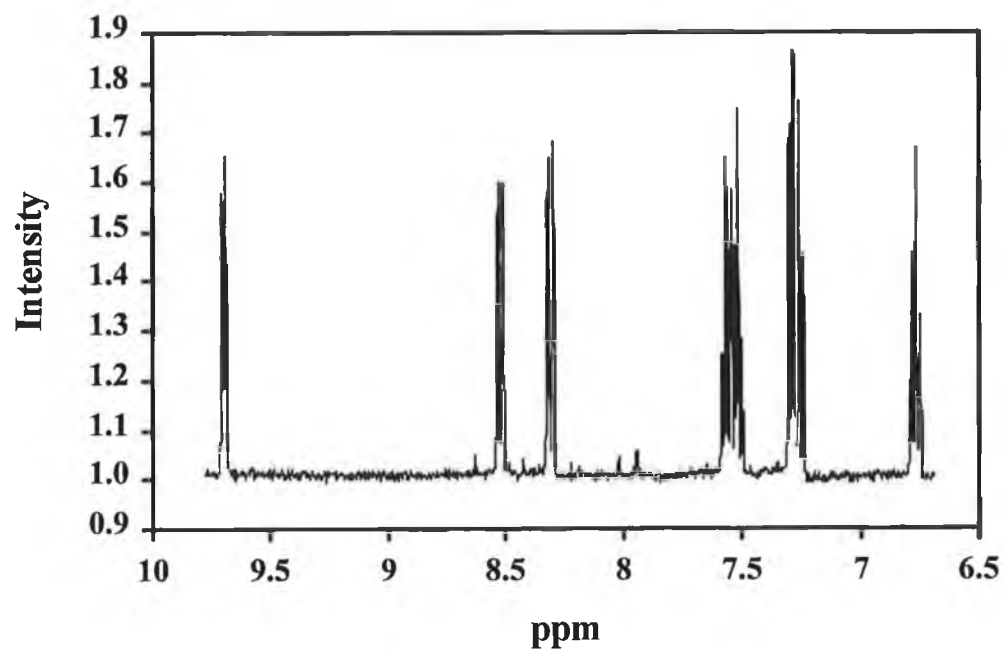


Figure 4 ^1H NMR of $[\text{Os}(\text{bpy})_2\text{Cl}_2]$ in d-DMSO at 296 K.

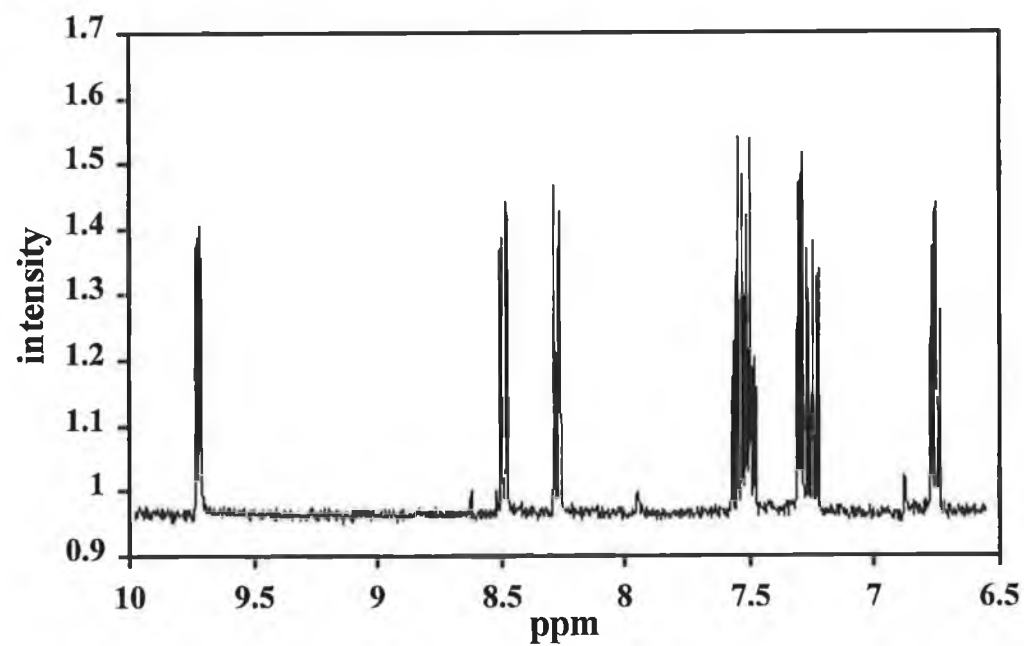


Figure 5 ^1H NMR of $[\text{Os}(\text{bpy})_2\text{Cl}_2]$ in d-DMSO at 336 K.

2.4 N₅ - Cl Osmium Complexes

The osmium N₅ – Cl complexes, [Os(bpy)₂LCl]⁺, where bpy = 2,2' bipyridine, L = 4,4'-dipyridyl, 1,2-bis(4-pyridyl)ethane, or 4,4'-trimethylenedipyridine were synthesised following a procedure described by Acevedo and Abruña²¹ with minor modifications. [Os(bpy)₂Cl₂] was refluxed with an excess of the appropriate bridging ligand in ethylene glycol. Excess ligand ensures the complete reaction of all the electroactive starting material. In a typical procedure [Os(bpy)₂Cl₂.2H₂O] (400 mgs, 0.698 mmol) was dissolved by refluxing in deaerated ethylene glycol (50 cm³), under a nitrogen atmosphere for 20 minutes. A two fold molar excess of the appropriate ligand was added and reflux continued for approximately 4 hours. The reaction was monitored by HPLC until completion. Once cooled, an equivalent volume of water was added and the solution filtered. The complex was precipitated by the addition drop-wise to a saturated solution of ammonium hexafluorophosphate (NH₄PF₆) (10 cm³). The complex was subsequently filtered, washed with water (3x 20 cm³) and diethyl ether (3x 20 cm³), and dried overnight under vacuum. The precipitate was purified by recrystallisation from a 1:1 acetone:water solution, to give a red-brown powder.

[Os(bpy)₂(P0P)Cl], ¹H-n.m.r. (400 MHz) δ (CH₃CN): 6.95 – 7.2 (3H, m), 7.4 – 7.85, (11H, m), 8.00 – 8.4 (6H, m), 8.50 (1H, d), 8.65 (2H, d), 9.55 (1H, d).

Calculated for [Os(bpy)₂(P0P)Cl](PF₆). C, 42.90; H, 2.88; N, 10.01 %. Found C, 42.01; H, 2.97; N, 9.71 %. Yield = 433.5 mg, 82.2%.

[Os(bpy)₂(P2P)Cl], ¹H-n.m.r. (400 MHz) δ (CH₃CN): 2.50 – 3.00 (4H, m), 6.9 – 7.80 (14H, m), 8.30 – 8.50 (10H, m).

Calculated for [Os(bpy)₂(P2P)Cl](PF₆). C, 44.28; H, 3.25; N, 9.69 %. Found C, 43.77; H, 3.81; N, 8.63 %. Yield = 462.8 mg, 81.3%.

[Os(bpy)₂(P3P)Cl], ¹H-n.m.r. 400 MHz) δ (CH₃CN): 1.70 – 2.00 (2H, m), 2.50 – 2.70 (4H, m), 6.90 – 8.6 (23H, m), 9.7 – 9.8 (1H, d).

Calculated for $[\text{Os}(\text{bpy})_2(\text{P3P})\text{Cl}](\text{PF}_6)$. C, 44.98; H, 3.43; N, 9.54 %. Found C, 43.94; H, 3.51; N, 9.19 %. Yield = 474.2 mg, 82.0%.

2.5 N_6 -Osmium Complexes

The osmium N_6 complexes, $[\text{Os}(\text{bpy})_2\text{L}_2]^{2+}$, where bpy = 2,2'-bipyridine, L = 4,4'-dipyridyl, 1,2-bis(4-pyridyl)ethane, or 4,4'-trimethylenedipyridine were also synthesised following the procedure described by Acevedo and Abruña²¹ with a slight modification. This being the addition of an equal volume of de-ionised water to the dissolved $\text{Os}(\text{bpy})_2\text{Cl}_2 \cdot 2\text{H}_2\text{O}$ in deaerated ethylene glycol. The de-ionised water was added before the addition of the ligand. Purification was performed by recrystallisation in a 1:1 acetone:water solution to give dark green-black powder (bis-substituted).

$[\text{Os}(\text{bpy})_2(\text{P0P})_2]$, ^1H -n.m.r. (400 MHz) δ (CH_3CN): 7.05 (1H, t), 7.30 (1H, t), 7.55 – 7.60 (4H, d), 7.60 – 7.65 (4H, d), 7.65 – 8.05 (12H, m), 8.25 – 8.45 (5H, m), 8.70 (4H, d), 8.82 (1H, d).

Calculated for $[\text{Os}(\text{bpy})_2(\text{P0P})_2](\text{PF}_6)_2$. C, 43.45; H, 2.92; N, 10.14 %. Found, C, 43.00; H, 3.25; N, 9.64 %. Yield = 560.2 mg, 77.2%.

$[\text{Os}(\text{bpy})_2(\text{P2P})_2]$, ^1H -n.m.r. (400 MHz) δ (CH_3CN): 2.8 – 2.95 (8H, m), 7.00 – 7.05 (4H, d), 7.05 – 7.15 (4H, d), 7.25 (2H, t), 7.70 (4H, t), 7.75 – 7.80 (2H, d), 7.90 (2H, t), 8.00 – 8.05 (4H, d), 8.25 (2H, d), 8.35 (2H, d), 8.40 (4H, d), 8.65 – 8.70 (2H, d).

Calculated for $[\text{Os}(\text{bpy})_2(\text{P2P})_2](\text{PF}_6)_2$. C, 45.48; H, 3.47; N, 9.65 %. Found, C, 43.67; H, 3.57; N, 9.01 %. Yield = 578.8 mg, 76.0%

$[\text{Os}(\text{bpy})_2(\text{P3P})_2]$, ^1H -n.m.r. (400 MHz) δ (CH_3CN): 1.80 – 2.00 (4H, q), 2.50 – 2.70 (8H, m), 7.10 – 7.20 (8H, d), 7.30 – 7.35 (2H, t), 7.70 – 7.80 (6H, m), 7.95 (2H, t), 8.10 – 8.15 (4H, d), 8.35 – 8.45 (4H, d), 8.50 – 8.55 (2H, d), 8.6 (2H, d), 8.75 (2H, d).

Calculated for $[\text{Os}(\text{bpy})_2(\text{P3P})_2](\text{PF}_6)_2$. C, 46.43; H, 3.73; N, 9.42 %. Found, C, 42.42; H, 3.55; N, 8.62 %. Yield = 595.1 mg, 76.3%

2.5.1 HPLC

Table 1 shows the retention times for the N₅-Cl and N₆-substituted osmium polypyridyl complexes. As previously mentioned the flow rate was 2.0 ml/min and the solvent was 80:20 acetonitrile:water. The retention times of the N₅-Cl and N₆-substituted complexes are separated by approximately 2.5 minutes. The difference arises because of differences in the charge on the complexes, N₅-Cl is +1 and N₆ is +2. While there is a significant difference in elution times between the charged species, the same cannot be said for the neutral and +1 charged species, the difference being only 0.1 of a minute. The elution time of the N₅-Cl species seems to be too close to the dichloride to differentiate between the complexes. However, this is not unusual and similar findings have been found for analogous compounds containing ruthenium as the metal centre.²² In addition, by examining the UV-Vis spectra in Figure 2 for [Os(bpy)₂Cl₂] and Figure 6 for the N⁵-Cl complexes, it may be seen that the MLCT band for the latter has blue shifted due to the greater donor properties of the P0P, P2P and P3P ligands over that of chloride. One method for increasing the elution times between the two complexes is to decrease the concentration of competitive cations present in the mobile phase and also to decrease the flow rate of the solvent. The less cations present would lead to more of the complex interacting with the stationary phase resulting in a longer elution time and reducing the flow rate would increase the separation between the neutral and +1 species. Purity of the complexes is above 90% with the remaining complex being the non surface-active complex [Os(bpy)₂Cl₂]. This impurity was confirmed from the MLCT band in the UV-Vis spectrum. The HPLC traces may be found in Appendix 1 for the N₅-Cl and N₆-substituted osmium polypyridyl complexes.

Complex	Retention time / min
$[\text{Os}(\text{bpy})_2\text{P0P Cl}]^+$	1.81
$[\text{Os}(\text{bpy})_2\text{P2P Cl}]^+$	1.74
$[\text{Os}(\text{bpy})_2\text{P3P Cl}]^+$	1.72
$[\text{Os}(\text{bpy})_2(\text{P0P})_2]^{2+}$	4.40
$[\text{Os}(\text{bpy})_2(\text{P2P})_2]^{2+}$	4.44
$[\text{Os}(\text{bpy})_2(\text{P3P})_2]^{2+}$	4.41

Table 1 Retention time for the $\text{N}^5\text{-Cl}$ and N^6 osmium polypyridyl complexes.

2.5.2 UV-Vis

The UV-Vis spectrums for the $\text{N}_5\text{-Cl}$ complexes show very sharp bands at approximately 280 nm, $\pi\text{-}\pi^*$ transitions as seen in Figure 6. The bands in the visible portion of the spectrum correspond to MLCT transitions. The bands attributed to $[\text{Os}(\text{bpy})_2\text{P2P Cl}]^+$ and $[\text{Os}(\text{bpy})_2\text{P3P Cl}]^+$ are at a lower wavelength/higher energy than the band from $[\text{Os}(\text{bpy})_2\text{P0P Cl}]^+$. One possible reason for the shift to higher energy (blue shift) of the MLCT band may be due to the greater sigma donor capabilities of the ligands. Figure 7 represents the UV-Vis spectrums of the $\text{N}^6\text{-complexes}$. A sharp absorption band is noticed in the UV region for all complexes. This band signifies a high energy $\pi\text{-}\pi^*$ transition (bpy-bpy). In the visible region, broad bands exist between 320 and 520 nm. These bands are associated with metal-to-ligand-charge-transfer (MLCT) bands ($\text{d-}\pi^*$). The MLCT bands of the $\text{N}_6\text{-complexes}$ have blue shifted in relation to the $\text{N}_5\text{-Cl}$ complexes which is due to the presence of a second ligand attached to the metal centre further increasing the sigma donor capability to the metal.

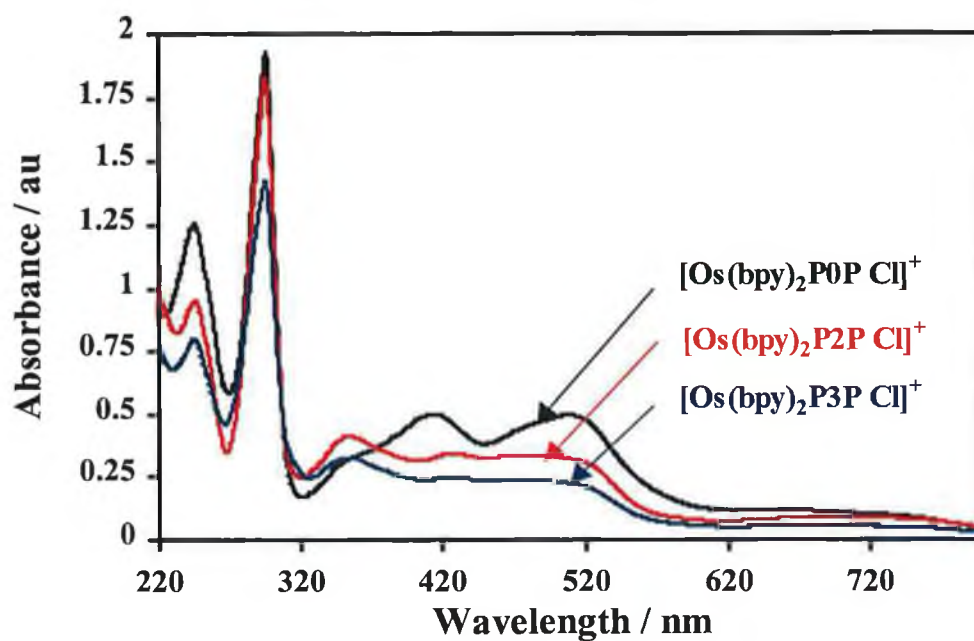


Figure 6 Overlaid UV-Visible spectrums of $[\text{Os}(\text{bpy})_2\text{P0P Cl}]^+$, $[\text{Os}(\text{bpy})_2\text{P2P Cl}]^+$ and $[\text{Os}(\text{bpy})_2\text{P3P Cl}]^+$ in acetonitrile:water, 80:20.

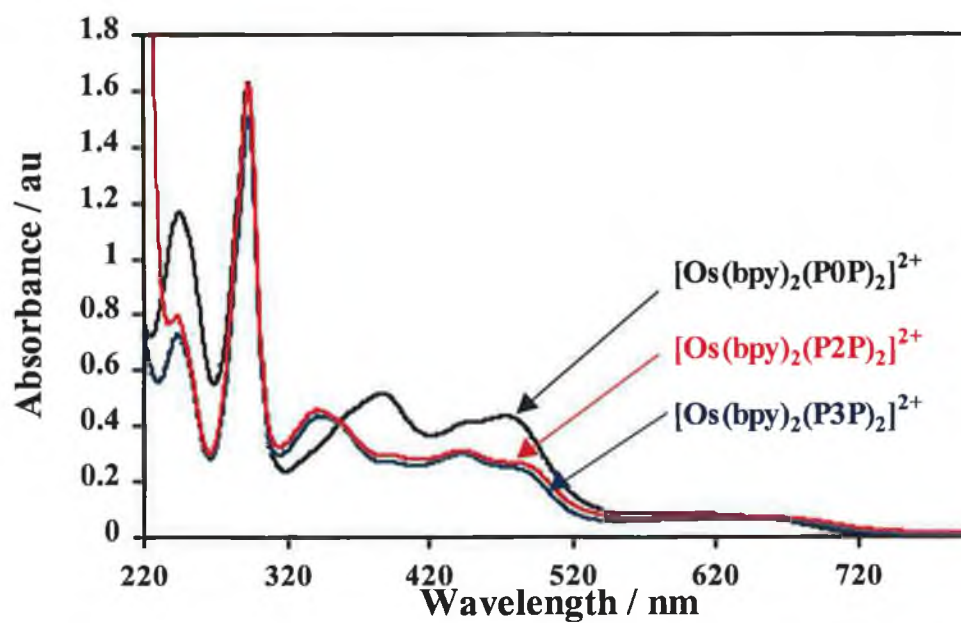


Figure 7 UV-Visible spectrum of $[\text{Os}(\text{bpy})_2(\text{P0P})_2]^{2+}$, $[\text{Os}(\text{bpy})_2(\text{P2P})_2]^{2+}$ and $[\text{Os}(\text{bpy})_2(\text{P3P})_2]^{2+}$ in acetonitrile:water, 80:20.

2.5.3 Electrochemistry

Figure 8 shows the cyclic voltammograms for $[\text{Os}(\text{bpy})_2\text{P0P Cl}]^+$, $[\text{Os}(\text{bpy})_2\text{P2P Cl}]^+$ and $[\text{Os}(\text{bpy})_2\text{P3P Cl}]^+$ in acetonitrile with 0.1 M TBABF₄ as electrolyte. The formal potentials for the three complexes are 0.469, 0.431 and 0.396 V, respectively. All three voltammetric responses are typical for osmium polypyridyl complexes containing one electronegative ligand (Cl) where the overall oxidation state of the complex is +1.^{4,5,7} Within experimental error, the peak to peak splitting between the anodic and cathodic peaks for each of the complexes is typically Nernstian (0.059 V).

Figure 9 illustrates the voltammetric responses for the N⁶ complexes. The formal potentials being 0.884 V, 0.855 V and 0.851 V for the $[\text{Os}(\text{bpy})_2(\text{P0P})_2]^{2+}$, $[\text{Os}(\text{bpy})_2(\text{P2P})_2]^{2+}$, $[\text{Os}(\text{bpy})_2(\text{P3P})_2]^{2+}$ complexes, respectively. All three formal potentials are representative of N₆-osmium complexes.^{4,5}

There is a sizeable difference of approximately 0.40 V separating the formal potentials of the N₅-Cl and N₆- complexes. This is due to the difference in electron density residing on the metal centre. The electron density present on the metal is attributable to the electron donating properties of the ligands. Chloride being more electronegative than nitrogen. Therefore, donating more electron density to the metal centre. The lower the electron density on the metal, the harder it is to oxidise, thus increasing the formal potential of the redox active species. Figure 10 shows the voltammetric response for the bipyridyl reductions for an N₅-Cl and N₆ osmium complex. It can be clearly seen the reduction of the first bipyridyl on the N₆ complex occurs before the first bipyridyl reduction of the N₅-Cl complex. This is expected due to less electron density present on the metal which makes it easier to reduce.

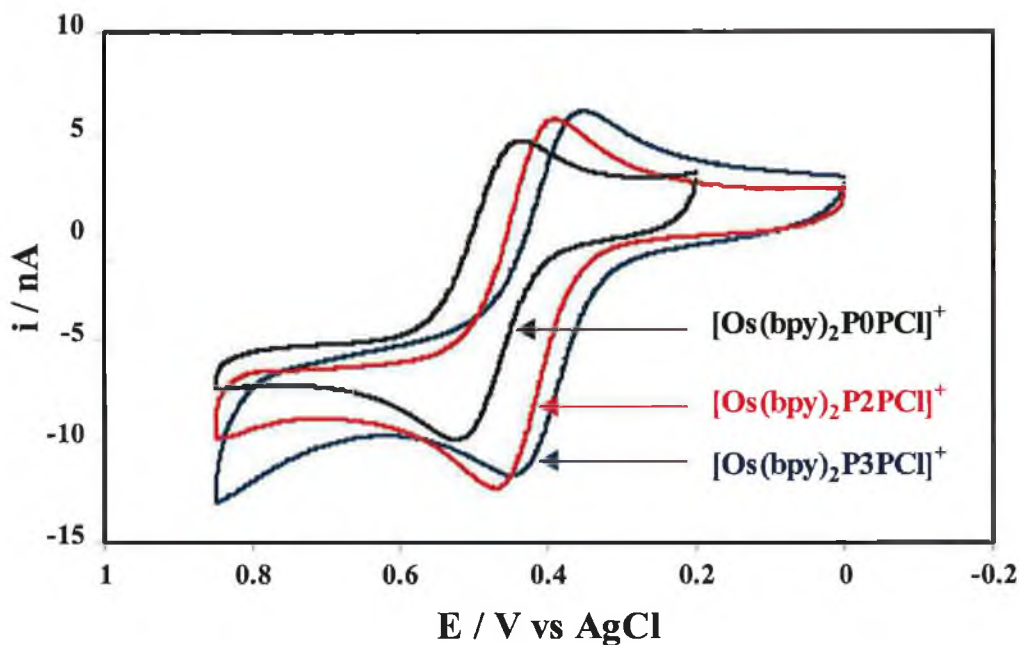


Figure 8 Solution phase CV of the N^5 -Cl complexes in acetonitrile with 0.1 M TBABF₄ as electrolyte. The scan rate was 0.1 Vs⁻¹ and a gold microelectrode (radius 25 μ m) was used. The initial potential was 0.00 V, in a positive direction.

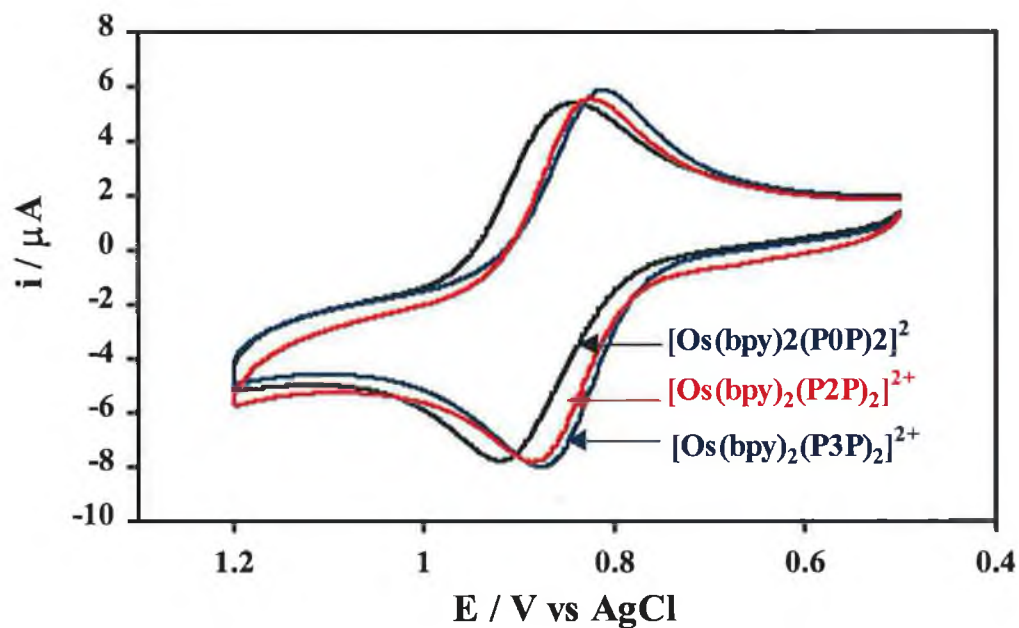


Figure 9 Cyclic voltammogram of the N^6 - complexes in acetonitrile with 0.1 M TBABF₄ as electrolyte. The scan rate was 0.1 Vs⁻¹ and a gold macroelectrode (radius 0.1 cm) was used. The initial potential was 0.50 V.

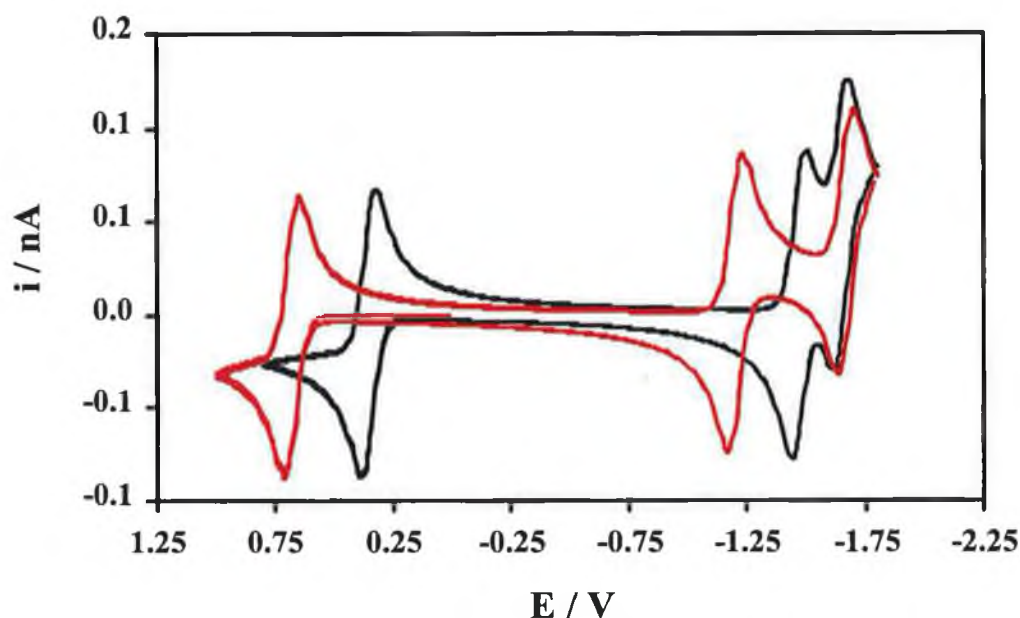


Figure 10 Solution phase cyclic voltammogram of $[\text{Os}(\text{bpy})_2\text{P3P Cl}]^+$ (black) and $[\text{Os}(\text{bpy})_2(\text{P3P})_2]^{2+}$ (red) in acetonitrile with 0.1 M TEAP as background electrolyte. The initial potential is 0.00 V in a positive direction.

2.5.4 NMR

Figure 11 show the proton spectra of the aromatic region for the complex $[\text{Os}(\text{bpy})_2\text{P0P Cl}]^+$. Full NMR data for $[\text{Os}(\text{bpy})_2\text{P2P Cl}]^+$ and $[\text{Os}(\text{bpy})_2\text{P3P Cl}]^+$ is present in Appendix 1. Identification of the individual protons peaks was difficult due to the unsymmetrical nature of the complexes. However, in all cases the integration was correct, showing the number of protons present to be 24, 28 and 30 respectively. In the spectra of $[\text{Os}(\text{bpy})_2\text{P2P Cl}]^+$ and $[\text{Os}(\text{bpy})_2\text{P3P Cl}]^+$ small impurity peaks are noticeable. However, when monolayers are formed on electrodes using this material, only one peak is observed in the voltammetric response. This observation suggests the impurity peaks are not surface-active.

Figure 12 shows the proton spectrum, in the aromatic region, for the N^6 -complex, $[\text{Os}(\text{bpy})_2\text{P0P Cl}]^+$. NMR spectra for the N^6 -complexes containing an aliphatic segment, $[\text{Os}(\text{bpy})_2(\text{P2P})_2]^{2+}$, $[\text{Os}(\text{bpy})_2(\text{P3P})_2]^{2+}$ may be found in Appendix 1. Due to the increased symmetrical nature of the N^6 -complexes over the N^5 -Cl complexes the identification of the

peaks present was more straightforward. Integration for all complexes gave the correct number of protons, i.e., 32, 40 and 44 for the complexes respectively.

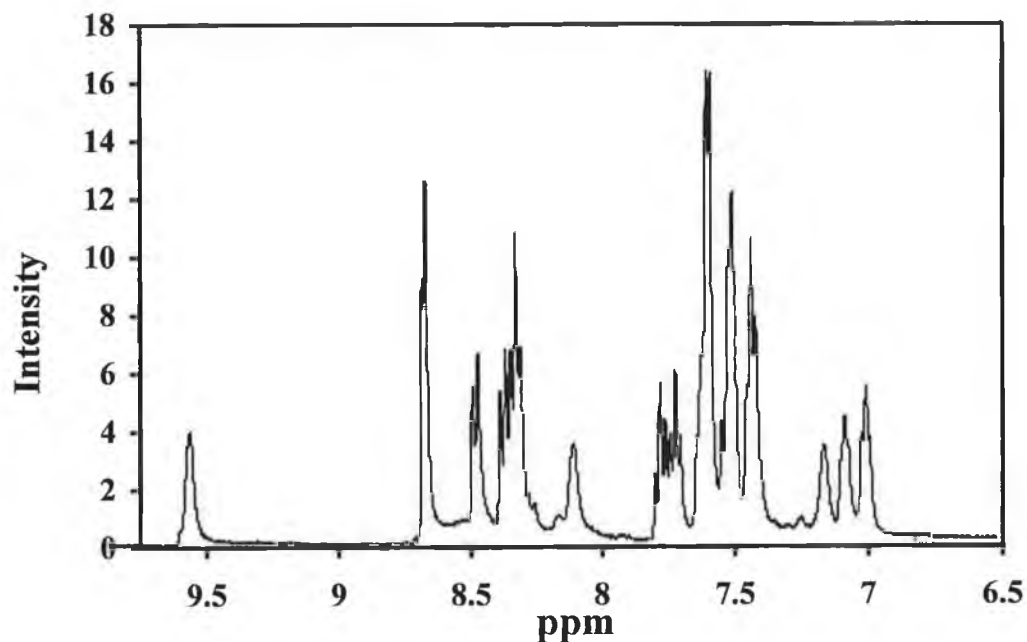


Figure 11 ¹H NMR of [Os(bpy)₂P0P Cl]⁺ in d-CH₃CN, aromatic region.

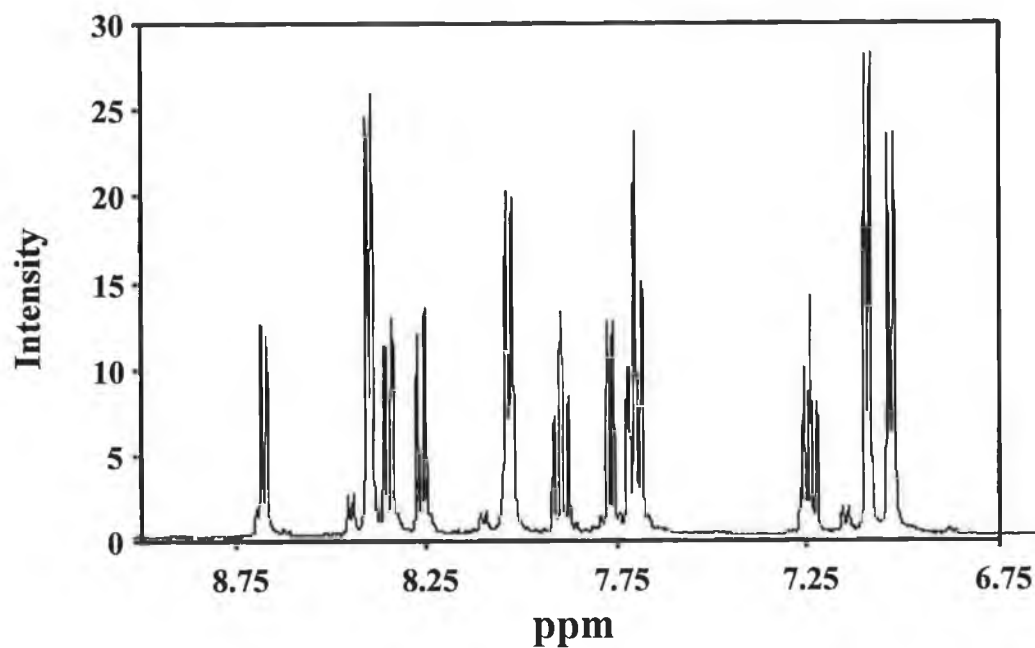


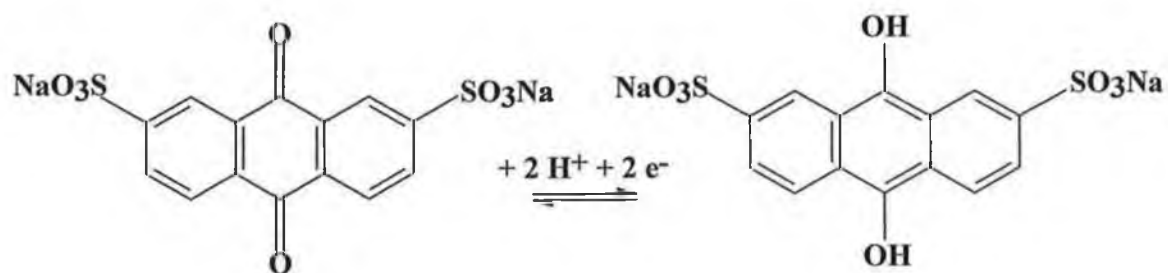
Figure 12 ¹H NMR of [Os(bpy)₂(P0P)₂]²⁺ in d-CH₃CN, aromatic region.

2.6 Anthraquinones

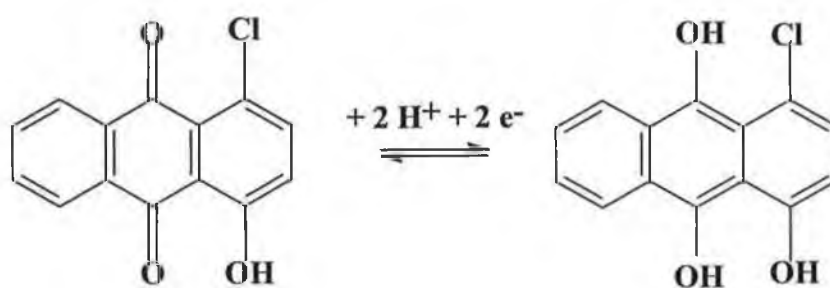
Quinones are cyclic ketones of such a structure that they are converted by reduction into hydroquinones; phenols containing two-OH groups. As they are highly conjugated, quinones are frequently coloured: p-benzoquinone for example, is yellow. Quinone complexes have been used in electrochemistry because of their ideal electrochemical behaviour. Research, using quinones has been conducted in areas such as sensor technology,²³ catalysis,²⁴ molecular devices,^{25, 26} polymer science²⁷ and corrosion inhibition²⁸. Quinones have been extensively studied in the medical field due to the structurally diverse quinone derivatives, which have been synthesised and because their coupled electron (e^-) and proton (H^+) transfer reactions play key roles in biological redox processes.^{29, 30, 31} Biological activities that have been reported for quinones and quinone derivatives include, enzyme inhibitors³² and antibacterial³³ and anticancer activities.^{34, 35, 36, 37, 38}

2.7 Characterisation of Anthraquinones

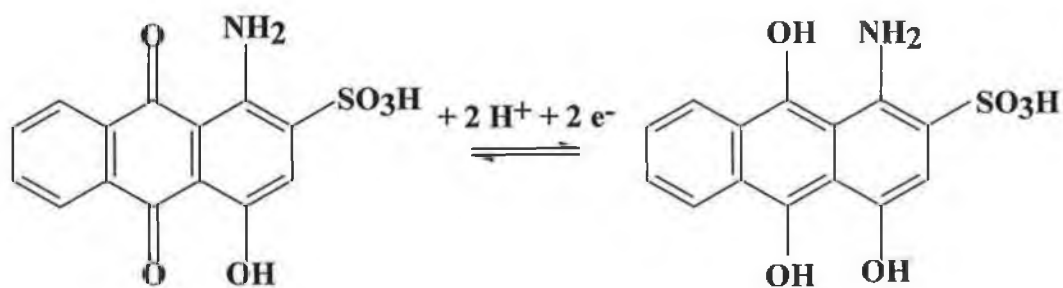
Anthraquinone-2,7-disulphonic acid (2,7-AQDS), 1-chloro-4-hydroxy-anthraquinone (1,4-AQClOH) and 1-amino-2-sulphonic-4-hydroxy-anthraquinone [AQNH₂SOH] were obtained from BASF (Ludwigshafen, Germany). Before their use, HPLC, UV-Vis, and NMR were performed on each species to analyse their purity.



Scheme 2 Anthraquinone-2,7-disulphonic acid sodium salt.



Scheme 3 1-chloro-4-hydroxyanthraquinone.



Scheme 4 1-amino-2-sulphonic-4-hydroxy-anthraquinone.

2.7.1 HPLC

Although HPLC can help identify a particular compound by its retention time and UV-Vis spectrum, it also plays the vital role of confirming the purity of the compound. HPLC for 2,7-AQDS, 1,4-AQCIOH and AQNH₂SOH revealed a single peak, in all cases. With the exception of 2,7-AQDS, which is negatively charged, all quinone compounds employed are neutral species under the analysis conditions. Table 2 shows the retention times observed. The charged quinone 2,7-AQDS elutes approximately one minute after the neutral species. Figure 18 shows the chromatographic response for each of the quinones analysed.

Complex	Retention time / min
2,7-AQDS	2.19
1,4-AQCIOH	1.39
AQNH ₂ SOH	1.60

Table 2 HPLC elution times for the anthraquinones investigated

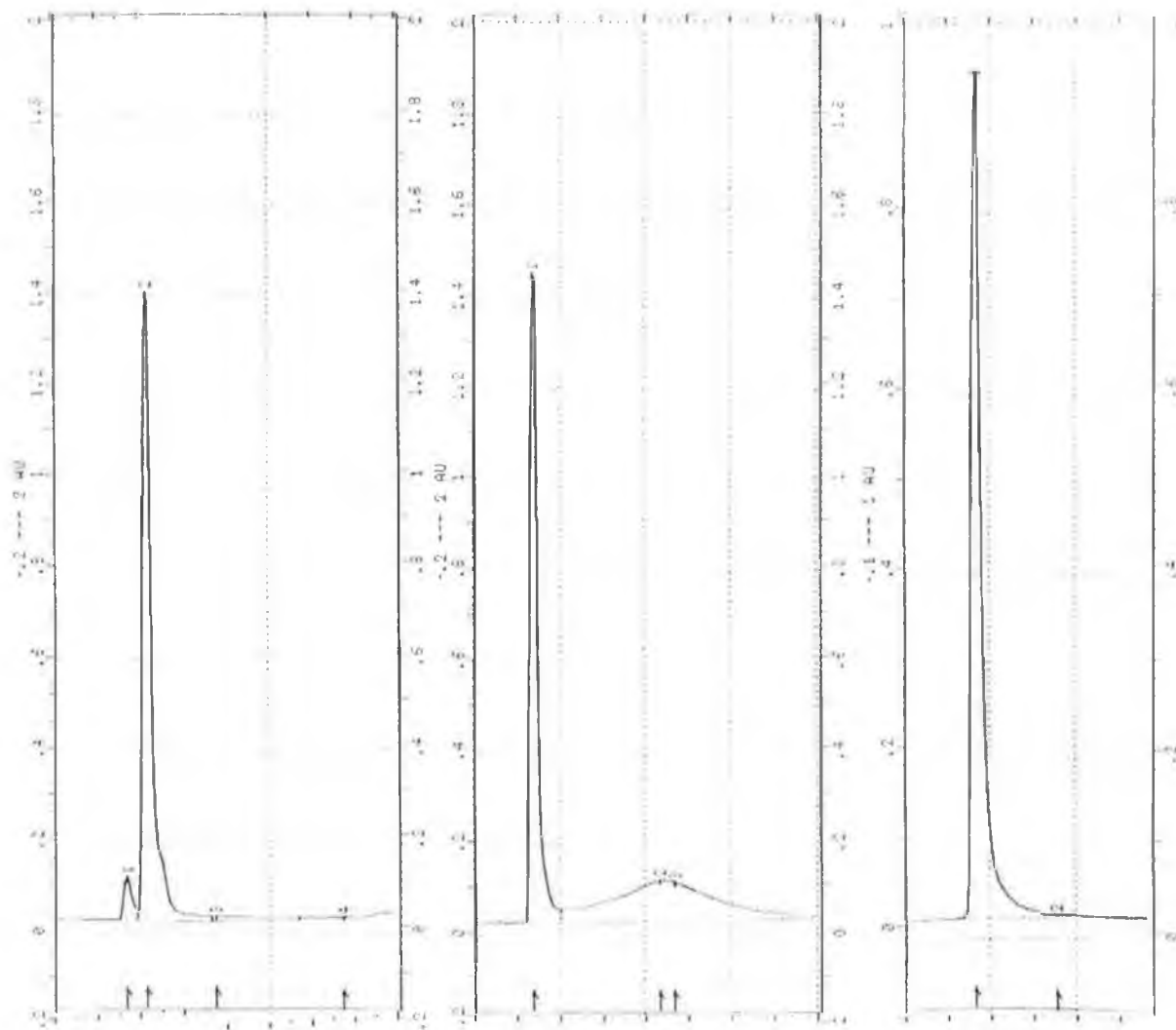


Figure 13 HPLC traces of 2,7-AQDS, 1,4-AQClOH, and AQNH₂SOH. The flow rate is 2.0 ml / min and the mobile phase 80:20 CH₃CN:H₂O, 0.08 M LiClO₄.

2.7.2 UV-Vis

Figure 14 represents the UV-Vis spectrum for the organic chromophores [2,7-AQDS], [1,4-AQCIOH] and [1,2,4-AQNH₂SOH]. The main strong bands are situated in the UV region below 300 nm in each case (π - π^* transitions).

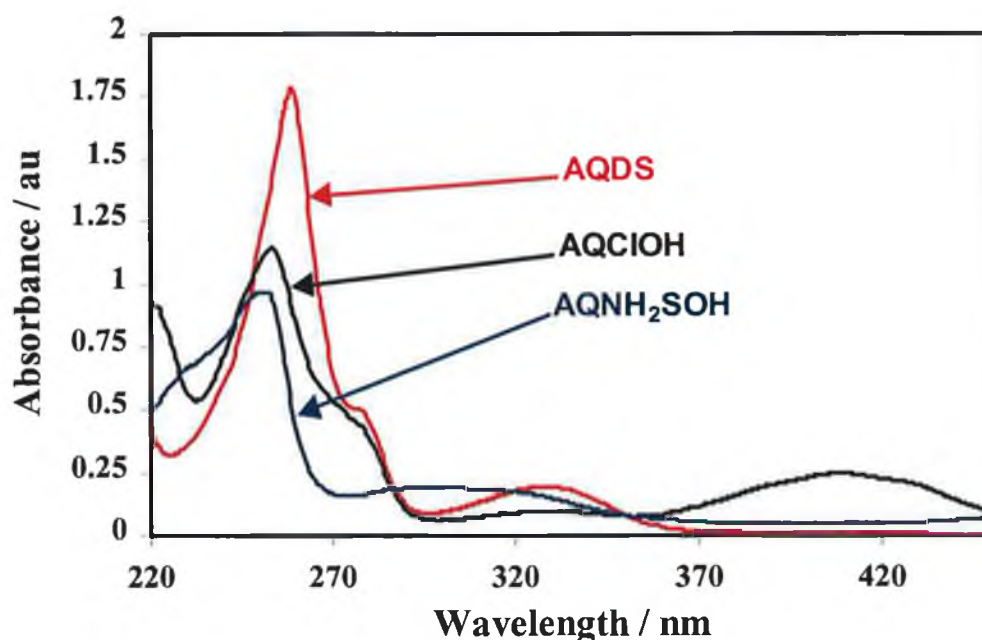


Figure 14 UV-Visible spectrum of the quinones [2,7-AQDS], [1,4-AQCIOH] and [1,2,4-AQNH₂SOH] in acetonitrile.

2.7.3 Electrochemistry

Figure 15 shows the voltammetric responses for the quinones used in these analyses at millimolar concentrations. The formal potentials are -0.020 V, -0.016 V and -0.08 V for [2,7-AQDS], [1,4-AQCIOH], [1,2,4-AQNH₂SOH], respectively. For quinone species that undergo a 2-electron transfer process, the peak to peak separation (ΔE_p) should be approximately 0.030 V, at slow scan rates. For these quinones, the ΔE_p is 0.039 , 0.035 and 0.061 V, respectively. Thus showing the ideality of the electrochemical responses.

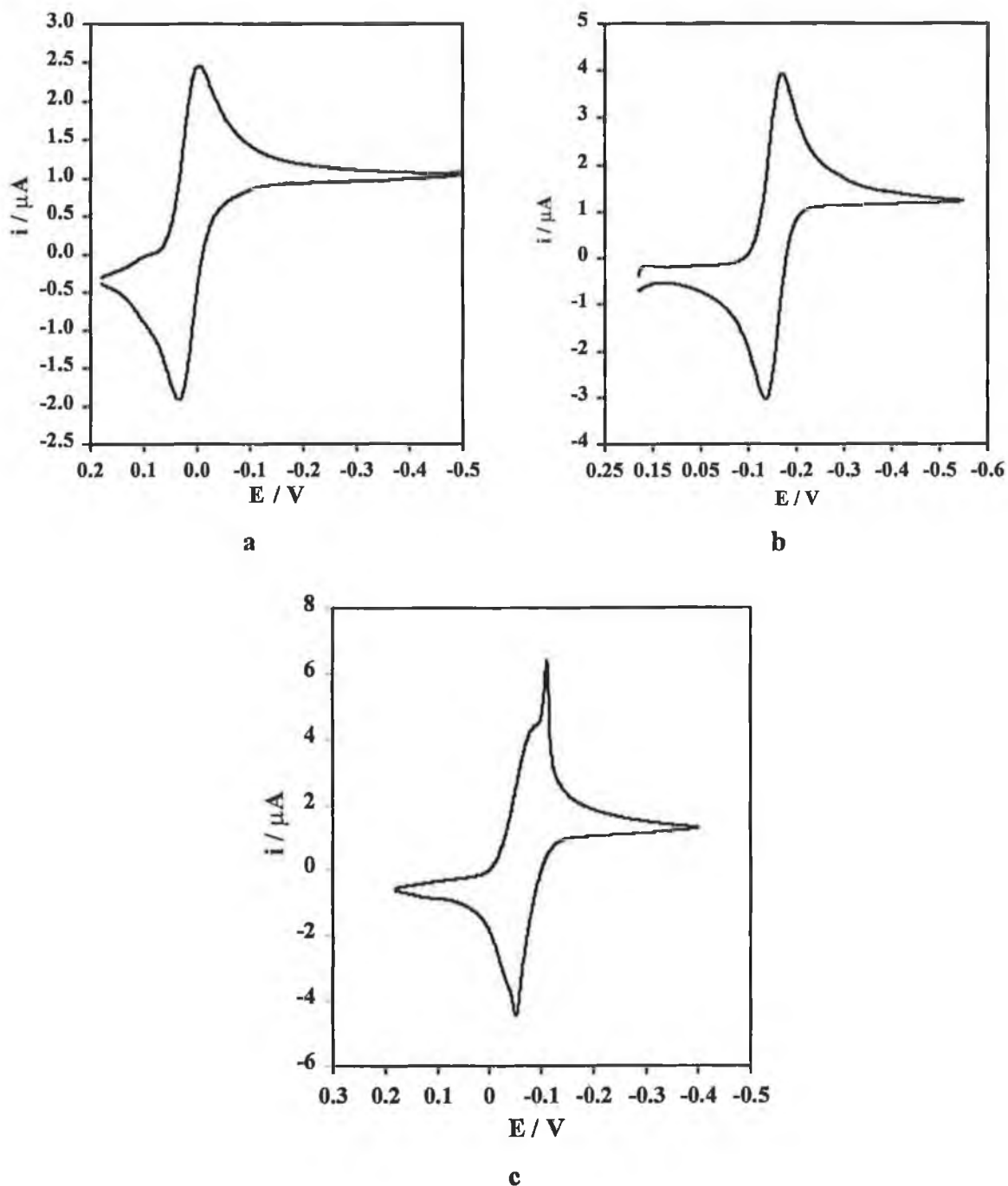


Figure 15 Solution phase CV responses of (a), [2,7-AQDS], (b), [1,4-AQClOH] and (c), [1,2,4-AQNH₂SOH] obtained from mM deposition solutions of the complex in ACN. The scan rate is 0.02 Vs^{-1} with the exception of the latter which is 0.1 Vs^{-1} .

2.7.4 NMR

Protons on a heteroatom differ from protons on a carbon atom in that: (1) they may be exchangeable, (2) they may undergo hydrogen bonding, and (3) they are subject to partial or complete decoupling by electrical quadrupole effects of some heteroatoms.³⁹

Figure 16 represents the NMR spectrum for [2,7-AQDS]. Integration of the spectra shows the expected six protons, two singlets and four doublets, two of which are assigned as a multiplet as overlapping of the spectra has occurred. The multiplet downfield is the H₄ and H₆ protons and resides downfield due to the presence of these protons from the carbonyl group in the H₅ position. The singlet and doublet peaks exhibit some peak splitting, which is most probably due to the cross communications from the adjacent protons on the aromatic rings.

Figure 17 shows the ¹H NMR for [1,4-AQCIOH] at 336 K. Integration gave a total of 6 protons, 4 doublets and 2 triplets. The H₄' and H₁' protons reside furthest downfield. This is due to the effect of the carbonyl atoms, which reside beside them. The proton which is the least affected by electronegativity is H₂, which is visible as a doublet at 7.35 ppm. No peak was present for the hydroxyl group. One possible reason is the presence of water in the d₄-DMSO solvent may cause the hydroxy peak to become flattened and more broad on the baseline.

Figure 18 shows the ¹H NMR for [AQNH₂SOH] at room temperature. Integration gave seven protons instead of the eight expected. The peak at 12.3 ppm gave an integration of one instead of the expected two. The NMR of amines attached to heteroatoms tends to be complicated. This is due to the following factors; the rate of exchange of the proton on the nitrogen atom with water present in the DMSO solvent and the electrical quadrupole moment of the ¹⁴N nucleus. We believe a rapid exchange is occurring which results in the observed sharp singlet with the integration of one. If intermediate or slow exchange were occurring, a broad NH peak would result along with coupling for slow exchange.

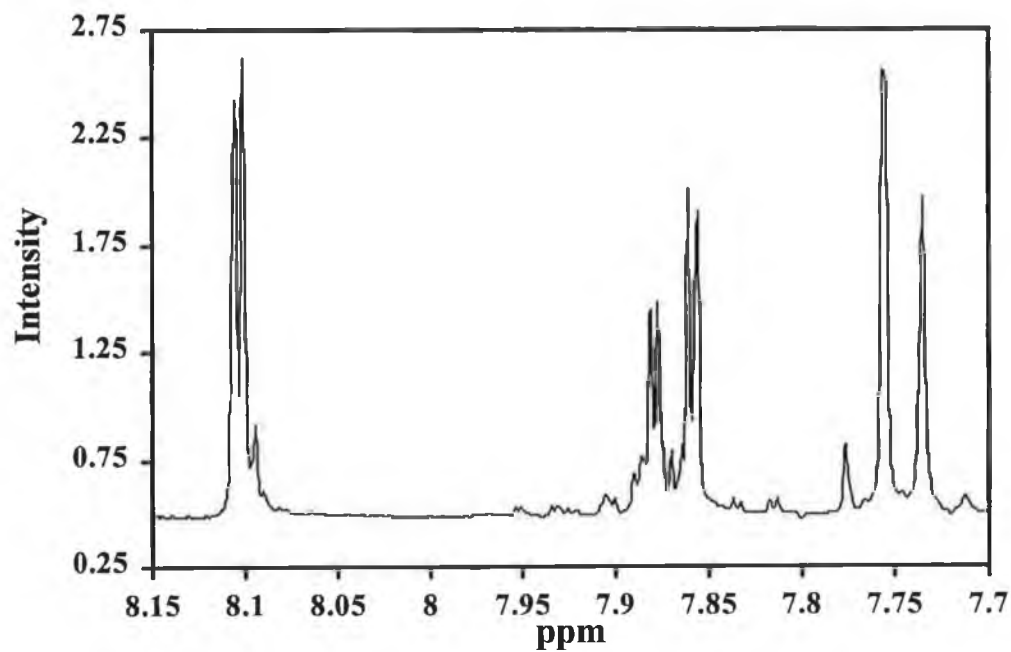


Figure 16 ^1H NMR of [2,7-AQDS] in $\text{d-D}_2\text{O}$.

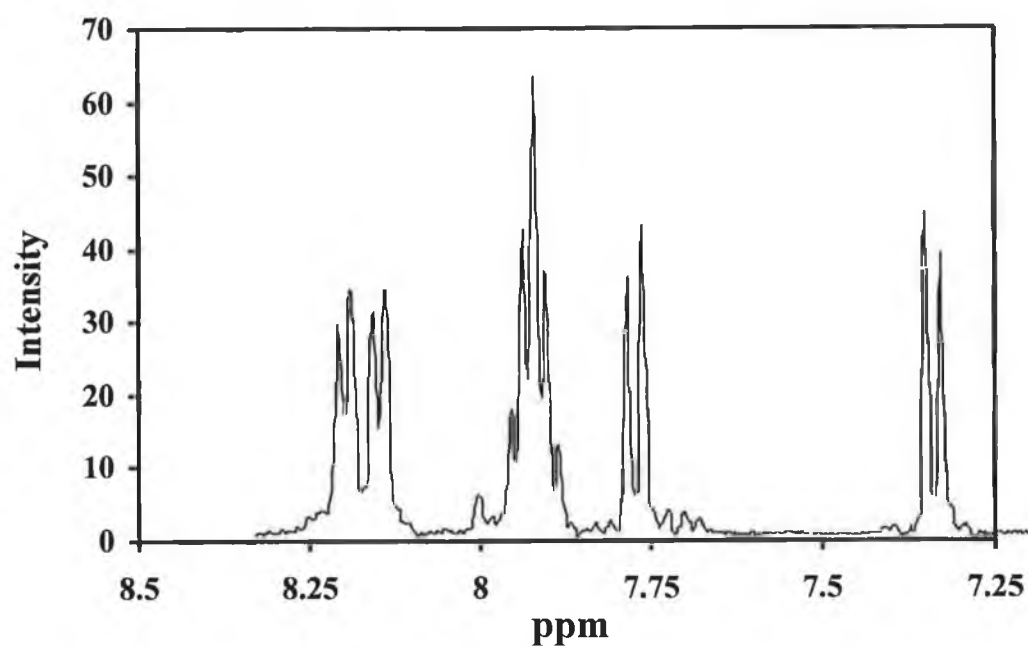


Figure 17 ^1H NMR of [1,4-AQCIOH] in $\text{d-CH}_3\text{CN}$ at 336 K.

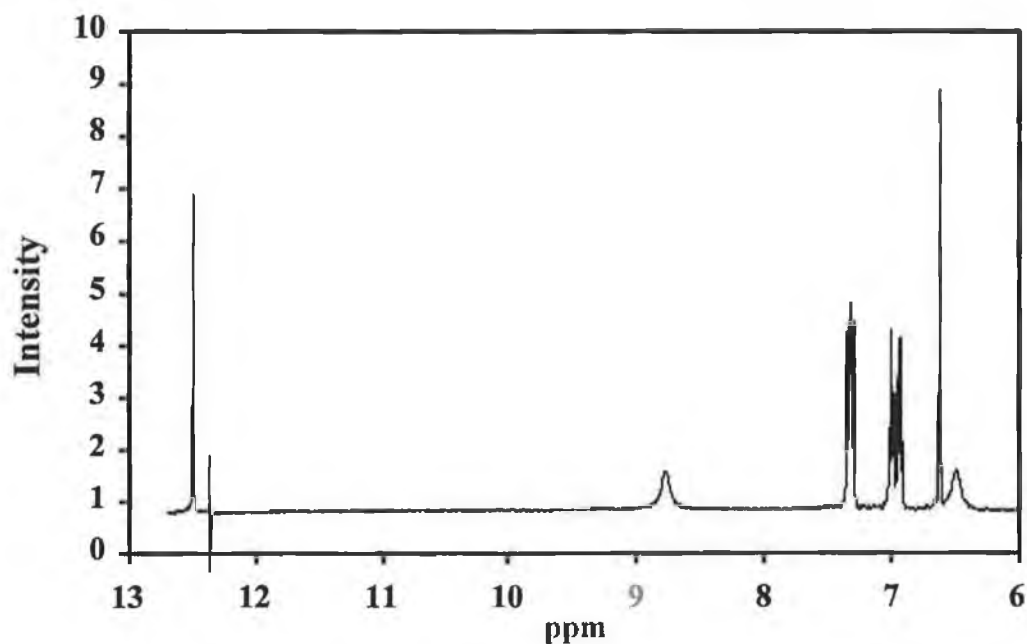


Figure 18 ^1H NMR of $[\text{AQNH}_2\text{SOH}]$ in d-DMSO.

[2,7-AQDS], ^1H -n.m.r. (400 MHz) δ ppm (DMSO): 7.72 – 7.74 (1H, s), 7.74 – 7.76 (1H, s), 7.86 (1H, d), 7.88 (1H, d), 8.1 (2H, m).

[1,4-AQCIOH], ^1H -n.m.r. (400 MHz) δ ppm (DMSO): 7.30 – 7.40 (1H, d), 7.77 (1H, d), 7.85 – 8.00 (2H, m), 8.10 – 8.17 (1H, d), 8.17 – 8.25 (1H, d).

$[\text{AQNH}_2\text{SOH}]$ ^1H -n.m.r. (400 MHz) δ ppm (DMSO): 6.5 (1H,), 6.6 (1H, s), 6.8 (1H, t), 7.1 (1H, t), 7.3 (1H d), 7.4 (1H d), 8.7 (1H), 12.3 (2H, s)

2.8 Conclusion

A series of osmium polypyridyl complexes have been synthesised in which the length of the bridging ligand varies by having 0, 2 or 3 methylene units present. Purification was performed by recrystallisation from acetone : water solutions. A thorough characterisation of these complexes has been performed using a variety of spectroscopic and chromatographic techniques. Elemental analysis was employed to confirm the % content of carbon, nitrogen and hydrogen. The oxidation and reduction potential of each redox-active complex was found using electrochemistry.

Anthraquinones obtained from BASF were also characterised using similar methods to those for the osmium polypyridyl complexes. Their purity was confirmed using NMR and HPLC and their solution phase redox properties were determined using electrochemistry.

2.9 References

1. Murray, R. W., *Electroanalytical Chemistry*, 13th Ed., Bard, A. J., New York, 1994
2. Schneeweiss. M. A., Kolb. D. M., *Phys. Status Solidi A*, **1999**, 173, 51
3. Hickman, J. J., Ofer, D., Labinis, P. E., Whiteside, G. M., Wrighton, M. S., *Science*, **1991**, 252, 688
4. Forster, R. J. Faulkner, L. R.; *J. Am. Chem. Soc.*, **1994**, 116, 5444
5. Forster, R. J. Faulkner, L. R.; *J. Am. Chem. Soc.*, **1994**, 116, 5453
6. Acevedo, D., Bretz, R. L., Tirado, J. D., Abruña, H. D., *Langmuir*, **1994**, 10, 1300
7. Campbell, J. L. E., Anson, F., *Langmuir*, **1996**, 12, 4008
8. Parsons, R., *Chem. Rev.*, **1990**, 90, 813
9. Schmickler, W., *Chem. Rev.*, **1996**, 96, 3177
10. Chidsey, C. E. D., *Science*, **1991**, 251, 919
11. Rowe, G. K., Creager, S. E., *Langmuir*, **1994**, 10, 1186
12. Creager, S. E., Rowe, G. K., *Anal. Chim. Acta.*, **1991**, 246, 233
13. Chidsey, C. E. D., Bertozzi. C. R., Putvinski. T. M., Muijsce. A. M., *J. Am. Chem Soc.*, **1990**, 112, 4301
14. Collard, D.M.; Fox, M.A., *Langmuir* ,**1991**, 7, 1192
15. Tirado, J. D., Abruña, H. D., *J. Phys. Chem.*, **1996**, 100, 4556-4563
16. Bretz, R. L., Abruña, H. D. *J. Electroanal. Chem.*, **1995**, 388, 123
17. Forster, R. J., Faulkner, L. R. *Langmuir* **1995**, 11, 1014
18. Forster, R. J., *Inorg. Chem.*, **1996**, 35, 3394
19. Forster, R. J., O'Kelly, J. P. *J. Phys. Chem.* **1996**, 100, 3695-3704
20. Buckingham. D. A., Dwyer. F. P., Goodwin. H. A., Sargeson. A. M., *Aust. J. Chem.*, **1964**, 17, 325
21. Acevedo, D., Abruña, H. D. *J. Phys. Chem.*, **1991**, 95, 9590
22. O'Connor. C., Ph.D., Thesis, Dublin City University, **1999**
23. Davidson. V. L., Jones. L. H., *Anal. Chim. Acta.*, **1991**, 249, 235

24. Lorenzo. E., Sánchez. E., Pariente. F., Tirado. J., Abruña. H. D., *Anal. Chim. Acta.*, **1995**, 309, 79
25. Joulié. L. F., Schatz. E., Ward. M. D., Weber. F., Yellowlees. L., *J. Chem. Soc., Dalton Trans.*, **1994**, 799
26. Wagner. R. W., Brown. P. A., Johnson. T. E., Lindsey. J. S., *J. Chem. Soc. Chem. Comm.*, **1991**, 1463
27. Wang. P., Martin. B. D., Parida. S., Rethwisch. D. G., Dordick. J. S., *J. Amer. Chem. Soc.*, **1995**, 117, 12885
28. Slavcheva, E., Sokolova. E., Raicheva. S., *J. Electroanal. Chem.*, **1993**, 360, 271
29. He, P., Crooks, R. M., Faulkner, L. R., *J. Phys. Chem.*, **1990**, 94, 1135
30. Chen. X., Zhuang. J., He. P., *J. Electroanal. Chem.*, **1989**, 271, 257
31. Keita. B., Nadjo. L., *J. Electroanal. Chem.*, **1984**, 163, 171
32. Hoffman-Ostenhof. O., *Metab. Inhib.*, **1963**, 2, 145
33. Hoover. J. R. E., Day. A. R., *J. Amer. Chem. Soc.*, **1954**, 76, 4148
34. Lin. A. J., Cosby. L. P., Sartorelli. A. C., *Cancer Chemother. Rep. Part 2*, **1974**, 4, 23
35. Driscoll. J. S., Hazard. G. F. Jr., Wood. H. B. Jr., *Cancer Chemother. Rep. Part 2*, **1974**, 4, 1
36. Haung. Z.-H., Chen. Y.-N., Menon. K., Teicher. B. A., *J. Med. Chem.*, **1993**, 36, 1797
37. Saito. H., Hirata. T., Kasai. M., Fujimoto. K., Ashizawa. T., Morimoto. M., Sato. A., *J. Med. Chem.*, **1991**, 34, 1959
38. Moret. E. E., de Boer. M., Hilbers. H. W., Tollenaere. J. P., Janssen. L. H. M., Holthuis. J. J. M., Dreibergen. R. J., Verboom. W., Reinhoudt. D. N., *J. Med. Chem.*, **1996**, 39, 720
39. Silverstein. R. M., Clayton Bassler. G., Morrill. T. C., *Spectrometric identification of organic compounds*, Fifth Ed., John Wiley and Sons, Inc., **1991**

CHAPTER 3

Fabrication and Characterisation of Microelectrodes

3 Introduction

Microelectrodes have been defined as electrodes whose critical dimension is less than about $10\text{ }\mu\text{m}$ ¹. The area of electrochemical research devoted to using microelectrodes has dramatically increased since the early 1980's.^{2, 3, 4, 5, 6, 7} The main reasons for this intense interest have been the availability of microscopic wires, namely platinum and gold and the tremendous improvement in performance offered by microelectrodes.

Section 1.4 deals with the geometry of microelectrodes, their applications, their advantages compared with macroelectrodes and their use in electrochemical experiments. Here, the fabrication and characterisation of gold, platinum and mercury microelectrodes is discussed.

The fabrication of these microelectrodes has changed and developed significantly over the last 20 years. In 1984, Howell and Wightman⁸ constructed microelectrodes of gold, platinum and carbon fiber. In the case of gold and platinum, the microwires were sealed in soft glass tubing and electrical contact to a copper wire was made from silver epoxy. Carbon fiber electrodes were prepared by sealing the fiber between two microscopic slides with epoxy. They found their electrodes responded extremely well at low (0.1 Vs^{-1}) and high scan rates ($100,000\text{ Vs}^{-1}$). In 1989 Wightman and Wipf⁹ improved the technique by sealing the electrodes using a coil of resistively heated Nichrome wire to melt the soft glass around the wire. They found the capacitance to be approximately 60 times greater than theoretically expected, which they attributed to stray capacitance between the micro-wire and the hook-up wire, caused by the use of silver epoxy and mercury to make the electrical connection. Pendley *et al.*,¹⁰ also using Nichrome wire to seal the glass, fabricated microelectrodes of less than $10\text{ }\mu\text{m}$ by stretching $75\text{ }\mu\text{m}$ platinum wire on a pipette puller. Martin and co-workers¹¹ developed a method of sealing imperfections based on forming silane monolayers. However, their method is laborious and time consuming. The electrode was prepared by depositing platinum based ensembles electrochemically into the pores of a host membrane, sealing by vacuum-impregnating with molten polyethylene and polishing to reveal the platinum electrode. The electrode was then exposed to neat octadecyltrichlorosilane (OTS), in an

Ar-filled glove bag, for 30 mins. The platinum was again exposed by polishing using 0.05 μm alumina. Their results show the OTS layer to be stable, with no loss after exposure to 0.2 M NaCl for up to 8 hours.

Malem and Mandler¹² published an inexpensive and efficient method for the construction of gold electrodes, in which they sealed a small piece of gold into a pasteur pipette. They placed glass powder in the barrel of a sealed pipette tip and heated to 420°C in order to melt the glass powder around the gold wire. The glass powder was selected so that it had a thermal expansion coefficient similar to that of the gold wire. Using this method they developed an efficient method for fabricating electrodes where no leakage of electrolyte between the metal and the insulator occurs. Tschunchy and Heinze¹³ produced a thorough paper examining different techniques to decrease stray capacitance. Their most significant innovation was to connect the micro and macro wires without using silver epoxy or mercury. Instead, the connection was completed by using a bunsen flame to fix the wires in-place. Also, two glass insulating tubes were used to shield the microelectrodes from interference and to minimise the stray capacitance.

Bond *et al*¹⁴ have provided a comprehensive picture on the comparison of polishing procedures by statistical analysis of voltammetric data. They investigated a variety of techniques in polishing and found the reproducibility of all data to be significantly improved when polishing was performed before each experiment. Also instrumental rather than manual polishing gave the most consistent results.

The manufacture of mercury microelectrodes has also received considerable attention over the years. Deposition has been performed on electrode materials such as carbon fibers,^{15,16} carbon microdiscs,¹⁷ iridium,¹⁸ gold,¹⁹ silver²⁰ and platinum.^{21,22,23} Platinum is the most commonly used platform for the formation of mercury microelectrodes as many problems arise from the use of other metals. For example, continuous coatings of mercury are difficult to achieve on carbon since mercury deposits are in droplet form. Moreover, gold has a significant solubility in mercury (0.14% at 25°C)²⁴ and mercury reacts with silver to form an amalgam over time.

Wightman,²² produced mercury microelectrodes electrochemically by holding the potential at 0.0 V while having a platinum electrode immersed in a Hg(I) aqueous solution. Faulkner and co-workers²¹ have developed a method for producing hemispherical mercury microelectrodes by etching a channel into a sealed platinum microelectrode. They silanised the channeled glass using 5% dichloromethylsilane in CCl₄ and deposited mercury into the silanised channel from an aqueous solution of mercurous nitrate. Their results indicated considerable improvement in cyclic voltammograms over electrodes produced without the silanising procedure.

The choice of method used for the production of platinum, gold, carbon fiber and mercury microelectrodes is highly dependent on the experiments in which they are to be utilized. In the case of kinetic analysis, electrodes need to have low RC time constants and therefore the connections between the wires are of utmost importance. In contrast, for analysis in highly resistive media, the connections between the microscopic wire and hook-up wire are not so critical. The use of microelectrodes will continue as manufacturing techniques improve, particularly as the size of micro-wires used for fabrication will decrease leading the way for increases in analysis in areas such as *in-vivo* analysis and fundamental studies of fast electron transfer.

3.1 Construction of gold and platinum microelectrodes

The technique used to prepare 5 and 25 μm gold and platinum electrodes for this work varied in their respective construction due to the diameter and melting point of the metal being employed. Both approaches are outlined below.

3.1.1 5 μm gold and platinum electrodes:

The glass used to house the electrodes is initially cut into lengths of 15 cm and soaked overnight in dilute nitric acid (HNO₃). This is performed in order to remove any dirt and grease, which may adhere to the inner surface of the glass. After soaking, the glass

is removed and washed copiously with Milli-Q water, acetone and finally rinsed with Milli-Q water. The glass is then dried in an oven.

The dried lengths of glass are then tapered by heating in the center and by gently drawing a taper that is approximately 4 cm long. Once cool, the glass is snapped at the center of the taper and the tapered end sealed, by rotating the glass in a bunsen flame.

A piece of gold wire approximately 1 cm in length is then washed with acetone, dried and placed into the sealed glass tube. A single drop of Milli-Q water is let drip into the glass chamber and onto the gold to hold the piece of gold to the glass wall as the glass is then sealed around the wire. This is achieved by creating a vacuum on the open end of the glass insulator and inserting the tapered end of the glass into a bunsen flame. The glass is only allowed to collapse around the wire for approximately 5 mm, as it is still necessary to connect the exposed gold to a connecting wire in order for electrical contact to be made.

A copper wire of approximate length 4 cm is connected to a “hook up” wire by wrapping the hook up wire around the copper wire and soldering the two together (Figure 1). The hook up wire, made from aluminium, is then bent in a zig-zag pattern in order to fit the internal diameter of the insulator. This bending of the transition wire is carried out to give rigidity to the overall electrode so when polishing is being performed, the chances of breaking the wire are reduced.

Using a micro-syringe, a small volume of silver conductive paint is injected into the glass and over the protruding gold wire. The hook up / copper wire assembly is then placed into the conductive paint. A cap is put over the open ended electrode and sealed using a small volume of araldite epoxy resin. The electrode apparatus is then placed into an oven overnight a temperature of 50°C in order to cure the conductive paint.

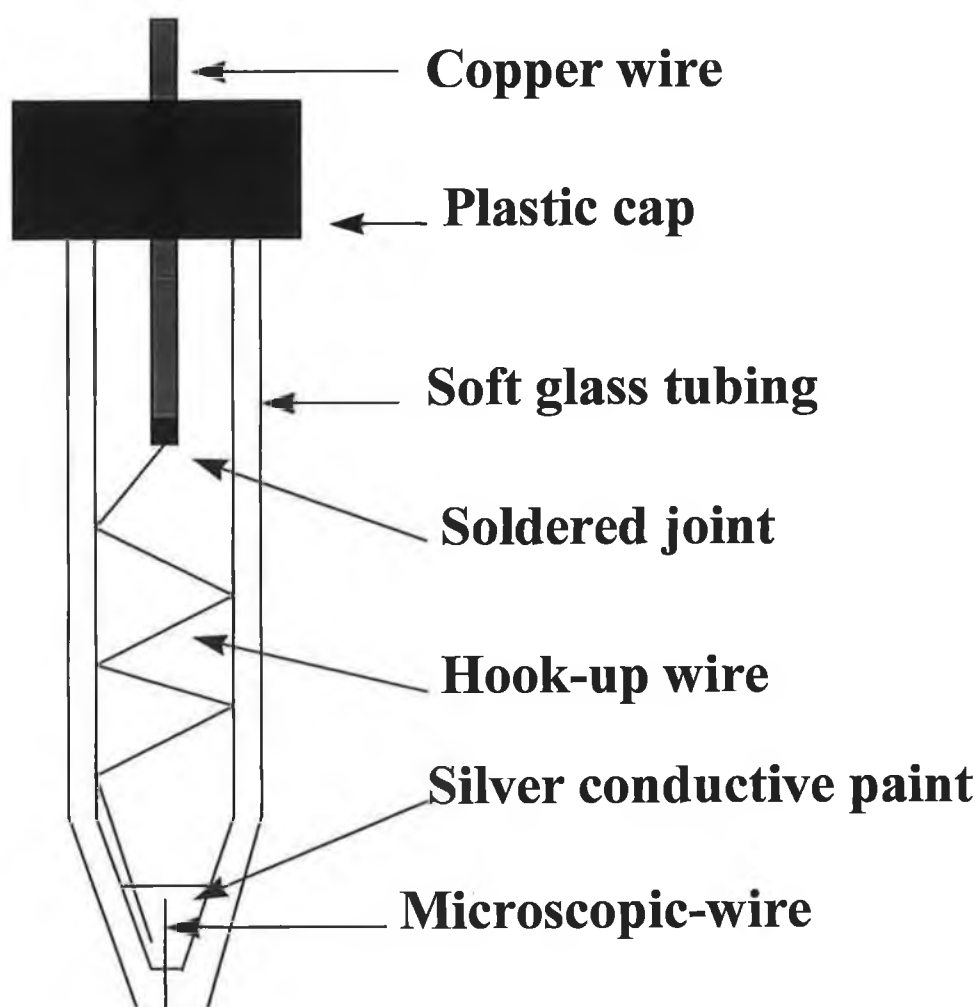


Figure 1 Cross section of the structure of a 5 μm gold microelectrode.

3.1.2 25 μm gold electrodes:

The difference in construction approach between the 5 and 25 μm gold electrode is due to the difficulty in handling of the small gold wires. Instead of using silver epoxy for electrical connection, as in the case of the 5 μm , the 25 μm gold wire is actually wound around the hook-up wire and soldered to make an electrical connection. This process is extremely difficult and it is recommended that before soldering the gold to the hook-up wire, the soldering iron should be let cool so as not to melt the gold upon contact. The process of encasing the electrode into the insulating body is the same, i.e., using a vacuum to seal the glass around the gold and sealing the open end using araldite epoxy resin.

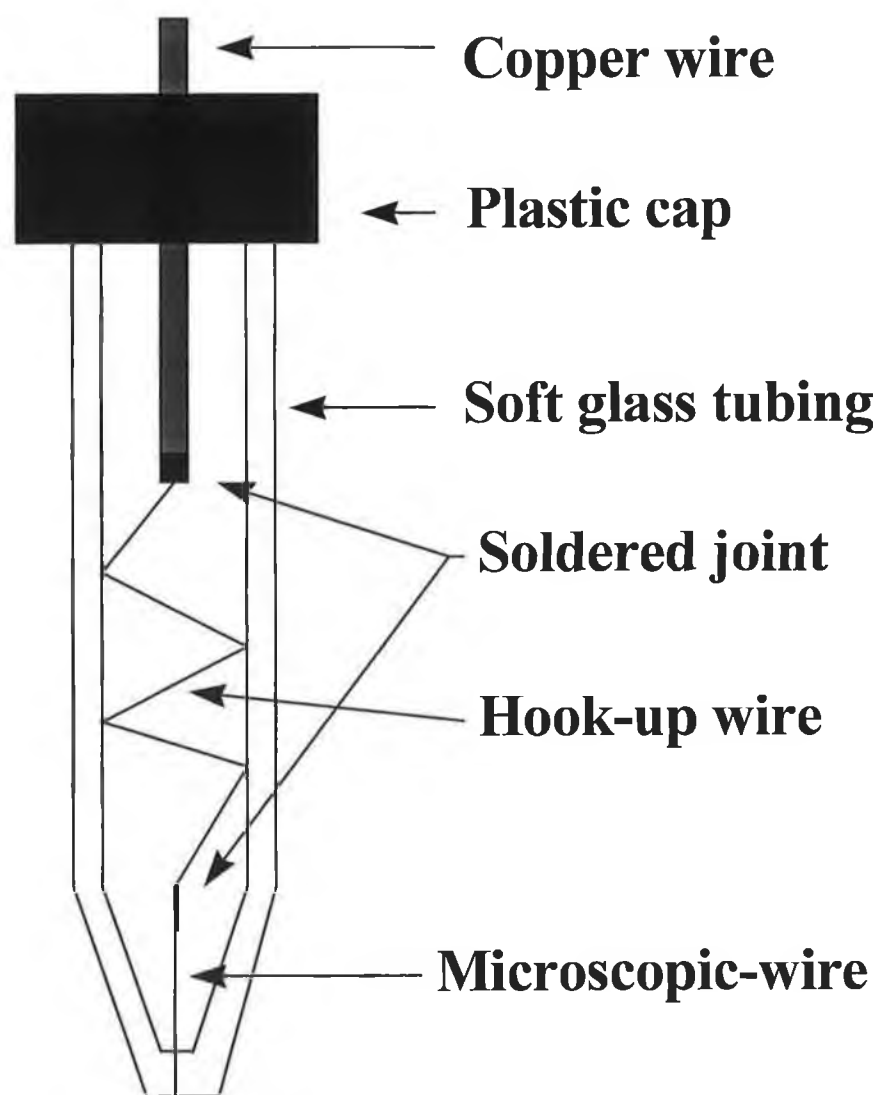


Figure 2 Cross section of the structure of a 25 μm gold microelectrode.

3.1.3 Exposing the metal electrode.

For all constructed electrodes the removal of excess glass and exposure of the metal is achieved using the same procedure. Initially the electrode is checked for electrical contact using cyclic voltammetry in a suitable background electrolyte such as 0.1 M LiClO_4 (Figure 3) and confirming the appearance of a background charging current. Once contact has been established, the electrodes are left overnight in Milli-Q water to test the quality of the seal. An increase in the background current is indicative of a leakage (Figure 4). When a leak becomes apparent the electrode is discarded.

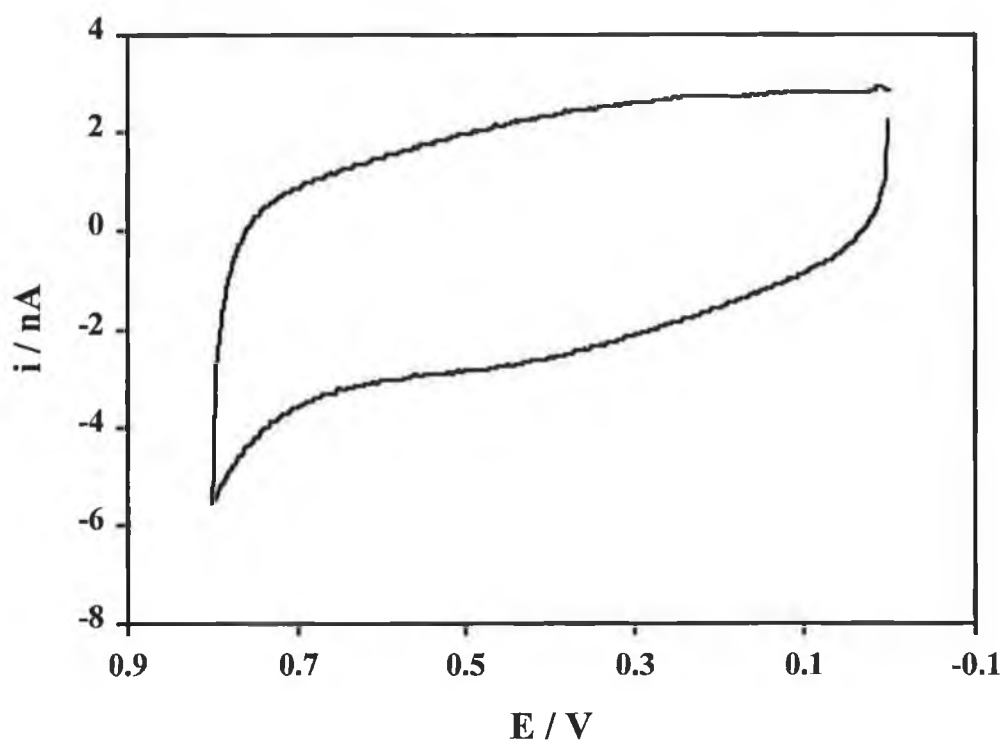


Figure 3 Cyclic voltammogram for a 25 μm gold microelectrode in 0.1 M LiClO_4 . The scan rate is 0.5 Vs^{-1} with the potential limits between 0.8 – 0.0 V. The initial potential is 0.0 V.

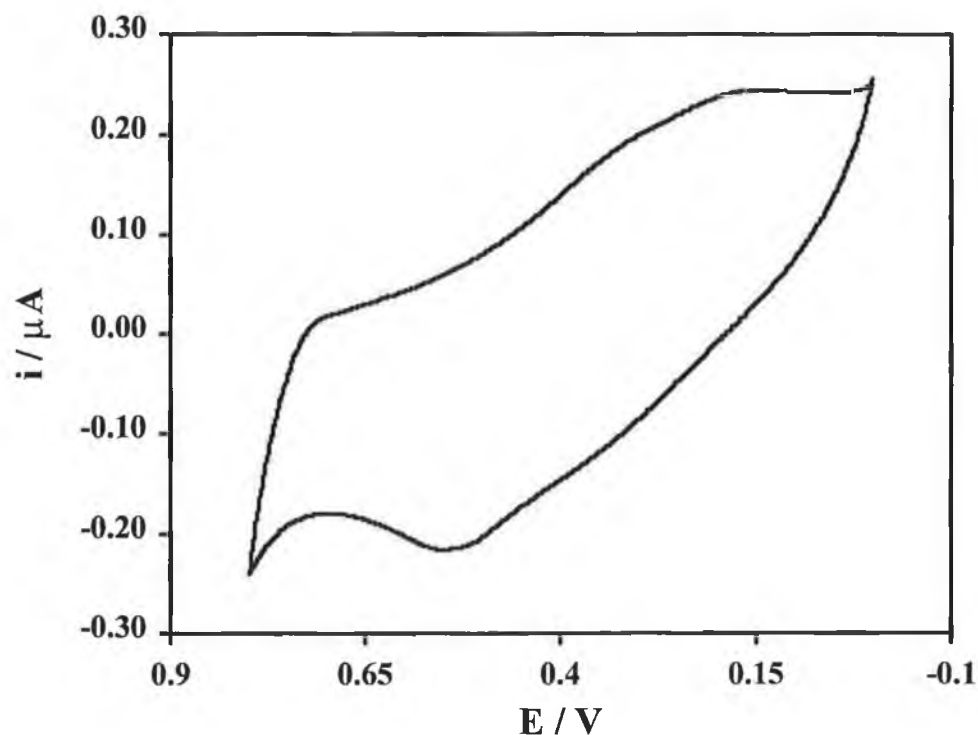


Figure 4 Cyclic voltammogram for a *leaking* 25 μm gold microelectrode in 0.1 M LiClO_4 . The scan rate is 0.5 Vs^{-1} with the potential limits between 0.8 – 0.0 V. The initial potential is 0.0 V.

The construction of the 5 and 25 μm gold microelectrodes was accomplished with approximately 80 – 90 % success rate.

3.2 Construction of mercury microelectrodes

The construction of mercury microelectrodes can be accomplished using either electro or electroless deposition. There are many advantages in using mercury electrodes over that of gold, carbon or platinum such as, the large negative potential window obtained and the fact that mercury has an atomically smooth electrode surface. Electrodeposition involves growing a hemispherical deposit of mercury onto a 5 μm microelectrode as outlined below.

A clean, polished platinum microelectrode, where the adsorbed hydrogen has been desorbed, is placed into a degassed deposition solution containing Hg (I) . The

deposition solution consists of 1.0 M KNO_3 with 5.7 mM mercury(I) nitrate dihydrate (Aldrich) and 0.5% HNO_3 . A potential of 0.00 V was applied to the platinum electrode and initially let run for 200 seconds. The electrode is then removed from the solution, rinsed and immersed in an electrolytic solution in order to check the background current to ensure the formation of a mercury film. The electrode was also placed in a 20 μM solution of 2-hydroxy-anthraquinone and a cyclic voltammogram recorded. Figure 6 shows a typical voltammetric response obtained when the potential window is extended out from 0.15 V to -0.9 V in order to observe the electrochemical response of the adsorbed complex and to ensure no other impurities were adsorbing on the electrode surface.

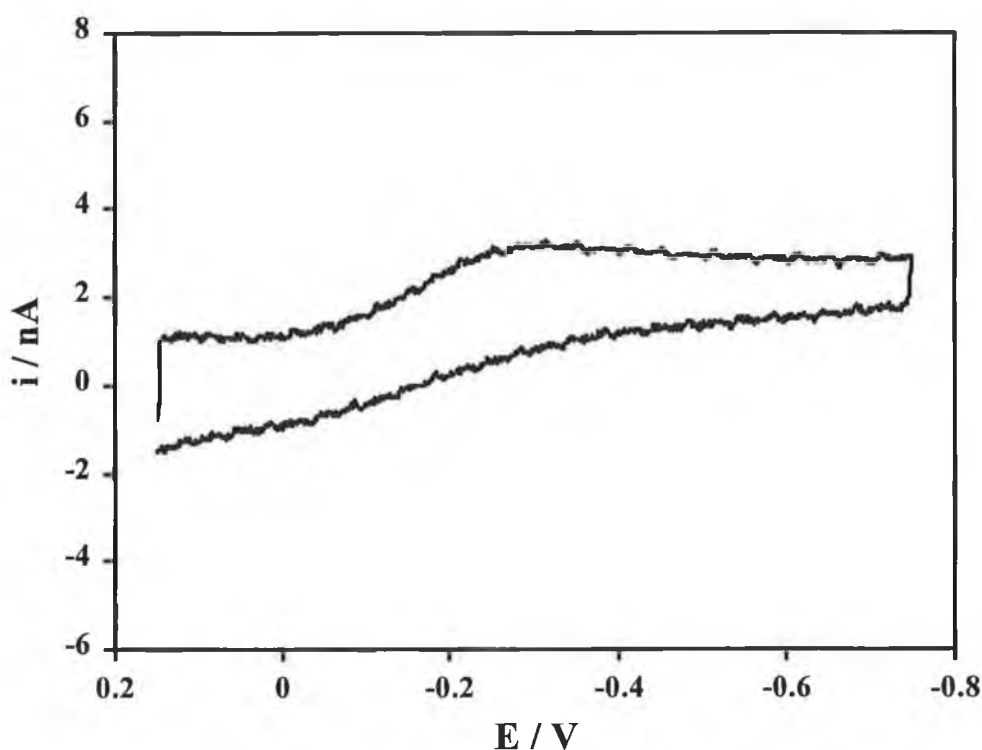


Figure 5 Cyclic voltammogram for a 5 μm platinum microelectrode in 1.0 M HClO_4 after being deposited with mercury. The scan rate is 5 Vs^{-1} and the potential limits between 0.15 - -0.75 V. The initial potential is 0.15 V.

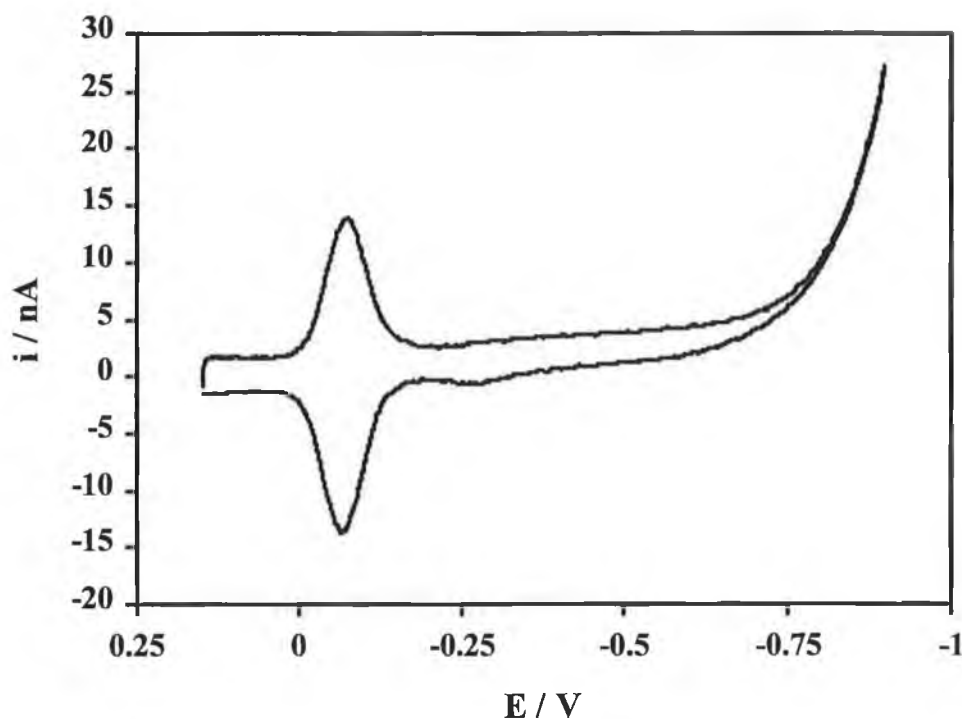


Figure 6 Cyclic voltammogram for a 5 μM platinum microelectrode after being deposited with mercury, in a solution containing 20 μM 2-hydroxyanthraquinone and 1.0 M HClO_4 . The scan rate is 5 Vs^{-1} and the potential limits between 0.15 and -0.9 V. The initial potential is 0.15 V.

Consistent with the behaviour observed at bulk Hg, after approximately -0.6 V a large reductive current is observed. Using a potential window from 0.15 V to -0.065 V and assuming saturation coverage of a monolayer is achieved ($1.1 \times 10^{-10} \text{ mol/cm}^2$) using a 20 μM solution, the charge passed to oxidise and reduce the redox-active adsorbed species may be used to determine the area and radius of the mercury microelectrode. Once the CV was recorded, the electrode was rinsed and the background charging current checked by CV to ensure desorption of the redox-active species had occurred and the electrode was again placed in the mercurous deposition solution and the same potential was applied for another 200 seconds. This process was continued several times to determine the relationship between deposition time and surface area. This was necessary to accurately determine the deposition time required to fabricate a preselected size mercury microelectrode from a 5 μM platinum microelectrode. Figure 7 shows that

this relationship is linear at least up to deposition times of 3000 seconds. An overlay of these CV's is presented in Figure 8.

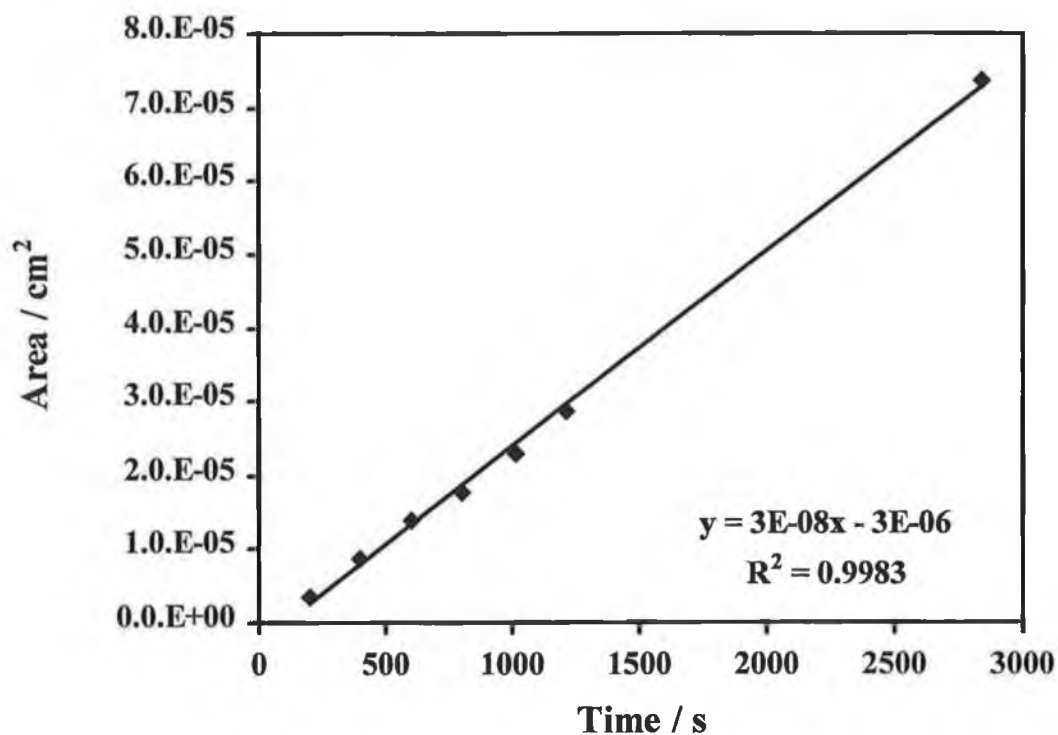


Figure 7 Graph showing the linear relationship between the dependence of the area of a platinum microelectrode deposited with mercury with increased deposition time.

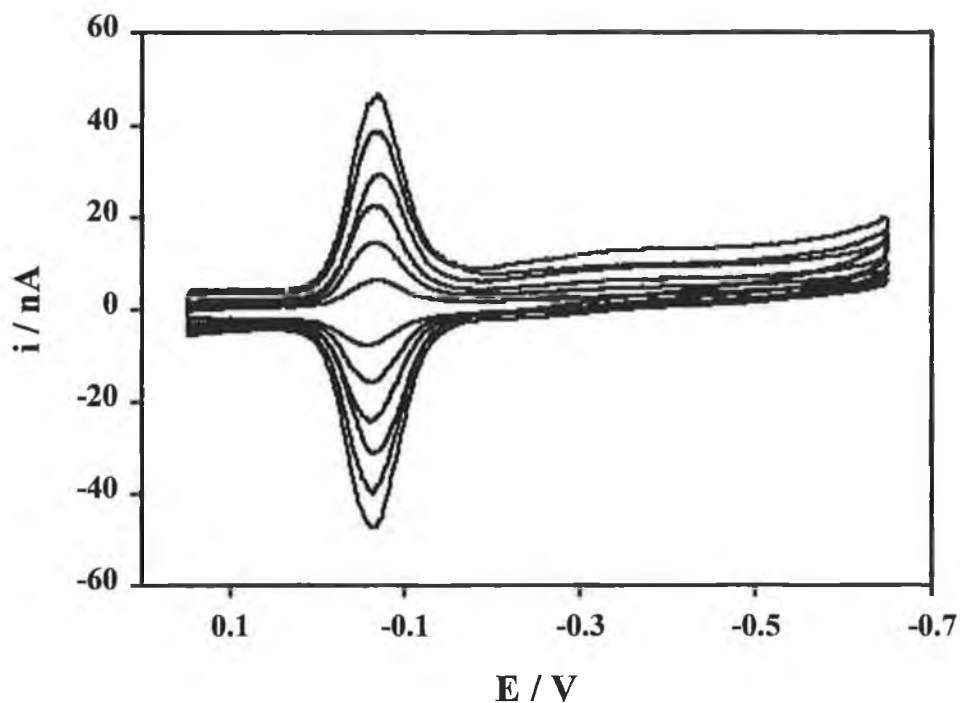


Figure 8 Cyclic voltammogram of the anthraquinone 2-hydroxy-anthraquinone adsorbed on a mercury microelectrode at various deposition times. The deposition times attributed to each CV are from top to bottom 200, 400, 600, 800, 1015 and 1215 seconds. The scan rate is 5 Vs^{-1} and the potential limits between 0.15 and -0.65 V. The initial potential is 0.15 V.

3.3 Characterisation of microelectrodes

3.3.1 Polishing technique

Once it has been established that the electrodes are of good quality with no leakage, they are mechanically polished using wet alumina on polishing cloths (Buehler). The sealed electrodes are polished using a variety of alumina particle sizes (Buehler), 12.5 μm down to 0.05 μm , in order to obtain a smooth electrode surface.

The alumina is placed on the cloth and a small volume of Milli-Q water is added. Starting with an alumina particle size of 12.5 μm , the electrodes are polished by holding the electrode at 90° to the felt pad and rotating the electrode in a figure of eight motion, approximately 50 times. To ensure uniform polishing, the electrode is then rotated and polishing is repeated on another part of the polishing pad.

After polishing for approximately 10 minutes the electrode is washed with Milli-Q water, sonicated in Milli-Q water (to remove attached alumina) and rinsed again with Milli-Q water, before a cyclic voltammogram is run in a relevant background electrolyte. A typical voltammetric response is illustrated in Figure 9.

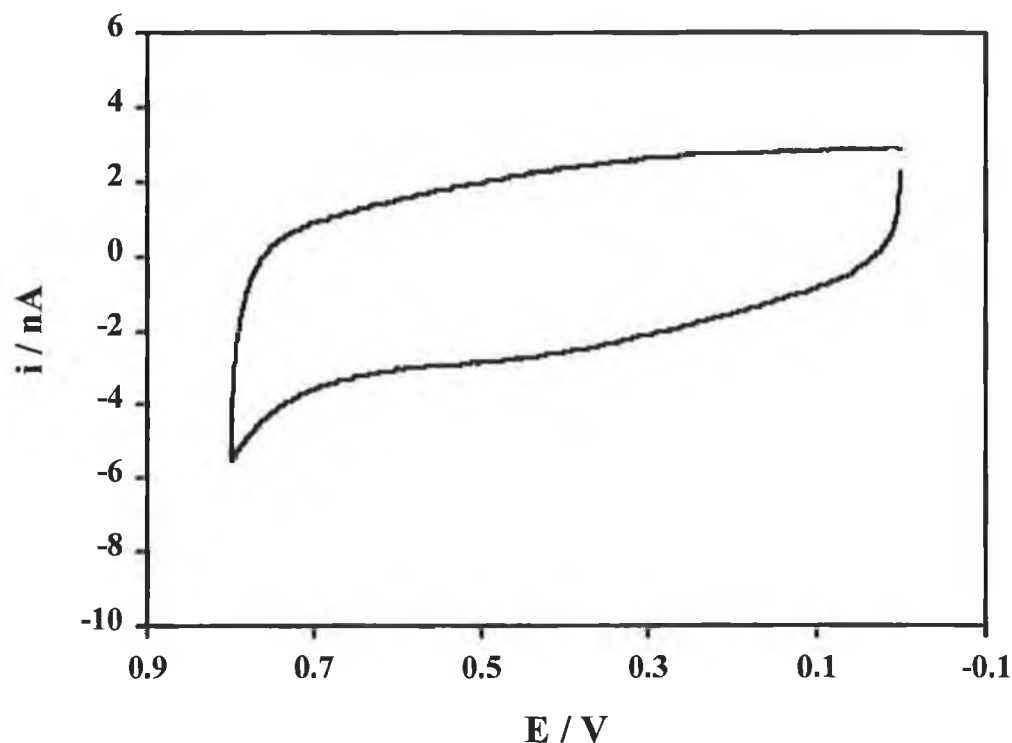


Figure 9 Background cyclic voltammogram of a 25 μm gold microelectrode in 0.1 M LiClO_4 . The scan rate is 0.1 Vs^{-1} . The potential limits are 0.7 – 0.0 V. The initial potential is 0.0 V.

The process described above of polishing, sonicating and running voltammograms is continued until no change occurs in the capacitive current. An unchanging flat capacitance is indicative of a clean electrode with low resistance whereas a sloped background current is characteristic of a high level of resistance flowing between the electrode and the electrolyte solution (Figure 10). If the resistive background does not improve with continued polishing, the only solution is to start the polishing procedure again starting with fine sand paper.

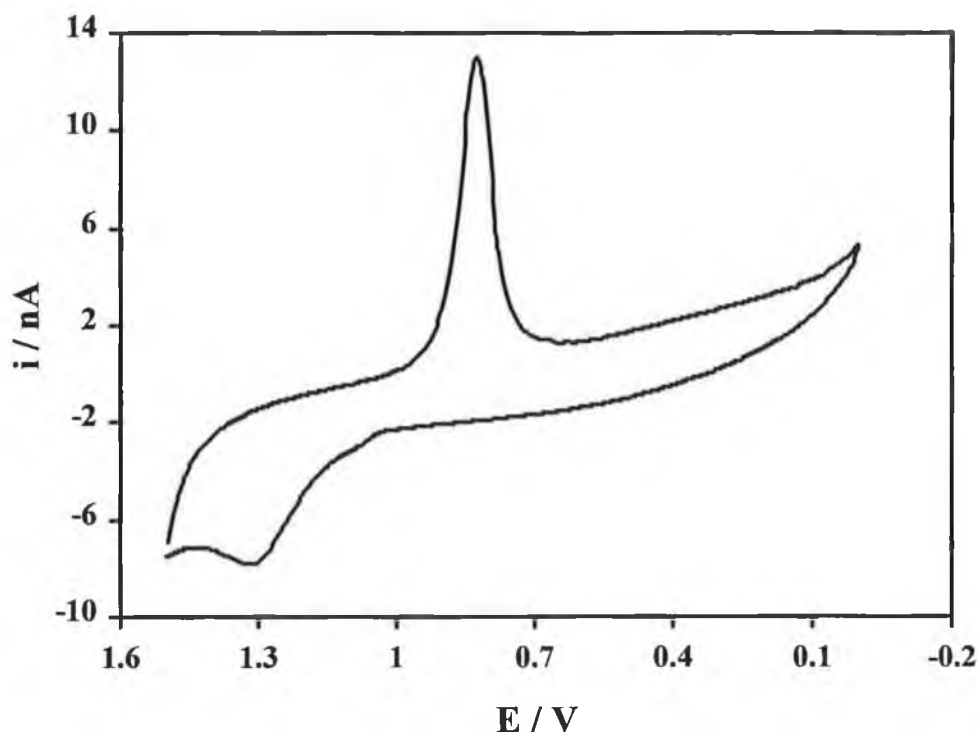


Figure 10 Cyclic voltammogram showing the electrochemical response of a 25 μm gold microelectrode immersed in 0.1 M H_2SO_4 , showing a resistive effect. The scan rate is 0.1 Vs^{-1} . The potential limits are 0.0 and 1.5 V. The initial potential is 0.0 V.

When no change occurs in the capacitive current using 12.5 μm alumina, the electrodes are successively polished with alumina of particle size 5 μm , 1.0 μm , 0.3 μm and finally 0.05 μm , rinsing and sonicating between each alumina particle size.

3.3.2 Electrochemical cleaning of microelectrodes

Figure 11 is representative of the CV recorded for the electrochemical response of a 25 μm platinum electrode in 1.0 M H_2SO_4 obtained after the polishing procedure. As can be seen, the CV shows no apparent signs of resistive effects. Another way to check that the electrochemical area of a gold microelectrode is decreasing is to immerse the microelectrode in an 0.1 M solution of H_2SO_4 and record the cyclic voltammogram. Figure 12 shows overlaid, a series of CV's representative of a 25 μm gold microelectrode at different stages in polishing, after cycling in 0.1 M H_2SO_4 . The peak at approximately 0.9 V is due to the reduction of a gold oxide monolayer. This method

of cleaning enables the electrochemical area of the electrode can be determined. Depending on the metal, the solution and potential window used to determine the electrochemical area differ.

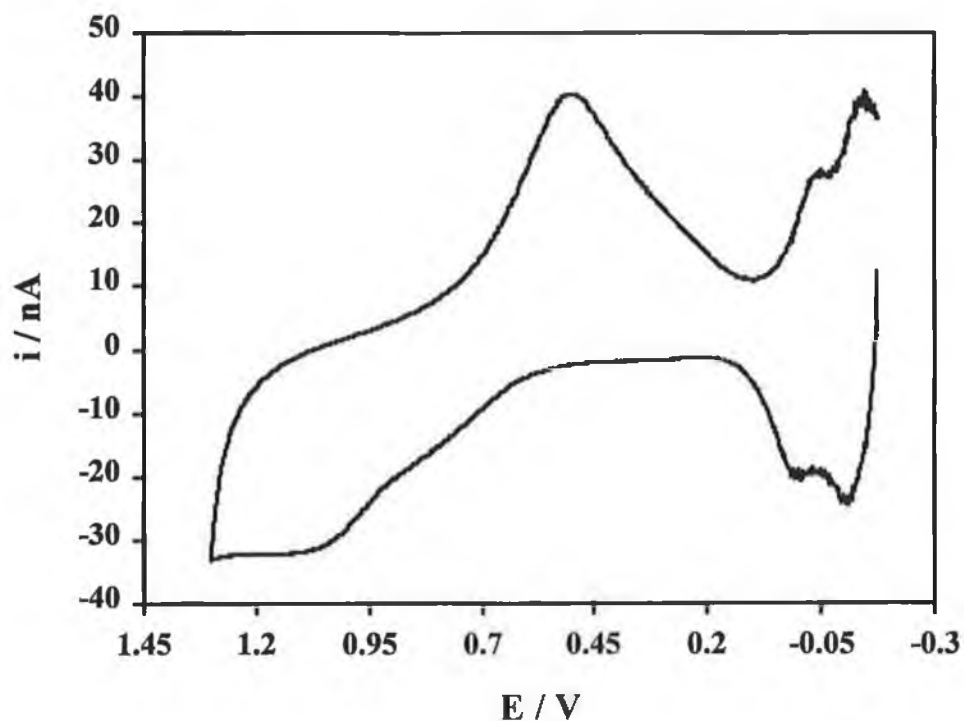


Figure 11 Cyclic voltammogram showing the electrochemical response of a 25 μm platinum microelectrode immersed in 1.0 M H_2SO_4 . The scan rate is 0.5 Vs^{-1} . The potential limits are $-0.175 + 1.3 \text{ V}$. The initial potential is -0.175 V .

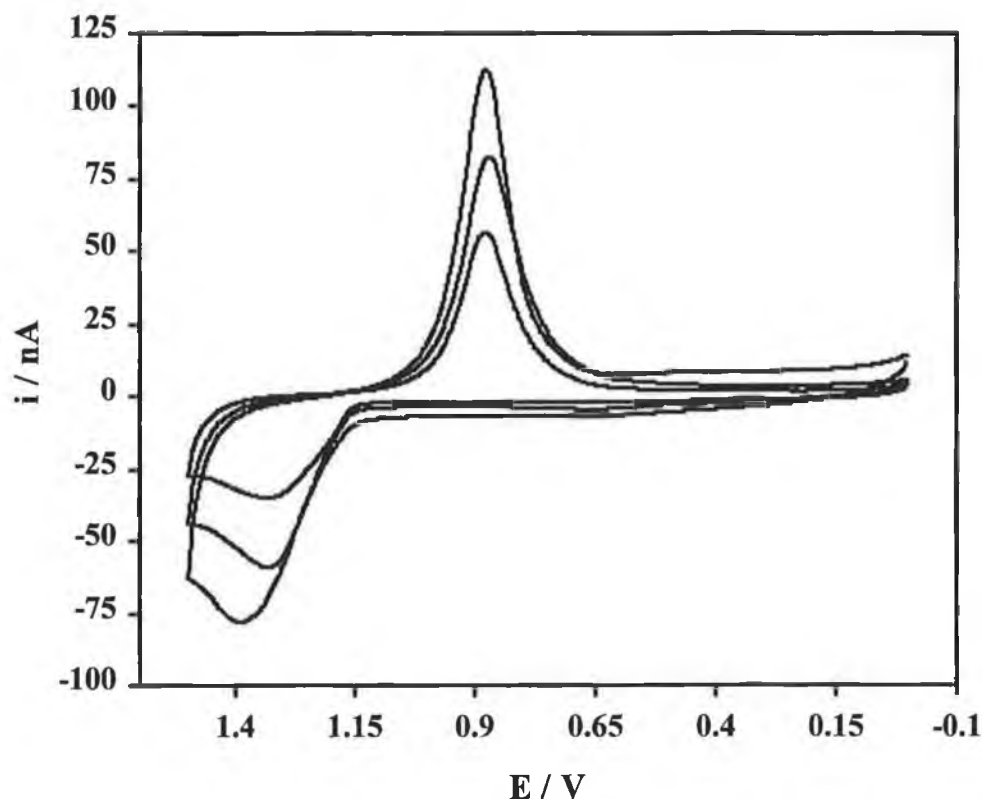


Figure 12 Electrochemical response for a 25 μm gold microelectrode immersed in 0.1 M H_2SO_4 at various stages during the polishing procedure. From top to bottom the CV's represent polished microelectrodes using 5, 1 and 0.3 μm alumina. The scan rate is 0.1 Vs^{-1} . The potential limits are 0.0 and +1.5 V. The initial potential in all cases is 0.0 V.

Once the microelectrode have been polished with 0.03 μm alumina and no change in the background current occurs, the electrodes are sonicated in Milli-Q water and the electrochemical area is determined for the metal. In the case of platinum electrodes, after the electrochemical areas have been measured, the electrodes are cycled in 0.1 M LiClO_4 to desorb the adsorbed hydrogen. The electrodes are then ready for modification with spontaneously adsorbed monolayers.

3.4 Surface Area Measurements

In the study of surface processes, whether at gas solid or electrode electrolyte interfaces, it is fundamentally important to accurately know the active surface area. The most useful approach for measuring surface area takes advantage of the inherent surface activity of the native electrode material. For the study of chemisorption phenomena at clean surfaces, this approach is most reliable since perfectly smooth crystalline surfaces are extremely difficult to achieve for microelectrodes and electrode reactions can occur even at surfaces where adsorption sites have been de-activated by chemical impurities.²⁵

The geometric surface area (A_g) of an electrode is the projection of the real surface on a plane parallel to the macroscopic visible phase boundary. For liquids such as mercury, the real and geometric areas are identical since the surface is atomically smooth. For solid electrodes the microscopic area needs to be experimentally determined since it is rare that atomically smooth solid electrodes exist.

In the case of gold electrodes, the approach used is the adsorption of oxygen from solution or the use of a redox active probe. For platinum electrodes, adsorption of oxygen from solution may be used as well as the adsorption of hydrogen from solution. For mercury the drop weight method was employed.

3.4.1 Electrochemical technique for the determination of surface area

3.4.1.1 Gold: oxygen adsorption from solution

For metals which show well-defined regions for oxide monolayer formation and reduction, the method of oxygen adsorption from solution allows the microscopic surface area to be determined. In the case of gold polycrystalline substrates, procedures for estimating the surface area range from the use of the Sand equation,²⁶ to the simple utilisation of the geometric area with or without allowance for an assumed surface roughness,^{27,28,29} as well as the chemisorption of iodine on the electrode surface.³⁰ The method of underpotential hydrogen deposition is not applicable since formation of a

single atomic layer of hydrogen on gold does not occur prior to the hydrogen evolution reaction.

The method of oxygen adsorption is based on the same principle as that of the hydrogen adsorption method. Prior to oxygen evolution, oxygen is assumed to be chemisorbed in a monoatomic layer on the surface of the electrode. This chemisorption also assumes a one-to-one attachment with surface metal atoms. The charge associated with the formation or reduction of the layer is:

$$Q_o = 2eN_A\Gamma_oA \quad \text{Eq. 1}$$

Where N_A is the Avogadro constant, Γ_o the surface concentration of atomic oxygen assumed to be equal to the surface density of metal atoms. The value for the reference charge Q_o^s is calculated from the value number of metal atoms per unit surface area, so that;

$$A = \frac{Q_o}{Q_o^s} \quad \text{Eq. 2}$$

In the polycrystalline gold a value of $390 \pm 10 \mu\text{C cm}^{-2}$ has been accepted^{31,32} for Q_o^s .

Although it is generally a less reliable method for the determination of surface area compared to hydrogen adsorption, oxide formation is non-destructive to the metal substrate and rapid. Cyclic voltammograms of gold microelectrodes were obtained using a potential window between 0.0 and 1.5 V, using a 0.1 M H_2SO_4 solution. Figure 13 shows the response after a gold microelectrode has been polished with 0.05 μm alumina and is ready for immersion into a deposition solution for adsorption to occur. The division of the electrochemical area by the geometric area determines the surface roughness of the electrode.

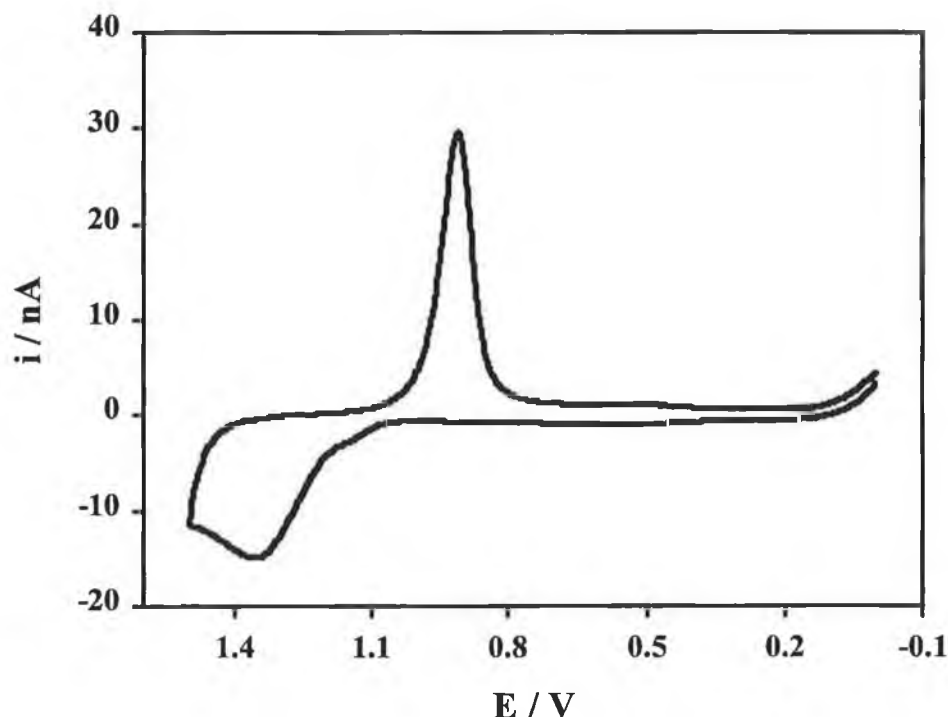


Figure 13 Cyclic voltammogram for a gold microelectrode polished with $0.05\ \mu\text{m}$ alumina in $0.1\ \text{M}\ \text{H}_2\text{SO}_4$. The scan rate is $0.1\ \text{Vs}^{-1}$. The potential limits are 0.0 and $1.5\ \text{V}$. The initial potential is $0.0\ \text{V}$.

It is important to note that the actual geometric area will depend on the preparation of the electrode, i.e., using the relationship $A_{\text{geom}} = \pi r^2$ is accurate only if a perfect disk shape electrode is exposed. While forming an elliptical electrode does not affect any experimental data as the electrochemical area is determined before individual experiments, it is important in determining a true surface roughness of a microelectrode when comparing theoretical and experimental data. In order to determine the true roughness of fabricated $25\ \mu\text{m}$ gold microelectrodes, a series of solution phase experiments were performed and geometric areas determined by the use of the Randles-Sevcik equation. The diffusion coefficient for a probe species, in this case, $[\text{Os}(\text{bpy})_3]^{2+}$ was initially determined from a series of solution phase cyclic voltammograms at various scan rates (0.02 to $0.5\ \text{V s}^{-1}$), with $0.1\ \text{M}\ \text{LiClO}_4$ in DMF as electrolyte.

Figure 14 shows a typical cyclic voltammogram obtained at low sweep rates. This data was used in conjunction with the Randles-Sevcik equation;

$$i_p = 2.69 \times 10^5 D^{1/2} C V^{1/2} A n^{3/2} \quad \text{Eq. 3}$$

where i_p is peak current, D is the diffusion coefficient, V is the scan rate, A is the geometric area of electrode and C is the concentration of the probe species to determine the diffusion coefficient of the electroactive probe.

The averaged diffusion coefficient was determined to be $1.1 \pm 2 \times 10^{-5} \text{ cm}^2 \text{ s}^{-1}$ for the probe species $[\text{Os}(\text{bpy})_3]^{2+}$. The average result was taken from the results of using three individual macroelectrodes.

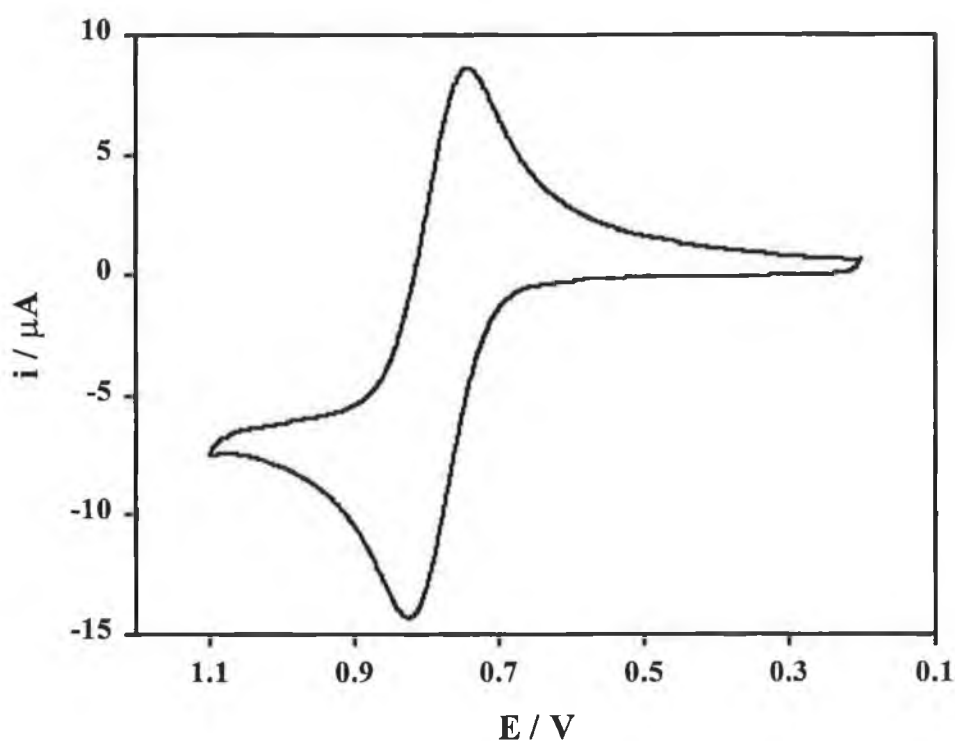


Figure 14 Cyclic voltammogram obtained from a solution of $[\text{Os}(\text{bpy})_3]^{2+}$, 0.5 mM in DMF with 0.1 M LiClO_4 as supporting electrolyte, using a macro gold electrode. The scan rate is 0.02 V s^{-1} . The initial potential is 0.2 V.

Subsequently, as illustrated in Figure 15, steady state cyclic voltammograms were obtained for 25 μm gold microelectrodes. The curves obtained are sigmoidal shaped and the limiting current is proportional to the concentration of the redox-active couple and the effective radius of the electrode.

$$i_d = 4nFrcD \quad \text{Eq. 4}$$

where n is the number of electrons transferred, F is the Faraday constant, r is the radius of the electrode and D is the diffusion coefficient of the probe species. Using the diffusion coefficient experimentally obtained and Eq. 4, the radius for the “25 μm ” microelectrodes were obtained. The results are given in Table 1.

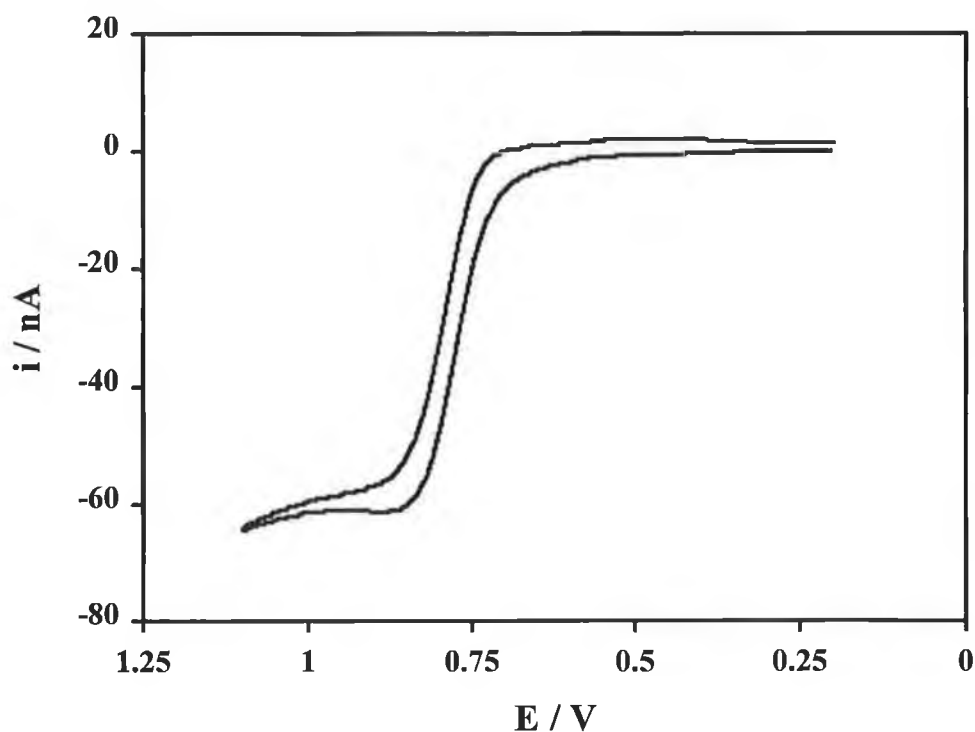


Figure 15 Steady state cyclic voltammogram obtained from a solution of $\text{Os}(\text{bpy})_3$, 0.5 mM in DMF with 0.1 M LiClO_4 as supporting electrolyte, using a 25 μm gold electrode. The scan rate is 0.02 Vs^{-1} . The initial potential is 0.2 V.

Electrode	i_{pa} (A / cm ²)	r (cm)	A (cm ²)	Roughness
1	6.73×10^{-8}	3.0×10^{-3}	28.2×10^{-6}	1.44
2	6.44×10^{-8}	2.9×10^{-3}	25.9×10^{-6}	1.32
3	6.18×10^{-8}	2.8×10^{-3}	24.6×10^{-6}	1.25
4	6.33×10^{-8}	2.8×10^{-3}	24.6×10^{-6}	1.25
5	6.21×10^{-8}	2.8×10^{-3}	24.6×10^{-6}	1.25

Table 1 Experimental electrochemical areas and surface roughness values for 5 x 25 μ m gold microelectrodes.

From the above results it may be seen that the actual radius obtained for the microelectrodes was higher than the quoted radius of the microwire. This difference is possibly due to taking an elliptical slice through the microwire during the polishing procedure, or variations in the radius of the microwires themselves. The differences in surface roughness (1.29 ± 0.15) most likely arises because of the manual polishing procedure employed. This experiment was performed to ensure that all actual surface roughness values lay below 2.

3.4.1.2 Platinum: Hydrogen adsorption from solution

Figure 11 shows the current-potential curve for a platinum electrode in an aqueous solution shows peaks for the formation and oxidation of both adsorbed hydrogen and adsorbed oxygen). The experimental technique used to probe the adsorption of hydrogen may be by CV or current step chronoamperometry.^{33,34} The method is also used for Rh and Ir^{7,35} and Ni.³⁶ However, the condition of reaching full monolayer coverage of hydrogen only takes place with Pt and not Rh and Ir.

The area under the peaks for adsorbed hydrogen (Q_H) and oxygen is typically assumed to represent monolayer coverage. For polycrystalline surfaces, the change associated with a one-to-one H-M correspond per unit surface areas (Q_f^s), is calculated on the basis of the distribution of metal atoms on the surface and is taken as an average value, between the main low-index faces. The true surface area, A, is derived from;

$$A = \frac{Q_f}{Q_f^s} \quad \text{Eq. 5}$$

For polycrystalline platinum the accepted value is $210 \mu\text{C cm}^{-2}$ for Q_f^s . This reference charge is based on the density of atoms on such a surface³⁷ in $1.31 \times 10^{15} \text{ cm}^{-2}$. The accepted value for polycrystalline platinum using the oxygen adsorption method is $420 \mu\text{C cm}^{-2}$.

There are limitations to the hydrogen adsorption method on platinum, such as the correction for double layer charging is arbitrary and the identification of the end-point for the metal adsorption of hydrogen is uncertain. However, this method does allow an *in-situ* estimate of the real surface area with reproducibility within $\pm 10\%$.³⁸ These values of reproducibility depend on the cleanliness of the electrode surface, solutions and glassware used.

A typical example of a CV from a $25 \mu\text{m}$ platinum microelectrode is found in Figure 11, showing peaks attributed to oxygen adsorption and hydrogen adsorption and the CV in Figure 16 shows the onset of hydrogen evolution.

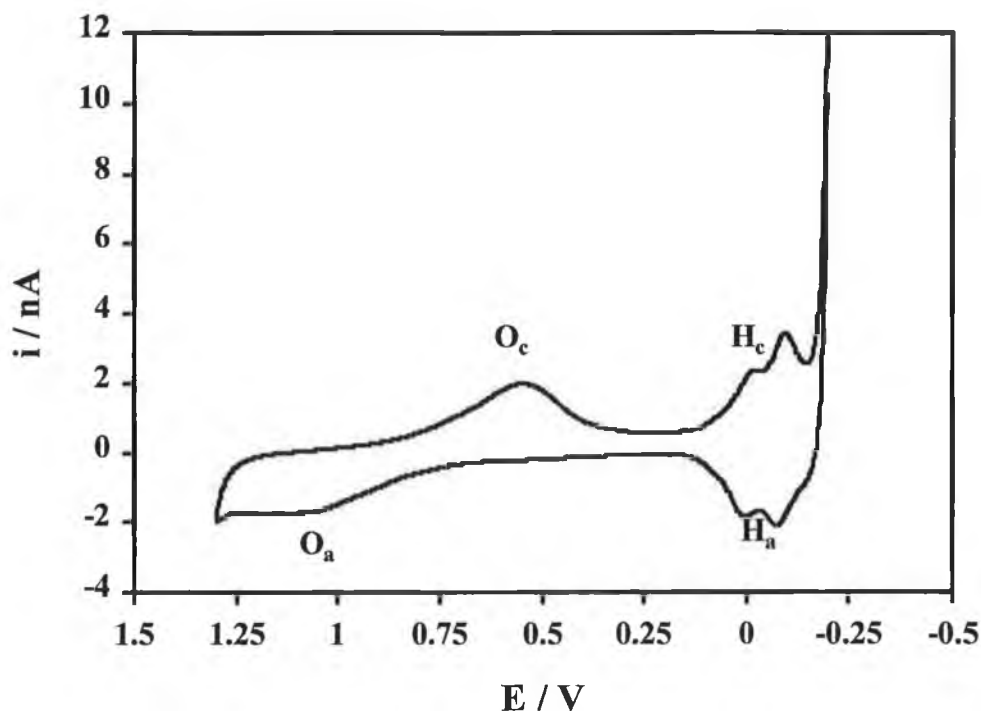


Figure 16 The electrochemical response of a polished 25 μm electrode immersed in 1.0 M H_2SO_4 showing the onset of mass H_2 evolution at approximately -0.22 V. The scan rate is 0.5 Vs^{-1} . The potential limits are -0.2 and $+1.3$ V. The initial potential is -0.2 V. Peaks H_c show formation of adsorbed hydrogen; H_a , oxidation of adsorbed hydrogen; O_a , formation of adsorbed hydrogen or platinum oxide layer; O_c , reduction of oxide layer.

3.4.1.3 Mercury: Drop Weight Method

The drop weight for surface area determination is used for liquid metal electrodes such as mercury, gallium and gallium liquid alloys.^{39,40} Although the method allows for the electrodes to be static, the procedure used here is that of a falling drop. 100 drops of mercury is collected in a cell containing methanol. The solvent is used as it allows for the drops to fall consistently, as without any solvent present in the cell the drop size and time is erratic. Once the solvent evaporates the weight of the mercury is determined. From a knowledge of the total number of drops and the density of Hg, the volume, radius and area of each drop was determined.

The measurement described above was performed five times and the area of the electrode is given as the average of the five experiments. The results are outlined below;

Sample	Weight (g)
1	0.1804
2	0.2001
3	0.2057
4	0.2028
5	0.1974

Table 2 Results from 5 consecutive experiments collecting 100 drops of mercury from a hanging mercury drop electrode.

Average 100 drops 0.1973 g Density of Hg 13.546 g / cm³

Average 1 drop 1.973 x 10⁻³ g Volume $\frac{4}{3}\pi r^3$

Volume of 1 drop 1.456 x 10⁻⁴ cm³ Area $4\pi r^2$

$$\text{Area} = 0.0134 \pm 0.0005 \text{ cm}^2$$

There are some limitations with this method, the main one being the fact that part of the drop is actually attached to the capillary. Therefore, the area calculated is actually greater than the area of mercury, which is extruding from the capillary. The order of magnitude of this excluded area is approximately 1% of the drop surface area.

3.5 Resistance and capacitance effects on gold microelectrodes

To understand the advantages that occur with very small electrodes, it is necessary to consider the flow of current through an electrochemical cell. For simplicity, consider a two-electrode system that contains a large, low-impedance reference electrode. The cell contains a solution including an inert, dissociated salt. The solution has a finite resistance (R), characterised by the specific resistivity (ρ). The working electrode, made from an inert material, has an associated capacitance (C). The apparent capacitance⁴¹ arises from the structure of ions in the double layer and is of the order of $20 \mu\text{F cm}^{-2}$.

Whenever the potential of the electrode is changed, a current must flow as electrons flow into or away from the electrode surface. The product of this charging current and the uncompensated resistance is known as the RC time constant and is in effect the product of the resistance by the capacitance. The use of microelectrodes reduce the RC time constant therefore making it possible for electrochemical measurements to be performed in a very short time regime, e.g., by rapid cyclic voltammetry^{42,43,44,45} or high-speed chronoamperometry.^{46,47,48} The solution resistance is not reduced with the use of microelectrodes but is actually increased. However, as the magnitude of the double layer capacitance is proportional to the electrode area or r^2 and the reduction is approximately six-fold over that of the increase in resistance, the overall RC is reduced.

The equation for determining the resistance (R) of a solution is given below for a disc shaped microelectrode;

$$R = \frac{1}{4\kappa r} \quad \text{Eq. 6}$$

Where κ is the conductivity of the solution, and r is the radius of the electrode. Investigations here have probed the potential dependence of the resistance and capacitance as the electrolyte concentration is systematically varied for a range of microelectrode radii.

These effects were characterised by performing cyclic voltammetry and chronoamperometry over a wide potential window. Figure 17 shows the chronoamperometric response of gold electrodes in electrolytic solutions ranging from 0.1 M to 1.0 M LiClO₄. As may be seen the decay in current varies and becomes sharper with increasing concentration. This transient current, following a potential step, decays exponentially in time according to Eq. 7;

$$i_c(t) = \Delta E / R \exp(-t / RC) \quad \text{Eq. 7}$$

Where ΔE is the magnitude of the potential step, R is the resistance, C , the capacitance. Semi-log plots of the decayed transients should be linear according to Eq. 7, with the slope providing the RC of the experiment and the intercept providing the value for resistance. The semi-log plots may be seen in Figure 18. For quantitative analysis the semi-log plots should be linear over at least two lifetimes. It is also noticeable that the slopes are decreasing with increasing electrolyte concentration, which represents a desirable decrease in RC with increasing electrolyte concentration.

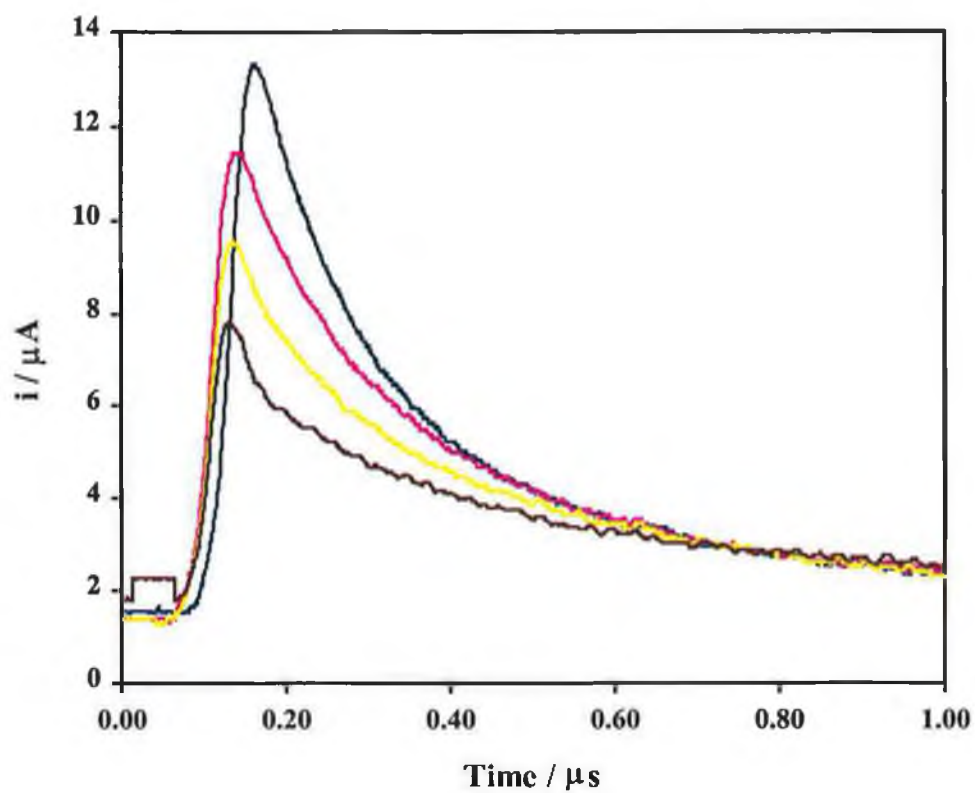


Figure 17 Dependence of the chronoamperometric response for a 12.5 μm gold microelectrode with increasing electrolyte concentrations. The concentration range from top to bottom is 1.0, 0.7, 0.5 and 0.3 M $LiClO_4$. The potential step is 0.05 V and is between 0.0 and 0.05 V.

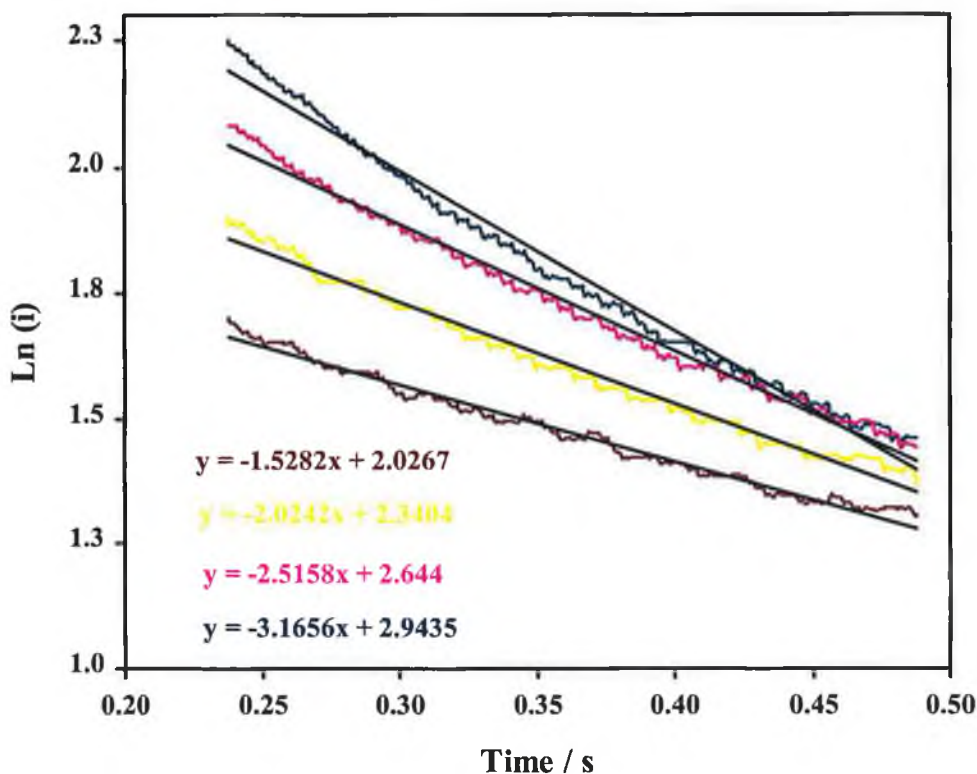


Figure 18 Semi-log plots of the transients in Figure 14. From top to bottom the concentrations are 1.0, 0.7, 0.5 and 0.3 M LiClO_4 .

Three sets of data were collected with the first set, with a potential step of 0.05 V (0.00 to +0.05 V), the second set at 0.35 and 0.40 V, and the third set at +0.75 to +0.80 V. The supporting electrolyte employed was LiClO_4 . The concentrations were between 0.1 to 1.0 M. Therefore, experimental data have been obtained negative of the potential of zero charge, PZC, positive of the PZC and at the edge of the potential window for gold, far from the PZC. Four different sized electrodes were used to see if the effect for resistance and RC was similar. The sizes chosen were 62.5, 25, 12.5 and 5 μm radius. The roughness of each electrode did vary from each other but all were under a roughness value of 2.

Figure 19 through Figure 21 shows the RC response obtained for each of the chosen electrodes, at each potential and at a concentration range of 0.1 to 1.0 M LiClO_4 . The most striking feature of the graphs is the significant *decrease* in RC with *increasing*

electrolyte concentration at all potentials studied and the difference in RC between theoretical and experimental results. In the case of the highest electrode radius studied, 62.5 μm , the RC decreases approximately 4 fold from 13 down to 3 μs . Theoretically, the decrease for a 62.5 μm electrode should be from 11 to 1 μs assuming a capacitance of $20 \times 10^{-6} \text{ F cm}^{-2}$. Table 3 outlines the theoretical and experimental RC values for all electrodes at all concentrations and potentials.

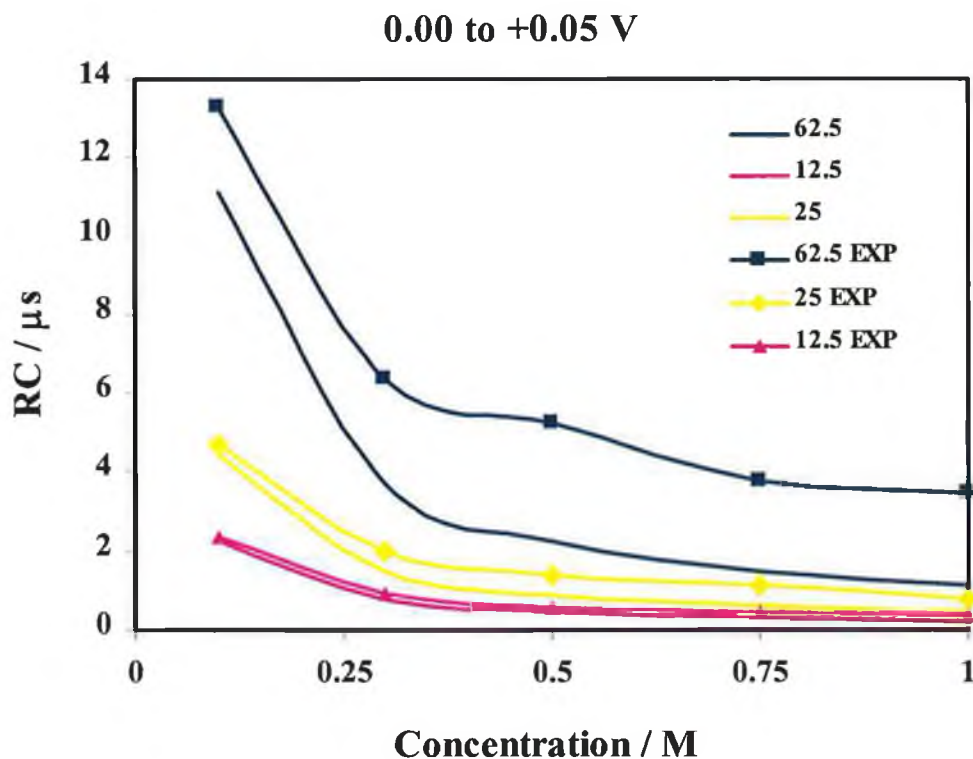


Figure 19 Dependence of RC time constant at various microelectrode dimensions with increasing concentrations. The heavy lines in the plot are the theoretical response expected for that particular sized microelectrode. The experimental results are in points. The concentration range used is 0.1, 0.3, 0.5, 0.75 and 1.0 M LiClO_4 . The potential step at which the experiment was carried out is 0.00 to 0.05 V.

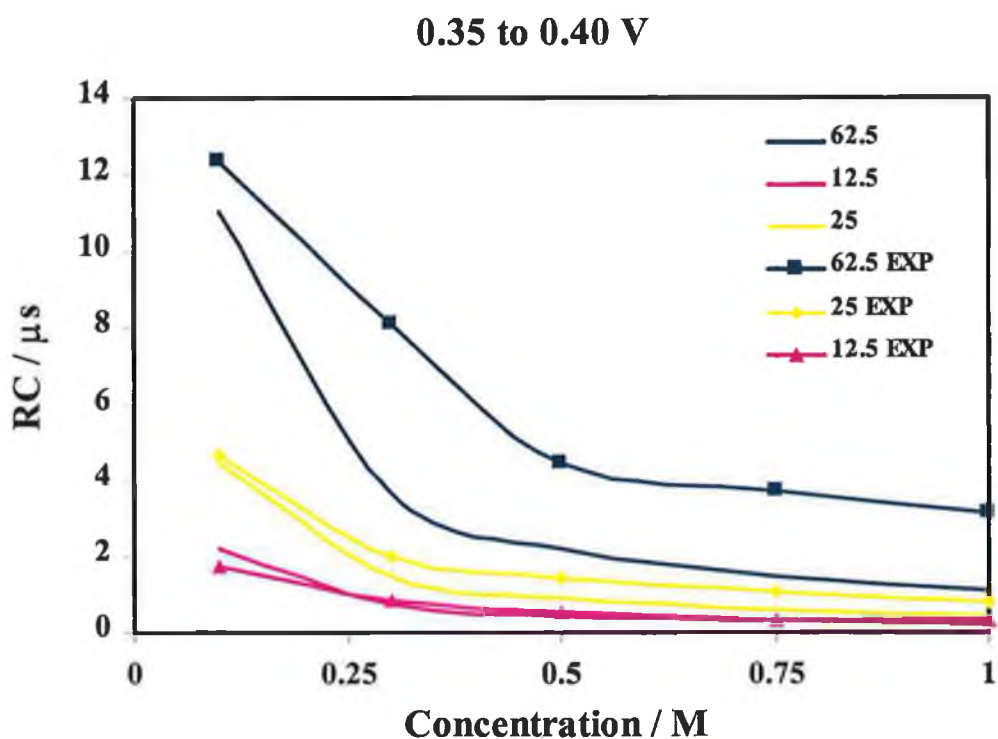


Figure 20 Dependence of RC time constant at various microelectrode dimensions with increasing concentrations. The heavy lines in the plot are the theoretical response expected for that particular sized microelectrode. The experimental results are denoted as points. The concentration range used is 0.1, 0.3, 0.5, 0.75 and 1.0 M LiClO₄. The potential step at which the experiment was carried out is 0.35 to 0.40 V.

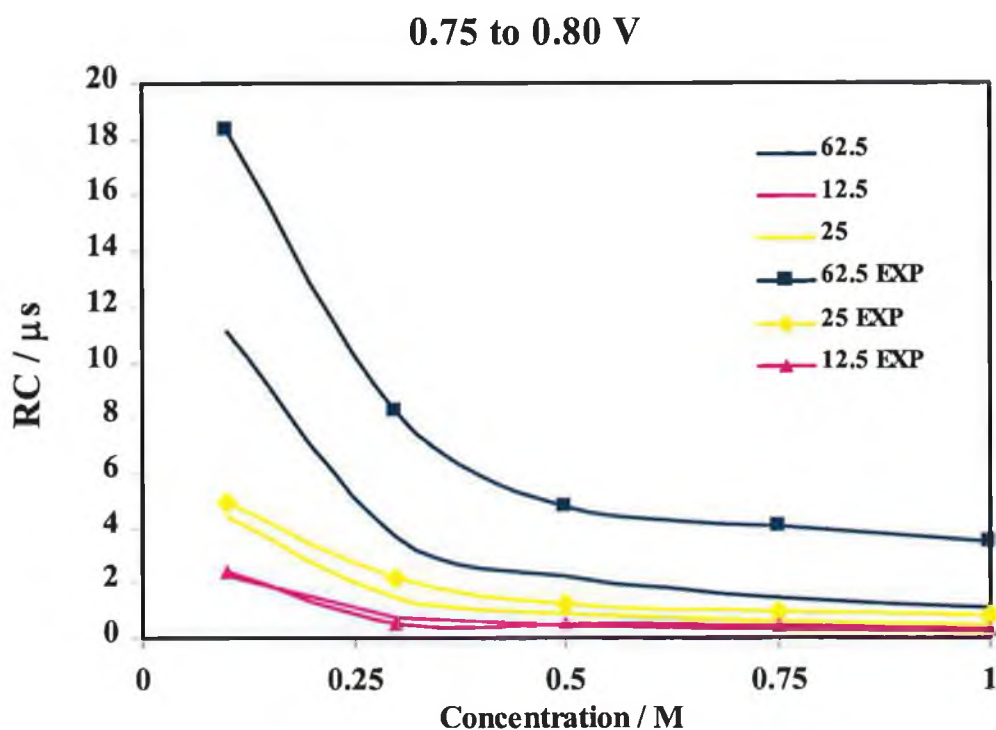


Figure 21 Dependence of RC time constant at various microelectrode dimensions with increasing electrolyte concentration. The heavy lines in the plot are the theoretical response expected for that particular sized microelectrode. The experimental results are denoted as points and lines. The concentration range used is 0.1, 0.3, 0.5, 0.75 and 1.0 M LiClO₄. The potential step at which the experiment was carried out is 0.75 to 0.80 V.

Concentration	Theoretical	0.0 – 0.05 V	0.35 – 0.40 V	0.75 – 0.80 V
M	RC / μ s	RC / μ s	RC / μ s	RC / μ s
62.5 μm Radius Electrode				
0.1	11.31	13.30	12.38	18.38
0.3	3.77	6.38	8.15	8.22
0.5	2.26	5.25	4.48	4.74
0.75	1.51	3.77	3.73	4.04
1.0	1.13	3.45	3.13	3.55
25 μm Radius Electrode				
0.1	4.53	4.69	4.64	4.88
0.3	1.51	2.00	2.01	2.14
0.5	0.96	1.40	1.39	1.19
0.75	0.60	1.12	1.06	0.92
1.0	0.45	0.78	0.78	0.80
12.5 μm Radius Electrode				
0.1	2.26	2.36	2.33	2.36
0.3	0.75	0.93	0.84	0.49
0.5	0.45	0.55	0.51	0.48
0.75	0.30	0.43	0.31	0.40
1.0	0.23	0.34	0.28	0.26

Table 3 Theoretical and experimental RC values for a series of electrode dimensions over a concentration range 0.1 to 1.0 M LiClO₄. Potential step experiments were performed at 3 points along the potential window.

The trend that is occurring between all electrode sizes is consistent with their corresponding theoretical RC value, i.e. a sharp decrease in RC with increasing concentration. The largest decrease in RC is between 0.1 and 0.3 M and is approximately 70% of the total decrease in RC, which for the case of 62.5 μ m is 13.3 μ s down to 6.4 μ s. This is due to the differences in conductivity at the lower concentrations over those at higher concentrations. From 0.3 to 1.0 M of the electrolyte, the decrease in RC is significantly reduced and from 6.4 μ s down to 3.45 μ s, approximately 30% of the total reduction in RC.

The experimental resistance values of these microelectrodes have also been compared to theoretical values against increasing electrolyte concentration. Figure 22 shows the response obtained for a series of microelectrodes graphed with their corresponding theoretical results. The concentration range is from 0.1 M to 1.0 M LiClO_4 . The roughness values for each microelectrode was also incorporated into the corresponding theoretical resistance values. This was performed, as the theoretical resistance values should contain the electrochemical area and not the geometric area in the calculation in order to reflect true resistances. The true and experimental results are closely related with the exception of the lowest concentration used (0.1 M), where conductivity in solution is at its lowest for these experiments.

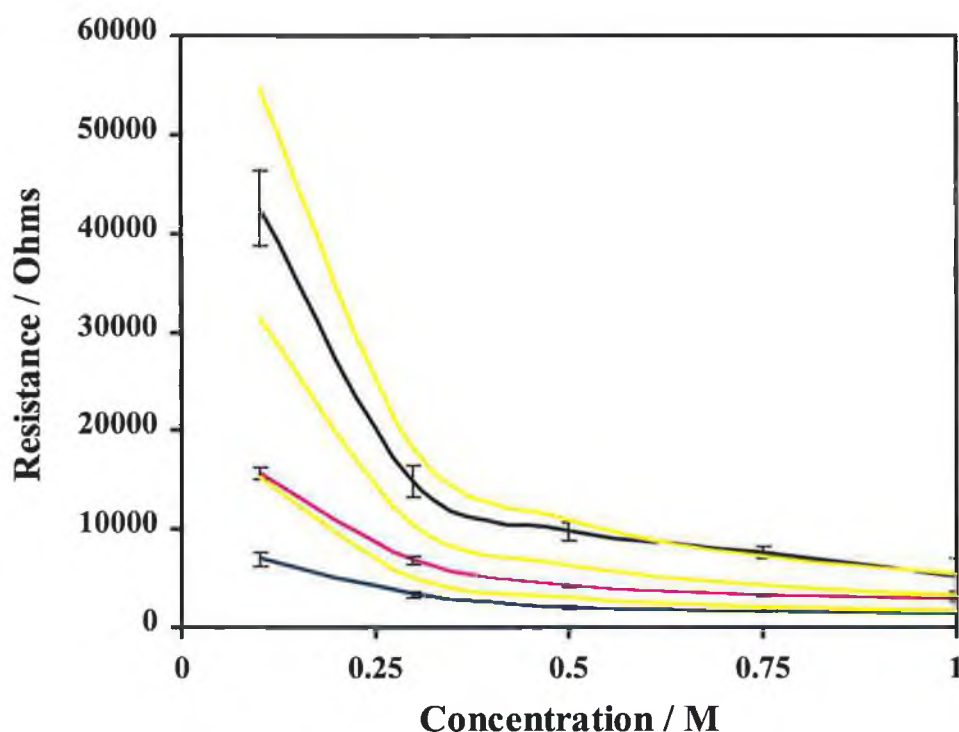


Figure 22 Comparison between the theoretical (yellow lines) and experimental responses for a variety of microelectrode dimensions with increasing electrolyte concentration.

3.6 Conclusion

The data presented in this chapter shows that microelectrodes with a wide variety of dimensions have been fabricated with a high success rate (approx. 85%). The electrochemical response of these electrodes responds rapidly to changes in the applied potential, shown by the RC data with values as low as 800 ns being observed for a 12.5 μm gold microelectrode in 1.0 M LiClO_4 . This rapid response enables these microelectrodes to be used in experiments where electrode kinetics are being investigated, allowing the separation of Faradaic and non-Faradaic components in current-time experiments. The fact that electrodes may be fabricated which have close to ideal theoretical response is of great significance when investigating electrode kinetics. The use of these microelectrodes also reduces iR drop, enabling cyclic voltammograms to be performed at scan rates as high as $1 \times 10^6 \text{ Vs}^{-1}$ ⁴⁹ and in highly resistive media.⁵⁰

3.7 References

1. Forster, R. J., *Chem. Soc. Rev.*, **1994**, 289
2. Sabatani, E., Rubinstein, I.; *J. Phys. Chem.*, **1987**, 91, 6663
3. Wehmeyer, K., Wightman, R. M.; *J. Electroanal. Chem.*, **1985**, 196, 421
4. Andrieux, C.P., Hapiot, P., Saveant, J. M.; *J. Electroanal. Chem.*, **1988**, 243, 321
5. Baldo, M. A., Daniele, S., Corbetta, M., Mazzocchin, G. A.; *Electroanalysis*, **1995**, 7, 980
6. Baranski, A. S., Quon, H.; *Anal. Chem.*, **1986**, 58, 407
7. Golas, J., Galus, Z., Osteryoung, J.; *Anal. Chem.* **1987**, 59, 389
8. Howell, J. O., Wightman, R. M.; *Anal. Chem.* **1984**, 56, 524.
9. Wipf, D. O., Michael, A. C., Wightman, R. M.; *J. Electroanal. Chem.*, **1989**, 269, 15
10. Pendley, B. D., Abruna, H. D.; *Anal. Chem.* **1990**, 62, 782
11. Cheng, I. F., Schimpf, J. M., Martin, C. R.; *J. Electroanal. Chem.*, **1990**, 284, 499
12. Malem, F., Mandler, D.; *J. Electrochem. Soc.*, **1992**, 139, L65
13. Tschuncky, P., Heinze, J.; *Anal. Chem.*, **1995**, 67, 4020
14. Cardwell, T. J., Mocak, J., Santos, J. H., Bond, A. M.; *Analyst*, **1996**, 121, 357
15. Golas, J., Osteryoung, J.; *Anal. Chim. Acta*, **1986**, 181, 211
16. Schulze, G. Frenzel, W.; *Anal. Chim. Acta*. **1984**, 159, 95
17. Ciszowska, M., Stojek, Z.; *J. Electroanal. Chem. Interfacial Electrochem.*, **1985**, 191, 101
18. De Vitre, R. R., Tercier, M. L., Tsacoupoulos, M., Buffle, J.; *Anal. Chim. Acta.*, **1991**, 249, 419
19. O'Shea, T. J., Lunte, S. M.; *Anal. Chem.*, **1993**, 65, 247
20. Ciszowska, M., Donten, M., Stojek, Z.; *Anal. Chem.*, **1994**, 66, 4112
21. Faulkner, L. R., Walsh, M. R., Xu, C.; *Contemporary Electroanalytical Chemistry*, Ed. Ivaska, A., Lewenstam, A., Sara, R., **1990**, 5
22. Wipf, D. O., Michael, A. C., Wightman, R. M.; *Electroanalytical Chemistry*, Ed. Bard, A. J., **1989**, 15, 267

23. Donten, M., Kublik, Z.; *Anal. Chem. (Warsaw)*, **1993**, 38, 789
24. Guminski, C. Galus, Z.; In *Solubility Data Series*; Ed. Kertes, A. S., Pergamon Press: Oxford UK, **1986**, 25
25. Trasatti, S., Petrii, O. A.; *J. Electroanal. Chem.*, **1992**, 327, 354
26. Roberts, J. L., Sawyer, D. T.; *J. Electroanal. Chem.*, **1964**, 7, 315
27. Li, J., Pons, S., Smith, J. J.; *Langmuir*, **1986**, 2, 297
28. Facci, J. S., Falcigno, P. A., Gold, J. M.; *Langmuir*, **1986**, 2, 732
29. Finklea, H. O., Robinson, L. R., Blachburn, A., Richter, B., Allara, D., Bright, T.; *Langmuir*, **1986**, 2, 239
30. Rodriguez, J. F., Mebrahtu, T., Soriaga, M. P.; *J. Electroanal. Chem.*, **1987**, 233, 283
31. Michri, A. A., Pshchenichnikov, A. G., Burshtein, R. Kh.; *Elektrokhimiya*, **1972**, 8, 364
32. Burshtein, R. Kh.; *Elektrokhimiya*, **1967**, 3, 349
33. Will, F. G., Knorr, C. A.; *Elektrochem*, **1960**, 64, 258
34. Frumkin, A. N., *Advances in Electrochemistry and Electrochemical Engineering*, Vol 3, Wiley-Interscience, New York, **1963**
35. Gilman, S.; *J. Phys. Chem.*, **1967**, 71, 4339
36. Pshchenichnikov, A. G., *Mat. Chem. Phys.*, **1989**, 22, 121
37. Biegler, T., Rand, D. A. J., Woods, R.; *J. Electroanal. Chem.*, **1971**, 29, 269
38. Barna, G. G., Frank, S. N., Teherani, T. H.; *J. Electrochem. Soc.*, **1982**, 129, 746
39. Grahame, D. C.; *J. Am. Chem. Soc.*, **1957**, 79, 701
40. Broadhead, J., Hills, G. J., Kinniburgh, D. R.; *J. Appl. Electrochem.*, **1971**, 1, 147
41. Bard, A. J., Faulkner, L. R.; *Electrochemical methods Fundamentals and Applications*; Wiley: New York, **1980**.
42. Winkler, K.; *J. Electroanal. Chem.*, **1995**, 388, 151
43. Wipf, D. O., Wightman, R. M.; *Anal. Chem.*, **1988**, 60, 2460
44. Chen, X., Zhuang, J., He, P.; *J. Electroanal. Chem.*, **1989**, 271, 257
45. Wipf, D. O., Kristensen, E. W., Deakin, M. R., Wightman, R. M.; *Anal. Chem.*, **1988**, 60, 306

46. Forster, R. J. Faulkner, L. R.; *J. Am. Chem. Soc.*, **1994**, 116, 5444
47. Forster, R. J. Faulkner, L. R.; *J. Am. Chem. Soc.*, **1994**, 116, 5453
48. Forster, R. J.; *Analyst*, **1996**, 121, 733
49. Andrieux, C.P., Hapiot, P., Saveant, J. M.; *J. Electroanal. Chem.*, **1988**, 248, 447
50. Norton. J. D., Benson. W. E., White. H. S., Pendley. B. D., Abruna. H. D., *Anal. Chem.*, **1991**, 63, 1909

CHAPTER 4

Ion-pairing, Capacitance and Temperature

Effects on N₅-Cl Osmium Monolayers

4 Introduction

Self-assembling monolayers have been the focus of much research effort over the past two decades.^{1, 2, 3, 4, 5, 6, 7, 8, 9, 10, 11} The ability to deliberately manipulate and control the chemical and electronic properties of a surface has wide ranging applications in fields as diverse as electronics¹² and catalysis.¹³ The incorporation of a redox-active transition metal head group into a self-assembling molecule provides a complex available for direct electrochemical analysis using voltammetric techniques.

Spontaneous adsorption can produce well-ordered, molecularly and in some cases atomically smooth, transition metal complex arrays. These arrays, which have already been used in electrocatalysis and chemical sensors offer considerable promise as building blocks in the growing field of nanotechnology¹⁴ and molecular electronics.

Previous interest in self-assembling osmium containing polypyridyl complexes has ranged from the analysis of the factors responsible for their strong adsorption,¹⁵ adsorption and desorption processes,⁶ solvent effects on formal potentials,¹ to electron transfer.^{2, 3, 4} However, there have been no reports on the extent of lateral interactions occurring within single and two-component monolayers as a function of oxidation state. For the osmium polypyridyl complexes considered here, in their reduced form the Os^{2+} complexes have a net +1 charge and in the oxidised form Os^{3+} , a net +2 charge is present. Therefore, in the oxidised form a higher level of repulsive forces between the adsorbates might be expected than when the complex is present in the reduced form. The formal potential of a monolayer is sensitive to changes which occur in its local microenvironment. With this in mind, we have focused our research in areas where we feel we will gain the most important information about these spontaneously adsorbed monolayers. Thus our focus is on ion-pairing, effects from temperature and the effect of the monolayers overall state of change on lateral interactions. To achieve these objectives, we have probed the ideality of the voltammetric response, electrolyte and temperature effects on the formal potential as well as the interfacial capacitance.

In seeking to use molecules as “building blocks” for supramolecular assemblies, it is frequently assumed that the molecule’s electronic and photonic properties will be retained when it is immobilised within the assembly. However, because of their close proximity, molecules within dense monolayers may interact significantly causing their

desirable properties to be perturbed. To address this issue of lateral interactions, we have synthesised and formed monolayers by spontaneously adsorbing similar osmium polypyridyl complexes $[\text{Os}(\text{bpy})_2\text{L Cl}]$ where $\text{bpy} = 2,2'$ bipyridine and $\text{L} = 4,4'$ -dipyridyl, 1,2-bis(4-pyridyl)ethane, or 4,4'-trimethylenedipyridine onto gold microelectrodes. The structures and abbreviations of the ligands to be discussed in this study are given in Chart 1 of Chapter 1. These complexes are attractive to use because they adsorb unusually strongly onto gold and platinum electrodes,¹⁵ their excellent stability over long periods and at elevated temperatures as well as their unusually ideal electrochemical responses.

4.1 Experimental Equipment

4.1.1 Apparatus

Cyclic voltammetry was performed using a CH instruments Model 660 electrochemical workstation and a conventional three-electrode cell. Potentials were measured against a potassium chloride saturated silver/silver chloride (Ag/AgCl) reference electrode. The auxiliary electrode was a platinum wire. All solutions were degassed using nitrogen and a blanket of nitrogen was maintained over the solution during all experiments.

For temperature dependent experiments a Julabo F10-HC refrigerated circulating bath, thermostated to within ± 0.2 °C was used. A non-isothermal cell was used in which the reference electrode was isolated from the main compartment by a salt bridge and held at constant temperature. The salt bridge was saturated with KCl since it has a low resistance and remains soluble at the lowest temperatures used.

4.1.2 Materials

Microelectrodes were fabricated as described in Chapter 3, with surface roughness values of less than 2.

Spontaneously adsorbed monolayers of osmium polypyridyl complexes were formed by immersion of the electrode into a deposition solution at the required concentration. The most stable monolayers were found to form when left to adsorb in the deposition

solution for up to 12 hours. Typically, adsorption took place from 50:50 acetone : water solutions with the complex present in the micromolar range. No attempt was made to exclude oxygen from the deposition solutions. All electrodes were rinsed with the solvent in which they were to be placed for electrochemical measurements, to remove any unbound, electrochemically active species. For immobilised species, all measurements were performed in electrolytic solutions containing no dissolved redox active complex.

4.2 Discussion

4.2.1 Electrochemical properties of osmium compounds

Figure 1 shows a representative cyclic voltammogram for a mono-substituted osmium polypyridyl complex, $[\text{Os}(\text{bpy})_2\text{P3P Cl}]^+$, spontaneously adsorbed onto a gold macro electrode through the pendant nitrogen on the P3P ligand. The supporting electrolyte is aqueous 0.1 M LiClO_4 and no dissolved redox-active compound is present in solution. The voltammetric response shown is typical for all of the N_5 -Cl investigated and formal potentials varied only slightly between all three. Depending on the solvent and concentration of electrolyte used, the formal potentials were between approximately 0.25 to 0.30 V. In addition, the FWHM values were consistent with a one electron transfer taking place, i.e., $90.6 / n$ mV. Thus, the voltammetry obtained is consistent with that expected for an electroactive species immobilised onto an electrode surface^{16,17,18} and corresponds to metal-based osmium^{+2 / +3} process¹⁹.

It is known that adsorption N_5 -Cl osmium complexes occurs through the pendant nitrogen since previous studies have shown no adsorption for similar systems^{20, 25} such as $[\text{Os}(\text{bpy})_2 \text{py Cl}]$, where py is pyridine. Also, the difference between the formal potentials of the surface confined species and the solution phase complex in DMF was typically between 0.020 and 0.030 V. The similarity between these complexes indicate that the surface confined species is solvated to a high degree.

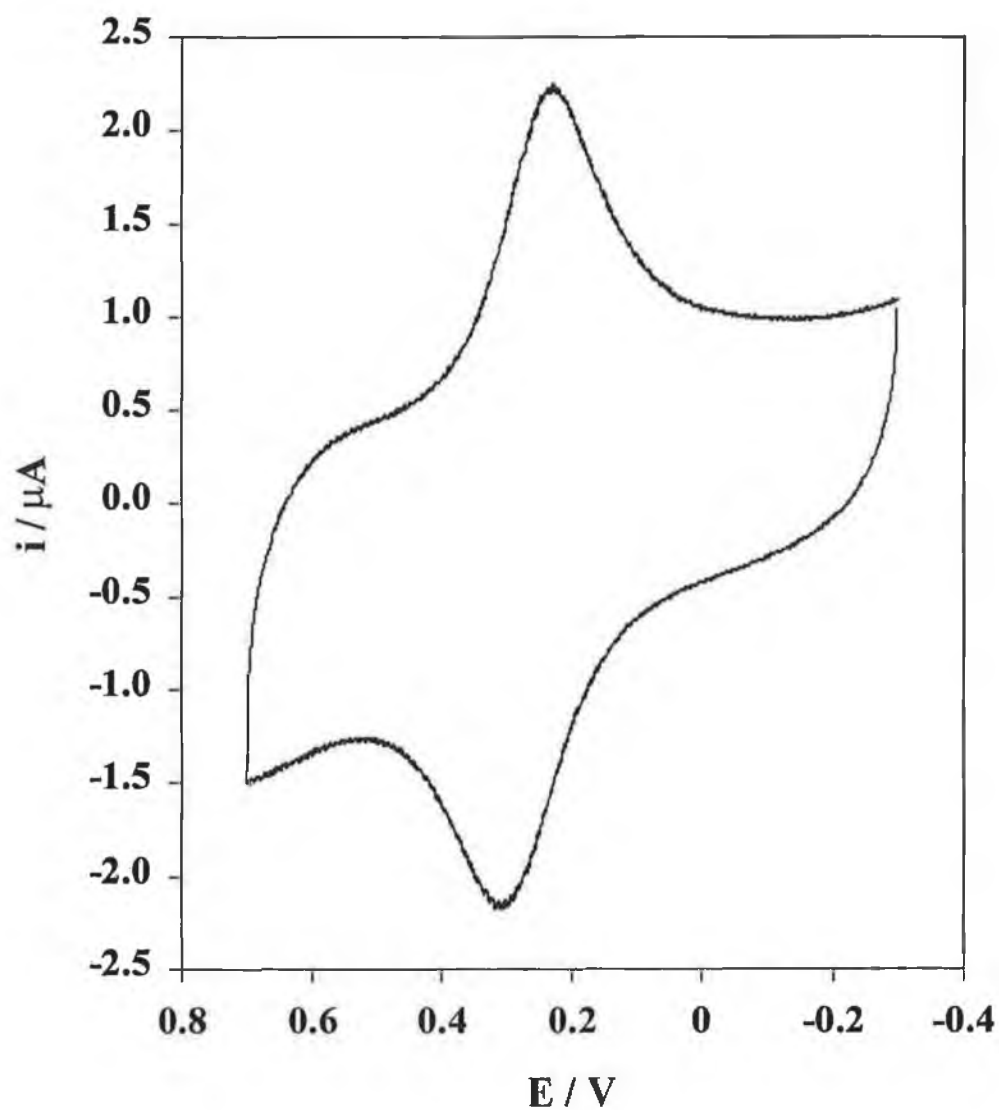


Figure 1 Cyclic voltammogram of a monolayer of $[\text{Os}(\text{bpy})_2\text{P3P Cl}]^+$. The scan rate is 0.5 Vs^{-1} and the electrolyte is 0.1 M LiClO_4 . Anodic peaks are down and cathodic peaks are up. A $25 \mu\text{m}$ gold electrode was employed. The surface coverage is $1.20 \times 10^{-10} \text{ mol cm}^{-2}$.

The Gaussian wave type shapes anticipated for a surface confined species were observed and are shown in Figure 2 and Figure 3 at varying scan rates. Figure 4 shows how the peak current depends on the voltammetric scan rate for the N_5 -Cl complex $[\text{Os}(\text{bpy})_2\text{P3P Cl}]^+$ in 0.1 M LiClO_4 . The peak current increases proportionally to the scan rate, ν , at least up to 50 Vs^{-1} . For example, at 10 Vs^{-1} , i_{pa} is $2.58 \times 10^{-8} \text{ A}$ and at 50 Vs^{-1} is $1.17 \times 10^{-7} \text{ A}$. Thus, to within experimental error, the peak current increases directly with scan rate. The linear response to scan rate is expected for modified electrodes, whereas for a freely diffusing species a $\nu^{1/2}$ dependence is expected. The linear response shown in Figure 4 indicates that the redox-active osmium complex is immobilised onto the electrode surface resulting in an electrochemically active immobilised film.

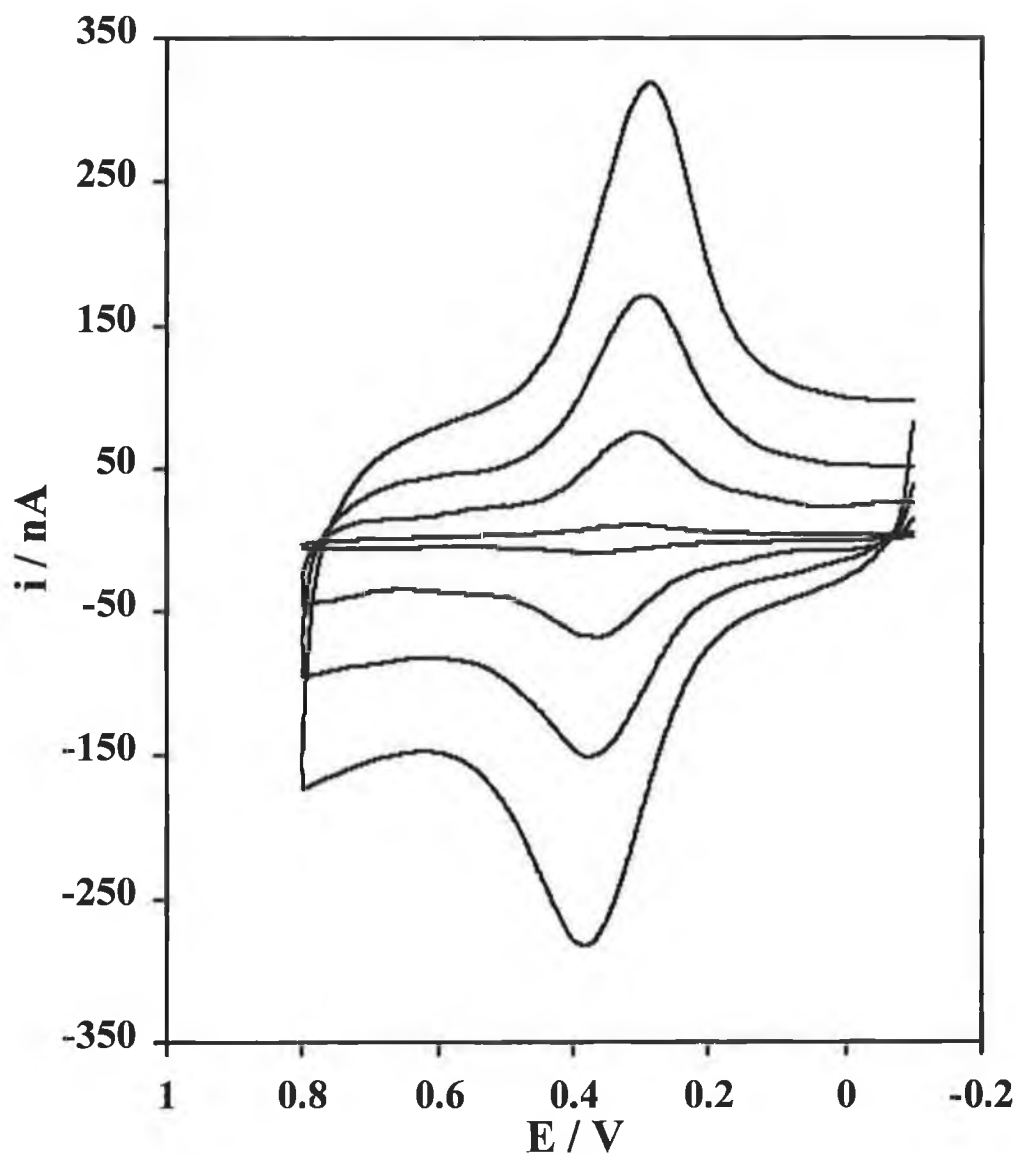


Figure 2 Overlaid cyclic voltammograms for a monolayer of $[Os(bpy)_2P3P Cl]^+$ in $0.1 M LiClO_4$. The scan rates are, from top to bottom, 50, 20, 10 and 1 Vs^{-1} . The radius of the gold microelectrode employed was $25 \mu m$. Each cycle was initiated at $-0.1 V$.

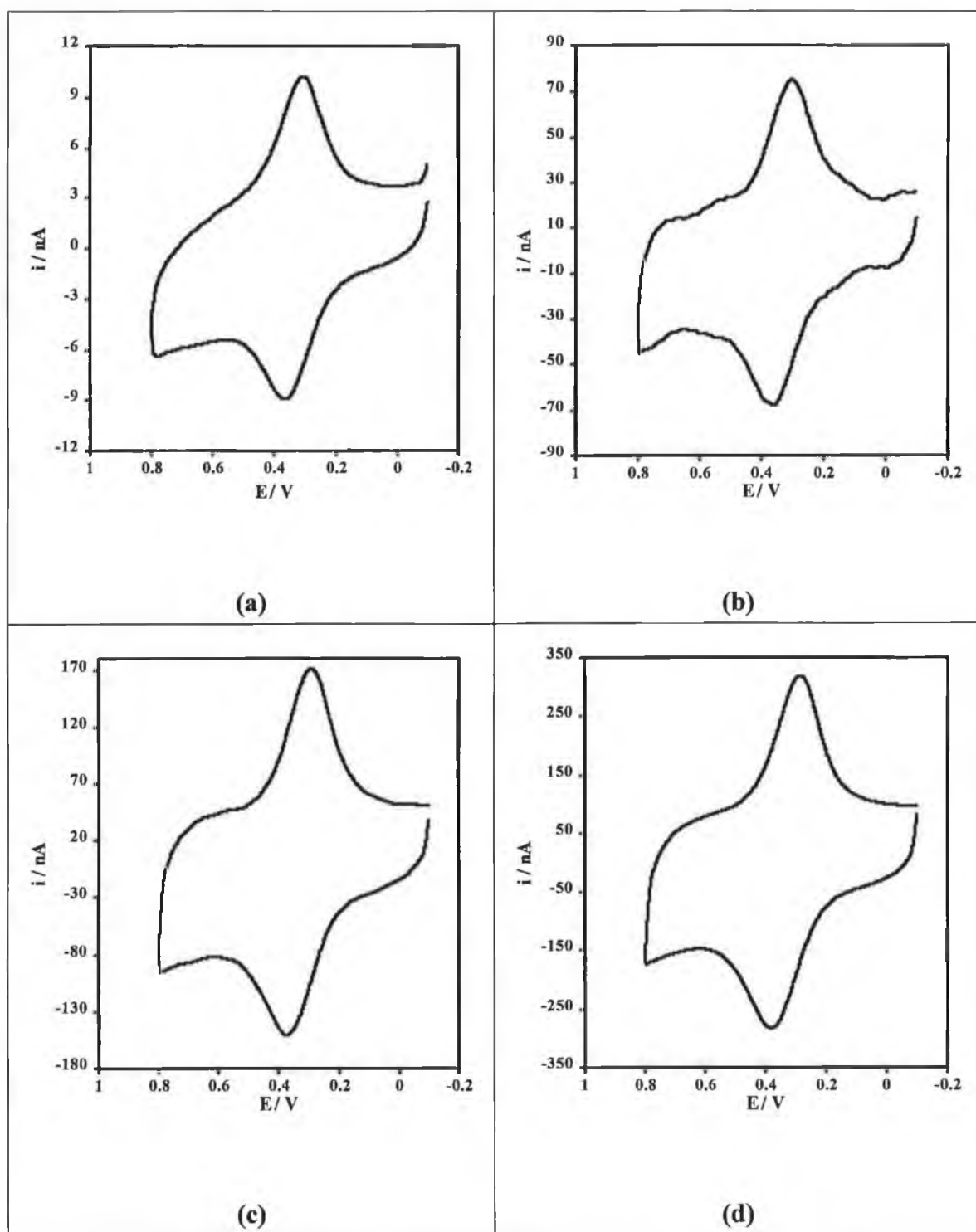


Figure 3 Cyclic voltammetric responses obtained for a 25 μm gold microelectrode for a monolayer of $[\text{Os}(\text{bpy})_2\text{P3P Cl}]^+$ in 0.1 M LiClO_4 . The scan rates are, (a), 1, (b), 10, (c), 25 and (d) 50 Vs^{-1} . The surface coverage is $1.2 \times 10^{-10} \text{ mol cm}^{-2}$.

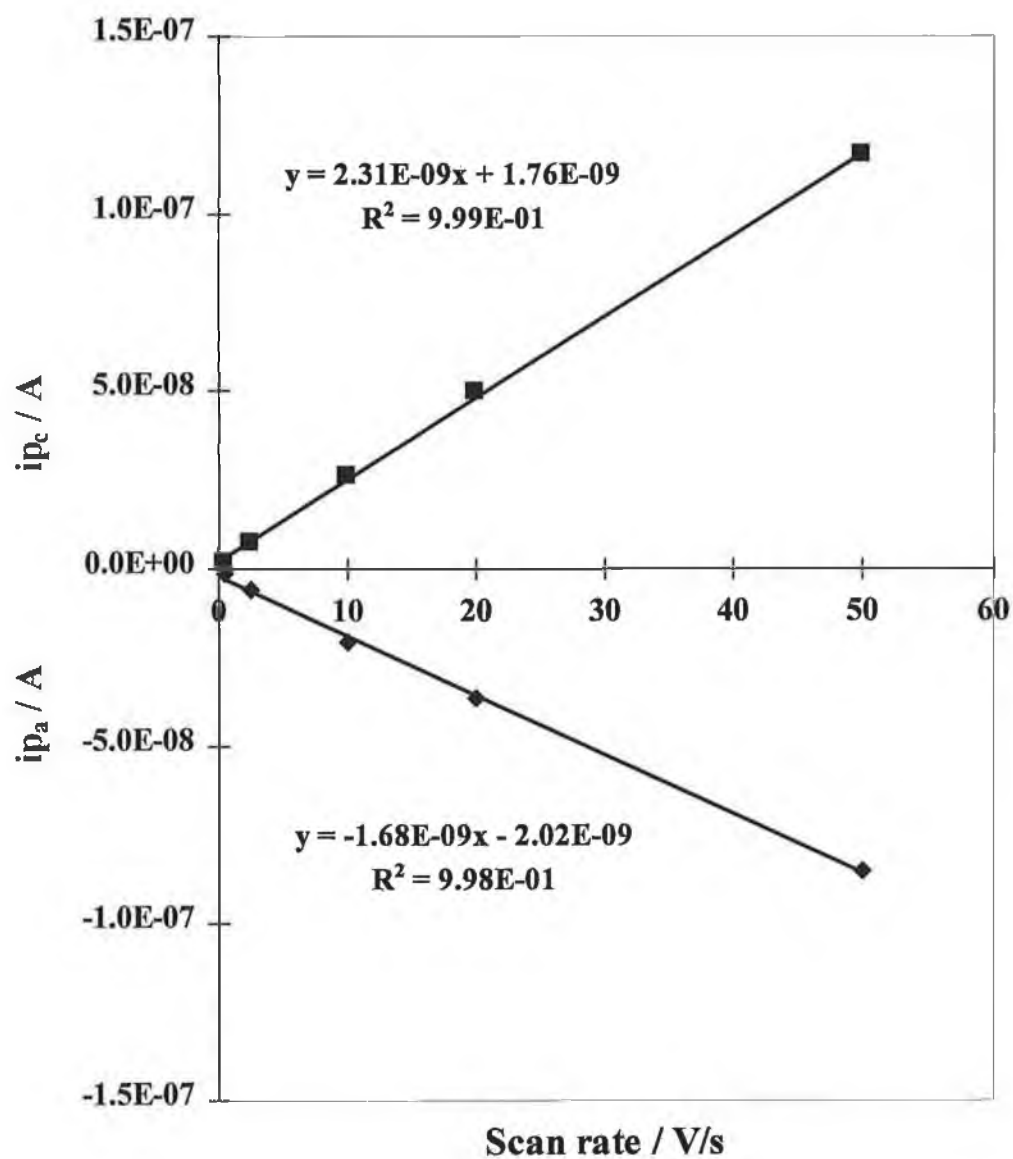


Figure 4 Scan rate dependence of the peak current for a monolayer of $[\text{Os}(\text{bpy})_2\text{P3P Cl}]^+$ up to 50 V/s . A $25 \mu\text{m}$ gold microelectrode was employed. The electrolytic solution was 0.1 M LiClO_4 .

By using one of Laviron's formulations²¹ it is possible to determine the standard rate constant for the transfer of electrons from the electrode to the adsorbed complex. Since we are dealing with an adsorbed species, diffusion does not need to be taken into account in the mathematical treatment for the rate constant, κ . In the situation presented here, the peak-to-peak separation is less than 200/n mV and κ is given by the following;

$$\kappa = \alpha n F v_c / RT = (1-\alpha) n F v_a / RT \quad \text{Eq. 1}$$

where α is the transfer coefficient and n , F , v , R and T have their usual meaning. Figure 5 shows the response obtained when the peak potentials for the anodic and cathodic wave as a function of $\log v$. It can be seen that the peak potentials vary little until high scan rates are applied to the system. At this point deviation occurs. Extrapolation of the deviated lines shows that they intersect at the same point on the horizontal at E^o . The slopes of the points which deviate are 59 and 69 mV for the anodic and cathodic data, respectively. The fact that the slopes are similar and they intersect with each other mean that α is equal and is 0.5. The value of κ is obtained from Eq. 1 where $v_a = v_b = 134 \text{ V s}^{-1}$. For $[\text{Os}(\text{bpy})_2\text{P0P Cl}]^+$ adsorbed onto a gold electrode κ was calculated to be $2.6 \times 10^3 \text{ s}^{-1}$. This calculated value is within that obtained by Forster for similar systems using high speed techniques

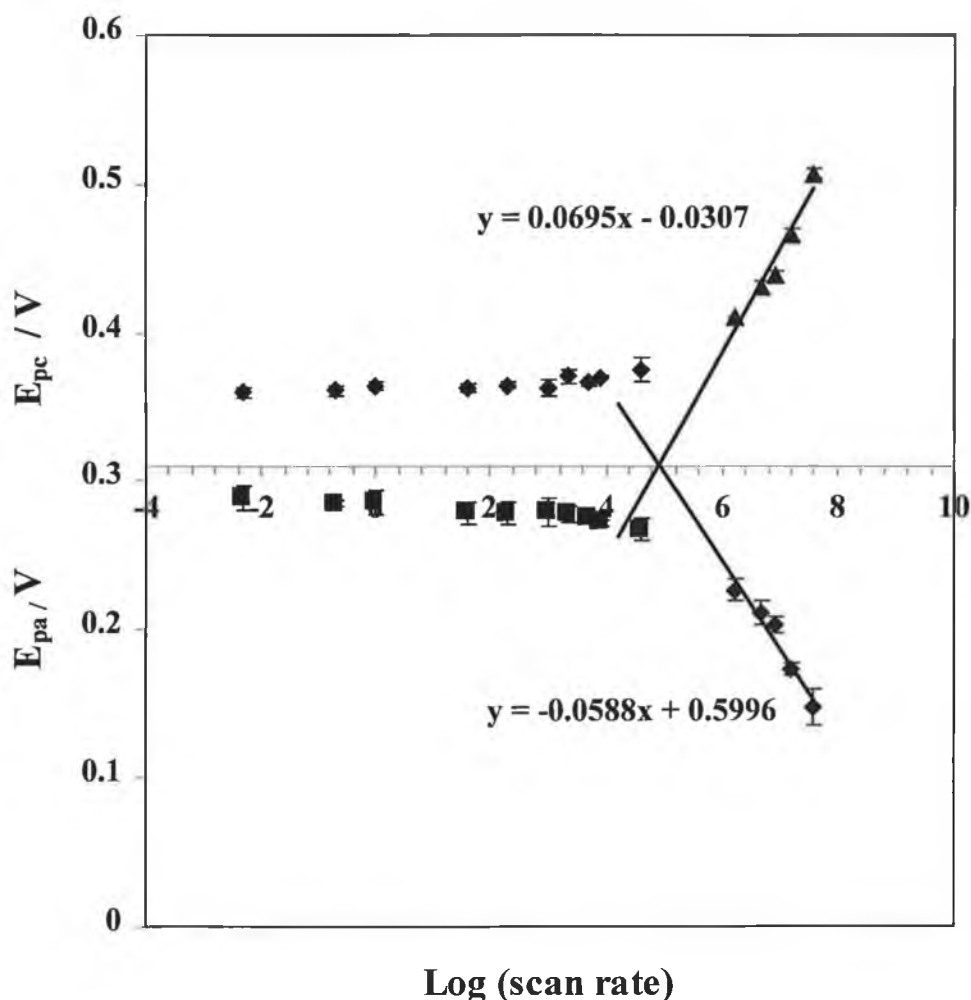


Figure 5 Laviron approach for the determination of the standard rate constant for a monolayer of a monolayer of $[\text{Os}(\text{bpy})_2\text{P}0\text{P Cl}]^+$. A 25 μm gold microelectrode was employed. The electrolytic solution was 0.1 M LiClO_4 .

For adsorbed species under ideal Nernstian conditions, where there are no lateral interactions occurring between the adsorbates, $E_{pa} = E_{pc}$, i.e., one expects a zero splitting (ΔE_p) between the two half wave potentials. Across a wide range of experimental timescales, temperatures, surface coverages and electrolyte we consistently observe a non-zero peak-to-peak splitting for each of these osmium polypyridyl complexes. This peak-to-peak splitting occurred at scan rates even as low as 0.1 Vs^{-1} . For example, the separation between the potentials of the oxidation and reduction peaks (ΔE_p) for the complex $[\text{Os}(\text{bpy})_2\text{P}3\text{P Cl}]^+$ was $0.073 \pm 0.017 \text{ V}$ at a scan rate of 0.05 Vs^{-1} . The condition of the substrate may also have an indirect bearing on the formal potential and

the FWHM due to the molecular scale defects introduced by the polishing procedure employed. Roughness values for these experiments are less than 2. Problems associated with a rough electrode surface may manifest itself in increased in defect sites which when adsorption has occurred may result in a decreased proximity between the head groups, which may increase or decrease electrostatic repulsions.

Where there are no lateral interactions between immobilised species and a rapid equilibrium is established with the metal electrode, the full width at half-maximum (FWHM) of either the anodic or cathodic wave is given by $90.6 / n$ mV from the following equation, where n is the number of electrons transferred:

$$\Delta E_{p,1/2} = 3.53 \frac{RT}{nF} = \frac{90.6}{n} \text{ mV}(25^\circ\text{C}) \quad \text{Eq. 2}$$

The FWHM obtained for the $[\text{Os}(\text{bpy})_2\text{P3P Cl}]^+$ complex were approximately 0.148 ± 0.029 V at 0.5 Vs^{-1} . Publications on analogous osmium compounds have also reported similar observations in non-zero peak-to-peak splitting and an FWHM above $90.6 / n$ mV.^{20, 22, 23, 24, 25} Although not used here, Aoki^{26, 27, 28} has shown by three different methods that FWHM values may be used to determine the extent of interactions occurring between adsorbed osmium redox couples. The experimental observations here regarding the size of FWHM shows the interactions to be destabilising and repulsive rather than attractive and stabilising. These repulsive interactions are most probably electrostatic in nature between the head groups as the osmium complexes used have a net positive charge. An alternative interpretation for this effect is based on the assumption that within a layer of immobilised redox centres, there might be subtle variations in structure, solvation, environment etc., that give rise to a range of closely spaced formal potential values and that is responsible, at least in part, for observed broadening. Non-ideality within modified electrode coatings may be due to slow heterogeneous transfer kinetics, ohmic drop, ion movement or structural changes accompanying redox switching and has been discussed by Felberg and Rubinstein²⁹ in terms of unusual quasireversibility (UQR). In their model, UQR is a non-equilibrium behaviour arising because some rate processes are slow on the timescale of the experiment. However, the persistence of the non-ideal FWHM observed here even at

very slow scan rates suggests that slow kinetics are not responsible for the observed behaviour.

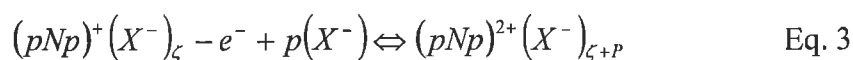
Integration of the voltammetric wave, that is measuring the Faradaic charge required to oxidise or reduce the electroactive film, together with the electrochemical area provides information about the surface coverage (Γ) of the electroactive film on the electrode. The surface coverage provides important information about the packing of the monolayer onto the metal surface. The limiting surface coverage determined for $[\text{Os}(\text{bpy})_2\text{P3PCl}]^+$ from Figure 1 was $1.20 \times 10^{-10} \pm 0.1 \text{ mol cm}^{-2}$. This gives an area of occupation per molecule of 140 \AA^2 . Forster,³⁰ for the same complex adsorbed onto platinum, observed maximum surfaces of the order of $7.7 \times 10^{-11} \text{ mol cm}^{-2}$, which is in reasonable agreement with that obtained here. Theoretically, the projected area per molecule is around 180 \AA^2 , using a radius^{31, 32, 33} of 7.5 \AA for $[\text{Os}(\text{bpy})_2\text{P3P Cl}]^+$. Differences in the area of occupation may be attributed to other contributions to the molecular volume such as the surrounding solvation shell and counter ions. Taking these considerations into account, it appears that adsorption can result in the formation of a dense monolayer in which repulsive interactions are present.

4.2.2 Electrolyte studies

The ability to spontaneously adsorb monolayers containing redox-active molecules onto electrode surfaces provides an opportunity to study redox processes within a well-defined chemical environment. One such process which has been studied in detail within ferrocenethiol monolayers, with and without diluent alkanethiols is the effect of changing the identity and concentration of the supporting electrolyte on the local microenvironment of the monolayer.^{34, 35, 36, 37, 38, 39} In systems of this type, the redox process changes the charge of the redox group within the monolayer. This switching of the charge introduces the possibility of various types of ionic interactions, which may influence not only the rate of the electron transfer but may also enhance interactions between redox-active head groups. It has been demonstrated by De Long and co-workers⁴⁰ on alkane thiol systems containing viologen groups that ionic interactions can significantly influence redox potentials between redox groups within such self assembled monolayers.

The formal potential ($E^{\circ'}$), can provide information about the local microenvironment of a monolayer since it is sensitive to the solvation shell of the redox centre and to the extent of ion pairing. For monolayers of $[\text{Os}(\text{bpy})_2\text{P3P Cl}]^+$, when oxidation occurs the net charge on the complex changes from 1+ to 2+. In this situation, anions are required to compensate the positive charge on the film. The extent of ion pairing has been examined for $[\text{Os}(\text{bpy})_2\text{P3P Cl}]^+$ when monolayers were exposed to varying electrolyte concentrations ranging from 0.05 M to 1.0 M and also the effect on the rigidity of the monolayer from the incorporation of anions into the monolayer framework.

Monolayers of $[\text{Os}(\text{bpy})_2\text{P3P Cl}]^+$ were exposed to electrolytic solutions with an overall fixed concentration, where one electrolyte does not ion pair significantly with the osmium redox centres. The background electrolyte used, which was shown to ion pair to the least extent, is NaSO_4 . The electrolytes studied were LiClO_4 , NaClO_4 , KNO_3 , KCl and H_2SO_4 . All experiments were performed with these electrolytes present in aqueous solutions. Figure 6 shows the voltammetric response for a $[\text{Os}(\text{bpy})_2\text{P3P Cl}]^+$ monolayer after exposure to increasing LiClO_4 electrolyte concentration. A significant negative shift in the formal potential of the P3P monolayer was observed. This shift in $E^{\circ'}$ indicates that oxidation of the monolayer becomes increasingly more facile as the concentration of electrolyte is increased and is consistent with an ion-pair formation of an anion with a redox centre. The situation is summarised in the following Nernstian reaction,



where both redox forms are considered to participate in the ion pairing equilibria. A linear relationship was found when the shift in $E^{\circ'}$ was plotted against the logarithm of the ClO_4^- concentration in NaClO_4 electrolyte as shown in Figure 7. From the slope it is theoretically possible to determine the number of anions which pair with the redox centres upon oxidation and reduction. Theoretically the slope of this plot should be 59/p mV / decade. The slope of the plot Figure 7 is -0.048 V. A value which is relatively close to that expected for a Nernstian response, i.e., 59 mV per decade. The difference between the theoretical and experiment slope values may be due in part to liquid junction potentials or activity effects. The effect of the liquid junction potential

would cause a variation of approximately 0.005 V over the concentration range studied. This value of 0.043 V / decade corresponds to at least a single extra perchlorate ion becoming paired with the redox centre upon oxidation. This result is not stating that the reduced form is not ion-paired, but that oxidation probably causes an extra anion to ion-pair with the redox centre.

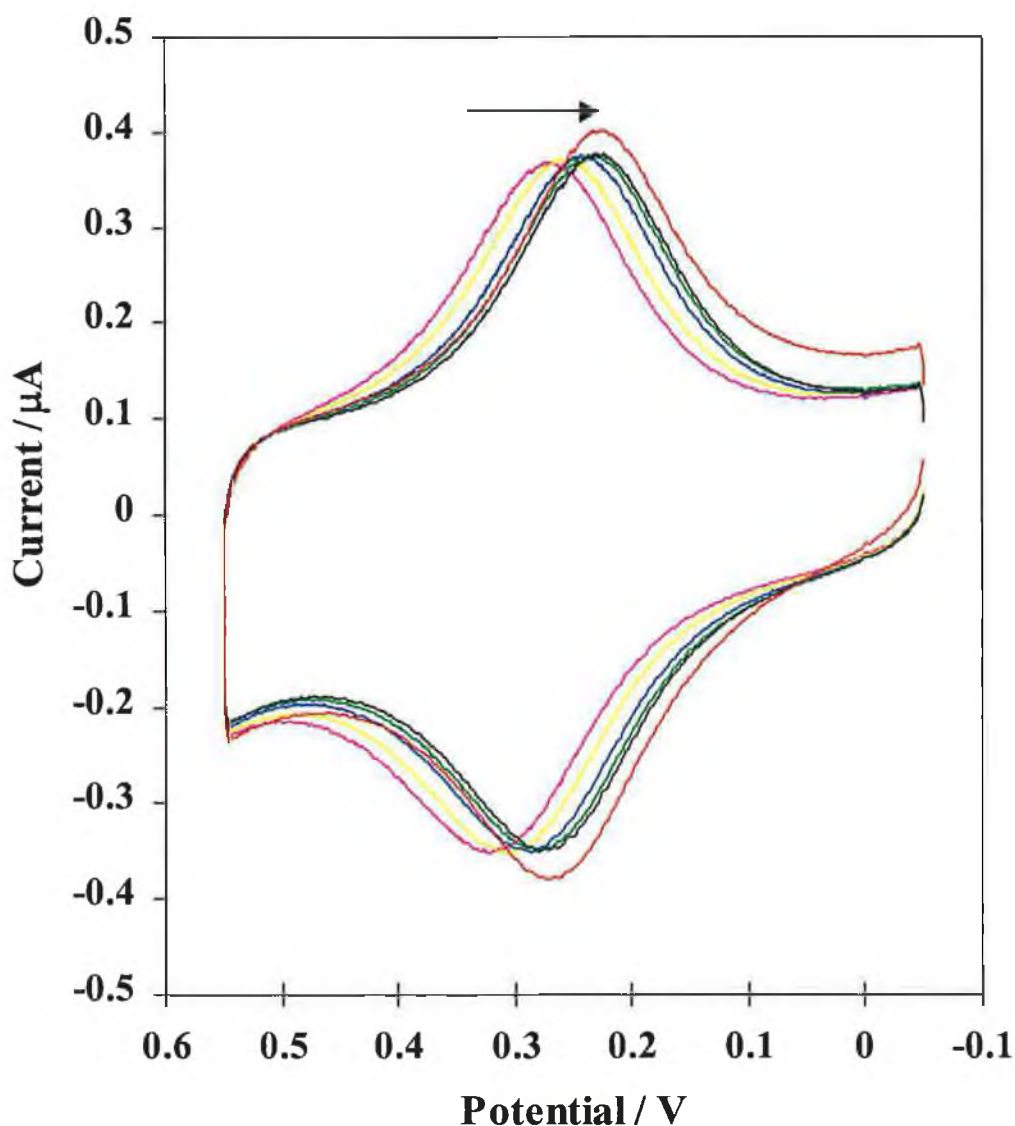


Figure 6 Cyclic voltammogram of a $[\text{Os}(\text{bpy})_2\text{P3P Cl}]^+$ monolayer at a scan rate of 0.5 Vs^{-1} where the electrolyte (left to right) is 0.1, 0.2, 0.4, 0.6, 0.8 and 1.0 M LiClO_4 . A overall fixed background electrolyte concentration of 1.0 M was employed with NaSO_4 acting as the swamping electrolyte.

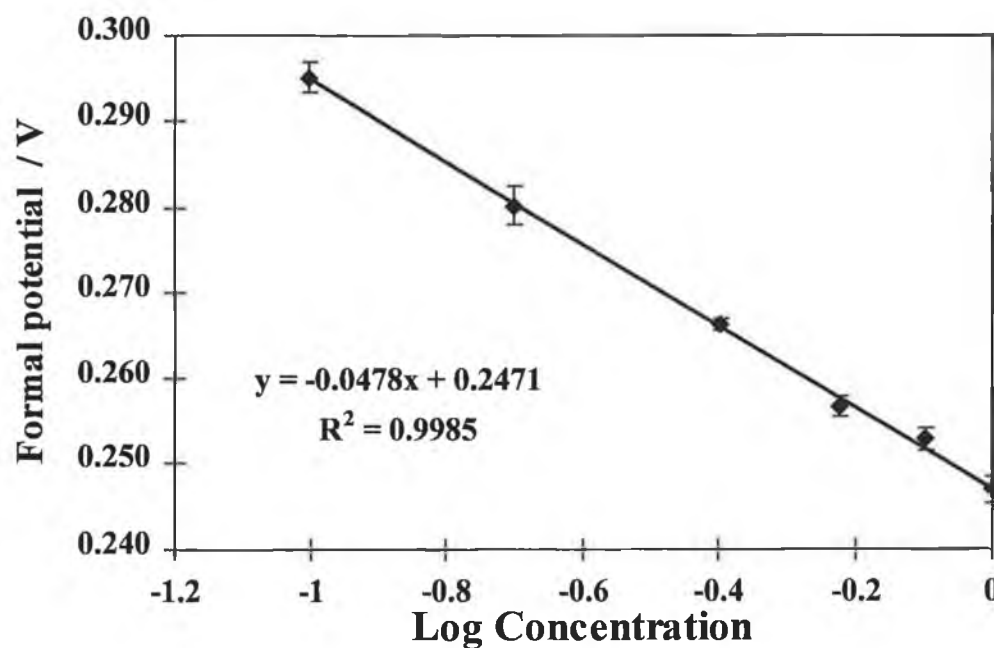


Figure 7 Dependence of the formal potential of a $[\text{Os}(\text{bpy})_2\text{P3P Cl}]^+$ monolayer on LiClO_4 electrolyte concentration.

Table 1 Redox and ion pairing properties for $[\text{Os}(\text{bpy})_2\text{P3P Cl}]^+$ monolayers in various electrolyte solutions.

Electrolyte (1.0 M)	E° / V^a	No. of ion-pairs
LiClO_4	0.247	1
NaClO_4	0.220	1
KNO_3	0.294	1
KCl	0.264	_____
H_2SO_4	0.242	_____

^a Potentials for KCl and H_2SO_4 are cathodic potentials due to degradation of monolayer at high electrolyte concentration.

When monolayers of $[\text{Os}(\text{bpy})_2\text{P3P Cl}]^+$ are exposed to perchlorate ions alone, the surface coverage of the monolayers remained constant over the electrolyte range studied. However, when similar monolayers were exposed to the hydrophilic anions used in this study, NO_3^- , Cl^- , and SO_4^{2-} , the monolayer was found not only to desorb but FWHM values increased dramatically. As previously mentioned Figure 6 illustrates the response when a monolayer of $[\text{Os}(\text{bpy})_2\text{P3P Cl}]^+$ is exposed to increasing concentrations of the hydrophobic perchlorate anion. The peak shapes remain unchanged with increasing electrolyte concentration and the surface coverage remains constant at $1.2 \times 10^{-10} \text{ mol cm}^{-2}$. In contrast, Figure 8 shows the response when similar monolayers were immersed in the hydrophilic anion SO_4^{2-} . For this electrolyte desorption of the monolayer was rapid. In fact when the immobilised monolayer was placed in the lowest electrolyte concentration used, 0.01 M, and cyclic voltammetry performed, the surface coverage had decreased rapidly. This is clearly evident from the peak shape response and the increase in the capacitive current either side of the redox peak. For presentation purposes, Figure 9 contains not only the voltammetric responses for the $[\text{Os}(\text{bpy})_2\text{P3P Cl}]^+$ monolayer in the minimum and maximum SO_4^{2-} concentration used, but also a cyclic voltammogram when the monolayer is exposed to perchlorate. The level of desorption is clearly evident. It is important to note that Na_2SO_4 can still be used as a swamping electrolyte since the perchlorate added to these ion-pairing experiments appears to stabilise the monolayers. pH is not considered a factor since recently O'Kelly⁴ has shown that the bis-substituted osmium complex $[\text{Os}(\text{bpy})_2(\text{P3P})_2]^{2+}$ exhibits well defined electrochemistry at pH levels as low as 2.5 where the FWHM values seem to slightly decrease as the pH decreased. This was however, in perchlorate electrolyte solutions where the pH was adjusted with HClO_4 and not H_2SO_4 .

Table 2 contains data for the formal potentials for a $[\text{Os}(\text{bpy})_2\text{P3P Cl}]^+$ monolayer after immersion in electrolytic solutions containing a hydrophobic and hydrophilic anions. There are several points to note in these data. First, the shift in the formal potential from 0.1 M to 1.0 M for the ClO_4^- anions was greater than the shift in the hydrophilic anion NO_3^- . This suggests the formation of enhanced ion pairing with perchlorate over nitrate. Second, comparison of the formal potentials also reveals the formal potential of the monolayer in perchlorate electrolyte solution to be more negative than in nitrate. Similar responses from the effects of hydrophobic and hydrophilic anions on the formal

potentials of monolayers have been found by a number of other researchers. De Long and Buttry³⁶ found shifts of over 100 mV in the formal potential of alkane groups containing embedded viologen moieties (V) in ClO_4^- and Cl^- . They attribute this shift in formal potential to increased ion-pairing between the V^{2+} state and the ClO_4^- . Creager had similar ion-pairing responses with ClO_4^- for ferrocene alkane thiols.⁴¹ Creager also points out the shift in apparent formal potential in ClO_4^- compared to Cl^- is a measure of the equilibrium constant for ion-pair formation.

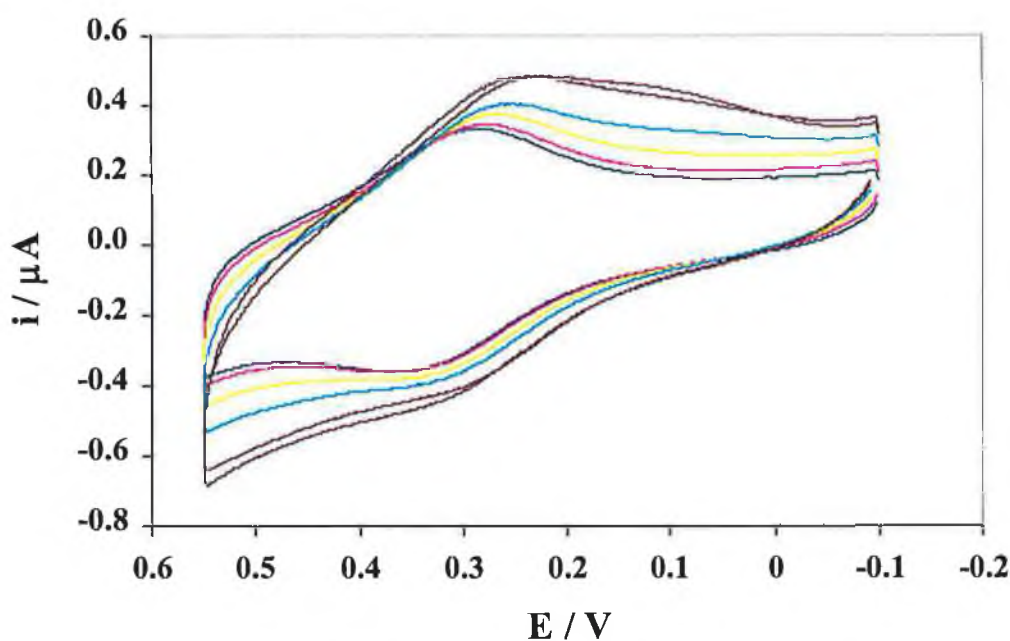


Figure 8 Cyclic voltammogram of a $[\text{Os}(\text{bpy})_2\text{P3P Cl}]^+$ monolayer at a scan rate of 0.5 Vs^{-1} where the electrolyte (left to right) is 0.1, 0.2, 0.4, 0.6, 0.8 and 1.0 M H_2SO_4 . A overall fixed background electrolyte concentration of 1.0 M was employed.

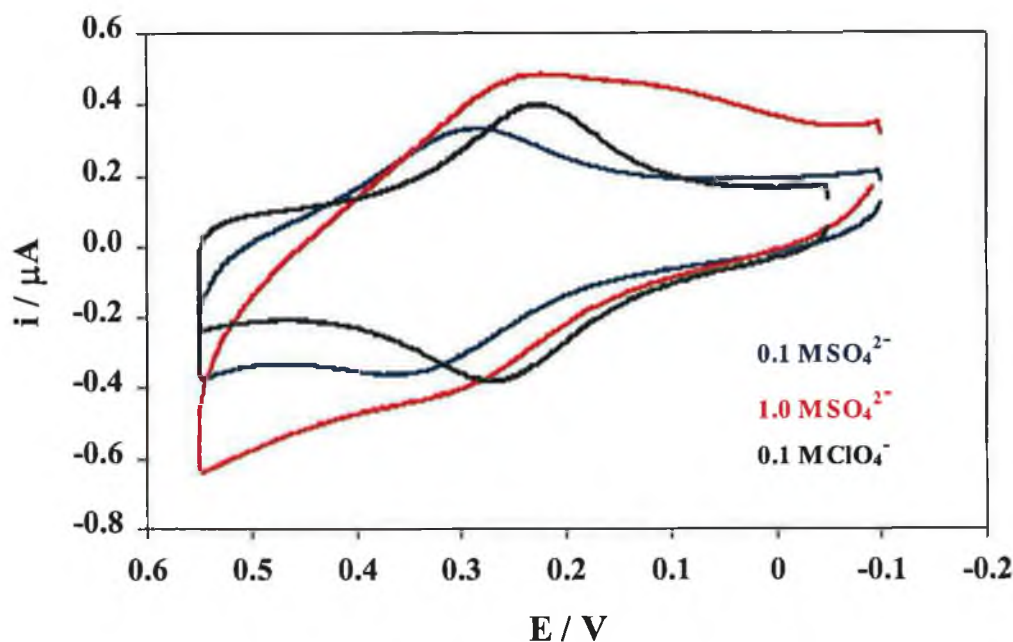


Figure 9 Overlaid cyclic voltammetric responses showing the effect sulphate electrolyte concentration on a $[\text{Os}(\text{bpy})_2\text{P3P Cl}]^+$ monolayer. A monolayer immersed in a perchlorate solution is shown to distinguish the differences between the two electrolytes.

Table 2 Influence of supporting electrolyte anions ClO_4^- and KNO_3^- on formal potential of $[\text{Os}(\text{bpy})_2\text{P3P Cl}]^+$ monolayers.

Electrolyte concentration	$E^{0'}$ of $[\text{Os}(\text{bpy})_2\text{P3P Cl}]^+$ in $\text{LiClO}_4^{\text{a}}$	$E^{0'}$ of $[\text{Os}(\text{bpy})_2\text{P3P Cl}]^+$ in KNO_3^{a}
0.1	293 (2)	315 (2)
0.2	279 (2)	312 (2)
0.4	269 (1)	306 (2)
0.6	255 (2)	302 (2)
0.8	252 (2)	293 (3)
1.0	247 (2)	290 (3)

^a Numbers in parentheses represent the standard deviation for at least three individual monolayers.

Figure 10 shows the logarithmic responses of the formal potential for a number of $[\text{Os}(\text{bpy})_2\text{P3P Cl}]^+$ monolayers exposed to varying electrolytes, both hydrophilic and hydrophobic. The intercept values represent the limiting formal potentials. The voltammetric responses in KCl and KNO_3 were not ideal and as a consequence the cathodic peak potential was plotted instead of the formal potential. However, the graphs in (a) and (d) clearly show the differences in the formal potentials obtained from hydrophilic and hydrophobic anions, respectively, with the hydrophobic anion resulting in a more negative formal potential as discussed earlier. The respective slopes give an indication of the number of anions, which ion-pair with the immobilised film. The results reveal no major difference in suggesting that the abilities of these anions to ion-pair with the monolayer are similar. This result is surprising considering the differences in the formal potentials obtained for hydrophobic and hydrophilic anions.

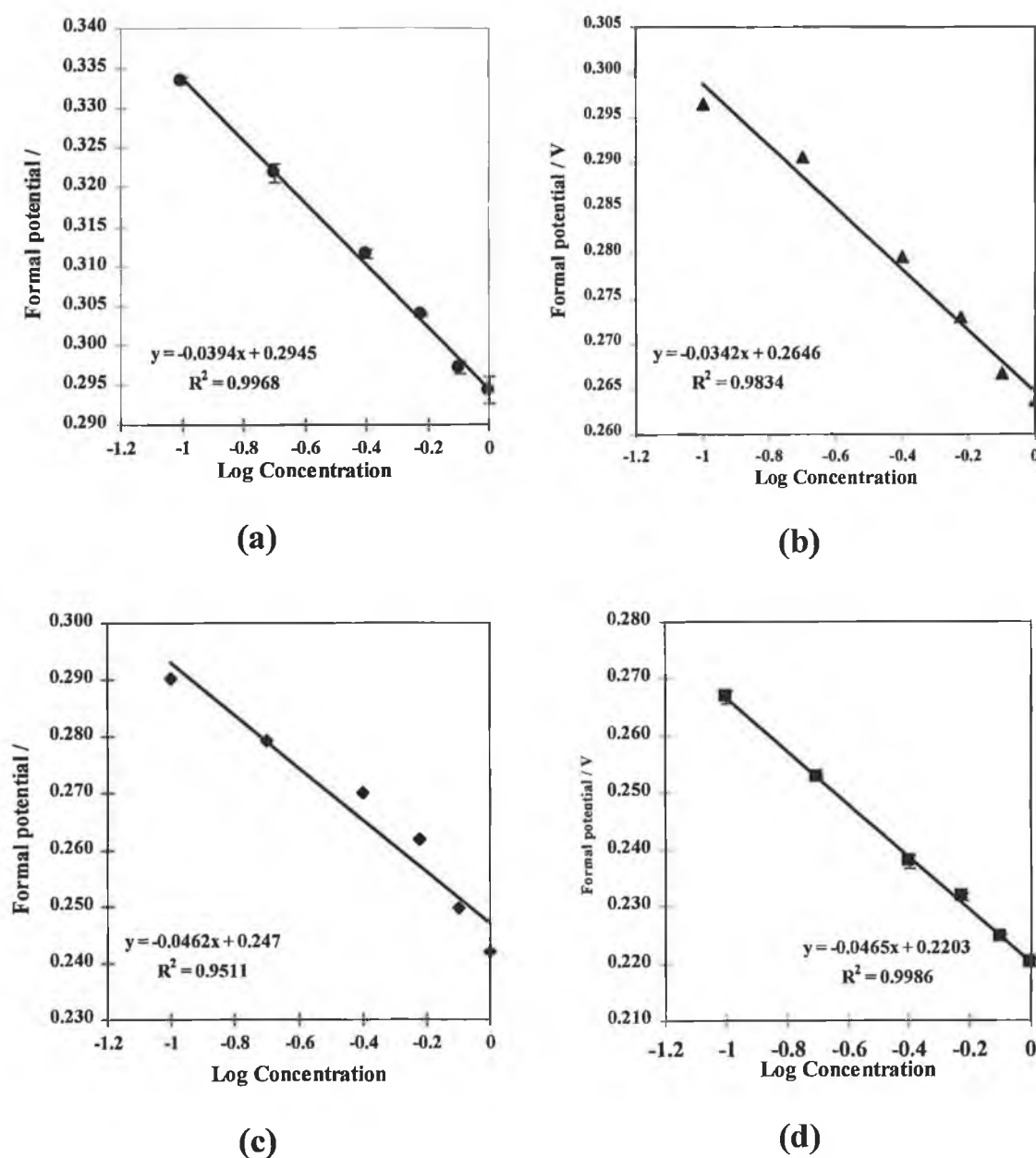


Figure 10 Dependence of the formal potential of $[\text{Os}(\text{bpy})_2\text{P3P Cl}]^+$ monolayers with the logarithm of varying electrolytes. The electrolytes employed were (a), KNO_3 (b), KCl , (c), H_2SO_4 and (d), NaClO_4 .

4.2.3 Capacitance effects

Investigating the double layer capacitance across a modified electrode enables us to monitor the changes in interfacial charge distribution, which accompany the formation of a spontaneously adsorbed monolayer and perhaps the packing density of the monolayer.^{2, 42, 43} The differential capacitance was monitored using potential step chronoamperometry as the electrolyte concentration was systematically varied. The potential step was performed where no redox reactions occur and only single exponential decays, due to double layer charging were observed. In this case, two steps were performed, i.e., at potentials where the monolayer is fully oxidised or reduced. The actual potential step used for each chronoamperogram varied depending on the concentration of electrolyte being used, since the formal potential shifted in a negative potential direction as the electrolyte concentration increased. The pulse amplitude ΔE was 0.100 V and four steps were applied to each monolayer for each electrolyte concentration studied. Two steps were applied on the oxidation wave, one before and after the E_{pa} , and two steps on the reduction wave, also one before and after the E_{pc} . Therefore, the capacitance values were measured at potentials where the net charge on the complex is 1+ and 2+.

Monitoring the double layer capacitance as the electrolyte concentration is varied enables us to gain an insight into the permeability of the film and also how the double layer sets up within the monolayer. The capacitance result for each potential step experiment was determined from plots of $\log i$ vs. time, where the slope is $-1/RC$ and the intercept is $\ln(\Delta E/R)$. Figure 11 and Figure 12 show examples of these type of plots. The transient decays in Figure 11 do not contain any Faradaic current as the potential step was not centred at or near the formal potential of the complex. The current from the decay is purely capacitive. The largest calculated double layer capacitance in 0.1 M LiClO_4 obtained from Figure 12 is approximately 12 μF . This value is considerable less than that observed for an unmodified electrode in the same electrolyte which is 40 – 50 $\mu\text{F cm}^{-2}$. This reduced double layer capacitance for the modified electrode is consistent with a decreased dielectric constant (ϵ) at the electrode interface when the monolayer is present.

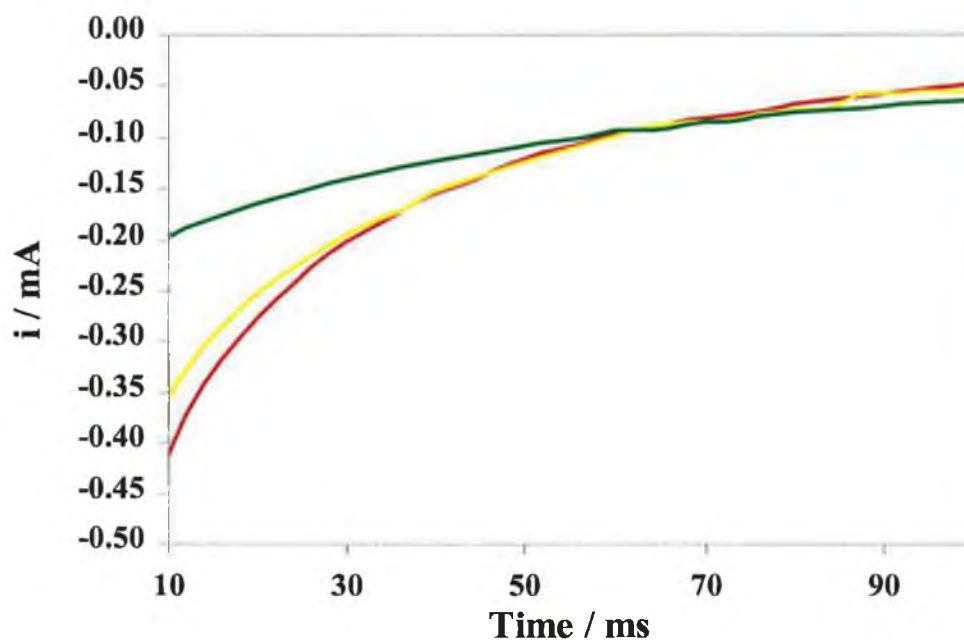


Figure 11 Current response of a 0.1 cm radius gold electrode modified with a spontaneously adsorbed $[\text{Os}(\text{bpy})_2\text{P3P Cl}]^+$ monolayer following a potential step of 0.05 V, centred at 0.35 V negative of the formal potential, which is 0.268 V. The concentrations of electrolyte present were from top to bottom, 0.4, 0.6, and 0.8 M LiClO_4

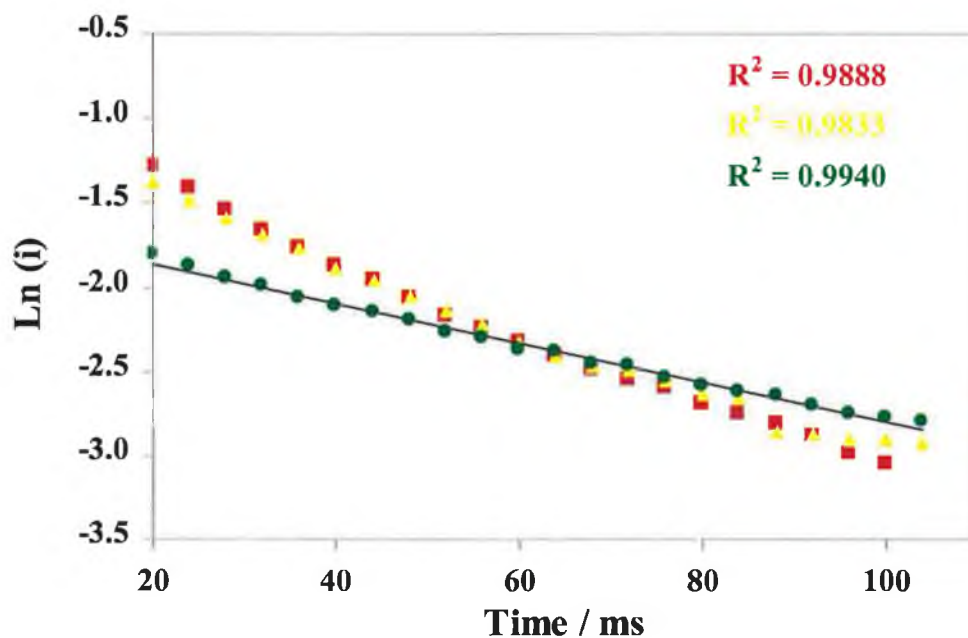
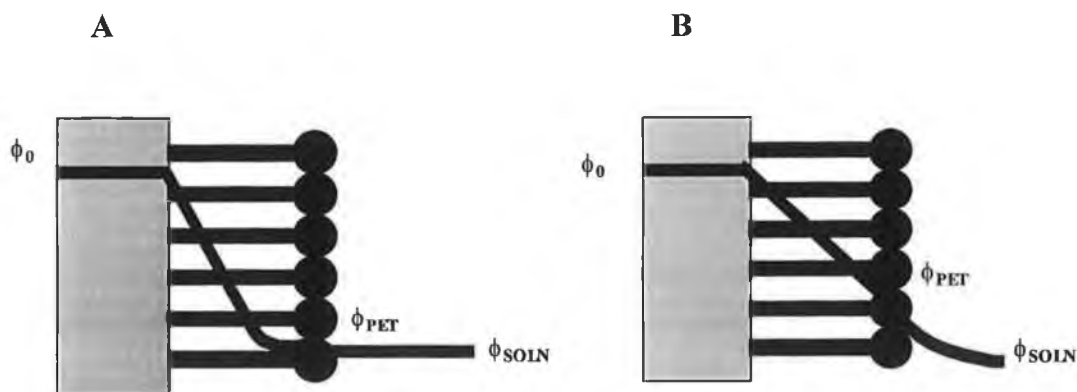


Figure 12 Semi-log plot for the transients in Figure 11. For clarity only one trendline has been shown. However, all R^2 values are presented.

There are two limiting models that may describe the potential profile across the monolayer/solution interface. First, the double layer for the modified electrode may be similar to that of a bare electrode with the applied potential being dropped close to the electrode/film interface, Chart 1 A, corresponding to the double layer setting up within the film. In order for this to occur, charge compensating counterions must permeate the monolayer. Ion influx will cause a decrease in the distance of closest approach of the ions to the metal surface, resulting in an increase in C_{dl} . The second limiting case assumes that the monolayer is impermeable, resulting in a low dielectric constant within the film due to the organic nature of the monolayer. Under these circumstances, the potential will decrease linearly across the thickness of the monolayer and then exponentially in the solution phase, Chart 1 B. The immobilised redox will thus experience a large electric field.

Chart 1



The differential capacitance was determined in order to probe the limiting case which best described our system. The concentration range studied was 0.025 to 0.8 M $LiClO_4$. Figure 13 represents the double layer capacitance values obtained when the capacitance was measured before and after the formal potential of a monolayer of $[Os(bpy)_2P3P Cl]^+$ and also as the supporting electrolyte concentration was varied. In all the potential step experiments performed, the differential capacitance data was consistently higher for the monolayer in the oxidised rather than the reduced form. This increase in differential capacitance may be attributed to the composition of the monolayer adsorbed onto the electrode. The metal complex has a 1+ charge while the

charge is 2+ when oxidised. A movement of charge compensating counterions accompanies oxidation of the monolayer, in this case perchlorate ions, through the monolayer, which causes the dielectric constant to increase, and as stated in the first case, the compression of the compact layer which in turn increases the differential capacitance. The fact that counterions pass through the monolayer reflect a higher degree of ionic permeability for the more densely charged oxidised layer than the reduced layer.

According to Figure 13, there is a sharp decrease in the capacitance data from $12.5 \pm 0.5 \mu\text{F}/\text{cm}^2$ to $7.7 \pm 0.1 \mu\text{F}/\text{cm}^2$ in the oxidised region of the monolayer for an increase in background electrolyte concentration from 0.025 M to 0.1 M. Forster and O'Kelly,⁴ working on the bis-substituted osmium complex adsorbed onto platinum, noticed that the double layer capacitance increased approximately linearly with increasing logarithm of the supporting electrolyte concentration for electrolyte concentrations of less than 0.2 M, before levelling off. Upon oxidation, compensating counterions permeate the monolayer. The influx of these ions and solvent molecules separates the osmium head groups sufficiently by charge screening with the effect of reducing the charge between them. This initial screening causes a decrease in capacitance until the concentration of ions permeating the monolayer is at a maximum. Therefore, a levelling off in capacitance occurs.

After 0.3 M the capacitance is very insensitive to either the redox composition of the monolayer or the direction of the step. This insensitivity indicates that the limiting value of C_T is obtained which may represent the film capacitance or the double layer has set up within the film in which case this value represents the small diffuse layer.

Although our capacitive data decreases with increasing electrolyte concentration contrary to what we expected from Chart 1 a, we still believe the osmium polypyridyl complexes are permeable to solvent and ions therefore, enabling the double layer to set up with the monolayer framework.

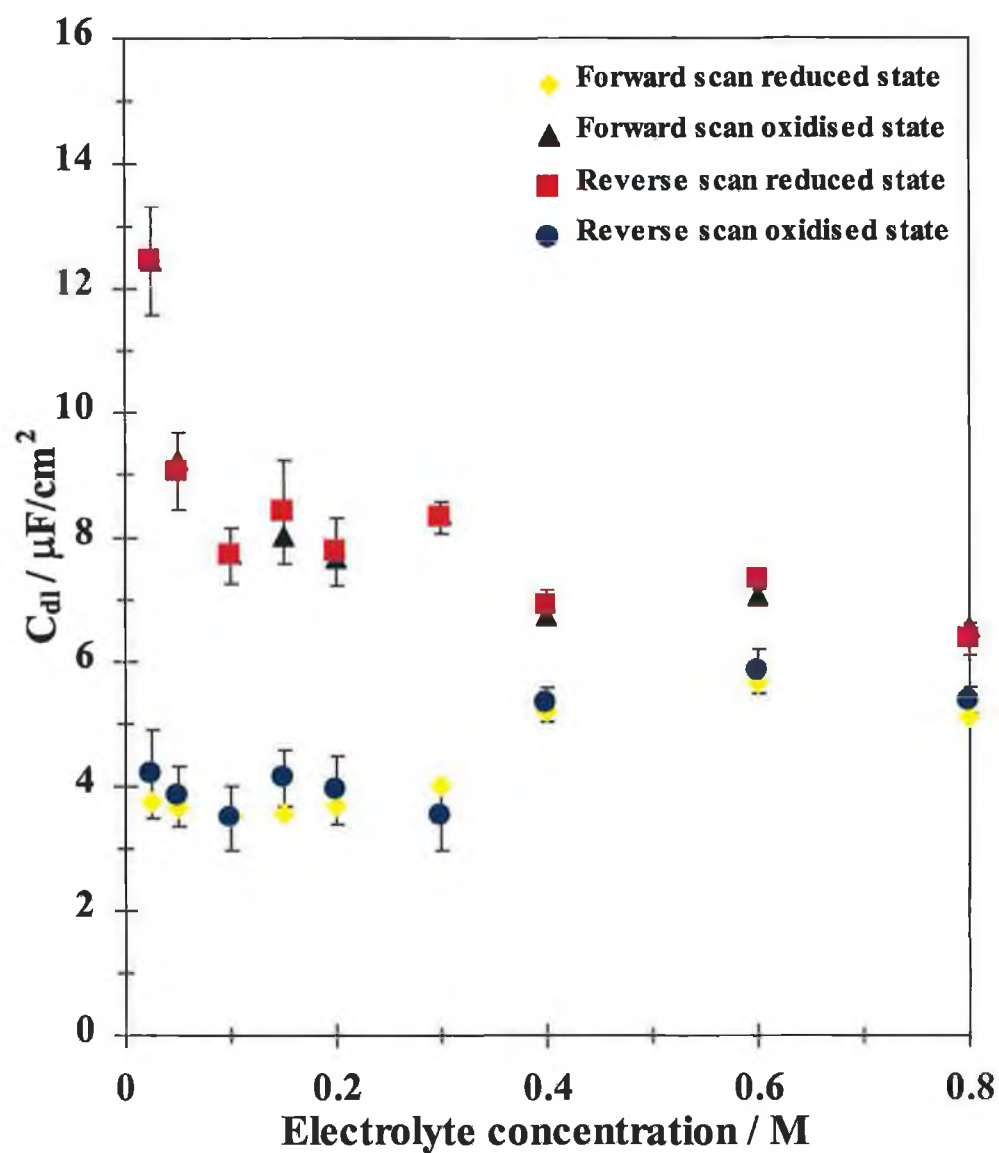


Figure 13 Dependence of the interfacial capacitance for a spontaneously adsorbed monolayer of $[\text{Os}(\text{bpy})_2\text{P3P Cl}]^+$ with increasing concentration. The electrolyte used is 0.1 M LiClO_4 .

4.2.4 Temperature dependence of mono-substituted osmium complexes

Not only can the reaction entropy ΔS_{rc}° be determined from the temperature dependence of the formal potential but an insight into the thermal stability and thermal effects from electrostatic interactions between adsorbates may also be monitored. ΔS_{rc}° which quantifies the entropy difference between the reduced and oxidised forms of the redox couple was determined using a non-isothermal cell as discussed by Weaver and co-workers^{44, 45} for monolayers of $[\text{Os}(\text{bpy})_2\text{P2P Cl}]^+$.

$$\Delta S_{rc}^\circ = F(\partial E^\circ/\partial T) \quad \text{Eq. 4}$$

where F is the Faraday constant and T is the absolute temperature. Figure 14 shows a plot of the effect on the formal potential for a P2P monolayer, when the temperature is varied from 0 to 40° C and where the supporting electrolyte is 0.1 M LiClO_4 . The formal potential of the redox centre was found to shift in a positive direction with increasing temperature. In these experiments, the integrated charge under the peaks remains constant with increasing temperature, indicating that these monolayers are thermally stable. Figure 15 represents the plot of the E° vs T which was linear and the slope $(\partial E^\circ/\partial T)$, when put into Eq. 4 gave a positive reaction entropy of $+32 \text{ J mol}^{-1} \text{ K}^{-1}$ for $[\text{Os}(\text{bpy})_2\text{P2P Cl}]^+$. The positive shift in E° is indicative of a higher degree of local ordering of osmium in the 2+ state.

A theoretical estimate of the reaction entropy may be provided using the dielectric continuum theory, via the Born equation.⁴⁶

$$\Delta S_{rc}^\circ(\text{Born}) = -N_A \Delta e^2 (\partial \epsilon_s / \partial T) (Z_R + 1)^2 - Z_R^2 / (2r\epsilon_s^2) \quad \text{Eq. 5}$$

where N_A is Avogadro's constant, e is the electronic charge, ϵ_s is the static dielectric constant, Z_R is the charge on the reduced form of the redox couple, and r is the radius of the complex (7.5 Å), when ϵ_s is taken as 78.4, i.e., the dielectric constant for water. A theoretical ΔS_{rc}° value of $+42.3 \text{ J mol}^{-1} \text{ K}^{-1}$ was obtained. The experimental result for $[\text{Os}(\text{bpy})_2\text{P2P Cl}]^+$ is comparable with this theoretical ΔS_{rc}° and further suggests that the

monolayer is highly solvated. This approach however, is only a guide as the value for $\partial\epsilon_s/\partial T$ is unknown and we have assumed no change for ϵ with T . Using a value of 78.4 for ϵ is also assumes that the dielectric constant is unchanged at the electrolyte interface. This is a fair assumption as electrochemical data show the modified electrode to be highly solvated. If the dielectric of the interface were to decrease and represent a more organic nature the Born equation predicts a ΔS_{rc}° value of over $2000 \text{ J mol}^{-1} \text{ K}^{-1}$. While the model may not be an accurate method for the determination of ΔS_{rc}° it may be used as a guide.

A similar ΔS_{rc}° value for the same complex has been reported by Forster², who found that theoretical values predicted by the Born equation and experimentally predicted values were highly correlated in a variety of solvents. This result is consistent with the capacitance data, in which we suggest that upon oxidation counterions and solvent permeate into the monolayer.

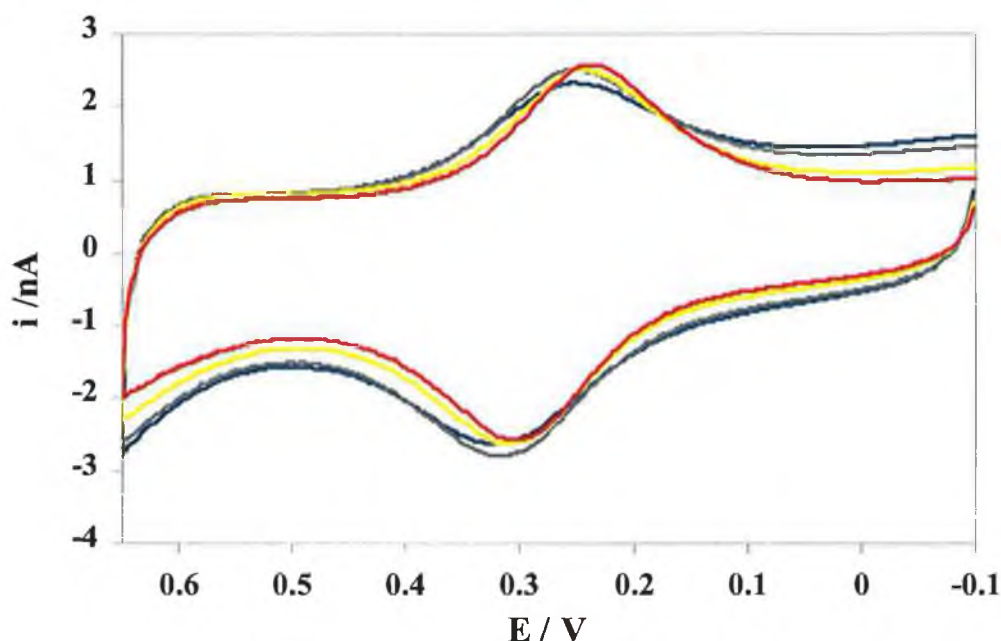


Figure 14 Cyclic voltammograms of adsorbed $[\text{Os}(\text{bpy})_2\text{P2P Cl}]^+$ as a function of temperature. The voltammograms are from right to left, (blue) 0, (grey) 10, (yellow) 30, (red) 40 °C. The scan rate is 0.5 Vs^{-1} . The electrolyte is aqueous 0.1 M LiClO_4 .

Table 3 contains the data obtained for the FWHM with increasing temperatures for monolayers of $[\text{Os}(\text{bpy})_2\text{P2P Cl}]^+$. As can be seen the peak width increases approximately 16 mV $[\text{Os}(\text{bpy})_2\text{P2P Cl}]^+$. While these peaks are somewhat larger than those expected in the absence of lateral interactions, the increase in peak widths over this range is consistent with thermal broadening rather than increased lateral interactions between the redox-active head groups.²

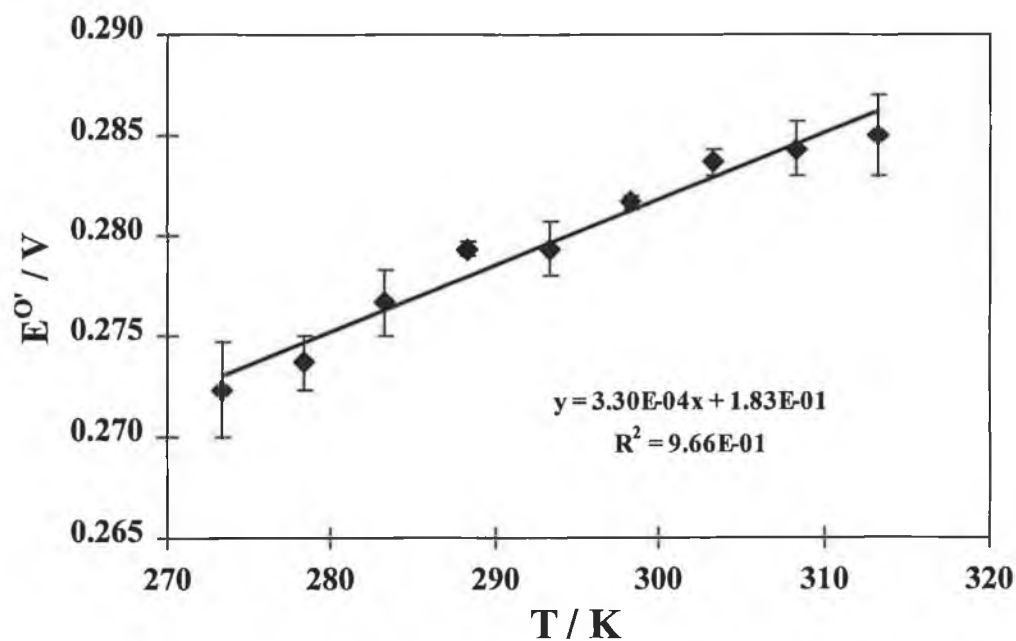


Figure 15 Temperature dependence of the formal potential for a $[\text{Os}(\text{bpy})_2\text{P2P Cl}]^+$ monolayer spontaneously adsorbed on a gold electrode.

Table 3 Dependence of the full width at half maximum (FWHM) for cyclic voltammograms of P2P and P3P monolayers on temperature.

Temperature ^a / °C	FWHM / mV P2P
0	144 ± 0
5	146 ± 2
10	144 ± 4
15	150 ± 4
20	155 ± 3
25	151 ± 5
30	157 ± 4
35	159 ± 2
40	161 ± 2

^a The temperature is controlled to within ± 0.2 °C.

4.3 Conclusion

The monolayers considered here, $[Os(bpy)_2L Cl]$ where $bpy = 2,2'$ bipyridine and L is 1,2-bis(4-pyridyl)ethane, or 4,4'-trimethylenedipyridine, have been formed by spontaneous adsorption from mM deposition solutions. The immobilised films exhibit nearly ideal voltammetry and are stable over long periods with continuous cycling in aqueous perchlorate electrolyte.

When the monolayers are exposed to increasing concentration of electrolyte, the microenvironment around the redox centre is perturbed. This perturbation manifests itself with a negative shift in the formal potential of the redox active species. This negative shift has been shown to be influenced by the type of anion in solution. Increased shifts are observed for hydrophobic anions over hydrophilic anions most likely due to the formation of an ion-pair between perchlorate with redox species. In addition, oxidation was found to occur more readily in hydrophobic electrolyte solutions.

We have found that when monolayers are exposed to electrolytic solutions, the double layer sets itself up within the monolayer and the films appear to be highly solvated. Although elevated temperatures increase the FWHM within the monolayer, the effect is not due to increased interaction between the adsorbates but rather due to increased thermal broadening. The observed reaction entropies also suggest highly solvated monolayers with dielectric constants close to that of bulk water.

4.4 References

1. Acevedo, D., Abruña, H. D. *J. Phys. Chem.*, **1991**, 95, 9590
2. Forster, R. J., Faulkner, L. R. *J. Am. Chem. Soc.*, **1994**, 116, 5444
3. Forster, R. J., Faulkner, L. R. *J. Am. Chem. Soc.*, **1994**, 116, 5453
4. Forster, R. J., O'Kelly, J. P. *J. Phys. Chem.* **1996**, 100, 3695-3704
5. Acevedo, D., Bretz, R. L., Tirado, J. D., Abruña, H. D., *Langmuir*, **1994**, 10, 1300
6. Hudson, J. E., Abruña, H. D., *J. Phys. Chem.* **1996**, 100, 1036
7. Bretz, R. L., Abruña, H. D. *J. Electroanal. Chem.*, **1995**, 388, 123
8. Bretz, R. L., Abruña, H. D. *J. Electroanal. Chem.*, **1996**, 408, 199
9. Tirado, J. D., Abruña, H. D., *J. Phys. Chem.*, **1996**, 100, 4556-4563
10. Forster, R. J., Faulkner, L. R. *Anal. Chem.*, **1995**, 67, 1232
11. Forster, R. J., *Inorg. Chem.*, **1996**, 35, 3394
12. Salaneck. W. R., Lögdlund. M., Birgersson. J., Barta. P., Lazzaroni. R., Brédas. J. L., *Synthetic Metals*, **1997**, 85, 1219
13. Swalen. J. D., Allara. D. L., Andrade. J. D., Chandross. E. A., Garoff. S., Isreallachvilli. J., McCarthy. T. J., Murray. R., Pease. R. F., Rabolt. J. F., Wynne. K. J., Yu. H., *Langmuir*, **1987**, 3, 932
14. Bard, A. J., Abruña, H. D. Chidsey, C. E. D., Faulkner, L. R., Felberg. S., Itaya. K., Majda. M., Melroy. M., Murray. R. W., Porter. M. D., Soriaga. M. P., White. H. S., *J. Phys. Chem.*, **1993**, 97, 7147
15. Campbell, J. L., Anson, F. C., *Langmuir*, **1996**, 12, 4008
16. Bard, A. J., Faulkner, L. R., '*Electrochemical methods*', Wiley, New York, **1980**
17. Laviron, E., *J. Electroanal. Chem.*, **1974**, 52, 395
18. Brown, A. P., Anson, F. C., *Anal. Chem.*, **1977**, 49, 1589
19. Sullivan, B. P., Conrad, D., Meyer, T. J., *Inorg. Chem.*, **1985**, 24, 3640
20. Acevedo, D., Abruña, H. D. *J. Phys. Chem.*, **1991**, 95, 9590
21. Laviron, E., *J. Electroanal. Chem.*, **1979**, 101, 19
22. Forster, R. J. Faulkner, L. R.; *J. Am. Chem. Soc.*, **1994**, 116, 5444
23. Forster, R. J., Faulkner, L. R. *Anal. Chem.*, **1995**, 67, 1232
24. Forster, R. J., O'Kelly, J. P. *J. Phys. Chem.* **1996**, 100, 3695

25. Campbell, J. L., Anson, F. C., *Langmuir*, **1996**, 12, 4008
26. Dafuku, H., Aoki, K., Tokuda, K., Matsuda, H., *J. Electroanal. Chem.*, **1985**, 183, 1
27. Matsuda, H., Aoki, K., Tokuda, K., *J. Electroanal. Chem.*, **1987**, 217, 1
28. Matsuda, H., Aoki, K., Tokuda, K., *J. Electroanal. Chem.*, **1987**, 217, 15
29. Feldberg, S.W.; Rubinstein, I. *J. Electroanal. Chem.* 1988, 240, 1
30. Forster, R. J., Faulkner, L. R. *J. Am. Chem. Soc.*, **1994**, 116, 5444
31. Ferguson, J.E. Love, J.L. Robinson, W.T. *Inorg. Chem.* 1972, 11, 1662
32. Rillema, D.P. Jones, D.S. Levy, H.A. *J. Chem. Soc. Chem Comm.* 1979, 849
33. Goodwin, H. A., Kepert, D. L., Patrick, J. M., Skelton, B. W., White, A. H., *Aust. J. Chem.*, **1984**, 37, 1817
34. Rowe, G. K., Creager, S. E., *Langmuir*, **1991**, 7, 2307
35. De Long. H. C., Donohue. J. J., Buttry. D. A., *Langmuir*, **1991**, 7, 2196
36. De Long. H. C., Buttry. D. A., *Langmuir*, **1992**, 8, 2491
37. Ju, H. Leech, D., *Phys. Chem. Chem. Phys.*, **1999**, 1, 1549
38. Shimazu, K., Yagi, I., Sato, Y., Uosaki, K., *J. Electroanal. Chem.*, **1994**, 372, 117
39. Uosaki. K., Sato, Y., Kita, H., *Langmuir*, **1991**, 7, 1510
40. De Long, H.C. Buttry, D.A. *Langmuir* **1990**, 6, 1319
41. Creager, S. E., Rowe, G. K., *Anal. Chim. Acta.*, **1991**, 246, 233
42. Creager, S.E.; Weber, K. *Langmuir*, 1993, 9, 844.
43. Porter, M. D., Bright. T. B., Allara. D. L., Chidsey. C. E. D., *J. Am. Chem. Soc.*, **1987**, 109, 3559
44. Barr. S. W., Guyer. K. L., Li. T. T.-T., Liu. H. Y., Weaver, M. J., *J. Electrochem. Soc.* **1984**, 131, 1626
45. Hupp. J. T., Weaver. M. J., *J. Phys. Chem.* **1984**, 88, 1860
46. Noyes. R. M., *J. Am. Chem. Soc.* **1962**, 84, 513

CHAPTER 5

Hydrogen bonding in 2-Dimensions:

Single component Anthraquinones as model systems

5 Introduction

The construction, characterisation and application of monolayers immobilised electrodes continues to be the focus of intense research activity.^{1, 2, 3, 4, 5, 6, 7} However, while systems such as ferrocene alkane-thiols^{8, 9} and osmium bipyridyl monolayers^{9, 10, 11} have provided significant new insights into the nature of the mechanism of electron transfer, relatively less attention has been paid to coupled proton and electron transfer reactions. In this regard, quinoid monolayers are important model systems because of their unusually ideal electrochemical responses and relevance to biological systems.^{12, 13, 14} Also, using functionalised anthraquinones as building blocks allows us to probe the effects of both inter- and intra-molecular hydrogen bonding on the overall stability of the assembly. This may be achieved by immobilising quinones onto electrodes and investigating the nature of lateral interactions using cyclic voltammetry. Beyond its fundamental importance investigations of this type will provide a better understanding of the processes occurring at the metal / monolayer / electrolyte interfaces for development of analytical sensors.

Recently, several reports have been published dealing with the adsorption of quinones onto metal substrates.^{15, 16, 17, 18} Soriaga^{19, 20, 21} has published extensively in this area reporting on the adsorption, mode of binding, orientation, effect of solute concentration and temperature on a series of quinones.

In this contribution, we will discuss the electrochemistry of 1-amino-2-sulphonic-4-hydroxy-anthraquinone [AQNH₂SOH]. We will show this quinone to exhibit a wide range of interesting electrochemistry. For example, [AQNH₂SOH] forms an organic film on mercury surfaces, that exhibit unusually ideal electrochemical responses. When the bulk solution contains a high concentration of [AQNH₂SOH] the monolayers show extremely sharp spikes on the cathodic wave during voltammetry. In this chapter, we report on the possibility that changes in the degree of inter- and intra-molecular hydrogen bonding triggered by switching the oxidation state of the monolayer may be important in dictating this non-ideal voltammetric behaviour.

5.1 Apparatus and materials

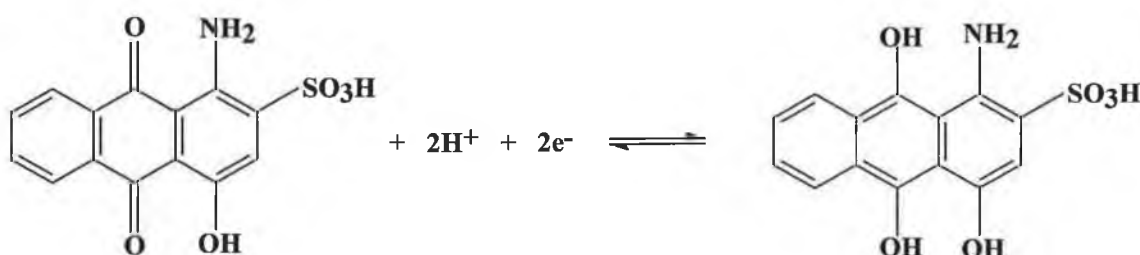
5.1.1 Apparatus

Cyclic voltammetry was performed using a CH instruments Model 660 electrochemical workstation, a PAR EG&G model 270 dropping mercury electrode and a conventional three-electrode cell. Potentials were measured against a potassium chloride saturated silver/silver chloride (Ag/AgCl) reference electrode. The auxiliary electrode was a platinum wire. For temperature dependent experiments a Julabo F10-HC refrigerated circulating bath, thermostated within ± 0.2 °C was used. All solutions containing [AQNH₂SOH] were thoroughly degassed by purging with nitrogen gas and kept free of oxygen by maintaining a blanket of nitrogen over the solution. The area of the mercury electrode was determined using the density of pure mercury (13.546 g cm⁻³) by dispensing, collecting, drying and weighing 100 drops of mercury. An electrochemical area of 0.0140 ± 0.0007 cm² was obtained. This area was also confirmed by recording cyclic voltammograms under steady state conditions using a solution phase probe of [Ru(NH₃)₆]²⁺.

5.1.2 Materials

1-amino-2-sulphonic-4-hydroxy-anthraquinone [AQNH₂SOH] (Scheme 1) was obtained from BASF and used as received. Deposition solutions were prepared using Milli-Q purified water and unless stated otherwise, the supporting electrolyte was 1 M HClO₄. Spontaneously adsorbed monolayers were formed by allowing the anthraquinone to adsorb onto the mercury electrode surface from electrolytic solutions, at the desired concentration, which was typically the micromolar range. At high bulk adsorption was (typically sub millisecond). At concentrations where sub-monolayer coverage was attained, repetitive cyclic voltammetry was performed until the peak current became independent of time. A scan rate of 5 Vs⁻¹ was used in cyclic voltammograms which is sufficiently fast to ensure that the current contribution from diffusion was less than 5% of the total current observed. For surface coverage experiments, repetitive cyclic voltammetry was performed until the peak currents observed in successive scans were identical.

Scheme 1



5.2 Discussion

5.2.1 General electrochemical properties of [AQNH₂SOH]

Figure 1 shows a cyclic voltammogram of a monolayer of 1-amino-2-sulphonic-4-hydroxy-anthraquinone [AQNH₂SOH] adsorbed onto a mercury electrode from a 1 μ M deposition solution in 1.0 M HClO₄. The coverage obtained from integration of the charge under the voltammetric waves is $6.8 \pm 0.1 \times 10^{-11}$ mol cm⁻². The voltammetry is consistent with that expected for a redox-active species immobilised on an electrode surface. For example, Figures 2 and 3 shows that the peak shapes are independent of scan rate, v , and that the peak height scales linearly with scan rate up to at least 50 Vs⁻¹, unlike the $v^{1/2}$ dependence for a freely diffusing species.²² Also, the slopes for the anodic and cathodic plots of both concentration of quinone are identical indicating that the kinetics of oxidation and reduction to be occurring on the same timescale. The responses shown in Figures 2 and 3 were also representative of those obtained for deposition solutions containing lower concentrations of [AQNH₂SOH] and those up to 1.5 μ M.

When equilibrium is established between the surface concentration of oxidised and reduced species adsorbed and the electrode potential the adsorbed monolayer should satisfy certain electrochemical conditions. They include a zero peak-to-peak splitting (ΔE_p) and a full width at half maximum (FWHM) of $90.6/n$ mV when n is the number of electrons transferred, where no lateral attractions or repulsions are observed between adsorbates.^{23, 24, 25} In these experiments at low coverage, ($<1.00 \times 10^{-10}$ mol cm⁻²), a ΔE_p of 0.017 ± 0.002 V and FWHM of 0.053 ± 0.003 V, 0.063 ± 0.008 V were observed for the cathodic and anodic branches, respectively. These values are consistent with the redox reaction proceeding by a two-electron transfer mechanism.^{26, 27, 28} Figure 4 shows the difference between the formal potential (E°) of the adsorbed complex, [AQNH₂SOH] and that of the solution phase species. The formal potentials are -0.068 V for the adsorbed species and -0.086 V for the solution species. That E° shifts in a positive potential direction upon surface confinement indicates that the reduced form is more strongly bound compared to the oxidised form.

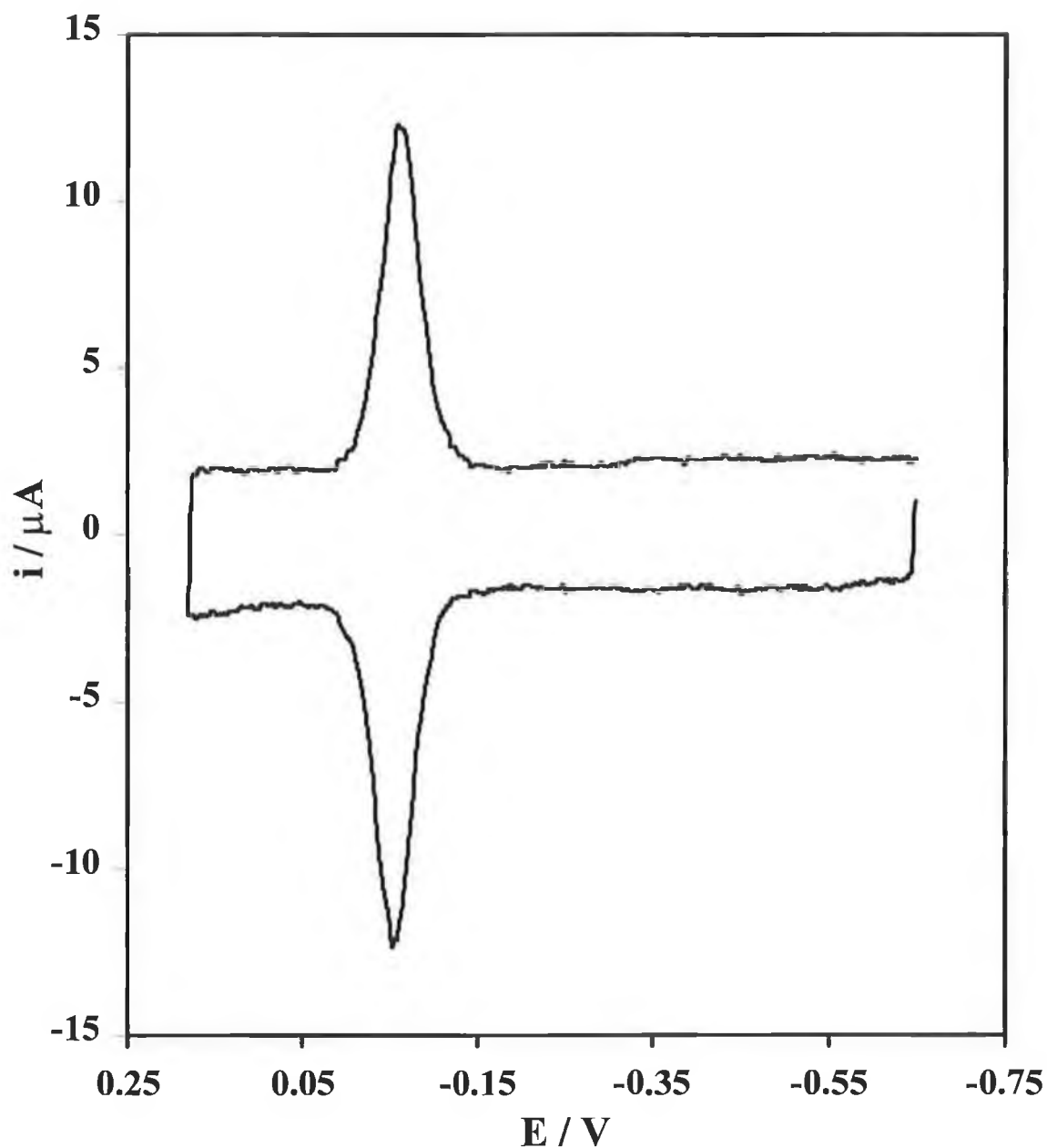


Figure 1 Cyclic voltammogram of a monolayer of [AQNH₂SOH] spontaneously adsorbed from a 0.5 μM deposition solution, in 1.0 M HClO₄. The scan rate was 5 Vs⁻¹ and the initial potential was 0.018 V. The surface coverage was calculated to be 6.8×10^{-11} mol cm⁻². The electrode area is 0.0134 cm².

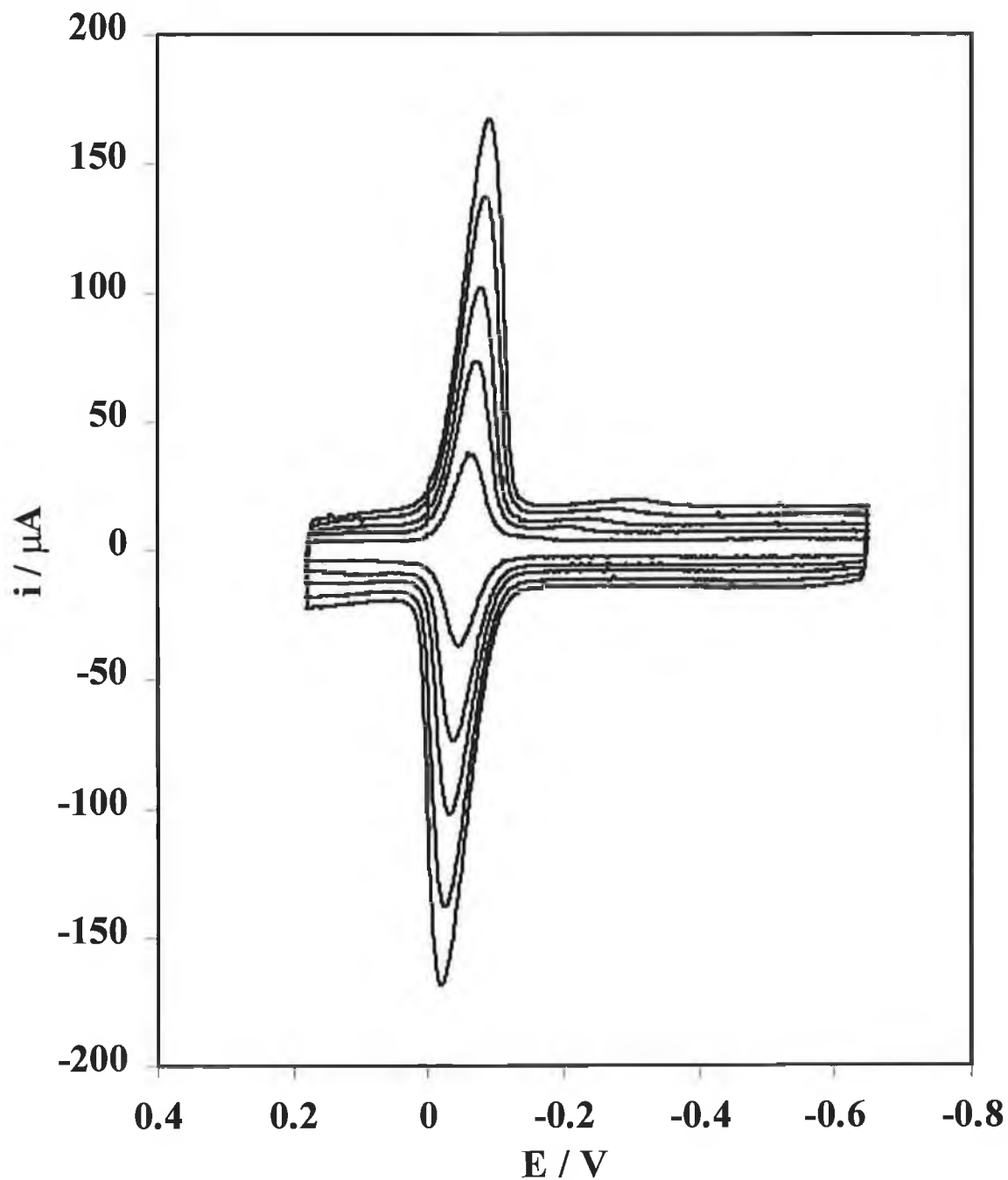


Figure 2 Cyclic voltammograms for a mercury electrode immersed in a 5 μM solution of $[\text{AQNH}_2\text{SOH}]$ in 1.0 M HClO_4 . Scan rates are from top to bottom, 50, 40, 33, 20 and 10 Vs^{-1} . The initial potential is -0.65 V .

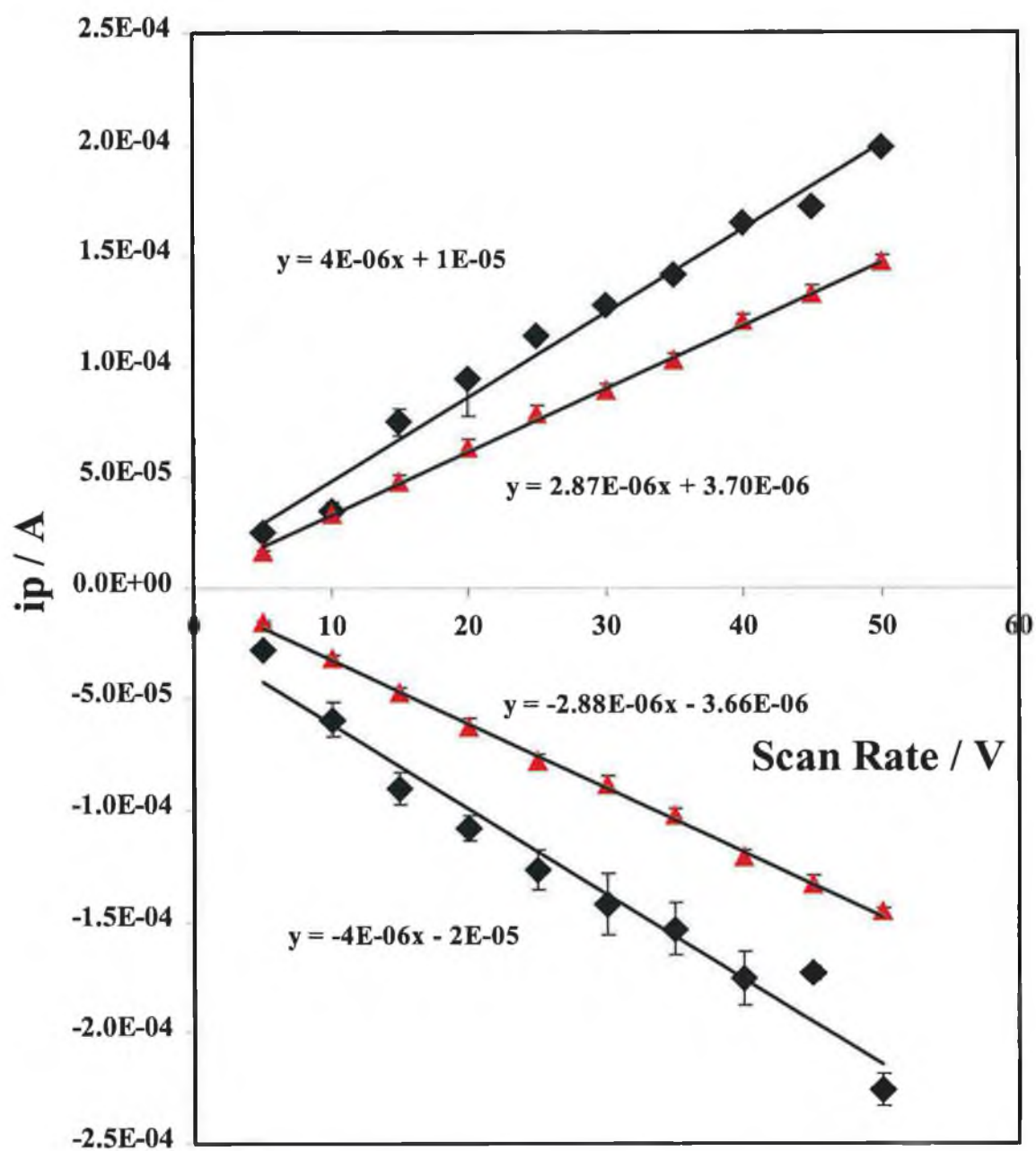


Figure 3 The effect of peak current for a 1 (○) and 5 μ M (◆) deposition solutions of [AQNH₂SOH] with increasing scan rate. Cathodic currents are up and anodic currents are down. The diamond symbols represent 1 μ M and the triangle symbols represent 5 μ M. The area of the electrode is 0.0134 cm².

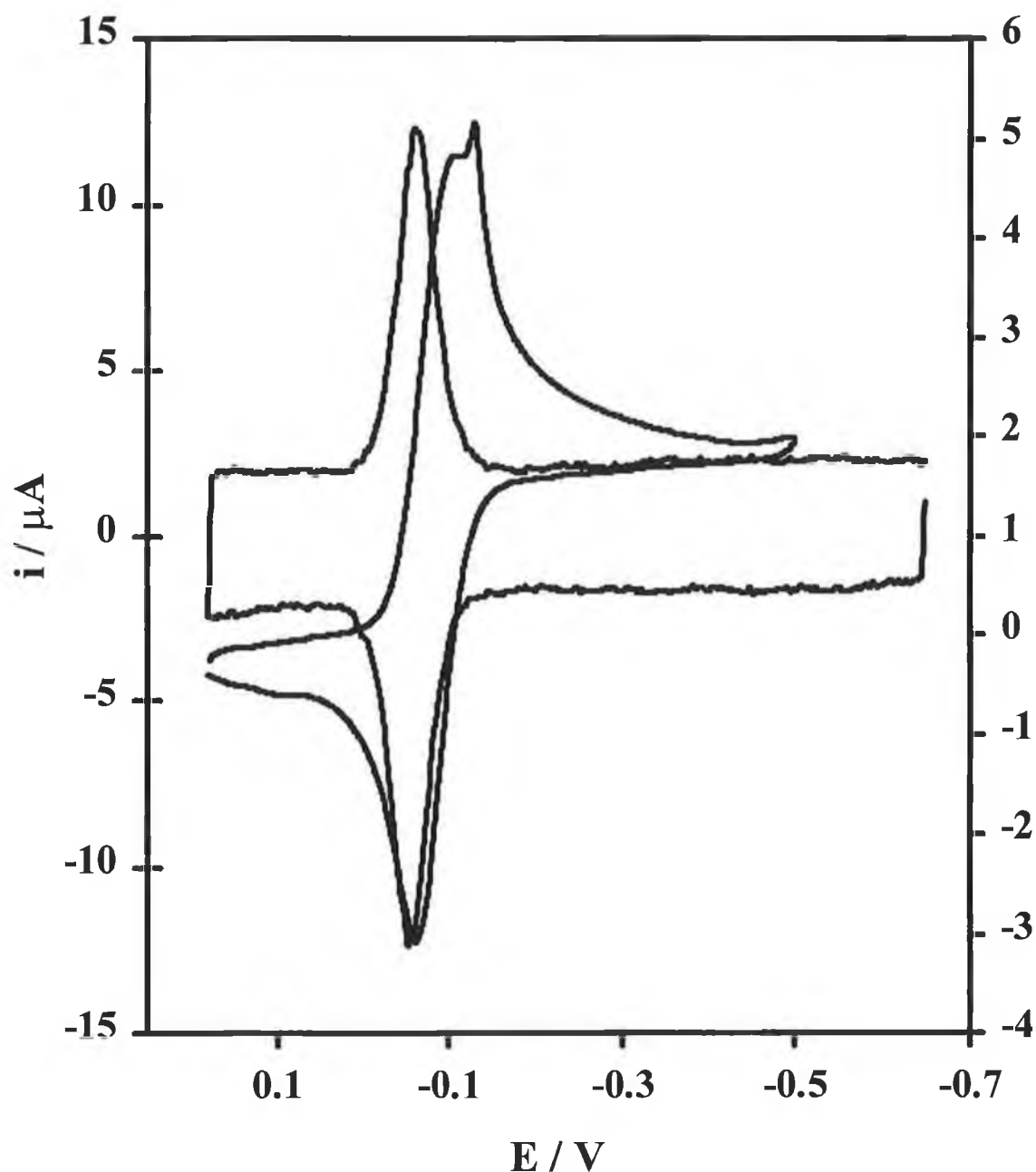


Figure 4 Solution phase and monolayer cyclic voltammograms for [AQNH₂SOH]. The monolayer was formed using a 1 μM deposition solution while the solution phase response was obtained for a solution of the quinone in the mM range. The scan rates for the monolayer CV is 5 Vs⁻¹ and 0.05 V s⁻¹ for the solution phase CV. The current scale is the same for both axis.

5.2.2 Effect of concentration on monolayers of [AQNH₂SOH]

Immobilising a quinone onto a metal support allows for the analysis of the interfacial layer residing between the electrode the electrolytic solution and results in the preconcentration of the analyte on the electrode surface. When the concentration of redox-active species changes on the electrode surface it is possible to determine the strength of adsorption, ΔG_s , the saturation coverage, Γ_{\max} , and lateral interactions.

An increase in the bulk concentration of the anthraquinone in the deposition solution results in a systematic increase in the quantity of species adsorbed until saturation coverage occurs. However, in the case of [AQNH₂SOH] the voltammetric peak shapes change significantly as the surface coverage is varied. For example, Figure 5 shows a cyclic voltammogram for a 3 μ M solution of [AQNH₂SOH] in 1.0 M HClO₄ showing that a *spike* occurs on the cathodic wave of the voltammogram. Figure 6 shows an overlay of cyclic voltammograms from sub-monolayer to saturation coverage. It may be seen that the spike develops in intensity as the concentration of the deposition solution increases. This sharp spike occurs at -0.043 V on the positive potential side of the anodic peak potential during oxidation of the adsorbed species. After the spike reaches its maximum value, the current decreases sharply back to the background charging current and no corresponding cathodic spike is observed during the reductive scan. However, the voltammetric peak is distorted (which may be seen in Figure 5) resulting in a change in the cathodic peak potential to 0.097 V. As the spike is very sharp, only a few milli-volts wide, it is most likely due to some surface phenomenon, as it is too narrow to be due to a diffusional process.²⁴

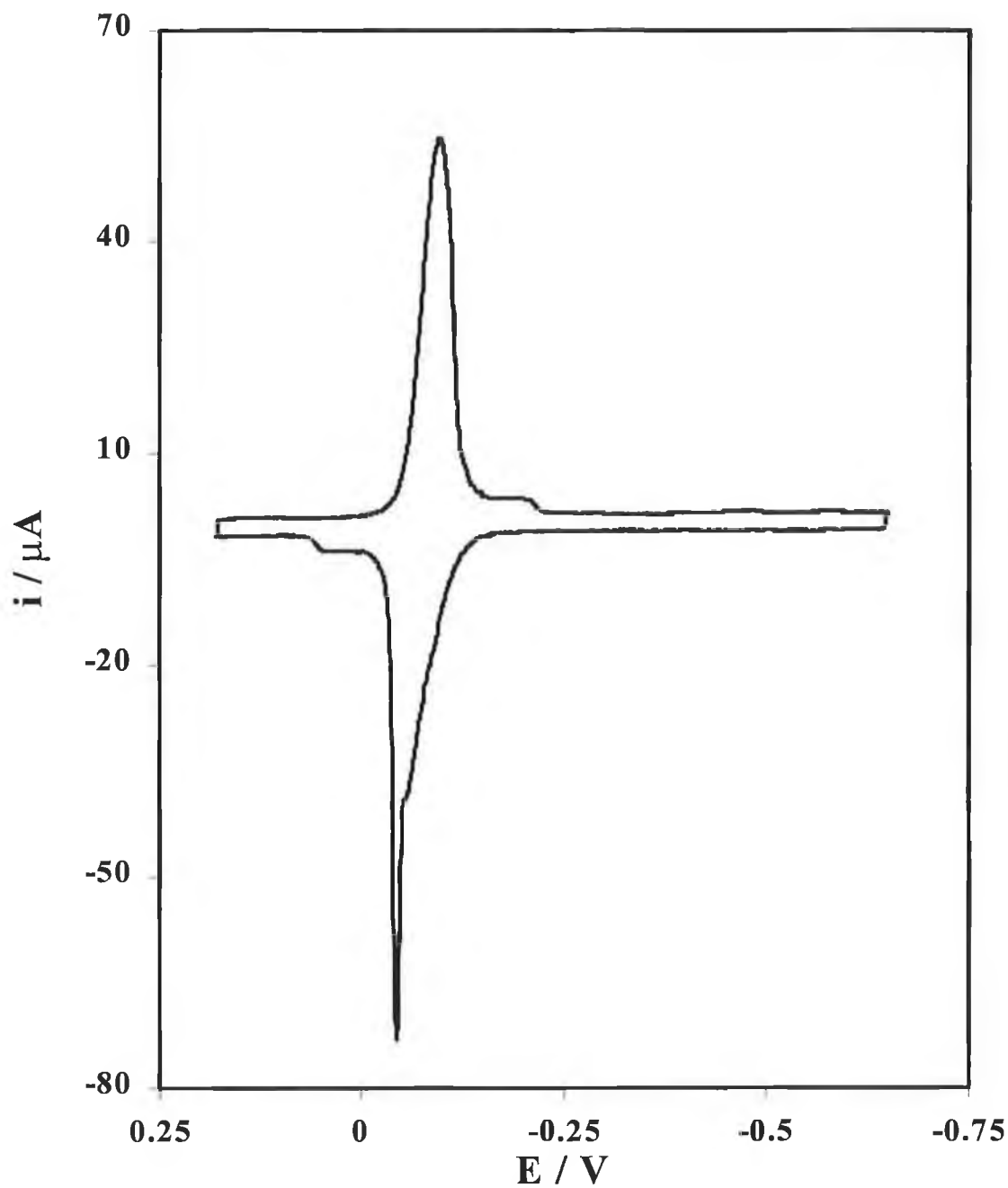


Figure 5 Cyclic voltammogram of a monolayer of [AQNH₂SOH] spontaneously adsorbed from a 5 μM deposition solution, in 1 M HClO₄. The scan rate was 5 Vs^{-1} and the initial potential was 0.018 V. The surface coverage was $1.7 \times 10^{-10} \text{ molcm}^{-2}$.

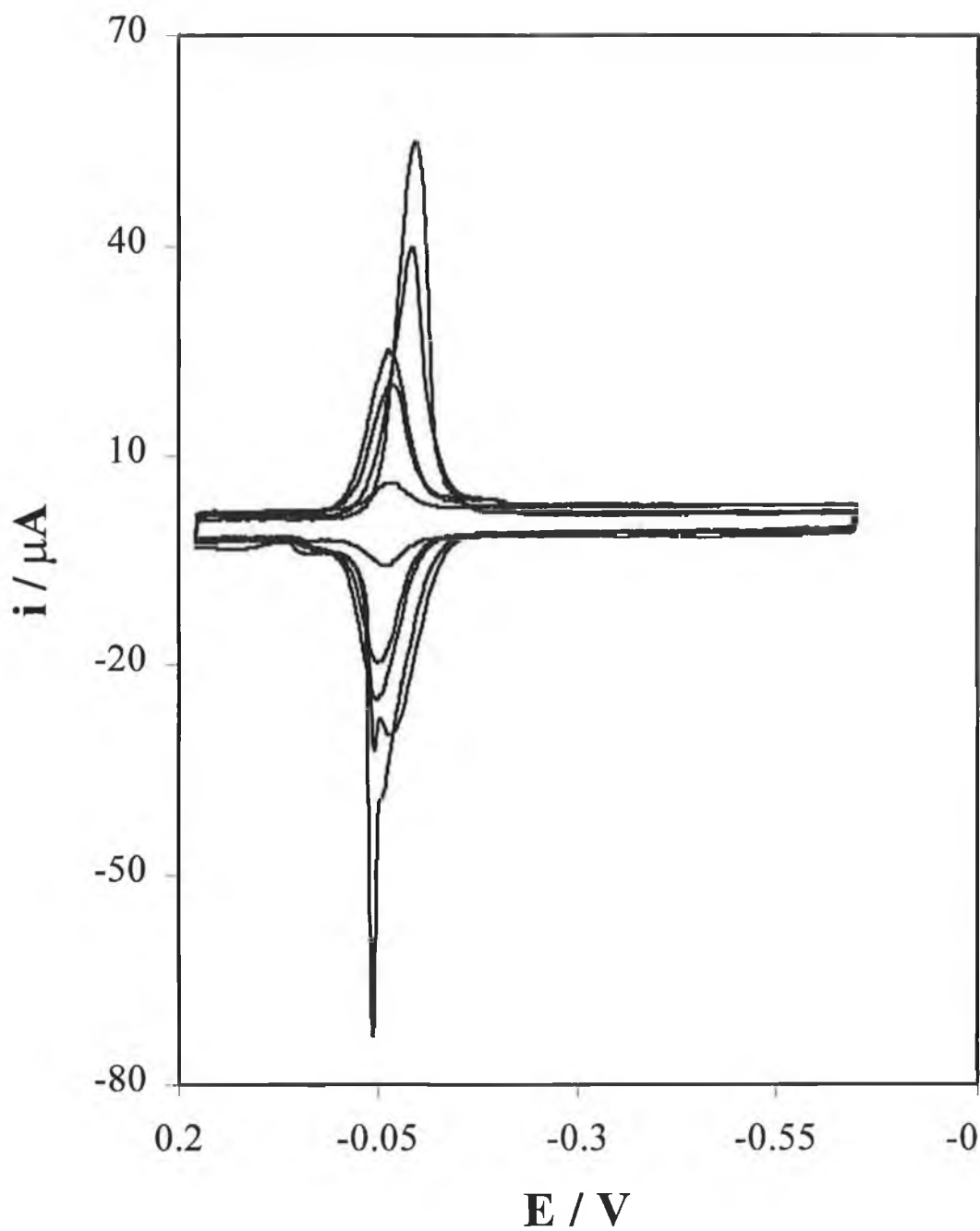


Figure 6 Dependence of the cyclic voltammetry observed for a mercury electrode on the concentration of $[\text{AQNH}_2\text{SOH}]$ in solution. The concentrations are from top to bottom, 3, 1.5, 1, 0.5 and 0.1 μM . The supporting electrolyte is 1.0 M HClO_4 . The scan rate is 5 Vs^{-1} . The electrode area is 0.0134 cm^2 .

The appearance of spikes in the voltammetry of quinones is not uncommon and has previously been reported by Anson,¹⁷ Mc Dermott⁶ and Faulkner.⁵ They performed investigations on mercury and graphite electrodes and all suggest the spike is due to changes within the adsorbed monolayer through hydrogen bonding interactions.

Initial observations showed the following properties of the spike; the formal potential of the adsorbed quinone changed on going from a monolayer where no spike occurred to one where a definite spike arose. The spike only occurred at surface concentrations approaching Γ_{sat} and concentrations greater than Γ_{sat} . Its magnitude increases linearly with scan rate but not with increasing concentration. The spike became more defined in shape with increasing concentration and the spike was pH dependent.

The development of the spike only occurs when the voltammograms were scanned in the negative potential direction. It is important to note that, since electron transfer is coupled to proton transfer in this system there is no change in the charge on the upon redox switch, thus eliminating electrostatic effects as the possible cause for such interactions. Therefore, why should the potential direction of scanning have a bearing on the voltammetric response of the redox active species? To elucidate the possibility that inter- and/or intramolecular hydrogen bonding or structural changes in the monolayer might be the origin of the unusual voltammetric response, a series of experiments were performed to probe the time dependence of the response and the data are illustrated in Figure 7.

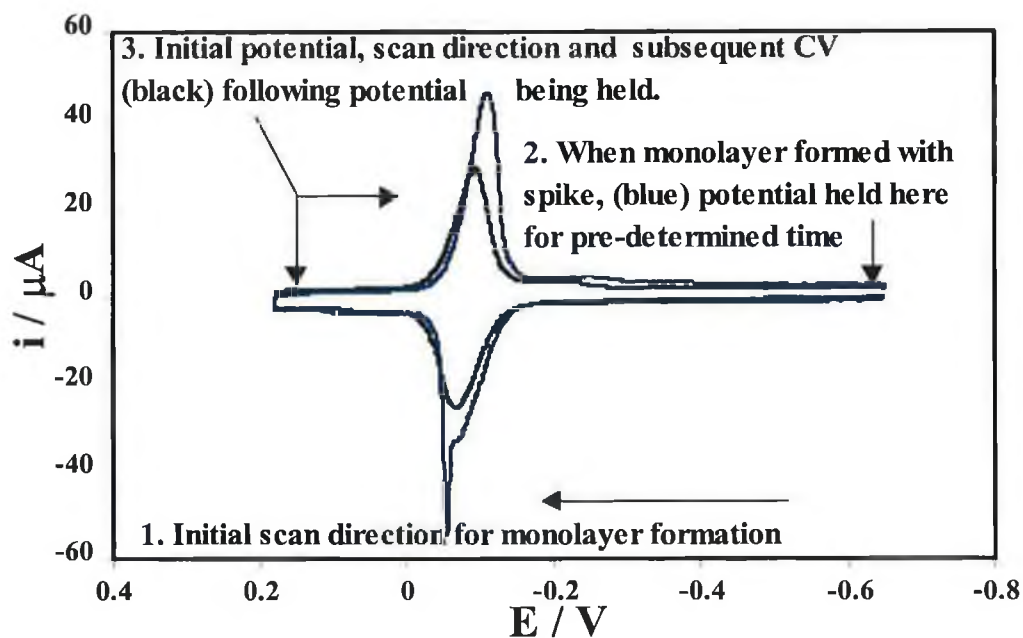


Figure 7 Illustration of the voltammetric response before and after a time delay is placed on the spiked voltammogram.

Initially a monolayer of [AQNH₂SOH] was formed from a 5 μ M deposition solution by scanning the potential in negative potential direction. This was performed to develop the spike. Using an in-built delay in the potentiostat, the current was held at a set potential for a period before continuing the voltammetric scan. The potential was delayed at -0.65 V from 60 to 10 seconds and the voltammogram run between potential limits of 0.18 and -0.65 . The effect on the cyclic voltammogram was as follows; a positive shift in the formal potential, the loss of the spike on the cathodic branch, a reduction in peak current and the return to the ideal voltammetry exhibited at low coverages. As-well as running the voltammetric scans after the time delay at the negative potential, the monolayer was also scanned in the positive direction, starting at 0.18 V. However, no change in the voltammetry was found. The fact that the spike disappears after holding the potential negative of the formal potential suggests a structural change occurs within the monolayer over time. The driving force for this structural change is probably redox state dependent attractive adsorbate-adsorbate interactions. Due to the limitations of the potentiostat, a time delay of less than 10 seconds was not available. Therefore, it was not possible to probe the

time-scale at which the re-organisational structural change occurred for the quinone adsorbed on the electrode surface.

5.2.3 Adsorption isotherms

5.2.3.1 The Langmuir Isotherm

The equilibrium surface coverage depends on the bulk concentration of the anthraquinone. To define the adsorption isotherm,^{22, 29} the surface coverages at equilibrium were determined by integration of the background corrected cyclic voltammograms for different bulk concentrations of the anthraquinone.

Figure 8 shows how the cyclic voltammetry for a mercury electrode immersed in 1.0 M HClO₄ changes as the concentration of the anthraquinone, [AQNH₂SOH], is varied between 0.5 and 3 μ M. In all cases, the adsorption was reversible, i.e., transferring the coated electrode into blank electrolyte caused the film to rapidly desorb. As monolayers of [AQNH₂SOH] exist in the oxidised form at the open circuit potential, isotherms were determined in both positive and negative scan directions. In this way, assuming that the surface coverage does not change during the voltammetric sweep, the effect of switching the oxidation state of the adsorbate on its free energy of adsorption can be investigated.

Figure 8 to Figure 10 show the data fit to the Langmuir isotherm, which assumes no lateral interactions between the adsorbates and that the limiting surface coverage is dictated simply by the size of the redox-active adsorbate. We show differences for our system using both the Langmuir and Frumkin isotherms since the quinone used here seems to be unusually Langmuirian until the saturation coverage is approached and distortions are seen in the voltammetry. We believe that there is a critical surface concentration beyond which lateral interactions become significant and deviations from the Langmuir isotherm are observed.

The Langmuir adsorption isotherm is described by the following expression:

$$\Gamma_i / (\Gamma_s - \Gamma_i) = \beta_i C_i \quad \text{Eq. 1}$$

where Γ_i is the surface excess of an adsorbed species i , Γ_s is the surface excess of species i at saturation, β_i is the adsorption coefficient and C_i is the bulk concentration. Equation 1 may be linearised to:

$$\frac{C_i}{\Gamma_i} = \frac{1}{\Gamma_{i,s} b_i} + \frac{C_i}{\Gamma_{i,s}} \quad \text{Eq. 2}$$

and a plot of C_i / Γ_i versus C_i should be linear with the slope providing the saturation coverage Γ_s and the intercept yields the adsorption coefficient. In this situation three such plots exist, the first Figure 8, representing the data points obtained when the cyclic voltammograms were scanned in a positive direction. The second and third Figure 9 and Figure 10 represent the data from scanning in the negative direction, cathodic and anodic, respectively. The reason two plots are examined is because of the differences in the cathodic and anodic branches of the cyclic voltammograms, i.e., when scanning took place in the negative direction a spike was noticeable in the cathodic branch only. It was not necessary to look at the anodic and cathodic branches individually when scanning was in the positive direction as the spike was not observed in these voltammograms.

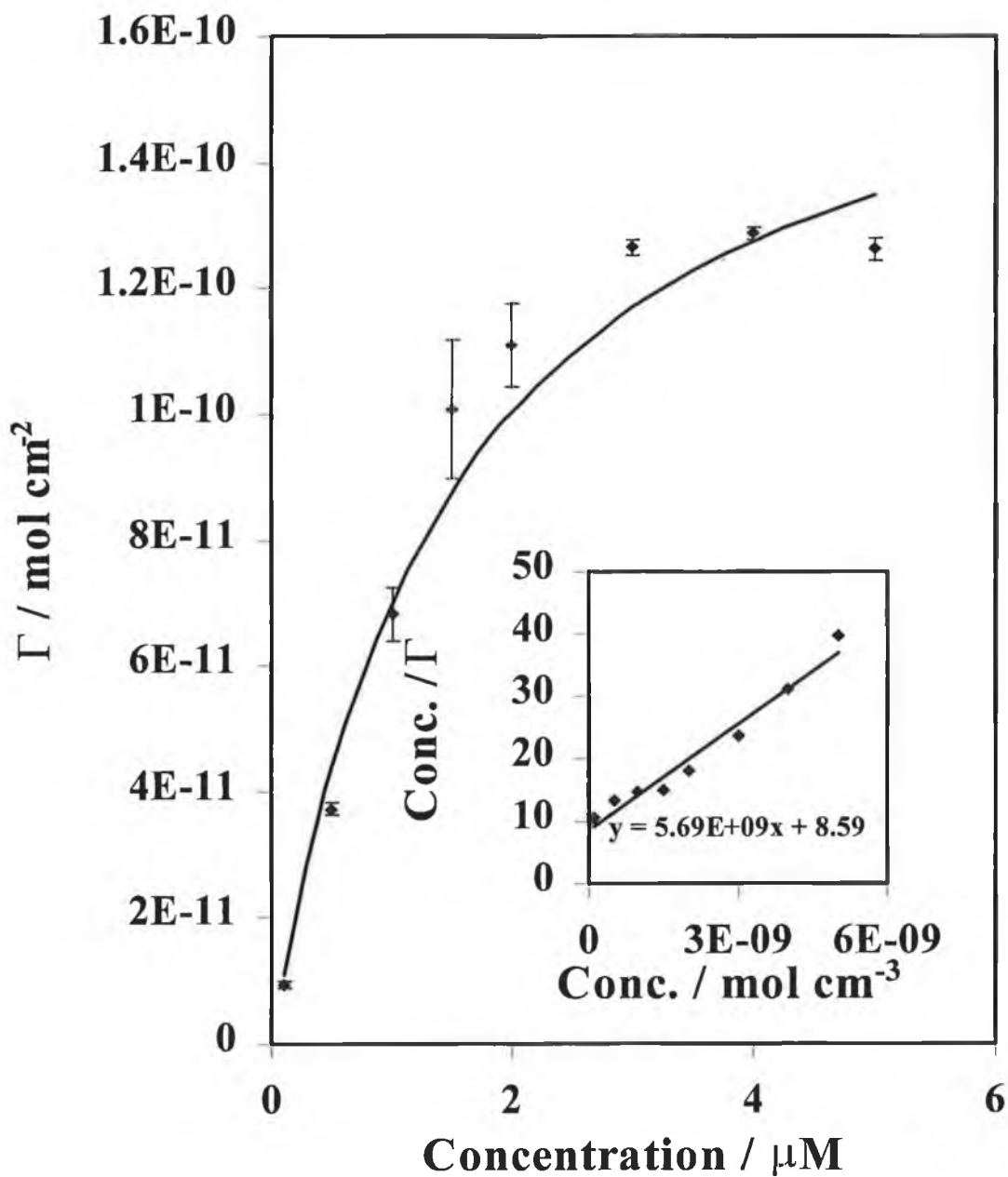


Figure 8 Dependence of surface coverage on the bulk concentration of [AQNH₂SOH]. The initial potential was -0.65 V. The solid line is the best fit to the Langmuir isotherm and the insert illustrates data plotted according to the linearised Langmuir isotherm. The supporting electrolyte is 1.0 M HClO₄. The area of the mercury electrode is 0.0134 cm².

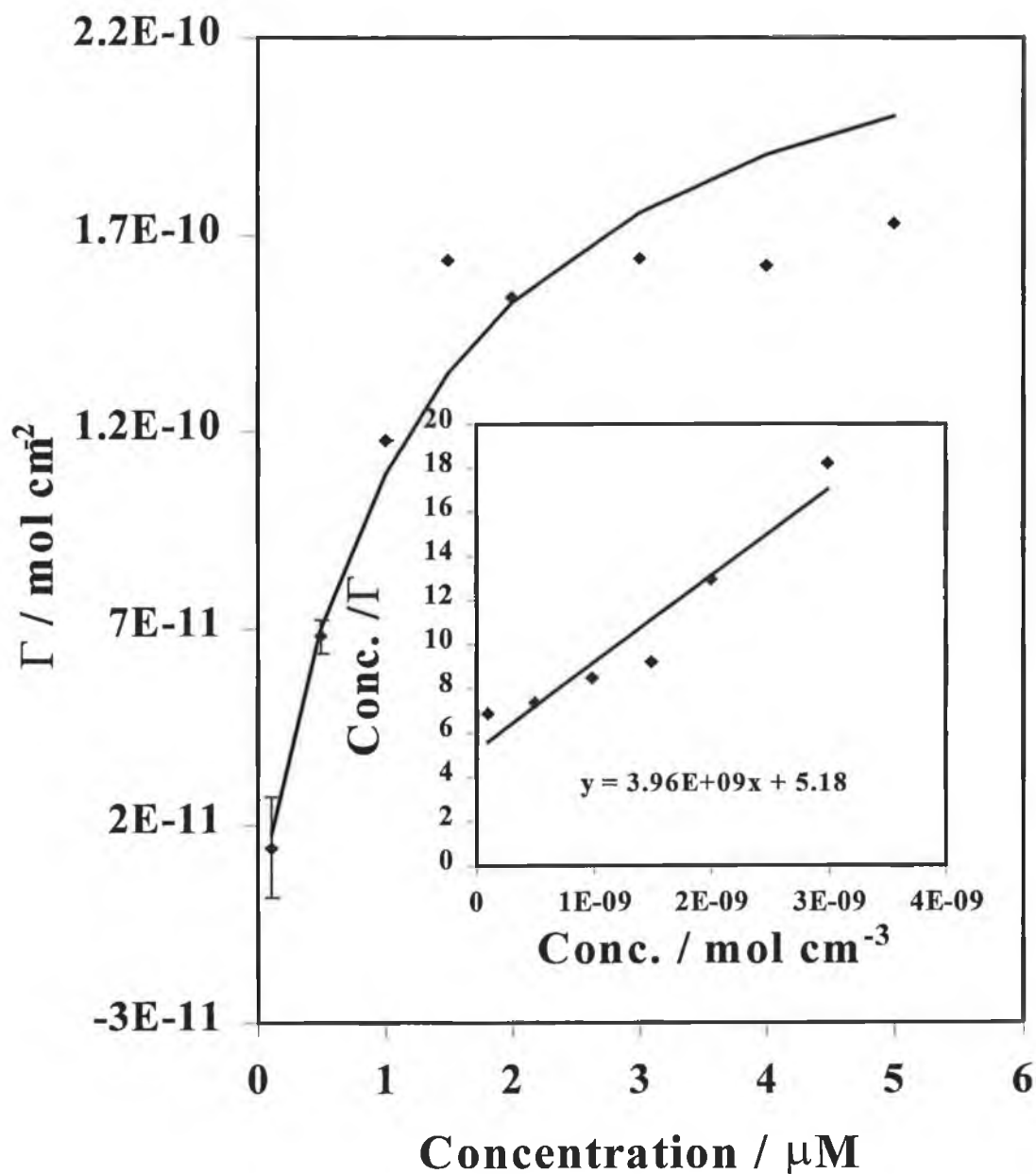


Figure 9 Dependence of the CATHODIC surface coverage on the bulk concentration of $[\text{AQNH}_2\text{SOH}]$. The initial potential was 0.18 V. The solid line is the best fit to the Langmuir isotherm and the insert illustrates data plotted according to the linearised Langmuir isotherm. The supporting electrolyte is 1.0 M HClO_4 . The area of the mercury electrode is 0.0134 cm^2 .

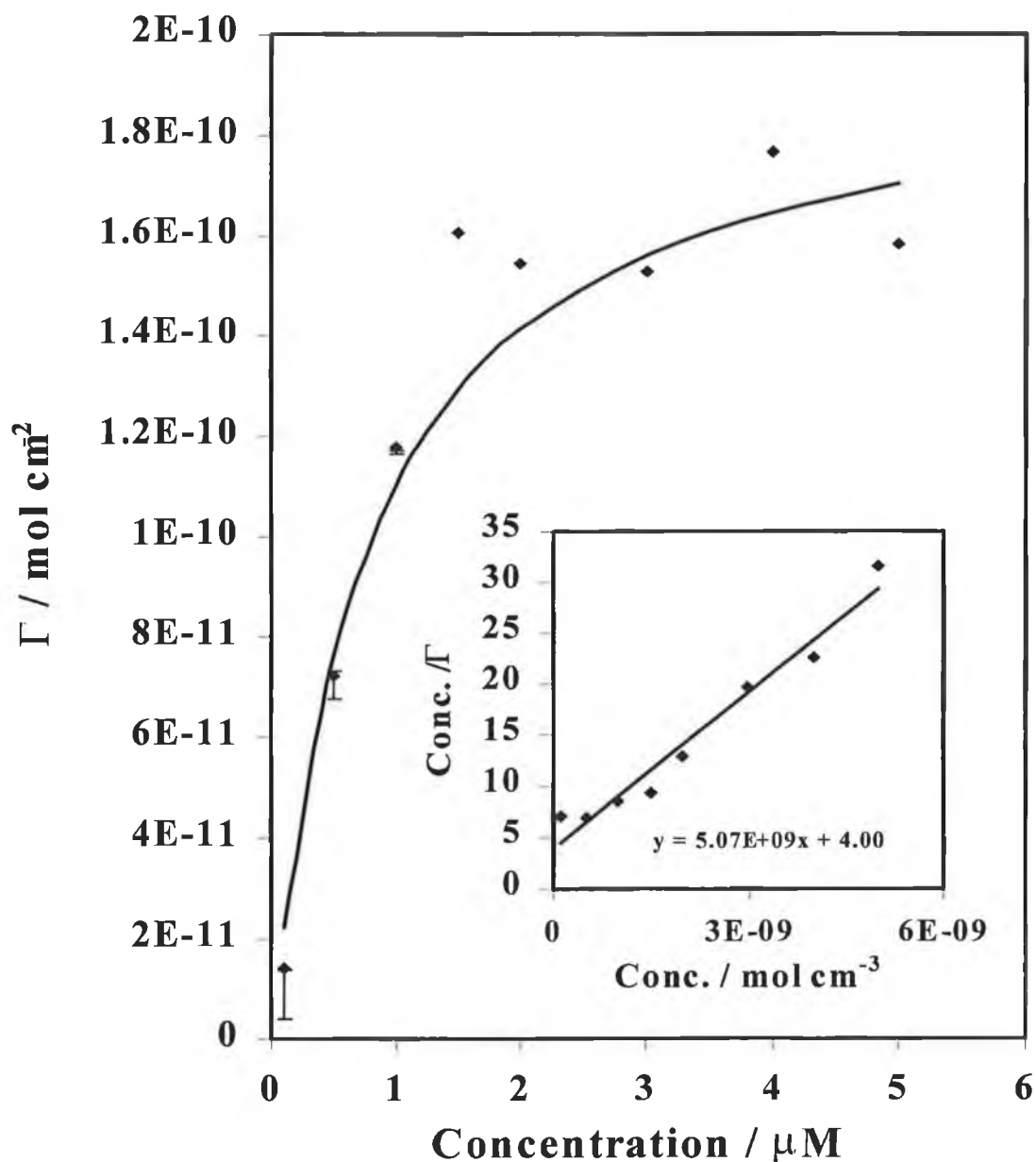


Figure 10 Dependence of the ANODIC surface coverage on the bulk concentration of [AQNH₂SOH]. The initial potential was 0.18 V. The solid line is the best fit to the Langmuir isotherm and the insert on each plot illustrates data plotted according to the linearised Langmuir isotherm. The supporting electrolyte is 1.0 M HClO₄. The area of the mercury electrode is 0.0134 cm².

The plots for the linearised form of the isotherm exhibit acceptably linear responses for [AQNH₂SOH] and were used to calculate Γ_{sat} and β . Table 1 contains these results for [AQNH₂SOH] in all situations presented. The solid lines in the adsorption isotherms are best fits to the Langmuir isotherm using the experimental data. Unsatisfactory agreement between the experimental data and theory suggest that for a monolayer of [AQNH₂SOH] adsorbed onto a mercury substrate and scanned in the positive direction, the Langmuir adsorption isotherm does not adequately describe the adsorption process. The case is the same for monolayers scanned in the negative direction. The fits are not in good enough agreement for the process to be described by the Langmuir isotherm and seem to deviate from adherence to the isotherm at a concentration where the voltammetric responses become distorted. This result suggests that possible adsorbate-adsorbate interactions depend not only on the concentration present in solution but on also the direction of scanning of the adsorbates and the time-scale involved. In order to probe the magnitude of these lateral interactions the experimental data was fitted to the Frumkin isotherm.

Using the determined β values and Equation 4 it is possible to determine the free energy of adsorption ΔG_{ads} . The Gibbs energy of adsorption is directly related to the equilibrium constant of the adsorption process. The values obtained include contributions from both activity effects and potential dependent adsorbate-electrode interactions. Table 1 contains these data;

$$-\Delta G_{\text{ads}} = RT \ln \beta_i \quad \text{Eq. 3}$$

Table 1 Γ_{sat} and β values determined from linearised plots of the Langmuir isotherm of monolayers of [AQNH₂SOH] and ΔG values calculated from the β values. Positive scanning is when scans are initiated at -0.65 V in the positive direction, while negative scans are initiated at $+0.18$ V in the negative direction.

	Positive potential scanning	Negative potential scanning Cathodic	Negative potential scanning Anodic
$\Gamma_{\text{SAT}} / \text{mol cm}^{-2}$	1.76E^{-10}	2.53E^{-10}	1.97E^{-10}
β / M^{-1}	6.62E^5	7.64E^5	1.27E^6
$\Delta G / \text{kJ mol}^{-1}$	-33.2	-33.6	-34.8

5.2.3.2 The Frumkin Isotherm

Figures 7 to 9 illustrate the dependence of the surface coverage on the concentration of [AQNH₂SOH] and show that significant deviations from the Langmuir isotherm are observed. This behaviour indicates significant interactions occur either between adjacent adsorbates or between adsorbates and metal electrode. At low coverage ($< 1.00 \times 10^{-10} \text{ mol cm}^{-2}$), all three isotherms exhibit excellent correlation to the Langmuir model. However, as the concentration of electroactive species on the surface approaches saturation coverage deviation occurs from a Langmuirian type system, indicating adsorbate-adsorbate interactions as the inter-site separation is reduced. With this in mind, the data were fitted to the Frumkin isotherm.^{22, 24, 29}

$$\beta_i C_i = \frac{\theta_i}{1 - \theta_i} \exp(g\theta_i) \quad \text{Eq. 4}$$

where $\theta_i = \Gamma_i / \Gamma_{\text{sat}}$, Γ_i is the saturation coverage of species i in mol cm^{-2} at a bulk concentration C_i , Γ_{sat} is the saturation coverage obtained at high bulk concentrations and β_i the adsorption coefficient. The Frumkin isotherm differs from the Langmuir isotherm by containing an interaction parameter (g), which allows for coverage dependent adsorbate-adsorbate interactions. Attractive interactions are indicated by $g < 0$ and repulsive interactions when $g > 0$.

Figure 11 shows the relationship between the experimental values and that predicted for a best-fit Frumkin isotherm. In this instance, scanning was performed in a positive potential direction where no spike was observed in the voltammogram. An improved fit was obtained using the Frumkin isotherm over that of the Langmuir isotherm (Figure 8), i.e., when coverage dependant interactions are considered. Table 2 contains the saturation coverages, adsorption coefficients and interaction parameters obtained from the best-fit Frumkin isotherm. The saturation coverages obtained from both isotherms are compatible to within 20% of each other and the adsorption coefficients agree within 15%. Typically the interaction parameter, g , for the Frumkin isotherm is ± 2 .²² Here the interaction parameter was determined to be -1.25 , indicating that attractive stabilising interactions are occurring between adsorbates on the electrode surface. This interaction parameter corresponds to an interaction energy value of -1.0 kJ mol^{-1} . This energy value lower than that typically associated with hydrogen bonding in solution where typical interaction energies are in the order of 20 kJ mol^{-1} .

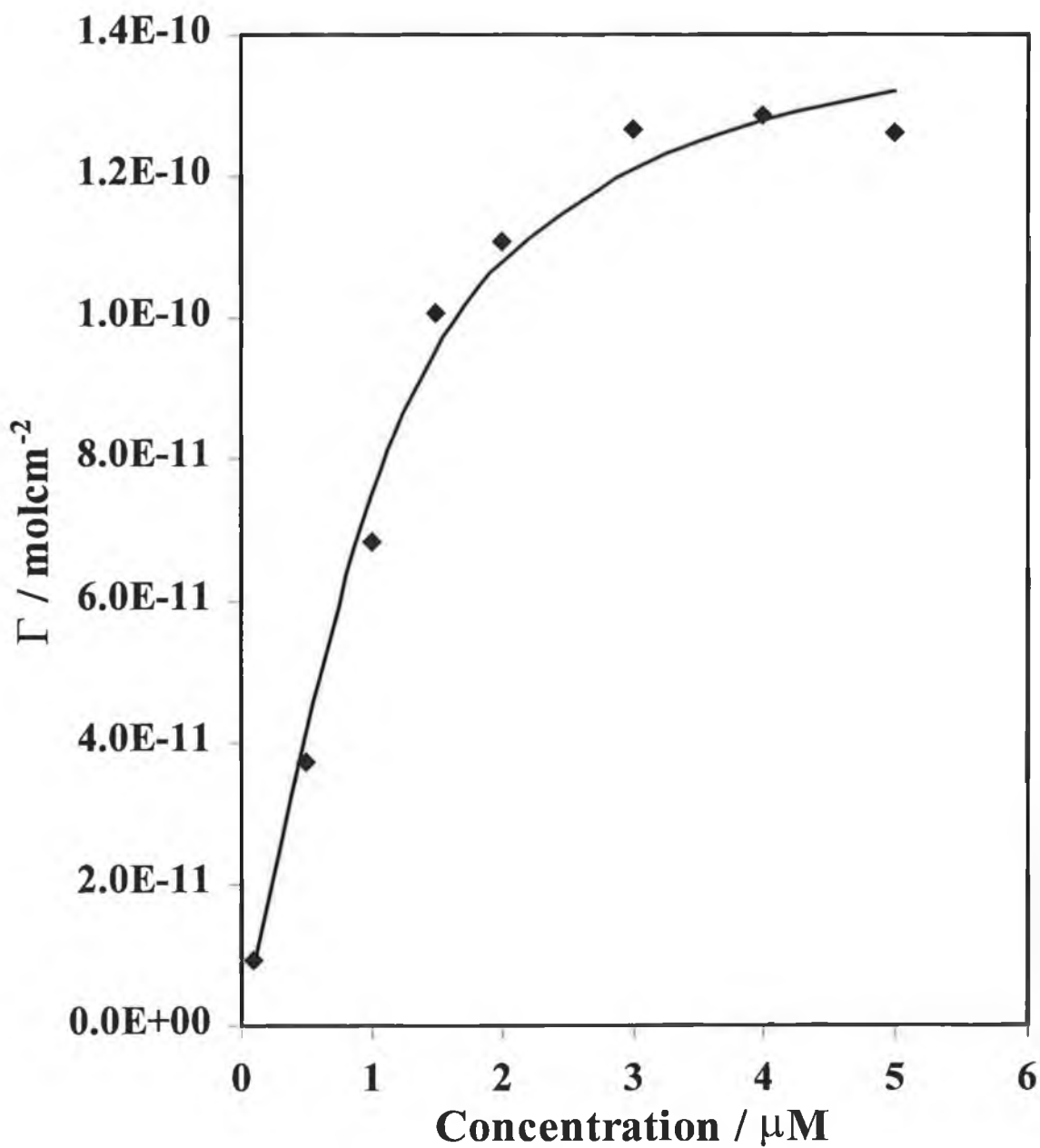


Figure 11 ♦ represents the dependence of $[\text{AQNH}_2\text{SOH}]$ with increasing concentration, where no spike was present in the voltammetry. The solid line represents the best-fit from the Frumkin isotherm using nonlinear optimisation.

Table 2 Saturation coverages, adsorption coefficients and Frumkin interaction parameters for 1, 2, 4-AQNH₂SOH.

	Spiked voltammogram	Non-spiked voltammogram
$\Gamma / \text{molcm}^{-2}$	1.60×10^{-9}	1.47×10^{-10}
β / M^{-1}	2.39×10^6	5.6×10^6
g	+ 18.6	- 1.25

The response when the Frumkin isotherm was fitted to the data where the spike was present in the voltammetric response may be found in Figure 12. An improved fit was obtained over the Langmuir isotherm. However, the fit was not ideal. As can be seen from Table 2 the saturation coverage obtained from the Frumkin Isotherm is $1.6 \times 10^{-9} \text{ mol cm}^{-2}$. This value seems extraordinarily high and suggests that multilayers instead of monolayers of [AQNH₂SOH] are adsorbing on the metal. An overlaid plot of a voltammetric response obtained from a 5 μM [AQNH₂SOH] solution which, may be found in Figure 13 does show a difference in area when the spike is present over one where ideal voltammetry is obtained. However, this difference is not of the order suggested by the best fit Frumkin isotherm. In fact there is only a two fold difference in area.

While the β values are similar with and without the presence of the spike, the interaction parameters are significantly different. An interaction parameter of 18.6 was determined from the Frumkin isotherm for data where a spike was present in the voltammetric responses. This value indicates highly repulsive destabilising interactions as would be expected for structural changes occurring on the electrode surface. Although the interaction parameter, β , corresponds to an energy parameter of 15 kJ mol^{-1} the magnitude of the g value of concern since the range²² of g is generally ± 2 . The Frumkin programme also calculated the concentrations, which can be seen in Figure 14.

The correlation of the Frumkin with the experimental concentration is excellent suggesting that the fitting procedure is accurate. In addition, when the data from the Langmuir isotherm was inserted into the Frumkin programme, no correlation was found to exist between the calculated and experimental concentration. Figure 15 shows such a response.

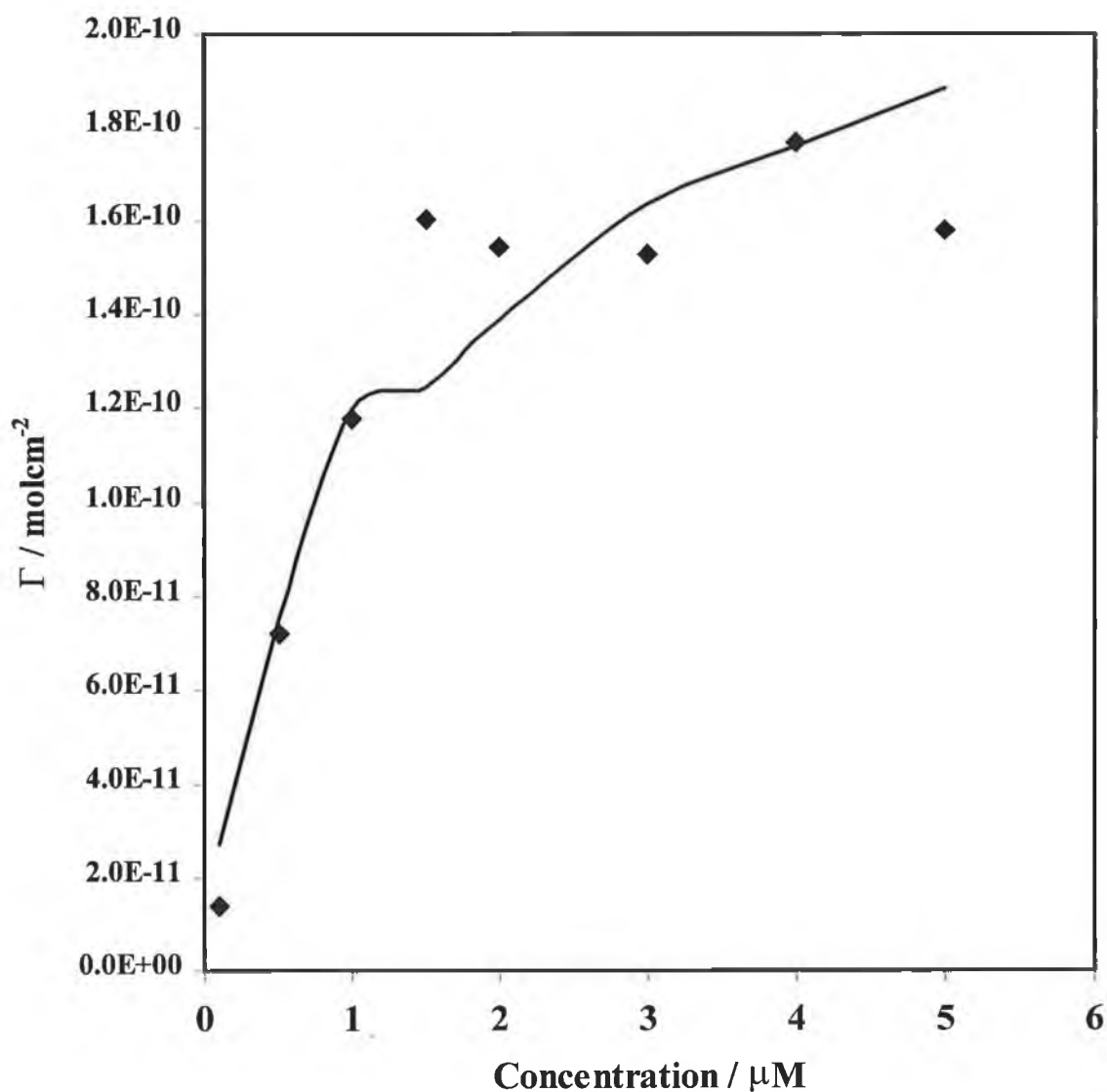


Figure 12 Dependence of the surface coverage ♦ on the bulk concentration of [AQNH₂SOH], where a spike was present in the voltammetry. The solid line represents the best-fit from the Frumkin isotherm using nonlinear optimisation.

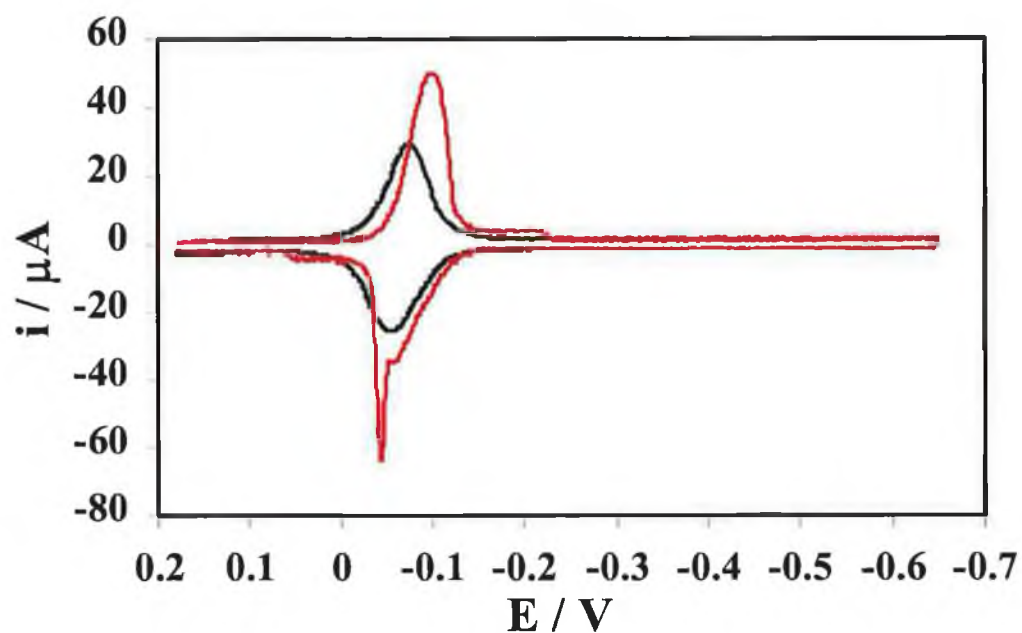


Figure 13 Cyclic voltammetric responses obtained from a 5 μM solution when the potential is scanned in the positive (black) and negative (red) direction. The electrode area is 0.0134 cm^2 .

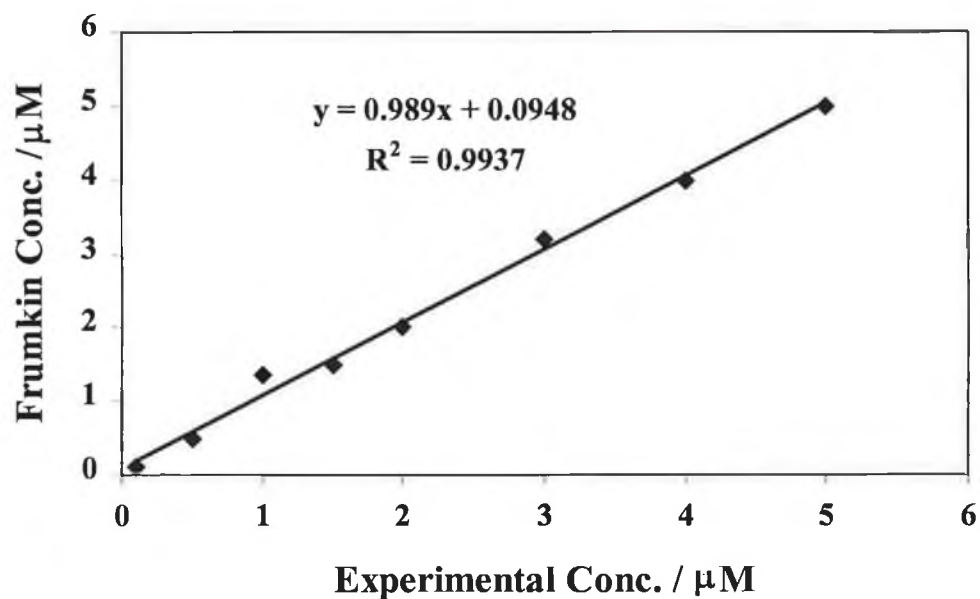


Figure 14 Correlation between the calculated Frumkin and the experimental concentrations.

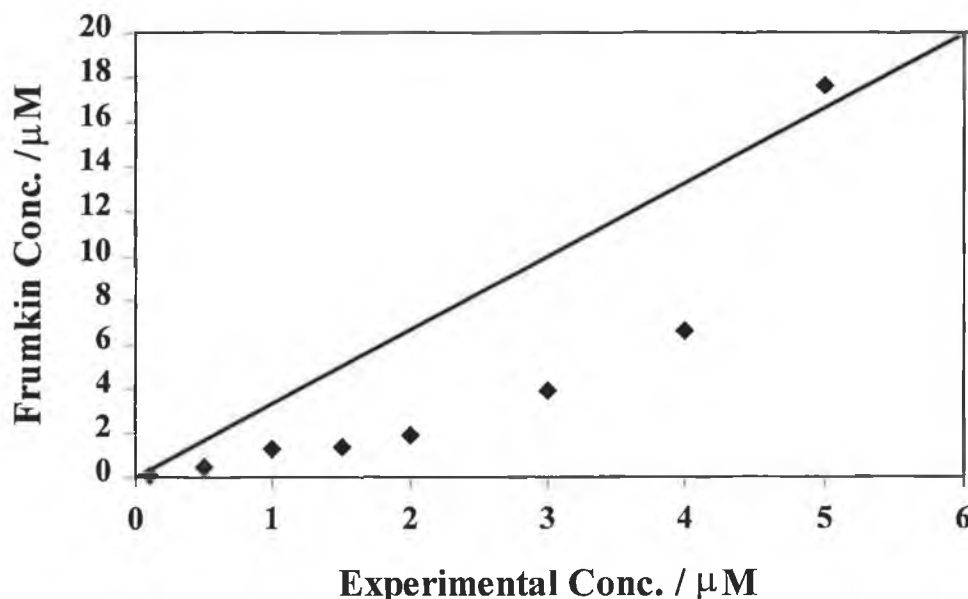


Figure 15 Correlation between the calculated concentrations from the Langmuir data using the Frumkin programme versus the experimental concentrations. An unbiased correlation is represented by the black line.

5.2.4 Origin of the non-ideal voltammetric response

The spike in adsorbed monolayers of $[\text{AQNH}_2\text{SOH}]$ occurs at surface coverages approaching saturation and above where the supporting electrolyte is 1.0 M HClO_4 and when the monolayer is converted from the hydroquinone to quinone form. It is at this point that the adsorbates may interact with each other due to their close molecular proximity as the inter-site separation between adsorbates has decreased. These interactions may take various forms such as, inter- and/or intra-molecular hydrogen bonding interactions or electrostatic interactions. However, intramolecular interactions are not expected to yield the coverage dependent responses observed. Moreover, since the adsorbates are neutral in both oxidised and reduced forms, changing electrostatic interactions are unlikely to explain the voltammetric properties of these layers.

If hydrogen bonding is the cause of the spike present in the voltammograms then increasing the concentration of adsorbates in the deposition solution should result in an increase in spike height due to reduced inter-site separation between adsorbates. Figure 16 shows such a response. An increase in spike height is seen. However, it does not increase linearly with

increasing adsorbate concentration. In order to further elucidate the likely inter- and intramolecular hydrogen bonding interactions, molecular modelling was performed using HyperChem.

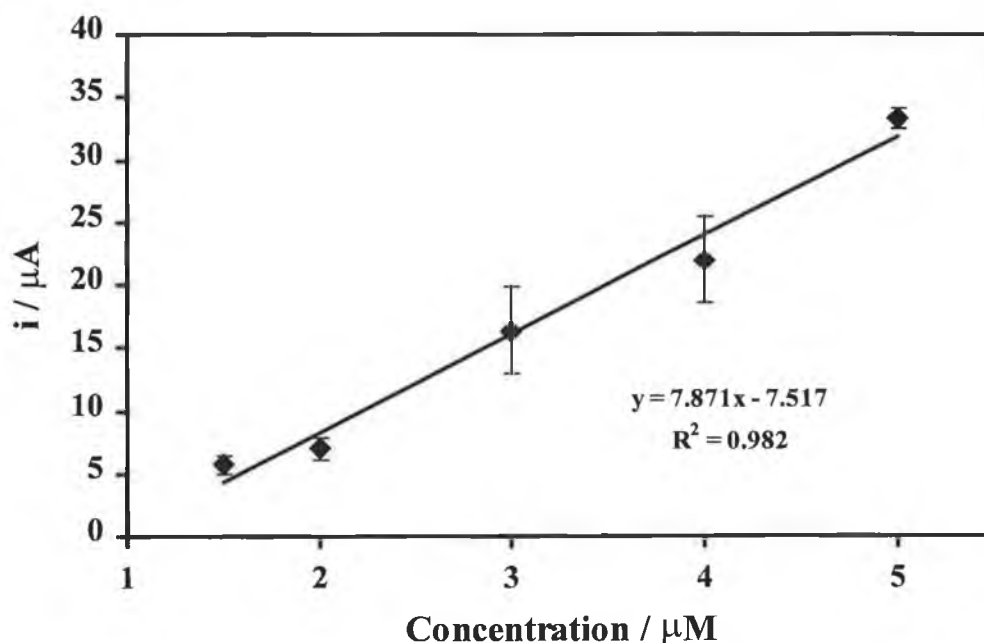


Figure 16 The effect of concentration on spike height. The sweep rate was 5 Vs^{-1} . Spike height was determined from the anodic peak maximum to the spike maximum.

5.2.5 Molecular modelling on [AQNH₂SOH]

The advent of computer technology has enabled computer packages such as HyperChem to model a wide variety of organic and inorganic species thus providing theoretical distances between moieties within molecules and between functional groups on different adsorbates.

Using the HyperChem package, the structure of [AQNH₂SOH] was to determine the extent of intra-molecular hydrogen bonding. This optimisation was performed on both the oxidised and reduced forms of [AQNH₂SOH] to calculate the extent and differences in the bond strengths of possible hydrogen bonding sites in each oxidation state, particularly between the following groups, C=O, NH₂, OH and SO₃H. Figure 17 represents the optimised structures using HyperChem for the quinone and hydroquinone form. The partial

charges of the oxidised and reduced forms of the quinone species can be found in Figure 18 which clearly show the attraction present for the groups where hydrogen bonding is most likely to occur. Figure 19 and Figure 20 represents the possible hydrogen bonding interactions both intra- and intermolecular for the hydroquinone and quinone form of the complex. The structure assumes that adsorption involves the formation of an ordered 2-D array. This assumption is consistent with results obtained by Mc Dermott *et al*⁶ whose recently observed linear domains within 2,6-AQDS monolayers formed on HPG electrodes using scanning force microscopy (SFM).

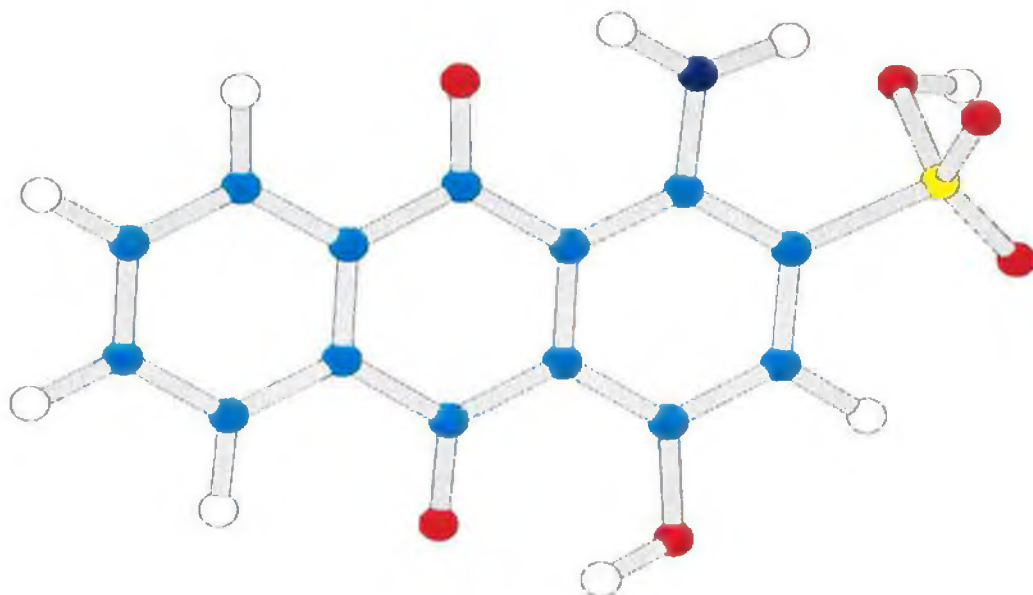
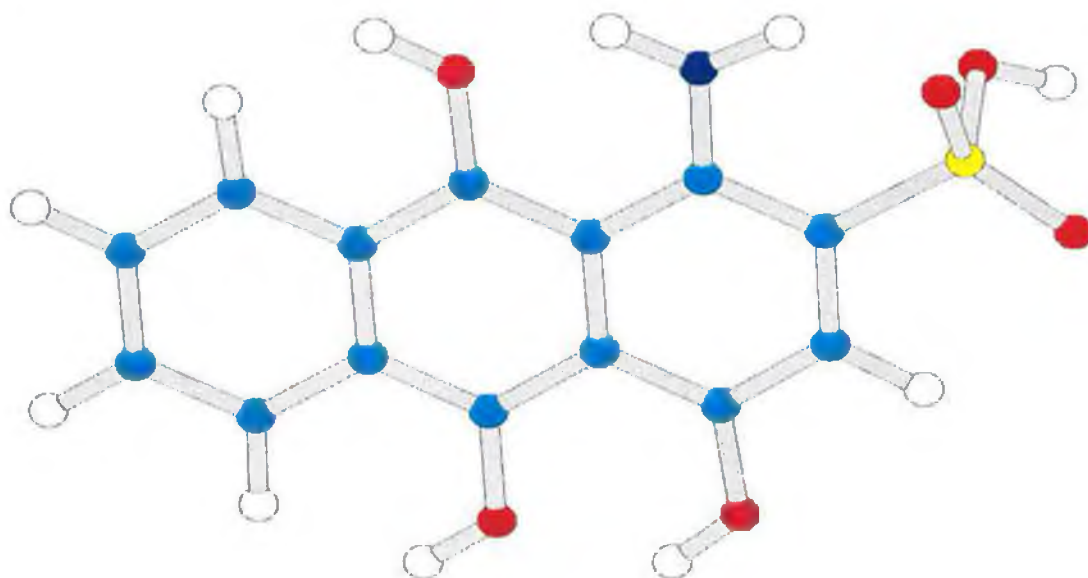
a**b**

Figure 17 Optimised structures for the quinone form (a) and hydroquinone form (b) of [AQNH₂SOH] using HyperChem.

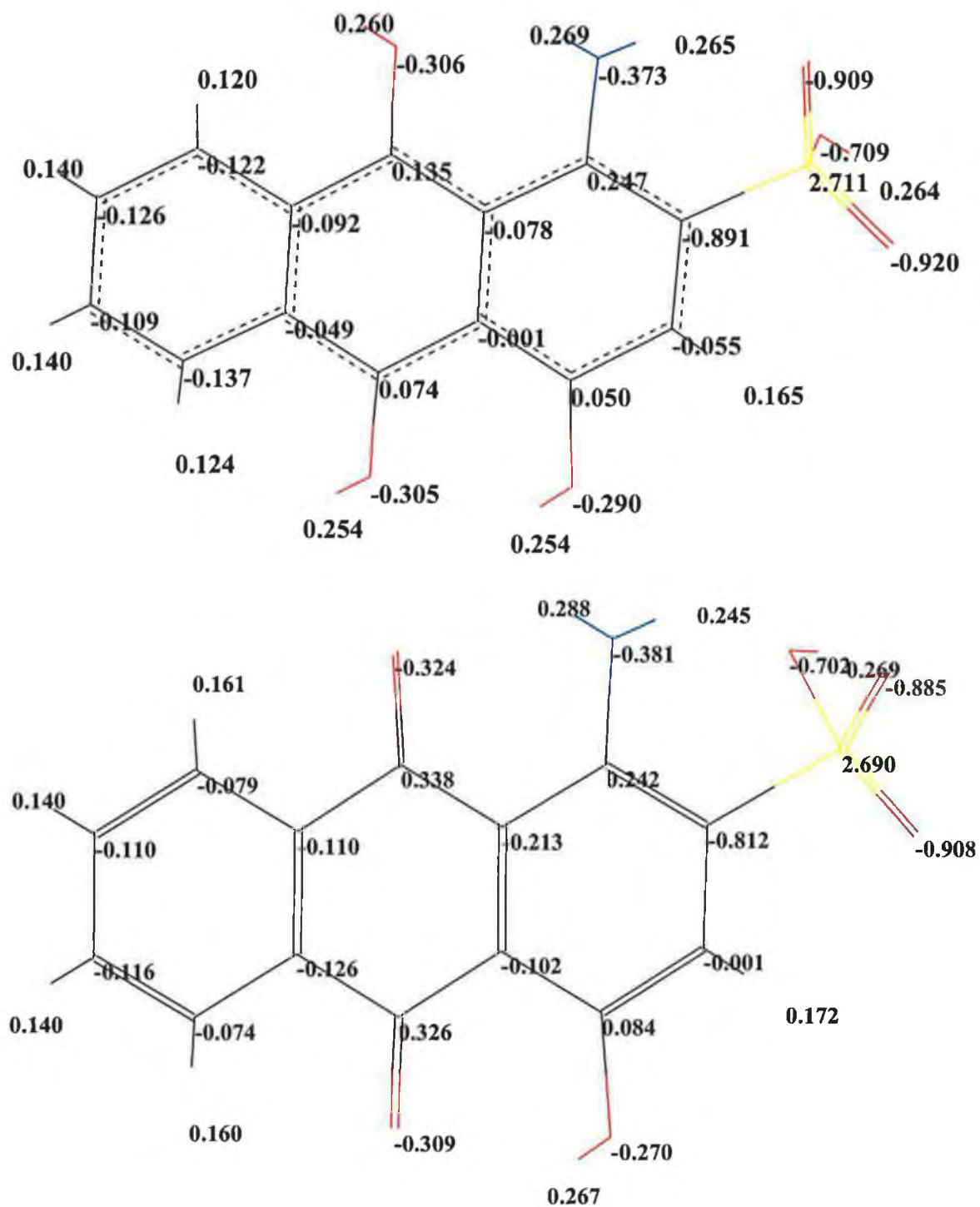


Figure 18 Partial charges for the oxidised (top) and reduced (bottom) forms of [AQNH₂SOH].

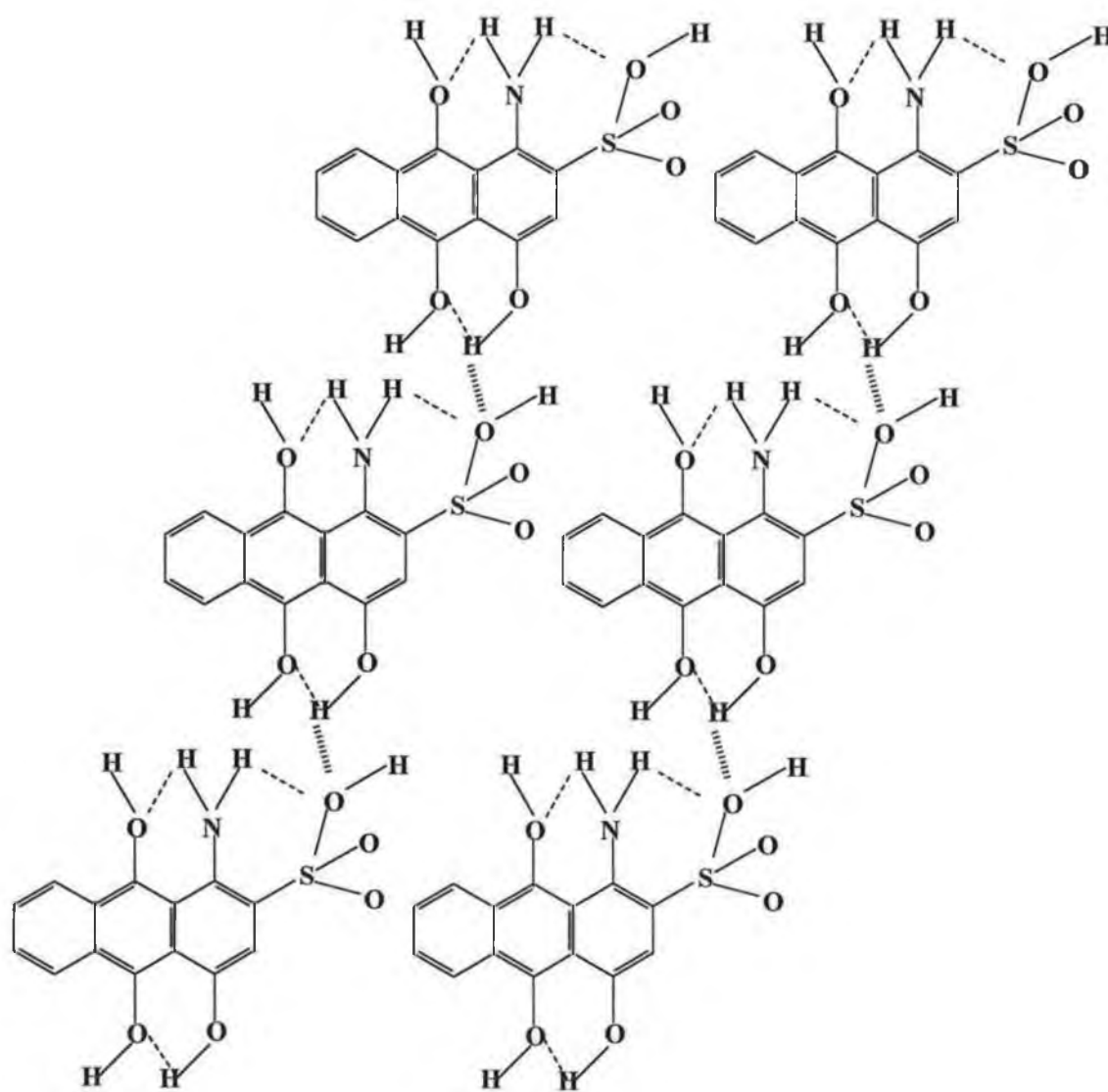


Figure 19 Linear structures proposed for intra- (thin dashed lines) and intermolecular (thick dashed lines) hydrogen bonding for the complex $[AQNH_2SOH]$ in the hydroquinone form.

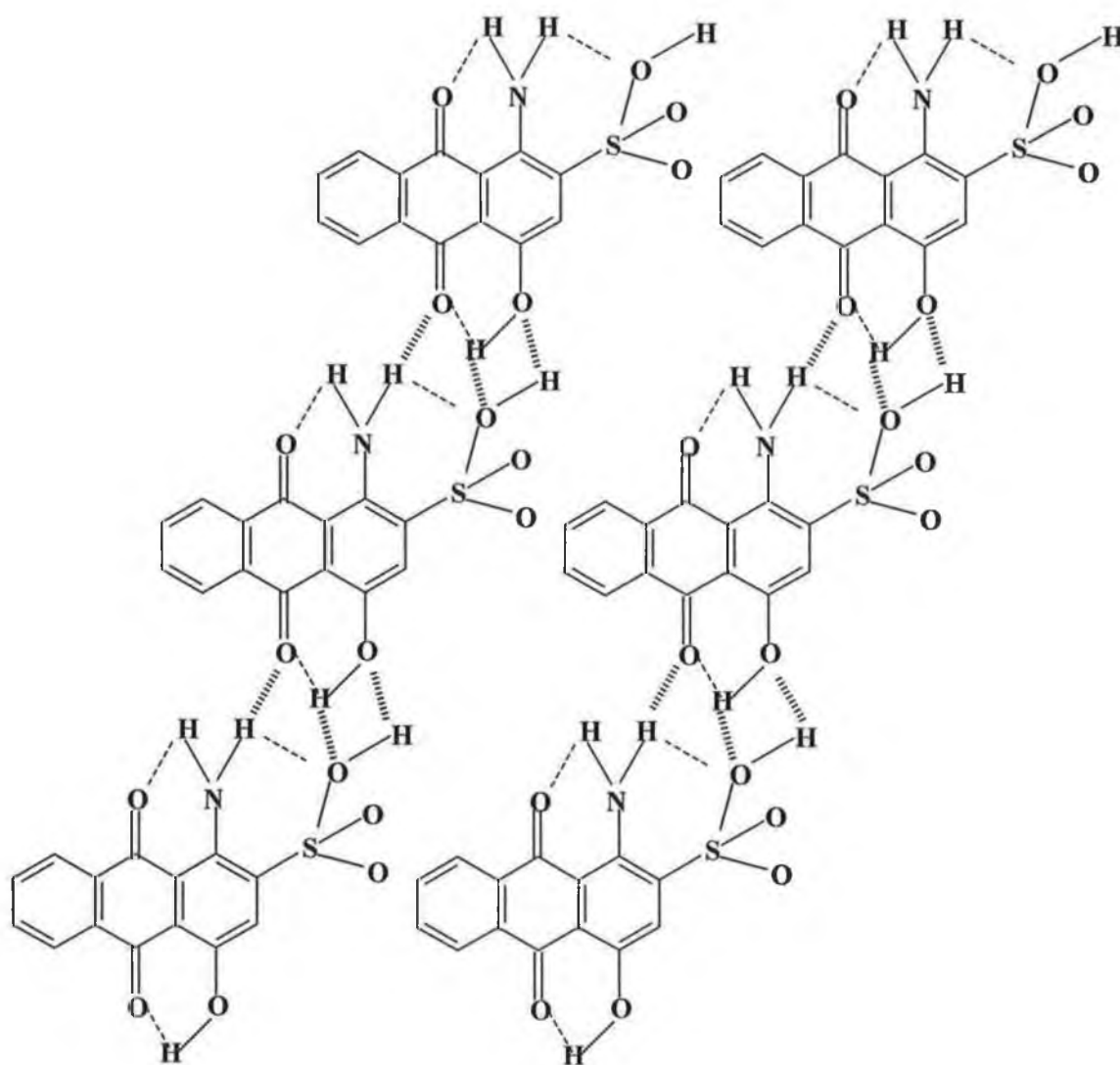


Figure 20 Linear structures proposed for intra- (thin dashed lines) and intermolecular (thick dashed lines) hydrogen bonding for the complex $[AQNH_2SOH]$ in the quinone form.

Table 3 Intra-molecular hydrogen bonding distances determined for the quinone and hydroquinone forms of [AQNH₂SOH] using HyperChem.

Hydrogen Bonding	Quinone form	Hydroquinone Form
	Distance / Å	Distance / Å
=O----OH	1.786	1.881
=O----NH ₂	1.741	1.722
NH ₂ ----SO ₃ H	2.171	1.973

From Figure 18 it can be seen that for the oxidised species there are three possible positions available for intra-molecular hydrogen bonding. First, between the carbonyl oxygen in the nine position with a proton from the amino group in the two position. Second, between the additional proton from the amino group with an oxygen molecule from the sulphonic group and third, between the proton from the hydroxy group in the four position with the carbonyl oxygen in the ten position. For the reduced species, the only difference in the chemical structure is the conversion of the carbonyl moieties at the 9 and 10 positions to hydroxyl moieties. It is still possible for hydrogen bonding to occur here between the oxygen in the 9 and 10 positions with one of the amino protons and the hydroxy proton, respectively. From Table 3 it can be seen that all distances observed in the positions stated for hydrogen bonding is within that expected 1.7-2.0 Å³⁰ with the exception of the amine-sulphonic acid interaction.

For the hydroquinone form, Hyperchem predicts intramolecular hydrogen bonding between three distinct pairs of functional groups. However, for the quinone form of the complex, hydrogen bonding occurred in only two positions with no hydrogen bonding between the amino proton and the sulphonic oxygen where the optimised distance was 2.171 Å, which

is rather too large to support hydrogen bonding. In the quinone form of the complex, the carbonyl group acts as a proton acceptor, while the amino and sulphonic groups act as proton donors and in the hydroquinone form all substituents act as proton donors. These differences in donor/acceptor properties may have an influence on the overall intramolecular distances between the substituents on the quinone complex. From these results it appears switching the oxidation state of the monolayer does affect the ability of the adsorbates to hydrogen bond.

HyperChem was also used to gain an insight into the extent of inter-molecular hydrogen bonding occurring in two-dimensions. This was achieved by strategically placing a series of complexes around each other. The results, however, were inconclusive as the structures re-orientated themselves from the two-dimensional network into a layered network. This occurred when modelling was performed in both the fully oxidised, fully reduced and partially oxidised/reduced forms.

The fact that the spike only appears at saturated surface coverages indicates the possibility that the major contributor to the overall interactions are inter-molecular rather than intra-molecular. This conclusion is reached on the basis that at low coverages when there is only the possibility of intra-molecular interactions between adjacent molecules of the quinone, no spike occurs. This is due to inter-site distance between adsorbates on the electrode surface being too far apart for inter-molecular interactions.

5.2.6 Orientational layout of structure

As-well as considering the effect of hydrogen bonding on the adsorbate one must not discount the possibility that the distorted voltammetry may arise as a result of a change in the orientation of the quinone on the substrate. Quinone molecules mainly adsorb with the aromatic ring parallel to the substrate, considered a flat orientation.^{19, 20, 21} However, some molecules adsorb edge on, through the substituents present on the ring or a combination of the latter two. The radius of [AQNH₂SOH], obtained from the optimised structure using HyperChem, is approximately 5.6 Å. This gives rise to an area of occupation per molecule of 98.5 Å², that is, 1.01×10^{14} molecules per cm². This corresponds to a theoretical saturation coverage for [AQNH₂SOH] 1.69×10^{-10} mol cm⁻² when adsorbed in a flat

orientation. There is excellent agreement between Γ_{sat} from the Frumkin adsorption isotherm which is $1.47 \times 10^{-10} \text{ mol cm}^{-2}$ and that predicted by theory.

It has also been observed that some organic molecules undergo a re-orientation from flat to edge plane with increasing concentration. Soriaga^{19,20,21, 31} recently published extensive work on numerous organic compounds, including anthraquinones showing certain organic molecules to be influenced by concentration, resulting in re-orientation of adsorbed species.

If re-orientation occurred in the [AQNH₂SOH] system in which the adsorbate re-orientated from co-planar to edge-on then an increase in the charge present under both the anodic and cathodic peaks should be observed due to the creation and subsequent filling of free area on the electrode surface. On the basis of molecular modelling, the saturation coverage of an edge on monolayer should be at least an order of magnitude greater than that observed for the complex adsorbed in a flat orientation. However, the increase in Γ observed for [AQNH₂SOH] when the spike occurs is not sufficiently large to be caused by molecular re-orientation and the theoretically surface coverage matched that found experimentally using the Frumkin isotherm. These observations lead us to believe that the process of re-orientation due to the effect of increasing concentration is not responsible for the distorted voltammetry of [AQNH₂SOH]. As there was no significant increase in the observed surface coverage and the experimental data satisfied the Frumkin Isotherm, the re-orientation from flat to edge plane may be effectively ruled out as the cause of the occurrence of the spike.

5.2.7 Proton dependence of surface confined [AQNH₂SOH]

Given that the non-ideal voltammetry most likely arises because of hydrogen bonding interactions and the known proton dependence of quinone electrochemistry^{5,17,32} monolayers of [AQNH₂SOH] were monitored in order to examine the effect of pH on the immobilised species. In these measurements, initial experiments were performed where coverage was low and no spike existed in the voltammetry. Subsequently, experiments were carried out in which the spike was present in the voltammetry. These analyses were performed in order to investigate the extent to which the proton concentration in solution

effects the adsorbed complexes and in particular the spike present in the anodic branch of the voltammetry.

At low pH, a negative linear shift in $E^{\circ'}$ with pH was observed for both situations which are illustrated in Figure 21 and Figure 24. The slope of the plot obtained from low coverage monolayers (Figure 21) was 69 mV/dec. A value within experimental error of that predicted by the Nernst equation (59 mV/dec.) for a redox reaction involving the transfer of equal numbers of electrons and protons.²² If intramolecular proton transfer were occurring between the sulphonate, amino and hydroxy groups then the formal potential would be independent of the proton concentration in solution. Figure 24 shows the effect of changing the pH from 1.03 to 4.1 on the spike present in monolayers of [AQNH₂SOH]. As the pH of the deposition solution is increased, not only does a negative shift in the formal potential of the monolayer occur, but also a linear decrease in the spike height is observed.

Since intramolecular proton transfer does not occur there must be interaction with the substituents on the aromatic rings and the protons in solution. With this mind the pK_a 's of the substituents were determined in order to see if beyond the known pH dependence of quinone / hydroquinone reaction, the pK_a 's of the functional groups present contribute to the observed behaviour. For [AQNH₂SOH], five dissociation constants were expected based on the structure (Scheme 1). The pK_a 's of [AQNH₂SOH] in order from low to high pH were $-SO_3H$, $-NH_2$, $-OH$ and the $C=O$ groups in the 9 and 10 positions. The order for the pK_a 's was assigned using relevant literature.³³ The pK_a of the $-SO_3H$ group was experimentally calculated to be 3.2 and is the only group to dissociate within the pH range tested. Therefore, protonation / deprotonation of the $-SO_3H$ group may effect hydrogen bonding within the monolayer framework contributing to the observed pH dependence of the voltammetric behaviour.

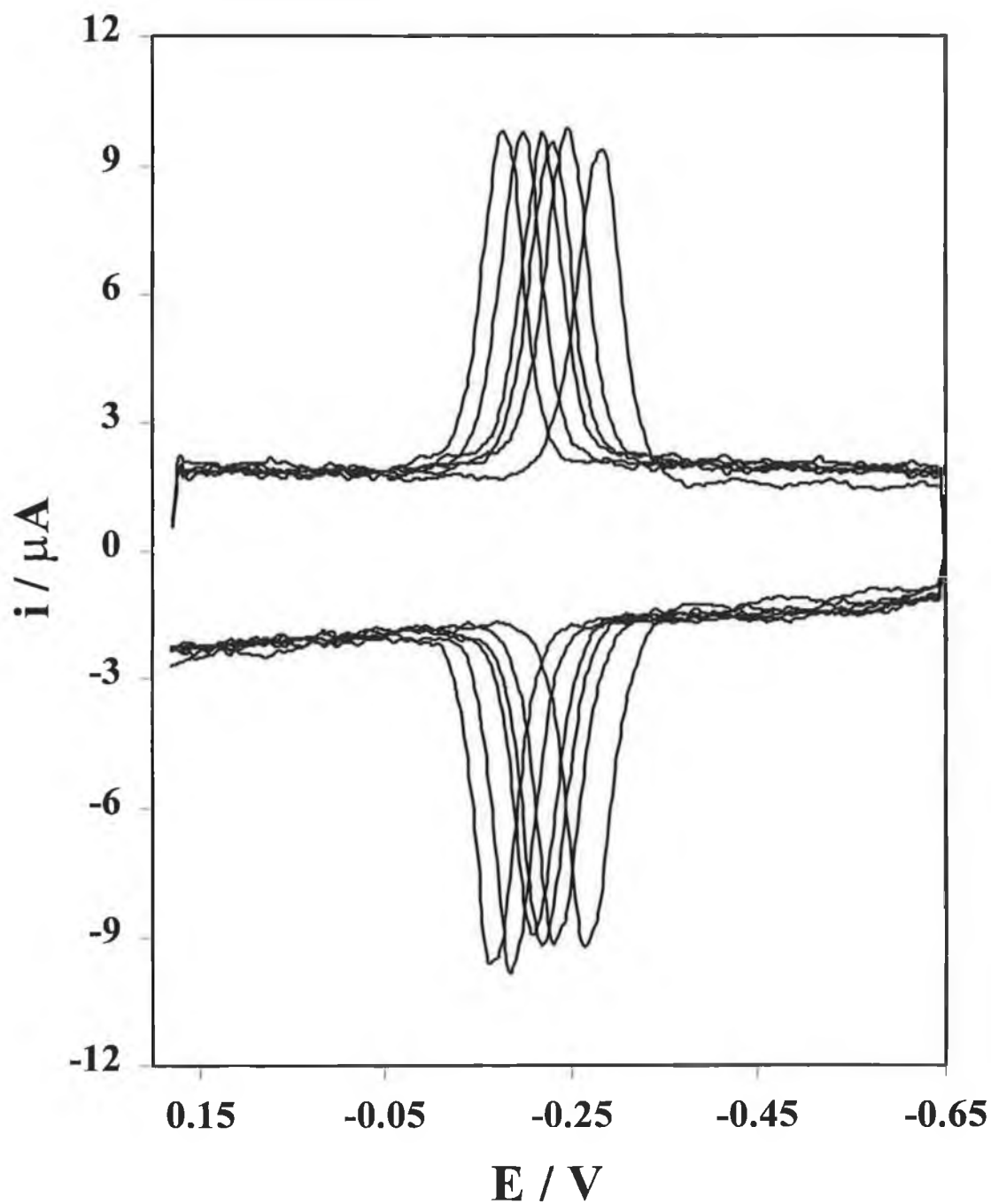


Figure 21 The effect on cyclic voltammograms from monolayers of [AQNH₂SOH] with pH. The pH of the solutions from which the CV's were obtained was, from left to right, 1.04, 1.30, 1.53, 1.73, 2.02 and 2.56.

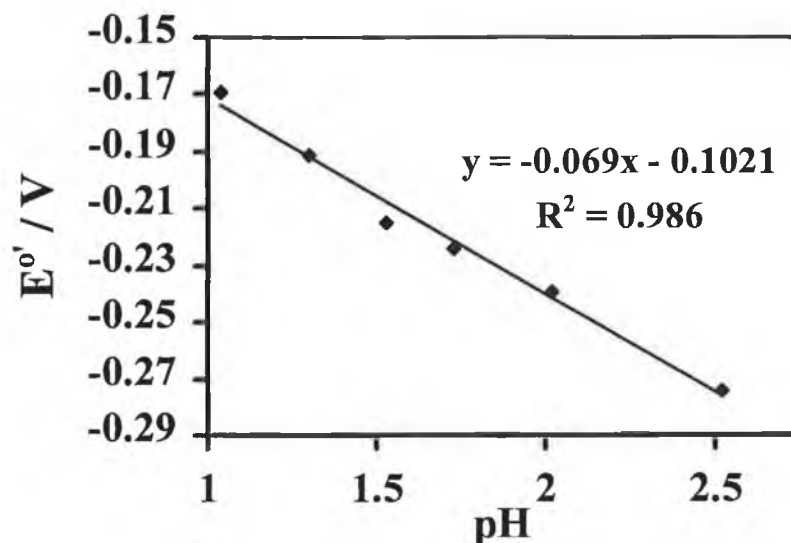


Figure 22 The effect on the formal potential of the quinone / hydroquinone reaction when the surface coverage is below saturation. Monolayers were formed from 1 μM deposition solutions in 1.0 M HClO_4 . The scan rate is 5 Vs^{-1} .

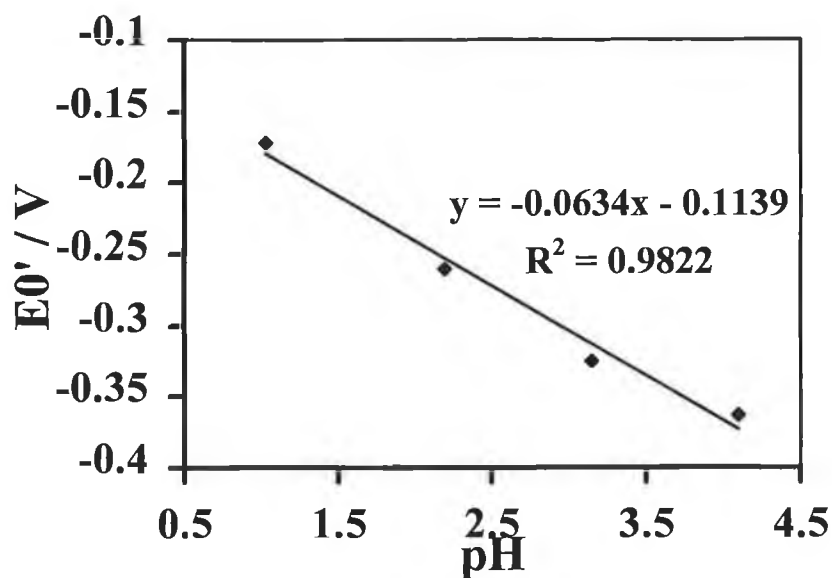


Figure 23 The effect on the formal potential of monolayers of $[\text{AQNH}_2\text{SOH}]$. Monolayers were formed from 5 μM deposition solutions in 1.0 M HClO_4 . The scan rate is 5 Vs^{-1} .

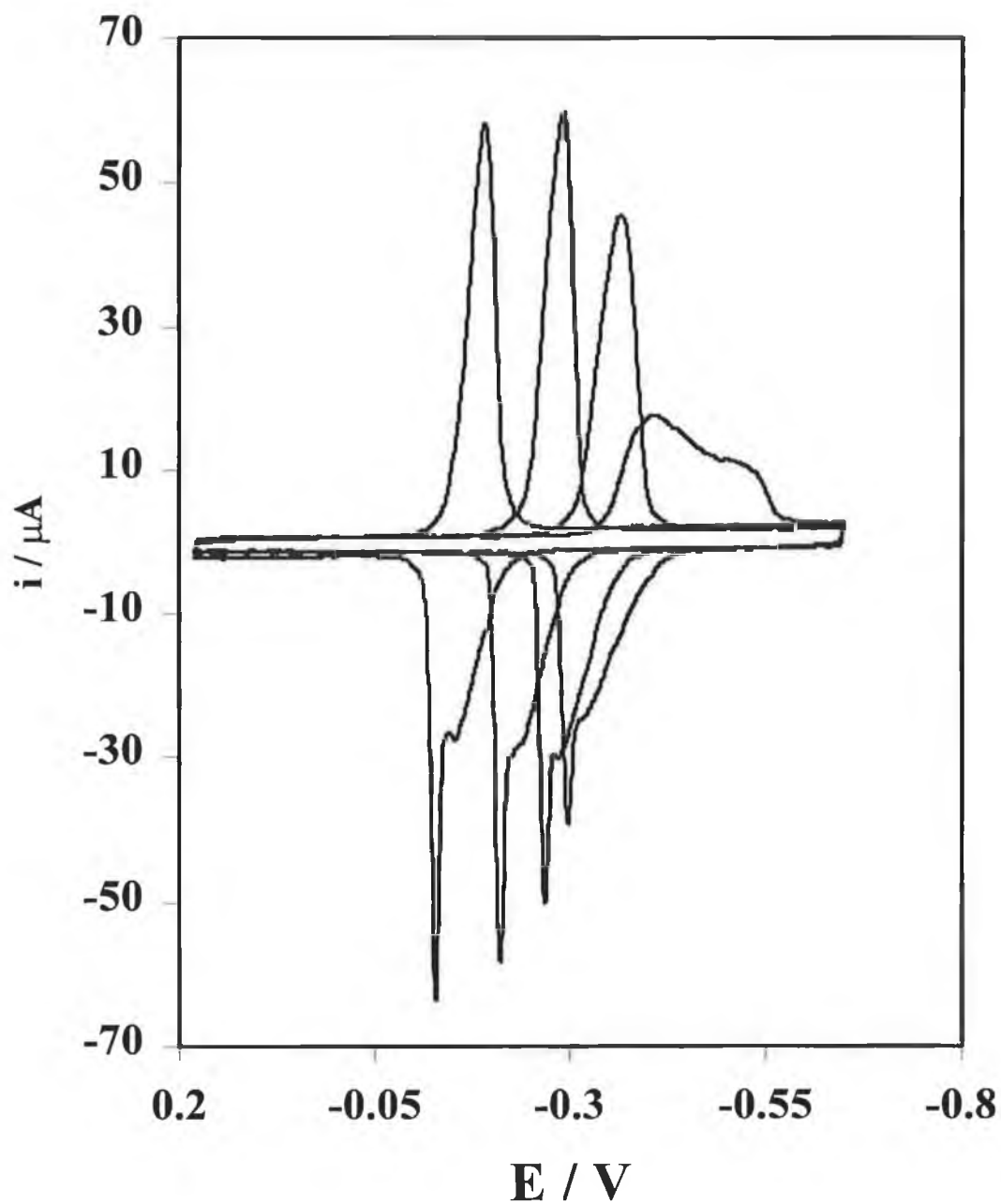


Figure 24 Cyclic voltammograms of a mercury electrode immersed in a $5 \mu\text{M}$ solution of $[\text{AQNH}_2\text{SOH}]$ as the pH of the electrolyte solution is varied. From left to right, the pH of the solution is 1.03, 2.20, 3.15 and 4.10. The scan rate was 5 Vs^{-1} and the supporting electrolyte is 1.0 M NaClO_4 .

5.2.8 Temperature dependence of the formal potential

When dealing with modified electrodes, it is essential that the monolayers are stable on the electrode for extended periods. One way of testing the stability of these redox active films is to examine the effects when subjected to increased temperatures. For monolayers of [AQNH₂SOH] both the stability of the monolayer and the effect on the spike (present in the voltammetric responses at high surface coverages) can be tested at elevated temperatures. Also, monitoring the effect of temperature on the formal potential of monolayers of [AQNH₂SOH] will provide the reaction entropy (ΔS_{rc}°) of the redox couple. ΔS_{rc}° quantifies the difference in entropy between the reduced and oxidised forms of the redox couple and has been determined using a non-isothermal cell. The temperature dependence of the formal potential may be expressed as equation 5 as discussed by Weaver and co-workers^{34,35}

$$\Delta S_{rc}^\circ = F(\partial E^\circ / \partial T) \quad \text{Eq. 5}$$

where F is the Faraday constant and T is the absolute temperature. As with the pH experiments, temperature dependence studies were performed on monolayers at both low and high surface coverage, i.e., with and without the spike being present, to see if any relationship exist between the two. Figure 26 shows the cyclic voltammetric response for a [AQNH₂SOH] film adsorbed from a 1 μ M deposition solution as the temperature is systematically changed from -5 to 40 $^\circ\text{C}$, where the supporting electrolyte is 1.0 M HClO₄. The formal potential of the film shifts in a negative direction with increasing temperature indicating a positive reaction entropy indicating a higher degree in local ordering in the reduced over the oxidised state. Figure 25 shows the resultant plot of E° Vs T , which was linear and the reaction entropy was calculated from the slope. The value obtained was 38 ± 2 J mol⁻¹ K⁻¹. Given that switching the oxidation state of the monolayer does not change it's charge (both the quinone and hydroquinone are neutral) the Born equation predicts ΔS_{RO}° should be zero. That non-zero ΔS_{rc}° values are observed supports our conclusion based on the voltammetric data that hydrogen bonding induces significant partial charges in this system. The negative shift in E° gave Figure 26 also shows that the increase in temperature results in a decrease in the peak current of both the oxidised and reduced forms

of the complex and increased separation between the anodic and cathodic redox peaks. This indicates that monolayers of [AQNH₂SOH] are not thermally stable at high temperatures, resulting in the possible decomposition of the monolayer from the electrode surface. Another feature, which may be seen in Figure 25 is that the shift in E_{pa} and E_{pc} with increased temperature are not equal. The cathodic peak potential shifts by 52 mV going from 0 to 40 °C, whereas the anodic shift for the same temperature range was only 10 mV. Therefore, increased peak to peak splitting also occurs with increasing temperature. When comparing the FWHM of both oxidation states at 0 and 40 °C it can be seen that increased broadening occurs which, is indicative of repulsive interactions between the absorbed species.

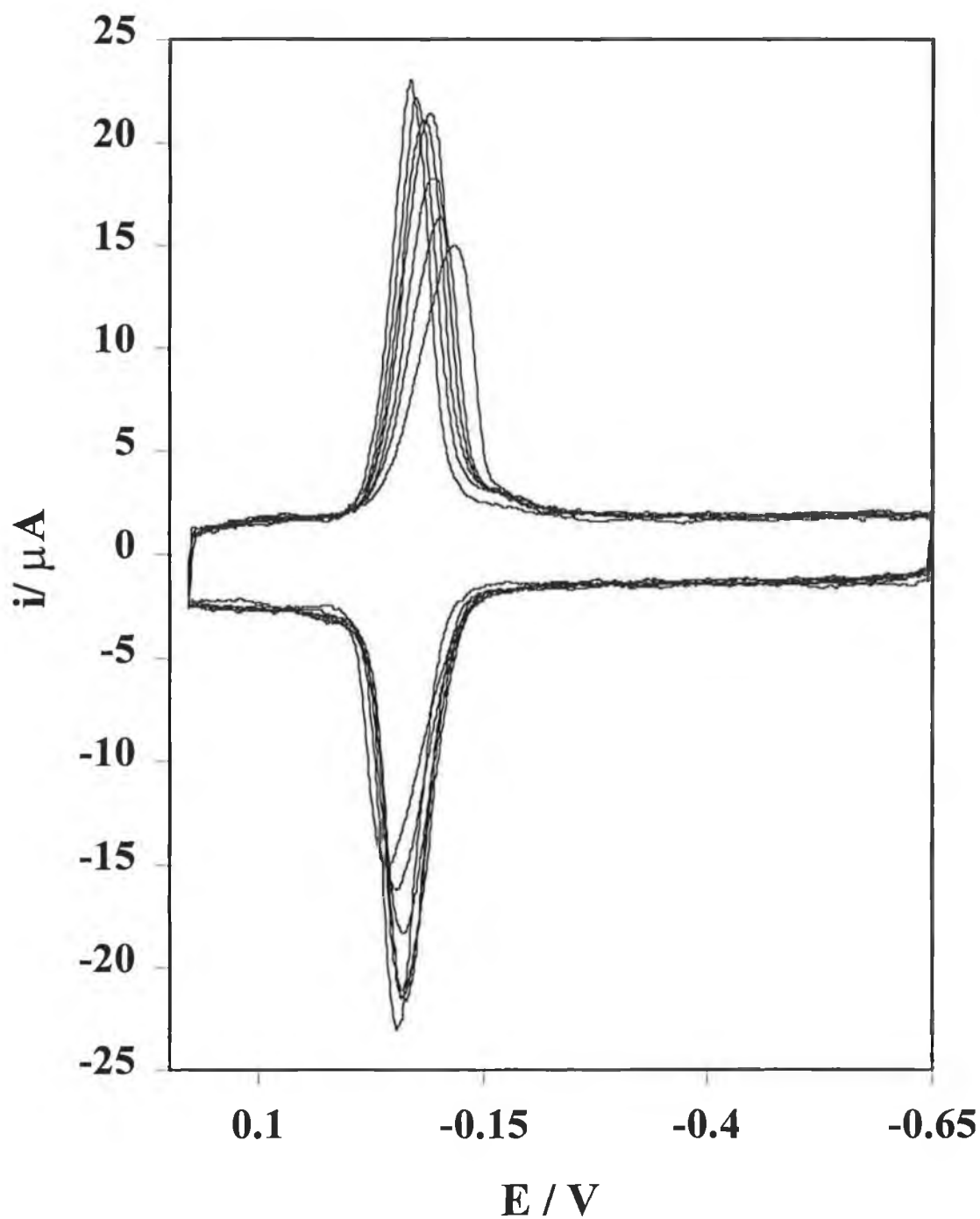


Figure 25 Dependence of the formal potential of [AQNH₂SOH] monolayers with temperature. The concentration present in solution was 1 μM with 1.0 M HClO₄ as the supporting electrolyte. The scan rate was 5 Vs⁻¹. The initial potential was 0.018 V.

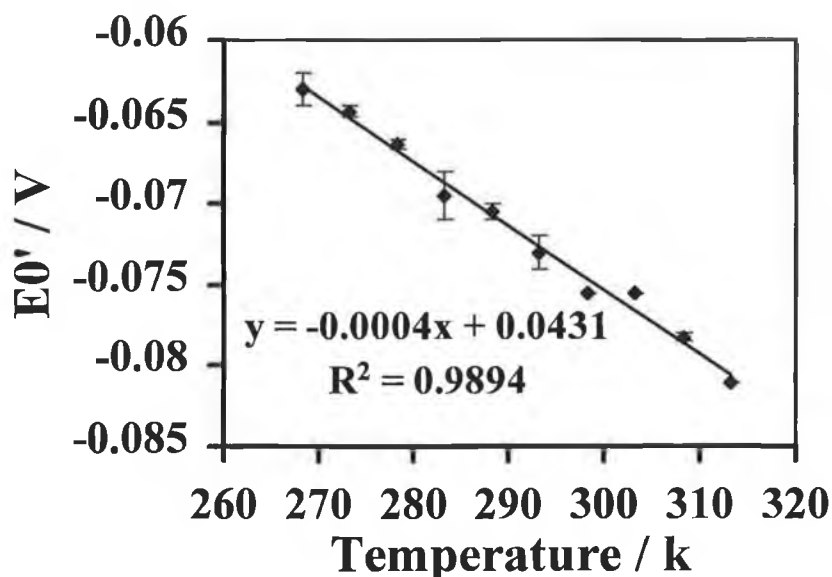


Figure 26 Temperature dependence of the formal potential monolayers of [AQNH₂SOH]. The surface coverage is $8.5 \times 10^{-11} \text{ mol cm}^{-2}$, obtained from a $1 \text{ }\mu\text{M}$ deposition solution of the complex. The temperatures studied were from 268 to 313 K.

The effect of temperature on the formal potential of dense monolayers formed from $5 \text{ }\mu\text{M}$ deposition solutions is quite different. Figure 27 illustrates the cyclic voltammetric responses for monolayers at coverages where the spike is present at temperatures between -5 and 35°C . Although the formal potential of the monolayer depended on temperature the change was not linear and therefore no reaction entropy could be determined for monolayers adsorbed from $5 \text{ }\mu\text{M}$ solutions. However, other interesting changes occurred at increased temperatures. At 30°C the spike was lost from all cyclic voltammograms, the peak currents for the monolayer decreased and the formal potential of the monolayer shifted positively. When the spike disappeared, the surface coverage changed from $1.81 \times 10^{-10} \text{ mol cm}^{-2}$ from to $9.81 \times 10^{-10} \text{ mol cm}^{-2}$. The free energies of adsorption (Table 1) determined from isotherms at 25°C are significantly larger than RT even at 40°C . Therefore, it appears that thermal desorption occurs because of a change in film structure at higher temperatures most likely causing loss of intermolecular hydrogen bonding.

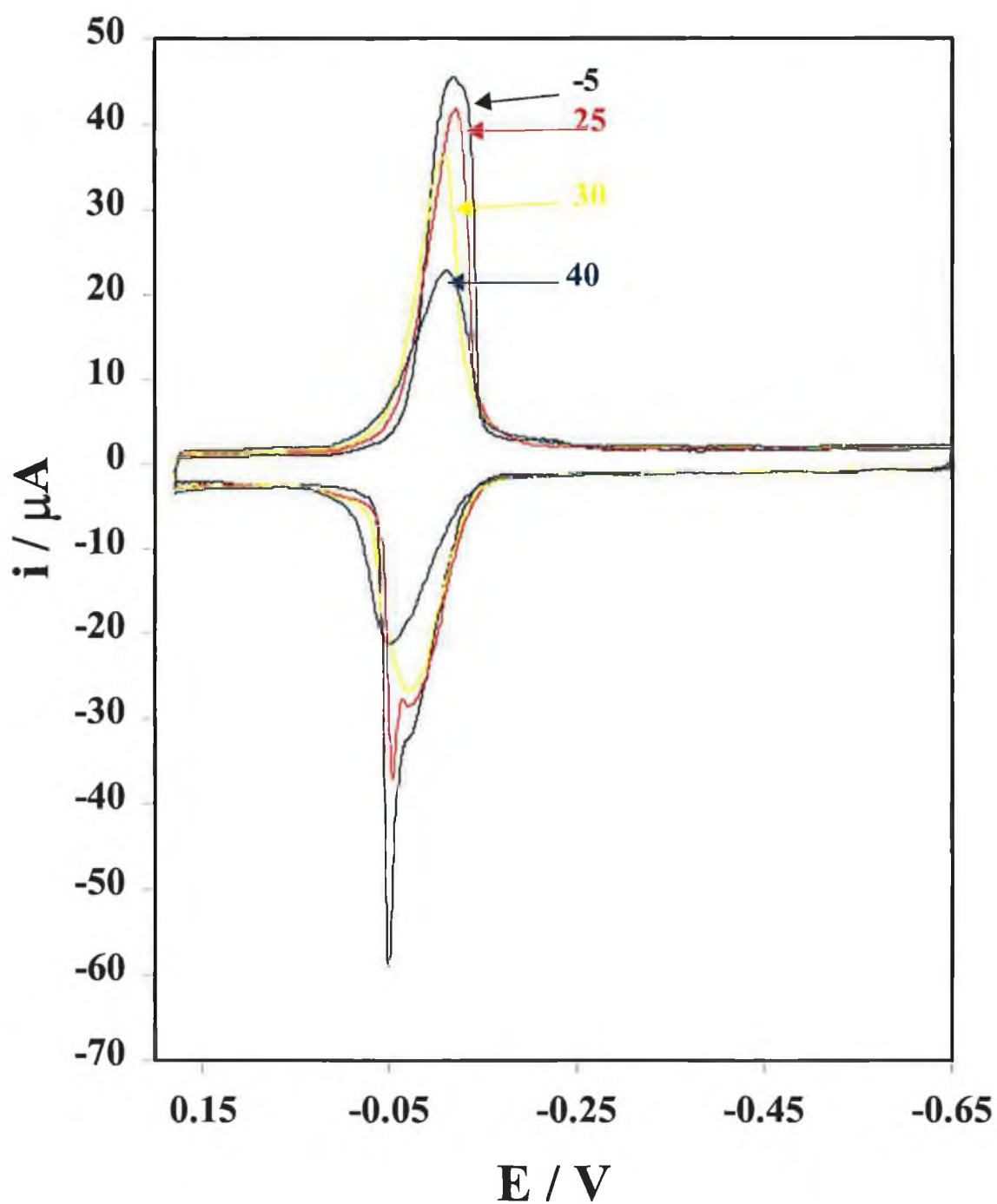


Figure 27 Dependence of the voltammetric response of [AQNH₂SOH] monolayers on temperature. The concentration present in solution was 5 μM in 1.0 M HClO₄. The CVs represent temperatures in °C. The scan rate was 5 Vs⁻¹. The initial potential was 0.018 V.

5.3 Conclusion

Monolayers of [AQNH₂SOH] have been formed by spontaneous adsorption onto mercury electrodes and their voltammetric responses have been extensively investigated. Voltammetry at low coverages seems ideal. However, at saturation coverage, when intersite separation is at a minimum, the presence of a narrow sharp spike emerges on the anodic wave of the voltammogram. As the spike is extremely sharp, it is most probably due to a surface effect rather than a diffusional one. This suggests that extensive lateral interactions exist between the adsorbates most probably through hydrogen bonding.

Both the Frumkin and Langmuir isotherms were employed in order to determine the surface coverages, free energy of adsorption and interaction parameters for these monolayers. The Frumkin isotherm was found to adequately describe this system, with an interaction parameter, g , when the spike was present in the voltammetric response of +18.6 and when no spike was present, -1.25. g indicated very strong destabilising interactions and relatively weaker stabilising interactions, depending on the presence of the spike within the voltammogram.

Analysis of the spike revealed some important insights into adsorbed organic films on electrodes. The spike height depends non-linearly on bulk concentration and is lost with increasing pH, and increased temperature. Moreover, the FWHM and ΔE_p increased with increasing temperature. We conclude that the spike is present due to changes in intermolecular hydrogen bonding for the following reasons. At low adsorbate coverage when intramolecular interactions may occur, ideal voltammetric responses are obtained and no spike is present. The non-ideal voltammetric response is observed only when the intersite separation is minimised and the coverage approaches saturation. When the pH of the electrolytic solution is raised, deprotonation occurs within the quinone breaking down the possibility of intermolecular hydrogen bonding, resulting in the reduction of the spike intensity. Finally, monolayers consist of a linear, ordered framework which facilitates intermolecular hydrogen bonding to occur. However, switching from the quinone to hydroquinone states at high surface coverage causes disruption of this hydrogen bonded network resulting in non-ideal voltammetric responses.

In the following chapter, we further investigate hydrogen bonding in anthraquinone monolayers by probing the properties of 2-component assemblies.

5.4 References

1. Forster, R. J., Faulkner, L. R., *J. Am. Chem. Soc.*, **1994**, 116, 5444
2. Forster, R. J., Faulkner, L. R., *J. Am. Chem. Soc.*, **1994**, 116, 5453
3. Forster, R. J., O'Kelly, J. P., *J. Phys. Chem.* **1996**, 100, 3695-3704
4. Campbell, J. L., Anson, F. C., *Langmuir*, **1996**, 12, 4008
5. He, P., Crooks, R. M., Faulkner, L. R., *J. Phys. Chem.*, **1990**, 94, 1135
6. Truong, C. Ta., Kanda, V., McDermott, M. T., *J. Phys. Chem.*, **1999**, 103, 1295
7. Bretz, R. L., Abruña, H. D., *J. Electroanal. Chem.*, **1995**, 388, 123
8. Chidsey, C. E. D., Bertozzi, C. R., Putvinski, T. M., Muijsce, A. M., *J. Am. Chem. Soc.*, **1990**, 112, 4301
9. Rowe, G. K., Creager, S. E., *Langmuir*, **1994**, 10, 1186
10. Acevedo, D., Abruña, H. D., *J. Phys. Chem.*, **1991**, 95, 9590
11. Tirado, J. D., Abruña, H. D., *J. Phys. Chem.*, **1996**, 100, 4556-4563
12. Lin, A. J., Cosby, L. P., Sartorelli, A. C., *Cancer Chemother. Rep. Part 2*, **1974**, 4, 23
13. Driscoll, J. S., Hazard, G. F. Jr., Wood, H. B. Jr., *Cancer Chemother. Rep. Part 2*, **1974**, 4, 1
14. Hoover, J. R. E., Day, A. R., *J. Amer. Chem. Soc.*, **1954**, 76, 4148
15. Forster, R. J., O'Kelly, J. P., *Analyst*, **1998**, 123, 1987
16. Forster, R. J., *J. Electrochem. Soc.*, **1997**, 144, 1165
17. Zhang, J., Anson, F. C., *J. Electroanal. Chem.*, **1992**, 331, 945
18. Xu, J., Chen, Q., Swain, G. M., *Anal. Chem.*, **1998**, 70, 3146
19. Soriaga, M.P., Hubbard, A.T., *J. Am. Chem. Soc.* 1982, 104, 2735
20. Soriaga, M.P., Hubbard, A.T., *J. Am. Chem. Soc.* 1982, 104, 3937
21. Soriaga, M.P., Soriaga, E. B., Hubbard, A.T., Benziger, J. B., Peter Pang, K. W., *Inorg. Chem.*, **1985**, 24, 65
22. Bard, A. J., Faulkner, L. R., *'Electrochemical methods'*, Wiley, New York, **1980**
23. Wopschall, R. H., Shain, I., *Anal. Chem.*, **1967**, 39, 1514
24. Laviron, E., *J. Electroanal. Chem.* 1974, 52, 395
25. Brown, A. P. Anson, F. C., *Anal. Chem.* 1977, 49, 1589

26. Forster, R. J., *Analyst*, **1996**, 121, 733
27. Forster, R. J., *Electrochemical Society Proceedings*, **1996**, 96, 65
28. Forster, R. J., *Langmuir*, **1995**, 11, 2247
29. Trassati, S., *J. Electroanal. Chem.*, **1974**, 53, 335
30. Yatsushashi, T., Inoue, H., *J. Phys. Chem*, **1997**, 101, 8166
31. Soriaga, M.P., White, J. H., Hubbard, A.T., *J. Phys. Chem.*, **1983**, 87, 3048
32. Bailet. S. I., Ritchie. I, M., *Electrochimica Acta*, **1985**, 30, 3
33. Dean. J. A., *Handbook of Organic Chemistry*, McGraw – Hill, New York, **1987**
34. Hupp, J. T., Weaver, M. J., *J. Phys. Chem*, **1984**, 88, 1860
35. Barr, S. W., Guyer, K. L., Li, T, T.-T., Liu, H. Y., Weaver, M. J., *J. Electroanal. Chem*, **1984**, 131, 1626

CHAPTER 6

Intermolecular Hydrogen bonding:

Two - Component Anthraquinone Monolayers

6 Introduction

A molecular-level understanding of the nature of interactions that occur at solid-liquid interfaces would remove many of the barriers to progress in areas such as corrosion protection,¹ chromatography,² adhesion,³ and sensors.⁴ The complex behaviour of these coatings, stationary phases and chemically sensitive films often arises because they lack a well-defined structure. Therefore, the fabrication of highly-ordered and easily prepared model systems is of vital importance.⁵ Self-assembled or spontaneously adsorbed monolayers, formed using a single surface-active component, represent useful systems for probing the distance dependence of non-covalent lateral interactions such as hydrogen bonding, dipole-dipole, hydrophobic and π - π interactions.^{6, 7} However, co-adsorption of surfactants at the solid/liquid interface represents a significantly more powerful approach to probing the nature and strength of lateral interactions between adsorbates since both the inter-site separation and the identity of the adsorbates can be changed.^{8, 9} In particular, surface confined monolayers allow the strong synergistic effects that exist in the co-adsorption of mixtures of surfactants to be probed in detail.^{10, 11}

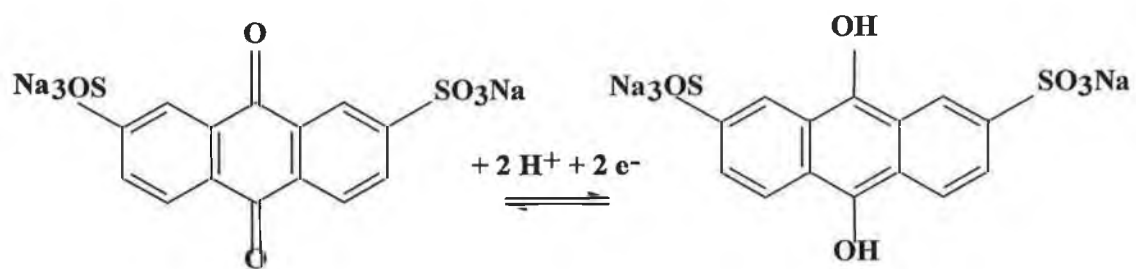
In this Chapter, we report on single- and two-component monolayers of anthraquinone-2,7-disulphonic acid (2,7-AQDS) and 1-chloro-4-hydroxy-anthraquinone (1,4-AQClOH) formed by spontaneous adsorption onto mercury (Chart 1). These large organic molecules are physically adsorbed onto the electrode surface because of their hydrophobic character. One might expect functionalised anthraquinones of this type to undergo significant intramolecular hydrogen bonding, e.g., between the quinone oxygens and the sulphonic acid groups of 2,7-AQDS. Moreover, when the packing density is such that the inter-site separation is less than approximately 2 Å, significant inter-molecular hydrogen bonding may occur. For example, Faulkner and co-workers¹² attributed the unusual multiple waves and sharp spikes observed in the voltammetric responses of dense assemblies of anthraquinone-2,6-disulfonate (2,6-AQDS) to differing degrees of intermolecular hydrogen bonding. The strength of hydrogen bonding interactions can be significantly different within monolayers compared to bulk water. For example, Kunitake¹³ and co-workers found that 5'-ATP and 5'-AMP bind to guanidinium-functionalised monolayers approximately 10^6

times more strongly than in bulk water. The enhancement in this hydrogen bonding interaction most likely arises because of the low dielectric constant of the monolayer phase.¹⁴ Therefore, controlling the solvent content by changing the hydrophilicity of the monolayer building blocks is an important objective if chemical sensors based on these interactions are to be constructed.¹⁵

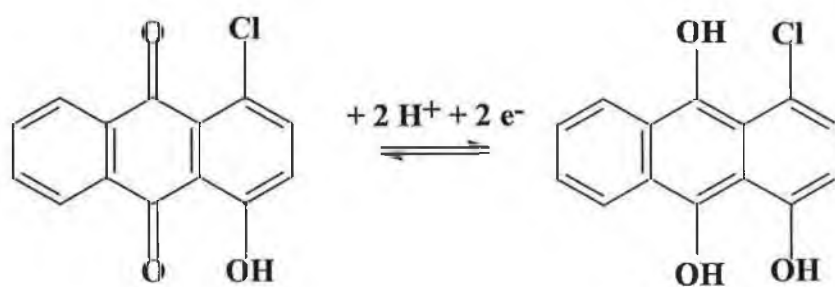
As reported previously for related systems,^{16,17,18} in low pH electrolyte, both 2,7-AQDS and 1,4-AQClOH can be reversibly switched between the oxidised quinone (Q) and reduced hydroquinone (H₂Q) forms. Therefore, not only would one expect significant intermolecular hydrogen bonding between functional groups in two-component monolayers, e.g., between the sulphonic acid groups of 2,7-AQDS and the hydroxy groups of 1,4-AQClOH, but switching the oxidation state of the monolayer might also influence the extent of lateral interactions. Another attractive feature of quinonoid monolayers is that because electron and proton transfer are coupled, switching between Q and H₂Q does not change the state of charge of the film. Thus, electrostatic effects are unlikely to significantly influence the nature or degree of lateral interactions.

Here, we consider these effects not only for single component monolayers, but also probe the lateral interactions that exist within more than 100 two-component monolayers spanning a wide range of compositions. Exploring this large range allows us to address the important question of phase separation as well as lateral interactions between like and unlike adsorbates within mixed monolayers. We have investigated the dependence of the formal potential, surface coverage and interaction parameters for these mixed monolayers. These studies reveal that lateral interactions between unlike molecules are sufficiently strong such that the dense mixed monolayers exist as a single phase, i.e., the adsorbates do not exhibit a preference for being surrounded by their own kind.

Chart 1



2,7-AQDS



1,4-AQClOH

6.1 Apparatus

Cyclic voltammetry was performed using a CH instruments Model 660 electrochemical workstation, a PAR EG&G model 270 dropping mercury electrode and a conventional three-electrode cell. Potentials were measured against a potassium chloride saturated silver/silver chloride (Ag/AgCl) reference electrode. The auxiliary electrode was a large surface area platinum wire. All solutions containing anthraquinones were thoroughly degassed by purging with nitrogen and a blanket of nitrogen was maintained over the solution throughout the experiments. The area of the mercury electrode was determined using the density of pure mercury (13.546 g cm^{-3}) by dispensing, collecting, drying and weighing 100 drops of mercury. An electrochemical area of $0.0140 \pm 0.0007 \text{ cm}^2$ was obtained. This area was also confirmed by recording cyclic voltammograms under steady state and semi-infinite diffusion conditions using $[\text{Ru}(\text{NH}_3)_6]^{2+/3+}$ as a solution phase electrochemical probe.

6.2 Materials and Procedures

Anthraquinone-2,7-disulphonic acid, disodium salt, (2,7-AQDS) and 1-chloro-4-hydroxy-anthraquinone, disodium salt, (1,4-AQClOH) were obtained from BASF. Deposition solutions were prepared using an 80:20 v/v mixture of Milli-Q purified water and DMF containing 1 M HClO_4 as supporting electrolyte. Spontaneously adsorbed monolayers were formed from electrolytic solutions containing the anthraquinone at the desired concentration, typically in the micromolar range. A scan rate of 5 Vs^{-1} was used in cyclic voltammetry which is sufficiently fast to ensure that the current contribution from diffusion was less than 5% of the total current observed. For surface coverage experiments, repetitive cyclic voltammetry was performed until the peak currents observed in successive scans were identical, i.e., the equilibrium surface coverage was attained. For two-component monolayers, the total surface coverage and the relative amounts of each species could be controlled by varying the solution phase concentration of the individual species.

To probe the effect of co-immobilisation on both the formal potentials and the free energies of adsorption, a series of mixed solutions were prepared using a factorial design. In this design, mixed solutions of 2,7-AQDS and 1,4-AQCIOH were prepared at 10 levels with 10 different mixed solutions in each level. For 2,7-AQDS, in level 1, the concentration was fixed at 2 μM in each solution while the concentration of 1,4-AQCIOH varied from 2 to 20 μM , each successive solution increasing by 2 μM . Consecutive levels also increased by 2 μM . Therefore, as the levels of mixed anthraquinone solutions increased the concentration of 2,7-AQDS present in the mixed solutions also increased. This design produces a total of 100 separate solutions that were individually used to form two-component monolayers. Cyclic voltammograms were recorded using a scan rate of 5 Vs^{-1} between potential limits of 0.18 V and -0.30 V. Repetitive scans were recorded until no change in the peak current was observed. Depending on the concentrations of the solutions employed, between 35 and 50 cycles were scanned to obtain invariant responses.

6.3 Results and Discussion

6.3.1 Electrochemical properties of single-component monolayers

Figure 1 shows representative cyclic voltammograms obtained in 0.1 M HClO₄ for individual monolayers of 2,7-AQDS and 1,4-AQCIOH where the solution contains 20 μ M of the anthraquinone. The voltammetric waves exhibit full-width-at-half-maximum (FWHM) values of 57 ± 2 and 58 ± 2 mV for 2,7-AQDS and 1,4-AQCIOH, respectively. The peak-to-peak separations, ΔE_p , are 7 ± 1 mV for 2,7-AQDS and 13 ± 2 mV for 1,4-AQCIOH monolayers. Moreover, the peak shapes are independent of scan rate, ν , and the peak heights are proportional to the scan rate up to at least 50 Vs⁻¹. These observations indicate that both the 2,7-AQDS and 1,4-AQCIOH behave as near ideal, reversible, surface bound redox species^{19,20} when adsorbed onto mercury electrodes from micromolar concentrations. When immobilised within dense monolayers, the formal potentials of both anthraquinones shift in a negative potential direction compared to their solution phase values with $E^{\circ'}_{2,7\text{-AQDS}}$ and $E^{\circ'}_{1,4\text{-AQCIOH}}$ shifting by approximately -7 and -35 mV, respectively as illustrated by Figure 2. That the formal potentials for the quinones within monolayers are more negative than their corresponding solution phase values indicate that the oxidised quinone form is more strongly adsorbed in both cases.¹⁷

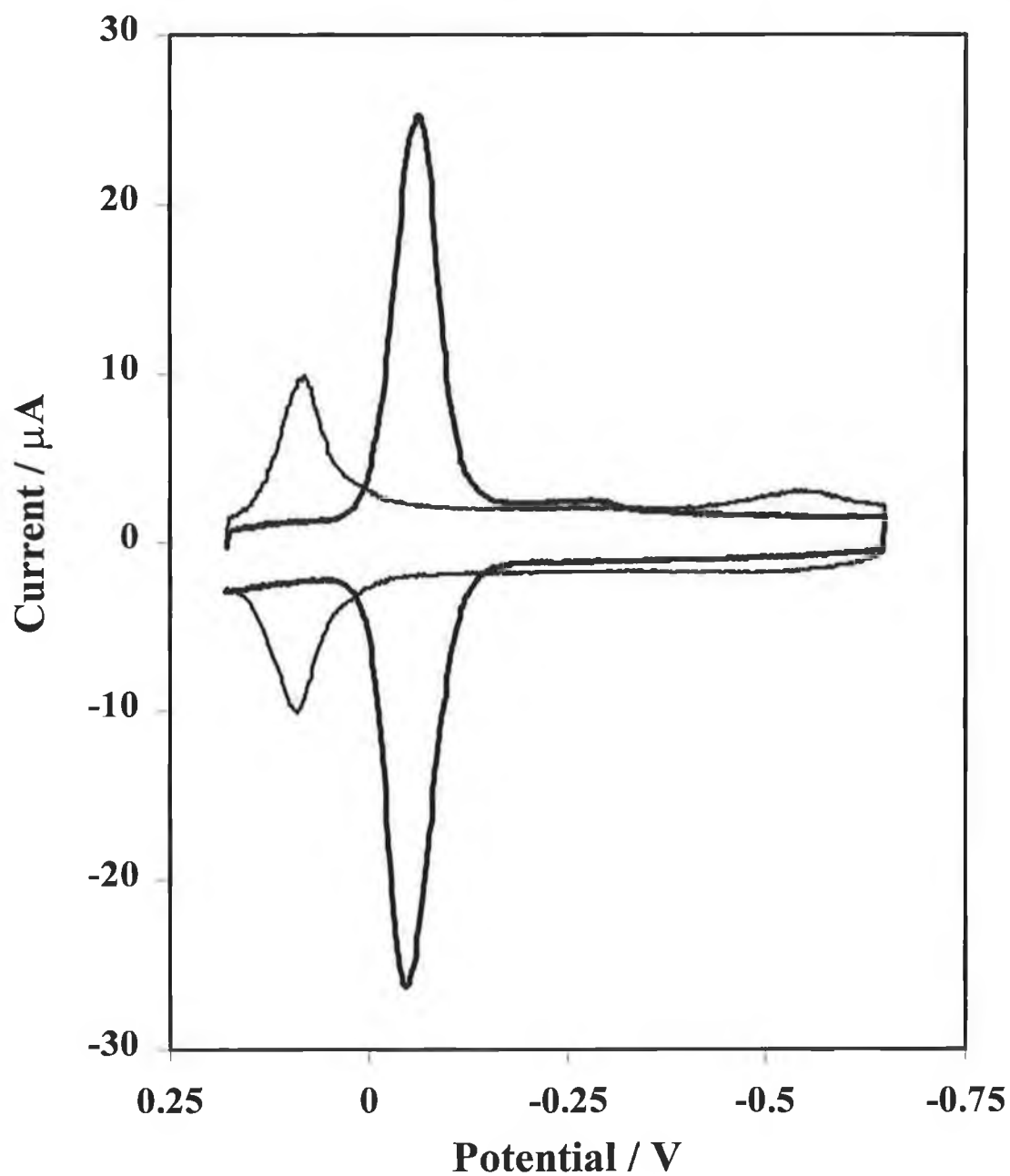


Figure 1 Cyclic voltammograms of a mercury electrode ($A = 0.014 \text{ cm}^2$) immersed in a $20 \text{ }\mu\text{M}$ solution of 2,7-AQDS (Left) or $20 \text{ }\mu\text{M}$ 1,4-AQClOH (Right). The solution is $20 \text{ }\%$ v/v DMF / H_2O containing 1.0 M HClO_4 as supporting electrolyte. The scan rate is 5 Vs^{-1} . Cathodic currents are up and anodic currents are down.

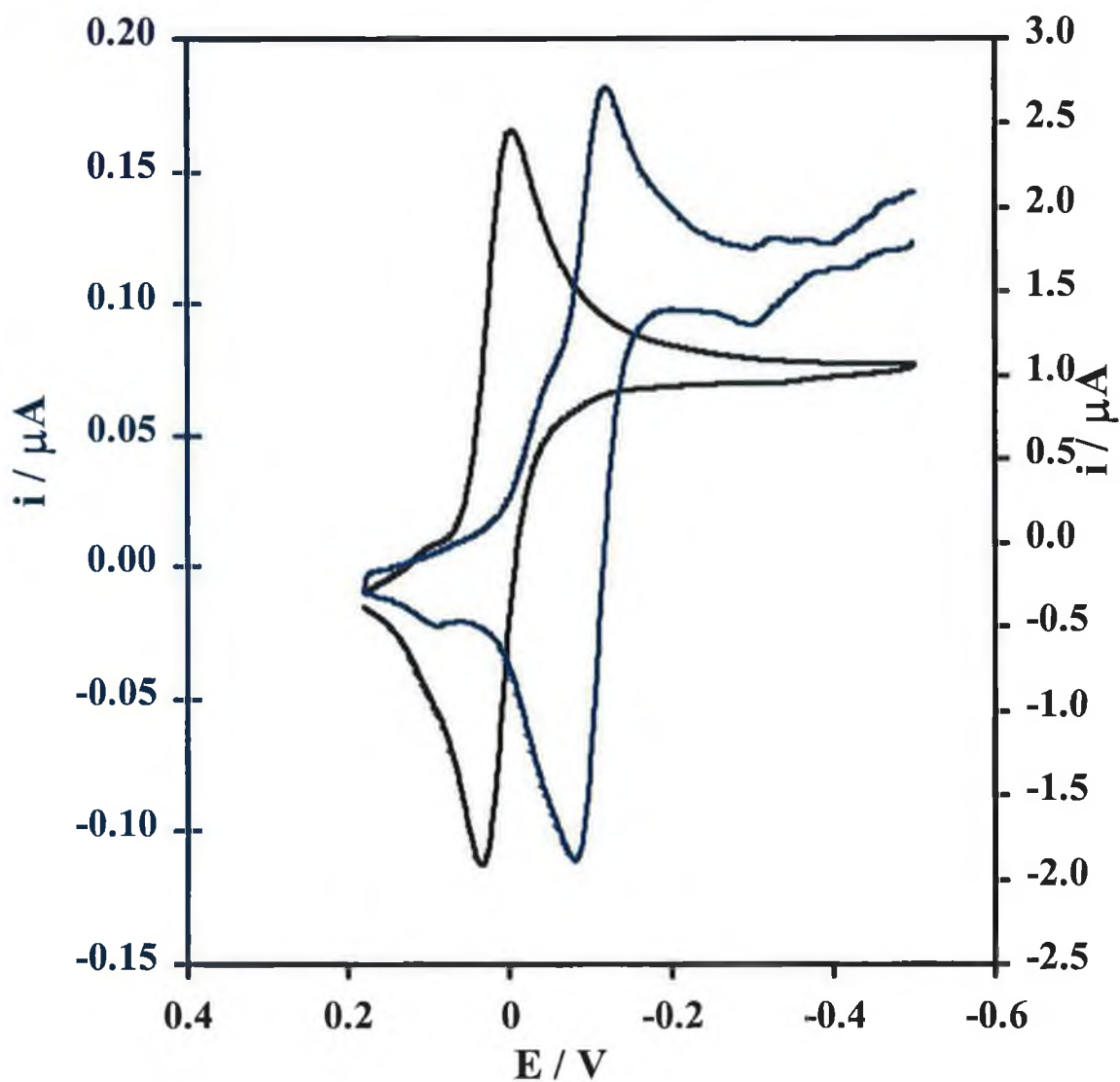


Figure 2 Solution phase cyclic voltammograms of 2,7-AQDS and 1,4-AQClOH obtained from mM deposition solutions. The scan rate is 50 mVs⁻¹. The initial potential is -0.5 V.

6.3.2 Adsorption isotherms.

The goal of this work is to probe the extent to which these quinones interact as both the inter-site separation and the composition of the monolayer is systematically varied. To achieve this objective, we first probe the behaviour of single component monolayers. Figure 3 shows that while the peak shape is independent of the concentration of the anthraquinone in solution, the area under the voltammetric peak increases significantly as the concentration of 1,4-AQClOH is increased from 1 to 10 μM . After correcting for background charging, the surface coverage, Γ , was determined from the charge obtained by integrating the area under the voltammetric peak.

The dependence of the surface coverage on the solution phase concentration is illustrated in Figure 3 and Figure 4 for both compounds. The Langmuir isotherm assumes a homogeneous surface and that either intermolecular interactions are absent or are independent of the surface coverage.^{21,22,23} For related anthraquinone monolayers formed from entirely aqueous solutions, we have previously observed excellent agreement^{16,18} between the behaviour predicted by the Langmuir adsorption isotherm and the experimental response. However, as illustrated in Figure 3 and Figure 4 the quality of the fit obtained using the Langmuir adsorption isotherm is not completely satisfactory, at least not for the 1,4-AQClOH monolayer, suggesting that the extent of inter-adsorbate interaction depends on the surface coverage.

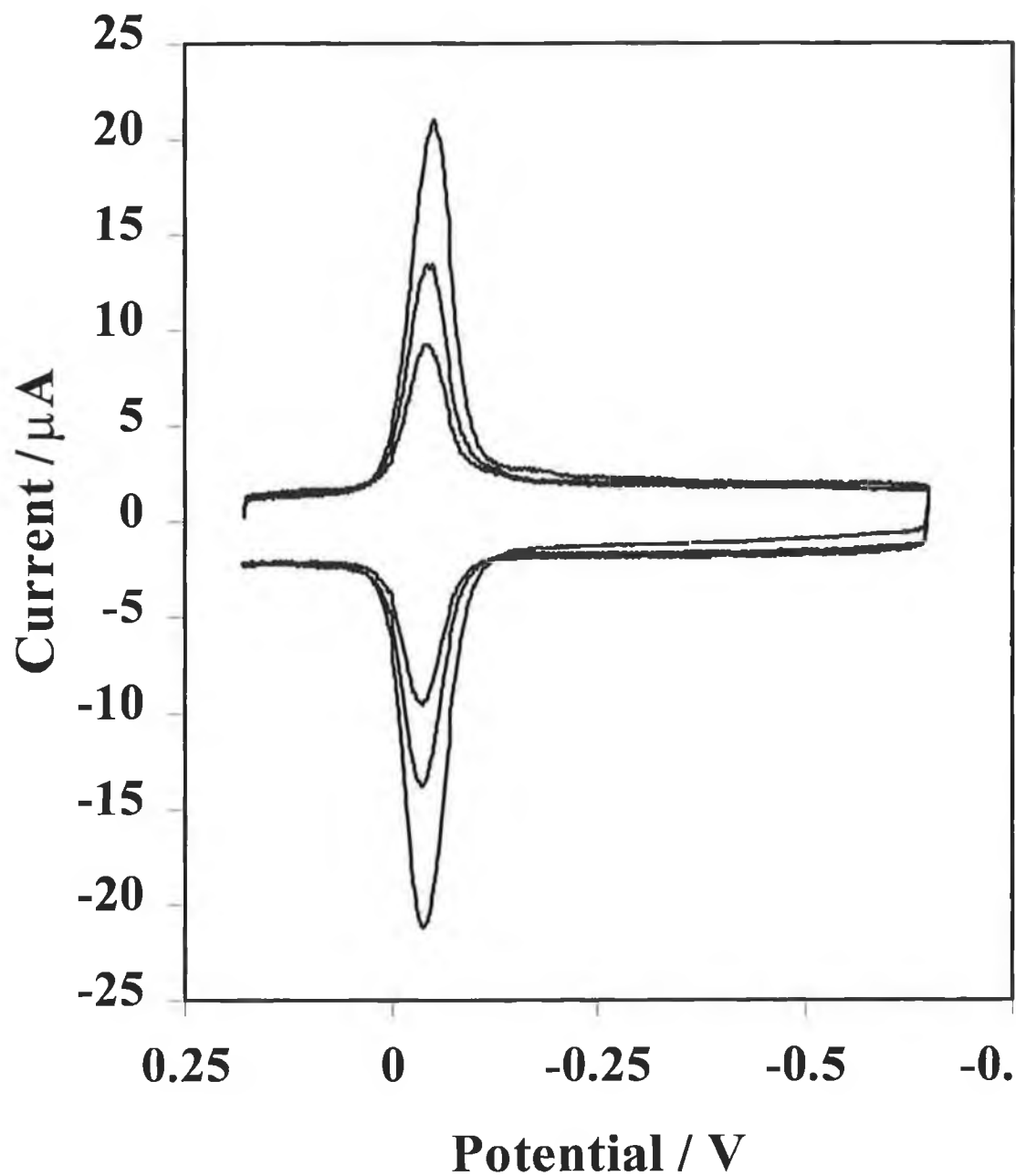


Figure 3 Dependence of the cyclic voltammetry response of a mercury electrode on the bulk concentration of 1,4-AQClOH in 1.0 M HClO_4 . The concentrations are from top to bottom 10, 2 and 1 μM . The scan rate is 5 Vs^{-1} . Cathodic currents are up and anodic currents are down.

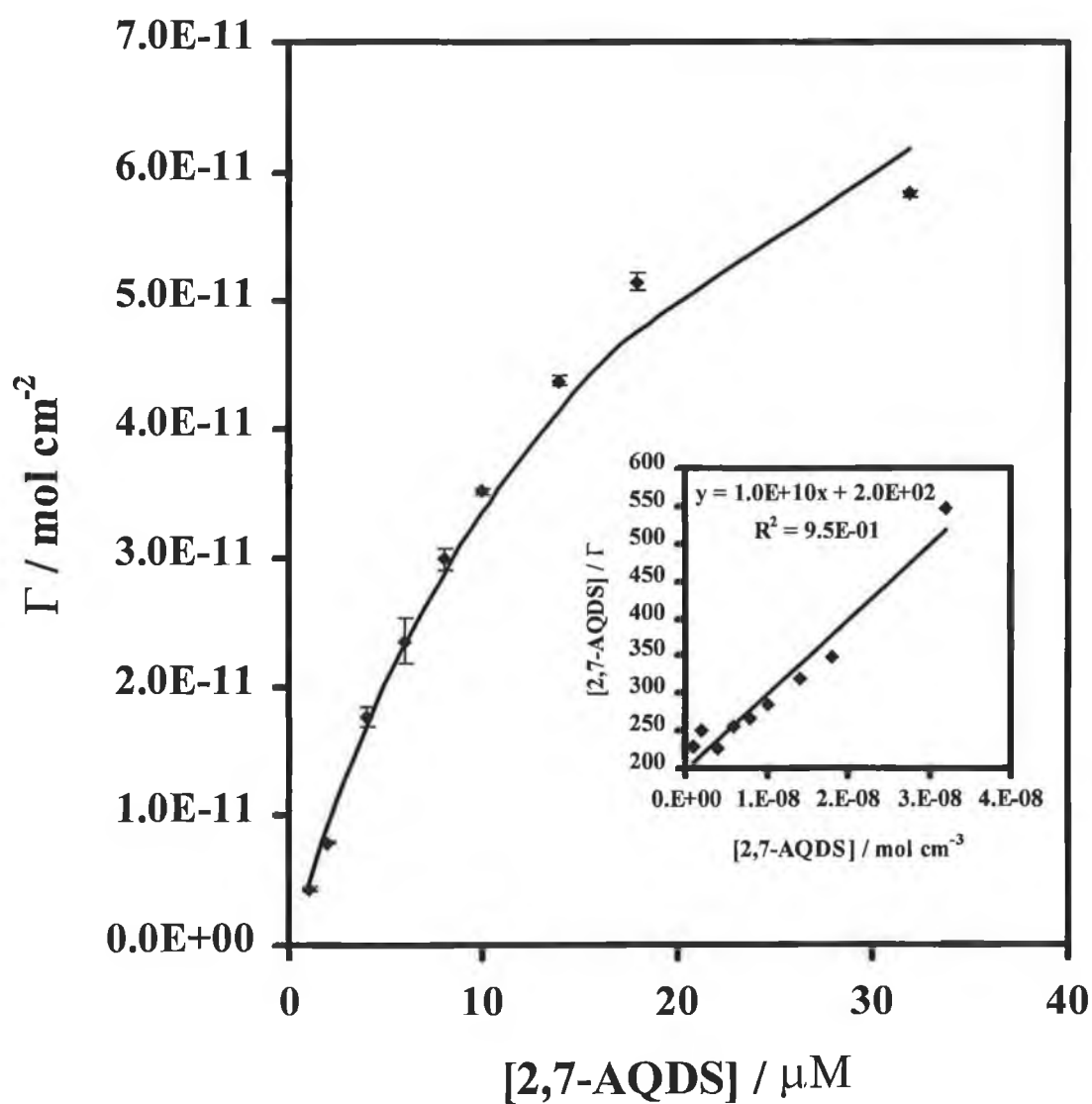


Figure 4 Dependence of surface coverage and bulk concentration of 2,7-AQDS. The solid line represents the best fit to the Langmuir adsorption isotherm. The insert represents the linearised isotherm.

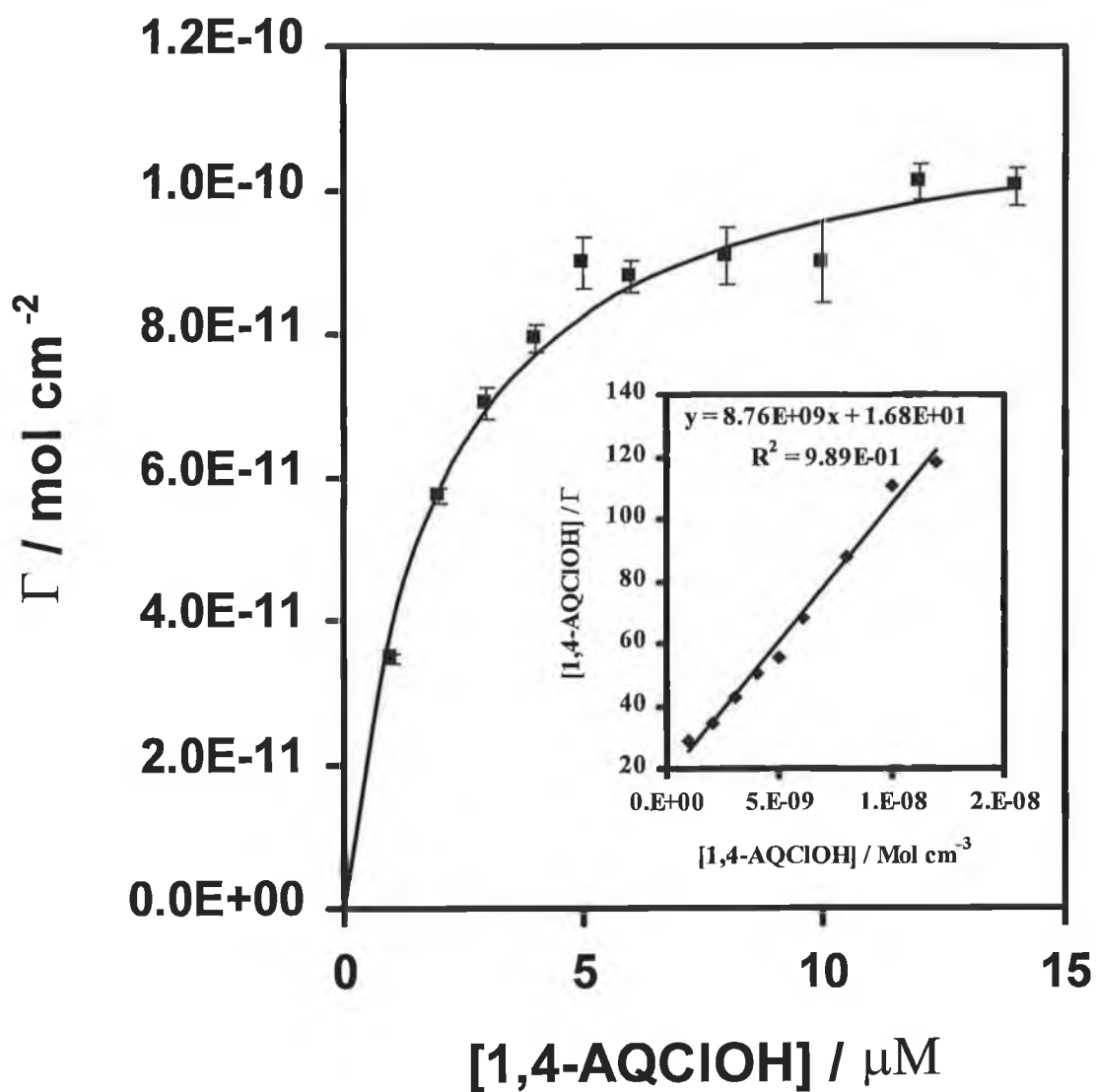


Figure 5 Dependence of surface coverage and bulk concentration of 1,4-AQClOH. The solid line represents the best fit to the Langmuir adsorption isotherm. The insert represents the linearised isotherm.

The Frumkin isotherm^{21,23,24} allows the extent of lateral interactions to be determined by including an interaction parameter and can be expressed in terms of the fractional coverage (θ) of the surface by an adsorbate:

$$\beta_i C_i = \frac{\theta_i}{1 - \theta_i} \exp(g \theta_i) \quad \text{Eq. 1}$$

$\theta_i = \Gamma_i / \Gamma_{\text{sat}}$ where Γ_i is the surface coverage of species i in mol cm^{-2} at a bulk concentration C_i , and Γ_{sat} is the limiting or saturation surface coverage obtained at high bulk concentrations. The interaction parameter, g , describes the surface coverage dependence of the lateral interactions and typically lies between ± 2 . Attractive or stabilising lateral interactions are represented by a negative interaction parameter. The strength of adsorption is described by the adsorption coefficient, β_i , which is related to the free energy of adsorption ΔG_i by:

$$\beta_i = \exp\left(\frac{-\Delta G_i}{RT}\right) \quad \text{Eq. 2}$$

where R is the gas constant and T is the absolute temperature.

Figure 6 shows the best-fit Frumkin adsorption isotherm to the experimental data obtained using nonlinear optimisation. The conditions used in the Excel SOLVER model are listed in the Appendix. The quality of the fit is significantly improved by considering coverage dependent intermolecular interactions. Table 1 contains the saturation coverages, energy coefficients and interaction parameters for both single component monolayers.

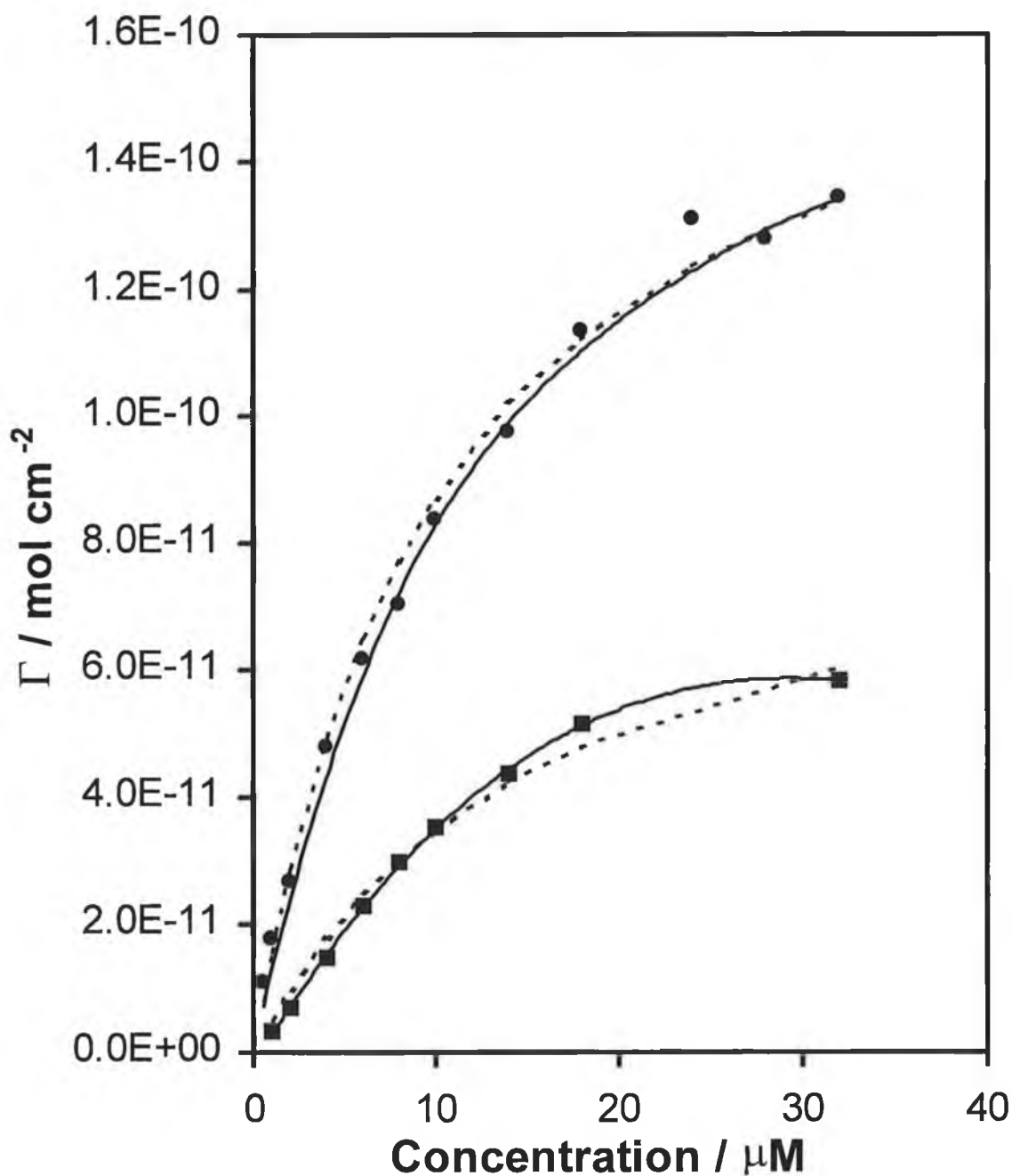


Figure 6 Dependence of surface coverage and bulk concentration of 2,7-AQDS (lower curve) and 1,4-AQCIOH. The solid lines and dashed lines represent the best fits to the Frumkin and Langmuir adsorption isotherm, respectively.

Table 1 Saturation coverages, energy parameters and Frumkin interaction parameters for single- and two-component monolayers of 2,7-AQDS and 1,4-AQCIOH.

	Single- Component	Two- Component
$\Gamma_{\text{Sat, 2,7-AQDS}} / \text{mol cm}^{-2}$	$6.8 \pm 0.32 \times 10^{-11}$	$1.1 \pm 0.05 \times 10^{-10}$
$\Gamma_{\text{Sat, 1,4-AQCIOH}} / \text{mol cm}^{-2}$	$1.9 \pm 0.15 \times 10^{-10}$	$1.2 \pm 0.04 \times 10^{-10}$
$\beta_{2,7\text{-AQDS}} / \text{M}^{-1}$	$4.9 \pm 0.25 \times 10^4$	$8.7 \pm 0.4 \times 10^3$
$\beta_{1,4\text{-AQCIOH}} / \text{M}^{-1}$	$7.5 \pm 0.5 \times 10^4$	$1.3 \pm 0.1 \times 10^5$
$g_{2,7\text{-AQDS}}$	-1.62 ± 0.21	-2.10 ± 0.21
$g_{1,4\text{-AQCIOH}}$	-0.21 ± 0.02	-1.71 ± 0.15
$g_{2,7\text{-AQDS}, 1,4\text{-AQCIOH}}$		-0.95 ± 0.1

The saturation surface coverage obtained for the 2,7-AQDS monolayer is $6.8 \times 10^{-11} \text{ mol cm}^{-2}$, which compares favourably with the value obtained previously, $7.2 \pm 0.6 \times 10^{-11} \text{ mol cm}^{-2}$, for monolayers deposited from entirely aqueous solutions.²⁵ This limiting coverage is also similar to that found for 2,6-AQDS monolayers by Faulkner,¹² and our own previous work.¹⁷ The most striking feature of Figure 3 and Table 1 is that the saturation coverage for 2,7-AQDS ($6.8 \pm 0.32 \times 10^{-11} \text{ mol cm}^{-2}$) is almost three times smaller than that observed for 1,4-AQCIOH ($1.9 \pm 0.15 \times 10^{-10} \text{ mol cm}^{-2}$). These limiting coverages correspond to areas per molecule of approximately 248 and 90 \AA^2 , respectively. Molecular modelling suggests that if solvation effects are ignored, the areas of occupation within a close packed structure in which the adsorbates lie co-planar with the electrode surface would be of the order of 60 \AA^2 for both adsorbates. Thus, when compared with the experimental data, these results suggest that even for the highest solution phase concentration of the quinones examined, dense monolayers are not formed. Moreover, it appears that while the 1,4-AQCIOH adsorbates may approach one another with average

inter-site separations of the order of 2 Å, the 2,7-AQDS adsorbates are separated on average by as much as 7.5 Å.

The β values obtained for 2,7-AQDS and 1,4-AQCIOH are $4.9 \pm 0.2 \times 10^4$ and $7.5 \pm 0.5 \times 10^4 \text{ M}^{-1}$, respectively. These results indicate that while both species interact strongly with the mercury surface, the 1,4 derivative binds relatively more strongly. The adsorption coefficient obtained for the 2,7-AQDS monolayer is approximately 50 times smaller than those previously reported for 2,7-AQDS,²⁵ or the 2,6 isomer deposited from an aqueous solution.¹² This reduction in β most likely arises because the strength of the hydrophobic interactions of the organic molecule with the mercury surface decrease when the deposition solution contains 20% DMF.

The interaction parameters for both anthraquinones are negative indicating attractive or stabilising lateral interactions. However, despite the larger average inter-site separation within the 2,7-AQDS monolayer, the Frumkin parameter is -1.62 ± 0.21 compared to -0.21 ± 0.02 for the 1,4-AQCIOH adsorbate. These values correspond to interaction energies of approximately -2.0 and $-0.26 \text{ kJ mol}^{-1}$, respectively. These values are both considerably less than the 20 kJ mol^{-1} typically associated with hydrogen bonding in aqueous solution. A quantum mechanical model developed by Kunitake and co-workers¹⁴ and a classical electrostatic model²⁶ based on the Poisson-Boltzmann distribution predict that the dielectric constant of the monolayer exerts a significant influence over the strength of the hydrogen bonding interactions. The interfacial capacitance observed for dense monolayers is approximately $25 \mu\text{F cm}^{-2}$, which is only about 20% smaller than that found for the unmodified mercury interface. Moreover, that the background charging current observed away from $E^{\circ'}$ in Figure 3 does not change significantly as the surface coverage is increased suggests that these films are highly solvated for all surface coverages and that the dielectric constant within the layer is similar to that found at an unmodified interface. Therefore, it appears that the magnitude of the interaction energies observed is controlled by the identity of the donor/acceptor groups and their inter-site separation rather than by the dielectric constant of the film. That $E^{\circ'}$ _{1,4-AQCIOH} shifts in a positive potential direction with increasing surface coverage, as illustrated in Figure 4, is consistent with the presence of

significant inter-molecular interactions within these assemblies. The direction of this shift indicates that the electron density on the 1,4-AQCIOH adsorbate decreases with increasing surface coverage.

6.3.3 Mixed monolayer systems

The cyclic voltammetry of a two-component monolayer deposited from a solution containing 20 μM of each anthraquinone is illustrated in Figure 5. The separation between the anodic and cathodic peak potentials of the mixed layers is 10.4 ± 2.2 and 16.5 ± 0.8 mV for 2,7-AQDS and 1,4-AQCIOH, respectively. When the experimental timescale is longer than the time constant for heterogeneous electron transfer, the ΔE_p value observed for the 2,7-AQDS derivative is similar to that found in single component monolayers. In contrast, ΔE_p for 1,4-AQCIOH is significantly larger in the two-component system suggesting that the two components interact laterally. However, the most striking difference between single- and two- component monolayers is the shift in the formal potentials for both redox couples.

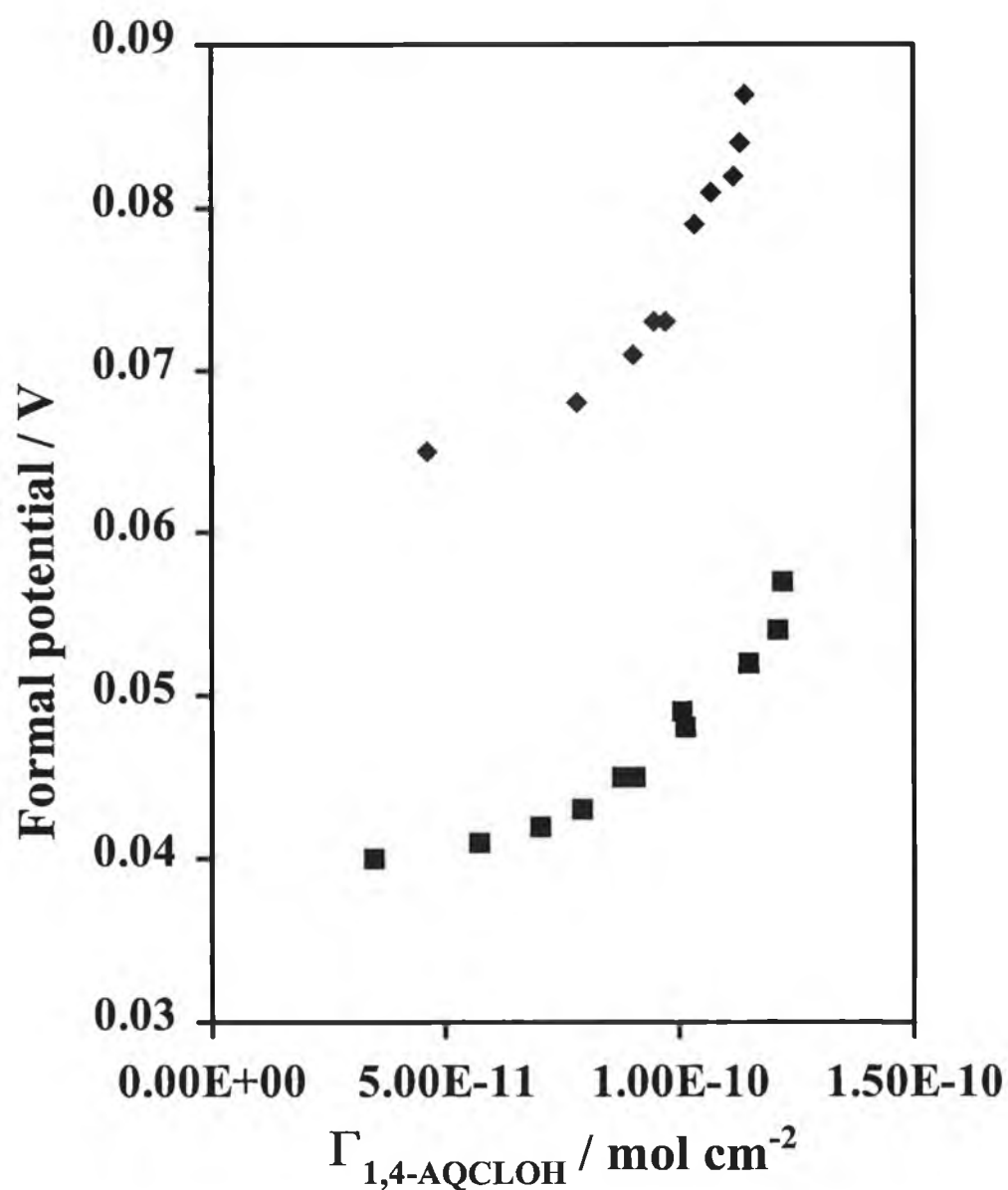


Figure 7 Effect of the surface coverage of 1,4-AQCLOH on its equilibrium formal potential. The upper (♦) and lower (□) data represent single- and two-component monolayers, respectively. In the mixed monolayers, the concentration of 2,7-AQDS is constant at 20 μM .

The formal potential, $E^{\circ'}$, for 2,7-AQDS in a pure monolayer is 0.087 ± 0.003 and -0.056 ± 0.005 V for 1,4-AQCIOH. That $E^{\circ'}_{2,7\text{-AQDS}}$ is more negative when it is part of the two-component assembly indicates that it is more easily oxidised and that the electron density on the adsorbate is higher. In contrast, the formal potential for the 1,4-AQCIOH component shifts in a positive potential direction compared to that observed for the single component monolayer indicating a lower electron density. These observations suggest that the adsorbates interact laterally through intermolecular hydrogen bonds in which 2,7-AQDS and 1,4-AQCIOH act as electron acceptors and donors, respectively. This conclusion is supported by the data presented in Figure 7 which show that $E^{\circ'}_{1,4\text{-AQCIOH}}$ shifts in a positive potential direction with increasing surface coverage suggesting that the electron density on this donor is lower at higher surface coverages. The extent and nature of these lateral interactions can be quantified by systematically varying both the total surface coverage (inter-site separation effects) and the relative concentration of each component.

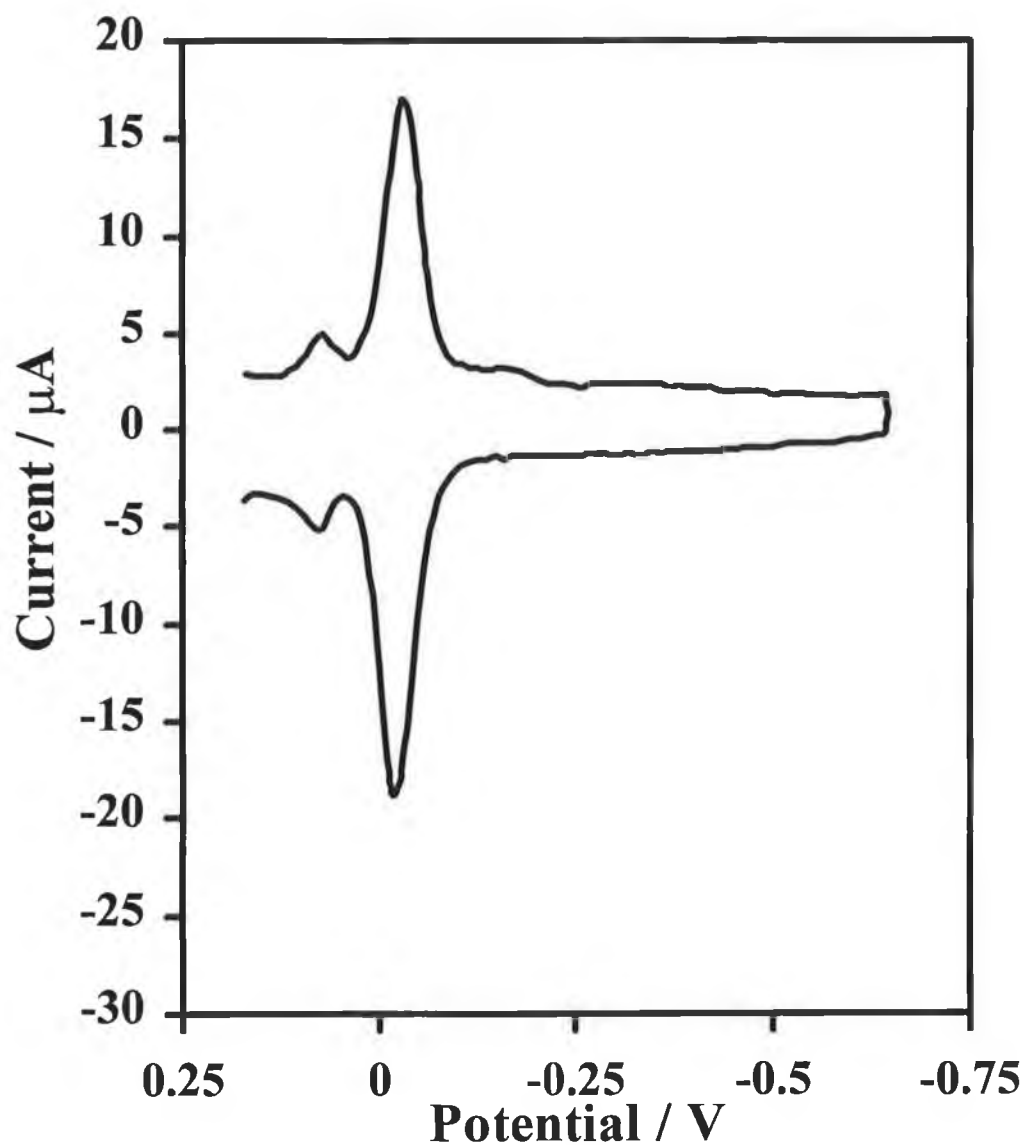


Figure 8 Cyclic voltammogram for a mercury electrode ($A = 0.014 \text{ cm}^2$) immersed in a solution containing $20 \text{ } \mu\text{M}$ of both 2,7-AQDS and 1,4-AQClOH. The solution is 20 % v/v DMF / H_2O containing 1.0 M HClO_4 as supporting electrolyte. The scan rate is 5 Vs^{-1} . Cathodic currents are up and anodic currents are down.

6.3.4 Relationship between solution concentration and surface coverage.

When a two-component monolayer is deposited from a solution containing equimolar concentrations of both species, one might reasonably expect that the ratio of the surface coverages would be given by $\beta_{1,4\text{-AQClOH}} / \beta_{2,7\text{-AQDS}}$, i.e., $\Gamma_{1,4\text{-AQClOH}} = 1.5 \Gamma_{2,7\text{-AQDS}}$. However, when a monolayer is formed from a solution containing 1 μM of both anthraquinones the surface coverage of 1,4-AQClOH is approximately four times that of 2,7-AQDS indicating preferential adsorption of the chloro derivative in the two component monolayers. Moreover, the ratio of the surface coverages depends on the total concentration of the quinones in solution. To quantify these differences in the adsorption parameters between single and binary monolayers, competitive adsorption isotherms have been measured. To achieve this objective 100 independent deposition solutions were prepared according to a factorial experimental design in which the concentrations of both anthraquinones were systematically varied between 2 and 30 μM . These solutions yielded monolayers in which the total surface coverages varied significantly and the ratio $\Gamma_{1,4\text{-AQClOH}} / \Gamma_{2,7\text{-AQDS}}$ ranged from 0 to 1.

An important objective when seeking to control interfacial properties such as wettability, friction and chemical selectivity using multicomponent monolayers is to determine whether the components intimately mix or if the films take the form of dense islands that contain only a single component. However, imaging these monolayers on mercury with the necessary molecular resolution is difficult. Therefore, as illustrated in Figure 9 we have investigated the relationship that exists between the solution composition and the corresponding monolayers when formed from water / DMF solutions that contain both 2,7-AQDS and 1,4-AQClOH. The data are presented as the mole fraction of each component within the layer as measured using the background corrected areas from cyclic voltammetry. The experimental data do not agree with the solid line which shows the response expected where the mole fraction in the monolayer is the same as that of the two quinones in solution. The sharp rise observed for the 1,4 derivative indicates the tendency of the system to move quickly from a monolayer consisting predominantly of one component to the other. This response is consistent with the two-component monolayers existing as a single phase at equilibrium rather than as two separate phases. That the two

anthraquinones intimately mix contrasts with the behaviour typically observed for Langmuir monolayers^{27,28} and suggests that the adsorbates may be able to diffuse on the electrode surface. Moreover, it suggests that it may be possible to control the properties of mercury / solution interfaces using mixed anthraquinone monolayers.

6.3.5 Competitive Adsorption.

Analysing the adsorption isotherm data for single component monolayers according to the Frumkin isotherm indicated that attractive or stabilising interactions exist between like molecules. However, Figure 10 indicates that the two-component films form a single phase suggesting that interactions between like and unlike molecules are comparable. To investigate the magnitude of the interactions between dissimilar adsorbates we have probed the thermodynamics of competitive adsorption using the Frumkin isotherm.

The Frumkin adsorption isotherm can be used to describe competitive adsorption of two species (*i* and *j*) present in a solution according to:

$$\beta_i C_i = \frac{\theta_i}{1 - \theta_i - \theta_j} \exp(g_{i,i}\theta_i + g_{i,j}\theta_j) \quad \text{Eq. 3}$$

$$\beta_j C_j = \frac{\theta_j}{1 - \theta_j - \theta_i} \exp(g_{j,j}\theta_j + g_{i,j}\theta_i) \quad \text{Eq. 4}$$

where $g_{i,i}$, and $g_{j,j}$ represent interactions between similar adsorbates while $g_{i,j}$ represents interactions between dissimilar adsorbates. Thus, by systematically varying the concentrations of each adsorbate it is possible to obtain a significant insight into how changes in the presence of a second adsorbate affects the extent of lateral interactions. Table 1 contains the saturation coverages of both species within the two-component monolayers and the three interaction parameters as determined from the concentration dependence of the experimental surface coverages using non-linear optimisation techniques. Figure 10 illustrates the correlation observed between the theoretical surface coverages obtained using these parameters and those measured experimentally. For both anthraquinones, the theoretical and experimental surface coverages agree closely with

slopes of 1.00 and 0.87 being observed for the 1,4-AQClOH and 2,7-AQDS adsorbates, respectively. Moreover, absolute intercepts corresponding to less 2% of the saturation coverages are observed. These results indicate that the Frumkin isotherm is capable of providing a direct and unbiased model of the experimental data.

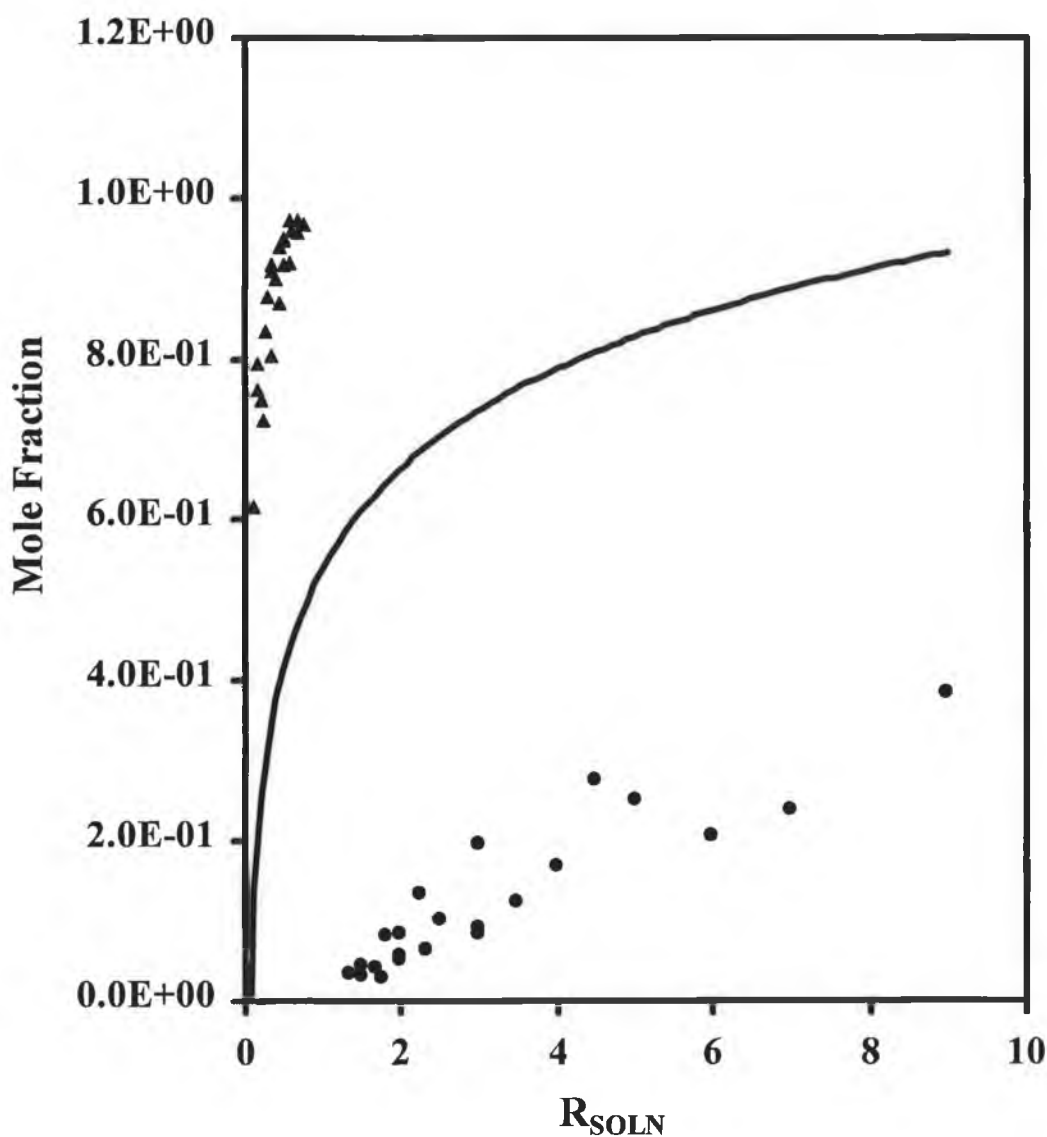


Figure 9 Dependence of the mole fraction of 1,4-AQClOH (▲) and 2,7-AQDS (●) within mixed monolayers on the ratio of the bulk concentration of the two species.

For two-component monolayers, the saturation coverages of both anthraquinones are substantially different compared to those found in single-component monolayers. Specifically, $\Gamma_{\text{Sat, 2,7-AQDS}}$ *increases* from $6.8 \pm 0.32 \times 10^{-11}$ to $1.1 \pm 0.05 \times 10^{-10}$ mol cm⁻² while $\Gamma_{\text{Sat, 1,4-AQCIOH}}$ *decreases* from $1.9 \pm 0.15 \times 10^{-10}$ to $1.2 \pm 0.04 \times 10^{-10}$ mol cm⁻² on going from single to two-component monolayers. However, the total coverage within dense single- and two-component monolayers agree with one another to within 10%. Consistent with the formal potential data discussed above, these results suggest that the two adsorbates interact significantly when co-immobilised.

The Frumkin parameters also provide an insight into the nature and strength of the interactions that exist between both like and unlike adsorbates. The interaction parameters describing self-interactions, $g_{2,7\text{-AQDS}}$ and $g_{1,4\text{-AQCIOH}}$ are -2.10 and -1.71, respectively. These values correspond to free energies of interaction of approximately -2.6 and -2.1 kJmol⁻¹. These values are consistent with electron-donor / acceptor interactions associated with hydrogen bonding among similar adsorbates. The interaction parameter between unlike molecules, $g_{2,7\text{-AQDS, 1,4-AQCIOH}}$, is -0.95 ± 0.1 indicating that attractive interactions exist between the 2,7-AQDS and 1,4-AQCIOH adsorbates. Moreover, this g_{ij} value corresponds to an interaction energy of approximately -1.1 kJ mol⁻¹ indicating that the interactions between unlike molecules are comparable in strength to those found between similar adsorbates. Thus, it appears that in mixed monolayers individual adsorbates do not have a significant preference for being surrounded by their own kind with the free energy of interaction between unlike adsorbates being sufficient to overcome the entropy of mixing.

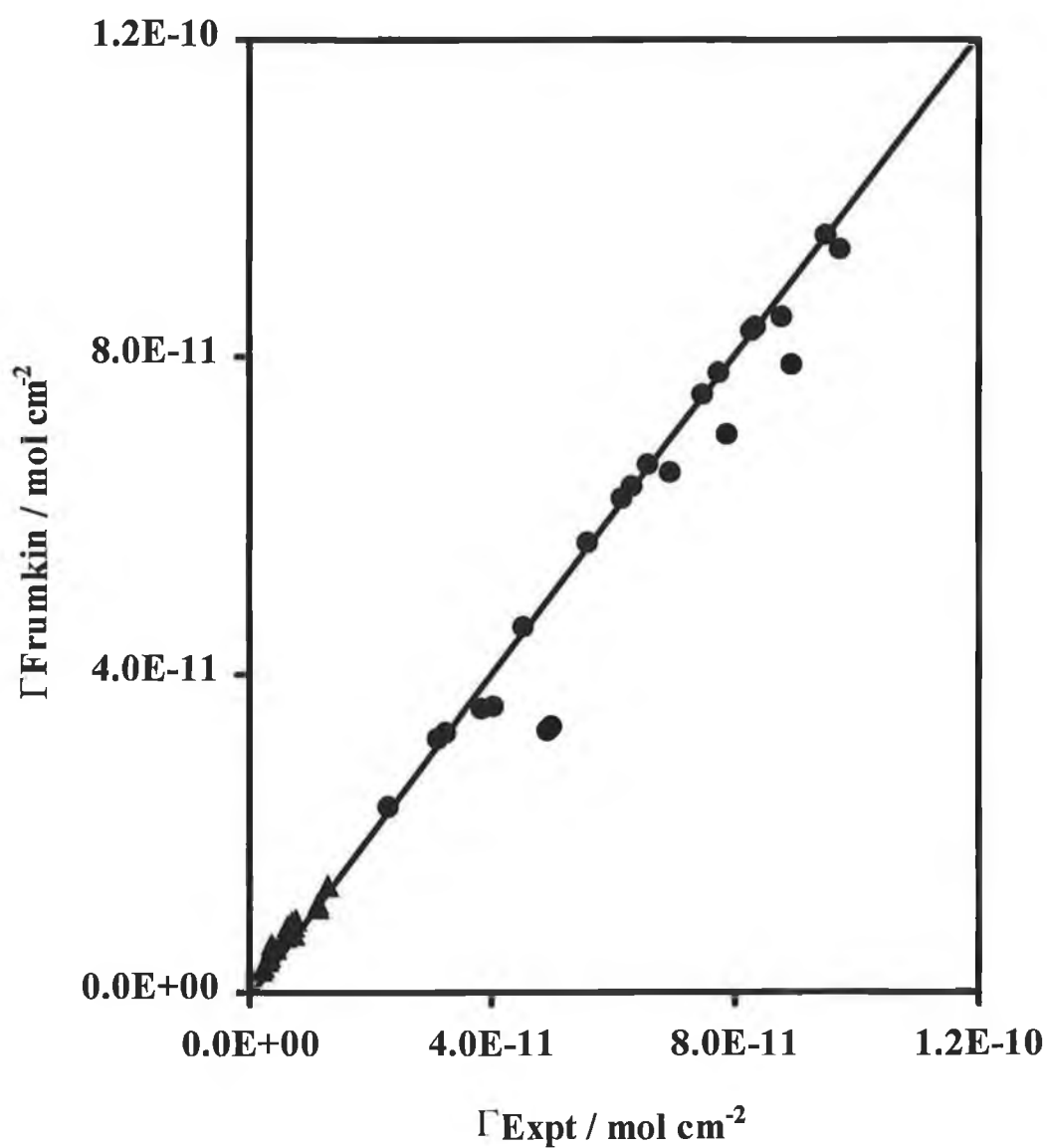


Figure 10 Ability of the competitive Frumkin adsorption isotherms to predict the experimental surface coverages of 2,7-AQDS and 1,4-AQCIOH within two-component monolayers. The solid line indicates the behaviour expected for a direct unbiased correlation.

6.3.6 Adsorption dynamics

Mixed deposition solutions of 2,7-AQDS and 1,4-AQClOH were prepared in order to study the adsorption process at binary monolayers. Table 2 shows the factorial design for the series of mixed deposition solution used. 10 different levels were used in this design with 10 different mixed solutions in each level. Using this system allows us to probe adsorption under a variety of conditions in order to further our understanding of adsorption from mixed quinone solutions. Table 2 also contains the surface coverages and adsorption coefficients for each of the 10 levels analysed for 1,4-AQClOH in the presence of 2,7-AQDS using the Langmuir isotherm.

Figure 11 shows the voltammetric response for a mercury electrode immersed in a deposition solution containing 20 μ M each of 2,7-AQDS and 1,4-AQClOH. The surface coverage can be seen to be markedly different for each quinone when adsorbed from equimolar deposition solutions. This result is not that surprising considering the differences in the adsorption coefficients of each quinone as determined from data for single component monolayers (Table 1).

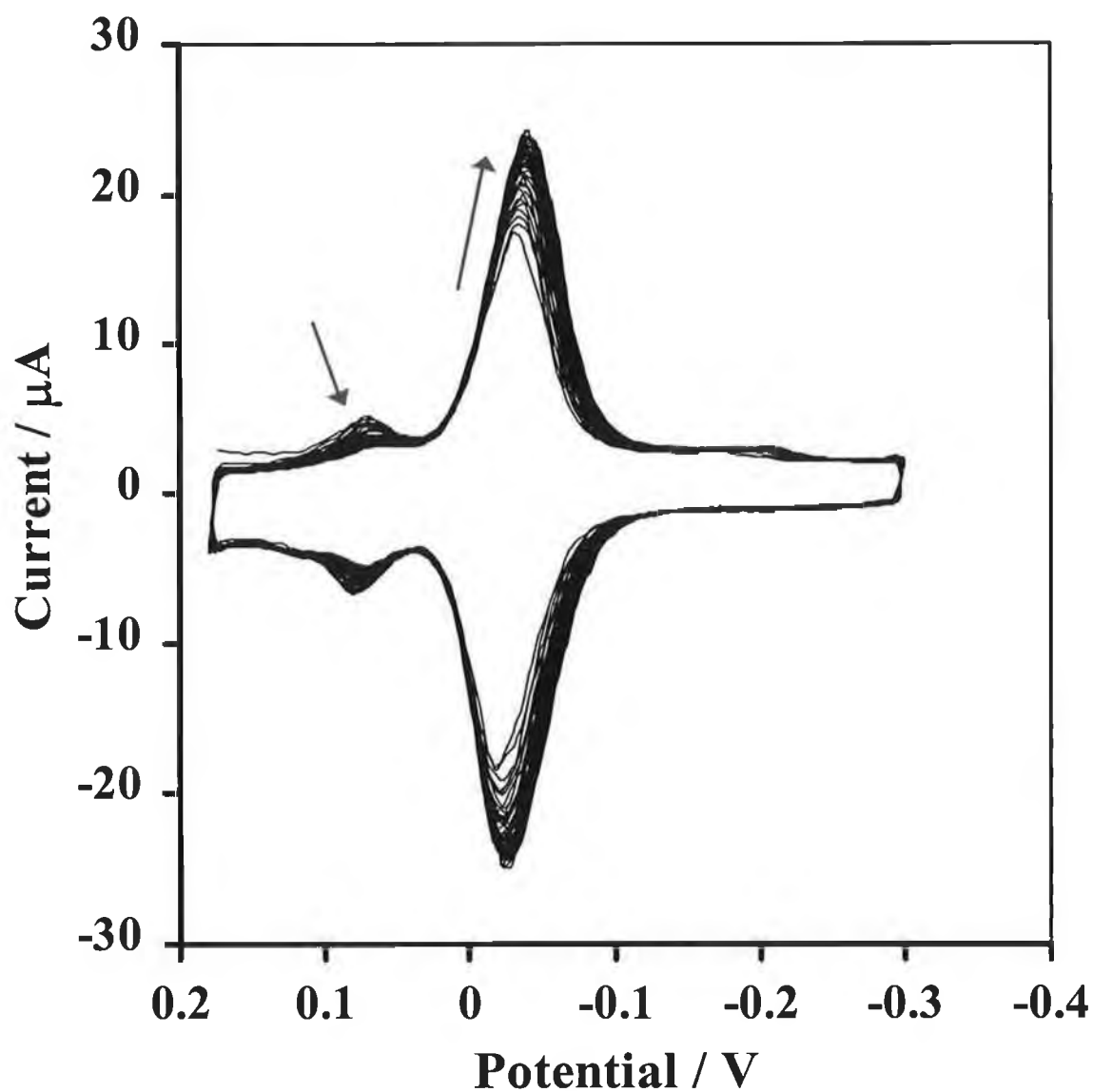


Figure 11 Cyclic voltammetry response of a mercury electrode immersed in a deposition solution containing 20 μM of 2,7-AQDS and 1,4-AQClOH. Fifty cycles were required for equilibrium coverage to be attained. The arrows indicate the direction of the peaks with successive scans.

Table 2

Factorial design system for 2,7-AQDS and 1,4-AQClOH.

Conc. 2,7	Conc. 1,4	Ratio 2,7:1,4	
20	20	1	$\Gamma / \text{mol cm}^{-2}$
20	18	0.9	
20	16	0.8	$1.33\text{E-}10$
20	14	0.7	
20	12	0.6	β / M^{-1}
20	10	0.5	
20	8	0.4	$3.05\text{E+}05$
20	6	0.3	
20	4	0.2	
20	2	0.1	

2,7	1,4	Ratio	
18	20	1.11	$\Gamma / \text{mol cm}^{-2}$
18	18	1.00	
18	16	0.89	$1.40\text{E-}10$
18	14	0.78	
18	12	0.67	β / M^{-1}
18	10	0.56	
18	8	0.44	$2.28\text{E+}05$
18	6	0.33	
18	4	0.22	
18	2	0.11	

2,7	1,4	Ratio	
16	20	1.25	$\Gamma / \text{mol cm}^{-2}$
16	18	1.13	
16	16	1.00	$1.57\text{E-}10$
16	14	0.88	
16	12	0.75	β / M^{-1}
16	10	0.63	
16	8	0.50	$1.80\text{E+}05$
16	6	0.38	
16	4	0.25	
16	2	0.13	

2,7	1,4	Ratio	
14	20	1.43	$\Gamma / \text{mol cm}^{-2}$
14	18	1.29	
14	16	1.14	$1.35\text{E-}10$
14	14	1.00	
14	12	0.86	β / M^{-1}
14	10	0.71	
14	8	0.57	$3.44\text{E+}05$
14	6	0.43	
14	4	0.29	
14	2	0.14	

2,7	1,4	Ratio	
12	20	1.67	$\Gamma / \text{mol cm}^{-2}$
12	18	1.50	
12	16	1.33	$1.60\text{E-}10$
12	14	1.17	
12	12	1.00	β / M^{-1}
12	10	0.83	
12	8	0.67	$1.71\text{E+}05$
12	6	0.50	
12	4	0.33	
12	2	0.17	

2,7	1,4	Ratio	
10	20	2.00	$\Gamma / \text{mol cm}^{-2}$
10	18	1.80	
10	16	1.60	$1.38\text{E-}10$
10	14	1.40	
10	12	1.20	β / M^{-1}
10	10	1.00	
10	8	0.80	$2.78\text{E+}05$
10	6	0.60	
10	4	0.40	
10	2	0.20	

Table 2 Continued factorial design table from previous page.

2,7	1,4	Ratio	
8	20	2.50	$\Gamma / \text{mol cm}^{-2}$
8	18	2.25	
8	16	2.00	$1.42\text{E-}10$
8	14	1.75	
8	12	1.50	β / M^{-1}
8	10	1.25	
8	8	1.00	$2.90\text{E+}05$
8	6	0.75	
8	4	0.50	
8	2	0.25	

2,7	1,4	Ratio	
6	20	3.33	$\Gamma / \text{mol cm}^{-2}$
6	18	3.00	
6	16	2.67	$1.40\text{E-}10$
6	14	2.33	
6	12	2.00	β / M^{-1}
6	10	1.67	
6	8	1.33	$3.21\text{E+}05$
6	6	1.00	
6	4	0.67	
6	2	0.33	

2,7	1,4	Ratio	
4	20	5.00	$\Gamma / \text{mol cm}^{-2}$
4	18	4.50	
4	16	4.00	$1.68\text{E-}10$
4	14	3.50	
4	12	3.00	β / M^{-1}
4	10	2.50	
4	8	2.00	$1.04\text{E+}05$
4	6	1.50	
4	4	1.00	
4	2	0.50	

2,7	1,4	Ratio	
2	20	10.00	$\Gamma / \text{mol cm}^{-2}$
2	18	9.00	
2	16	8.00	$1.45\text{E-}10$
2	14	7.00	
2	12	6.00	β / M^{-1}
2	10	5.00	
2	8	4.00	$1.33\text{E+}05$
2	6	3.00	
2	4	2.00	
2	2	1.00	

However, the most surprising result of Figure 11 is that the initial equilibrium coverages obtained change as the film is cycled. The peak attributed to 2,7-AQDS *decreased* in magnitude and the peak associated with 1,4-AQC1OH *increased* as the potential was swept repetitively. Three possible mechanisms could describe the process of “adsorbate exchange” within the mixed monolayers.

(1). When the concentration of anthraquinones in solution were at a level where saturation coverage was obtainable, a reduction in peak current for 2,7-AQDS occurred while the corresponding 1,4-AQC1OH peak increased. We believe equilibrium to be occurring in two successive ways. When the mercury drop is displaced and comes into contact with the deposition solution, equilibrium initially occurs between the complexes adsorbed on the electrode and present in solution as well as between both adsorbed anthraquinones on the electrode surface. The first scan in the cyclic voltammogram is representative of this total equilibrium. However, on successive voltammetric scanning the equilibrium on the surface changes. It appears that reduction of 2,7-AQDS to 2,7-H₂QDS disrupts the equilibrium on the surface and the corresponding peak current (1,4-AQC1OH) increases. The following mechanism may explain the observed behaviour. The reduced form of 2,7-AQDS, the hydroquinone, is more weakly adsorbed on the electrode than its oxidised counterpart. If so, the hydroquinone may either; (A), naturally desorb from the surface of the electrode and 1,4-AQC1OH adsorbs, due to the differences in adsorption strength (β) of the reduced form of the quinone relative to the oxidised form, or (B), the oxidised form of 1,4-AQC1OH may aid in the ejection of the hydroquinone and then itself adsorb. If A occurs then the process of adsorption of 1,4-AQC1OH onto the free space on the electrode may be due to natural diffusion of the redox-active species and follow modified first order kinetics. If B occurs, second order kinetics should apply. These two limiting cases can be distinguished by modelling the time evolution of the surface coverage.

Using the data obtained from the factorial design system we have successfully determined surface coverages for both quinones and have used this data to determine which order of kinetics the desorption of 2,7-AQDS follows. Figure 12 and Figure 13 illustrates the kinetic responses obtained for the cathodic branch of 2,7-AQDS when adsorption occurred

from a deposition solution containing 4 μm of each quinone. A linear response was observed for the first order plot whereas a curved plot was obtained for the second order plot. The former seems to account for the process of desorption of the 2,7-AQDS sub-monolayer. First order decays were observed for all 2,7-AQDS data.

(2). At coverages where saturation is not achieved and the concentration of 2,7-AQDS is at a much higher concentration in solution over 1,4-AQClOH, the effect of the quinones on the electrode is markedly different. Instead of observing a decrease in the concentration of 2,7-AQDS on the electrode surface during cyclic voltammetry an *increase* is noticed. This increase in current of the two quinones is not the same. The current of 1,4-AQClOH seems to increase approximately twice as much as 2,7-AQDS. This is most likely due to the stronger adsorption strength of 1,4-AQClOH.

(3). At coverages where the concentration of 1,4-AQClOH in solution is higher than that of 2,7-AQDS, then adsorbed 2,7-AQDS on the electrode surface desorbs until none remains. We believe this to be a consequence of the saturation coverages, free energy of adsorption and interaction parameter for the mixed system.

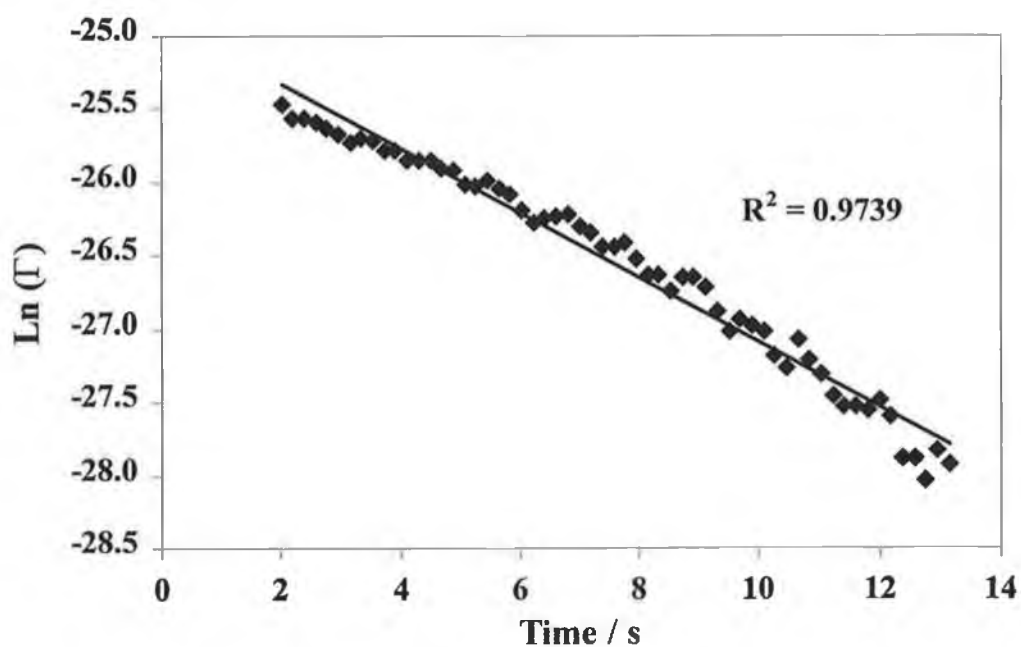


Figure 12 First order kinetic plot for the desorption of 2,7-AQDS from a mercury electrode.

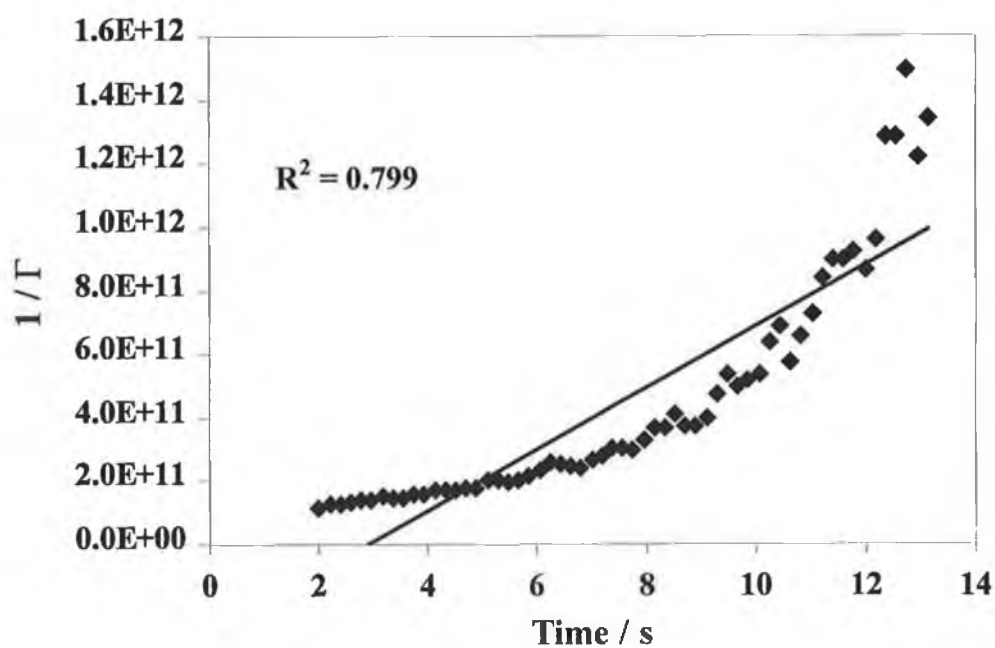


Figure 13 Second order kinetic plot for desorption of 2,7-AQDS from a mercury electrode.

The effect of adsorption of 1,4-AQClOH may be significantly more complicated when adsorption has already occurred and when free space becomes available for the subsequent adsorption of species from solution. In this situation, additional parameters need to be included to account for diffusion of the incoming adsorbate in solution. The treatment may include assumptions such as the degree to which adsorption equilibrium is attained before the electrochemical experiment is initiated and also the relative rate of electron transfer to the adsorbed species compared to that of the dissolved species. Using an equation²¹ to include these assumptions an estimate for the saturation surface coverage, adsorption coefficient and the diffusion were determined for mixed equimolar solutions;

$$\left(\frac{\Gamma_i(t)}{\Gamma_i} \right) = 1 - \exp\left(-\frac{D_i t}{b_i^2} \right) \operatorname{erfc} \left[\frac{(D_i t)^{1/2}}{b_i} \right] \quad \text{Eq. 5}$$

where $b = \beta\Gamma_s$. A plot of $\Gamma_i(t)/\Gamma_i$ vs t shows the rate of attainment of equilibrium. An example of which is illustrated in Figure 14. The results obtained for all equimolar solutions from 2 up to 20 μm of each quinone solution show approximately equal values for Γ_s , β , and the diffusion coefficient. These values obtained from Eq. 5 were compared to those determined using the Frumkin isotherm under true thermodynamic conditions. The averaged β value determined from Eq. 5, $9.9 \times 10^4 \text{ M}^{-1}$ is close to that found using the Frumkin isotherm, $7.5 \times 10^4 \text{ M}^{-1}$, whereas for Γ_s , Eq. 5 gives 1.00×10^{-10} while the Frumkin isotherm gives $1.9 \times 10^{-10} \text{ mol / cm}^2$. Although differences are observed, the correlation between thermodynamic and kinetic data is encouraging and supports the proposed mechanism. The diffusion coefficient obtained using Eq. 5 was $1.00 \times 10^{-6} \text{ cm}^2 \text{ s}^{-1}$. This value seems rather low for solution phase diffusion. It seems likely diffusion of the electroactive species on the electrode surface following 2,7-AQDS desorption influences the kinetics

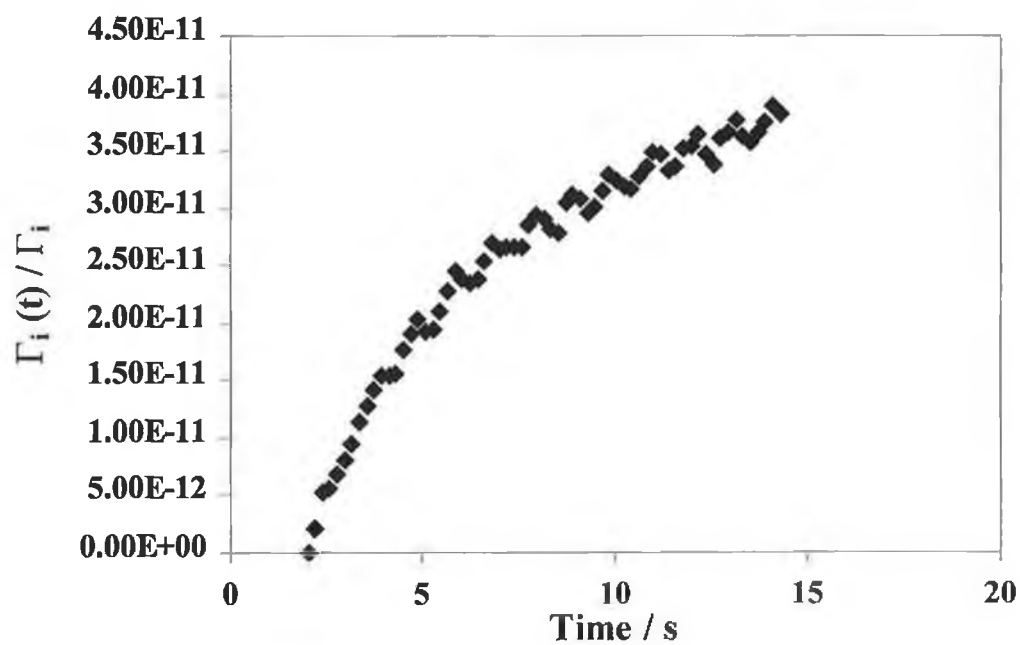


Figure 14 Rate of attainment of equilibrium coverage Γ_i for diffusion controlled adsorption of 1,4-AQClOH using equimolar deposition solutions of 2,7-AQDS and 1,4-AQClOH.

6.4 Conclusions

Single and binary monolayers have been formed by spontaneous adsorption of 2,7-AQDS and 1,4-AQClOH, both of which are stable in their reduced and oxidised forms. The adsorbates interact laterally within both single- and two-component monolayers with the concentration dependence of the surface coverage being adequately described by the Frumkin adsorption isotherm over the concentration range 1 – 30 μM . The formal potentials, saturation surface coverages, free energies of adsorption and Frumkin interaction parameters are all affected by co-adsorption of the second quinone. These observations suggest that dissimilar adsorbates interact laterally, most likely through intermolecular hydrogen bonding. The data suggest that dense two-component monolayers consist of a single phase which is in equilibrium with the contacting solution.

Our results provide important background information about the correlation that exists between intermolecular interactions and the interfacial structure which underpins important applications in chemical sensors and chromatographic stationary phases.

6.5 References

1. Notoya, T.; Polling, G. W. *Corrosion* **1979**, *35*, 193.
2. Lensen, H. G. W.; Bargeman, D.; Bergveld, P.; Smolders, C. A.; Feigen, J. J. *Colloid. Interface Sci.* **1984**, *99*, 1.
3. Kaelble, D. H. in *Physical Chemistry of Adhesion*; Wiley-Interscience, New York, 1971.
4. Forster, R. J.; Diamond, D. *Anal. Communications*, **1996**, *33*, 1H.
5. Ta, T. C.; Kanda, V.; McDermott, M. T. *J. Phys. Chem. B* **1999**, *103*, 1295.
6. Paleos, C. M.; Tsiourvas, D. *Adv. Mater.* **1997**, *9*, 965.
7. Xiao, K. P.; Buhlmann, P.; Umezama, Y. *Anal. Chem.* **1999**, *71*, 1183.
8. Folkers, J. P.; Laibinis, P. E.; Whitesides, G. M.; Deutch *J. Phys. Chem.* **1994**, *98*, 563.
9. Forster, R. J.; Faulkner, L. R. *Anal. Chem.* **1995**, *67*, 1232.
10. Peng, W.; Rusling, J. F. *J. Phys. Chem. B* **1995**, *99*, 16436.
11. Mirnada, P. B.; Pflumio, V.; Saijo, H.; Shen, Y. R. *J. Am. Chem. Soc.* **1998**, *120*, 12092.
12. He, P.; Crooks, R. M.; Faulkner, L. R. *J. Phys. Chem.* **1990**, *94*, 1135.
13. Ariga, K.; Kunitake, T. *Acc. Chem. Res.* **1998**, *31*, 371.
14. Sakurai, M.; Tamagawa, H.; Inoue, Y. Ariga, K.; Kunitake, T. *J. Phys. Chem. B* **1997**, *101*, 4810.
15. Sugawara, M. Kojima, K.; Sazawa, H.; Umezawa, Y. *Anal. Chem.* **1987**, *59*, 2842.
16. Forster, R. J. *Langmuir* **1995**, *11*, 2247.
17. Forster, R. J. *Anal. Chem.* **1996**, *68*, 3143.
18. Forster, R. J. *J. Electrochem. Soc.* **1997**, *144*, 1165.
19. Laviron, E. *J. Electroanal. Chem.* **1974**, *52*, 395.
20. Brown A. P.; Anson, F. C. *Anal. Chem.* **1977**, *49*, 158.
21. Bard, A. J. and Faulkner, L. R. *Electrochemical Methods: Fundamentals and Applications*; Wiley: New York, 1980.
22. Laviron, E. *J. Electroanal. Chem.*, **1982**, *12*, 53.
23. Trassatti S., *J. Electroanal. Chem.*, **1974**, *53*, 335.

24. Damaskin, B. D.; Petrii, O. A.; Batrakov, V. V. *Adsorption of Organic Compounds on Electrodes*, Plenum Press, 1971, New York.
25. O'Kelly, J. P.; Forster, R. J, *The Analyst*, **1998**, *123*, 1987.
26. Tamagawa, H.; Sakurai, M.; Inoue, Y.; Ariga, K. Kunitake, T. *J. Phys. Chem. B* **1997**, *101*, 4817.
27. Chi, L. F.; Johnston, R. R.; Ringsdorf, H. *Langmuir*, **1991**, *7*, 2323.
28. Subramaniam, S.; McConell, H., *M. J. Phys. Chem.* **1987**, *91*, 1715.

CHAPTER 7

Conclusions

7 Conclusions

The electrode / solution interface has fascinated electrochemists for decades due to variety of interesting processes such as, analyte detection, electron transfer, protective layers, electronic and optical devices and self-assembly that occur at solid / solution or solid / membrane interfaces. The latter, being one of the most recent advances in modern electrochemistry.

The self-assembly approach represents a very attractive means of combining structurally well-ordered films that offer precise control of spacing and orientation on a molecular level. This ability to control spacing of organic molecules adsorbed on metal substrates enables the local microenvironment to be controlled. Therefore, chemists are able to perform careful experiments to extract information on the mechanisms of electron transport, lateral interactions and ion-pairing of immobilised species.

The understanding of interfacial layers has been greatly improved through the advances in technology, namely, improved methods for surface characterisation at molecular dimensions and at short times. Changes in electrode dimensions has also offered the ability to explore the electrochemistry of adsorbed films at short timescales. Timescales as low as nanoseconds are now becoming commonplace within laboratories, with the picosecond timescale now becoming within reach for many researchers. This new time domain for these small electrodes has redefined the spatial limits for analysis and opened up areas once thought of as impossible to explore such as, the measure of oxygen concentrations in tissue and the concentrations of radicals in organic solvents that live for only a few nanoseconds. Current interests using microelectrodes has focussed on both solution phase and adsorbed species in terms of surface chemical bonding, packing and molecular level orientation.

Examination of immobilised species has ranged from polymers, alkanethiols and recently redox-active transition metal complexes and quinone species. The driving force in this area is to form materials that are ordered on the molecular level. The thickness of these films range from tens to hundreds of angstroms depending on whether monolayers or multilayers

are formed and their composition may be manipulated to suit particular situations. In this work we have used both transition metal complexes and quinones to explore the degree of electronic interaction between the redox centres themselves and with the underlying substrate on which they are spontaneously adsorbed. The results obtained will help remove some of the barriers to progress in areas such as corrosion protection, chromatography, adhesion, and sensors.

The electrochemistry of a series of osmium polypyridyl complexes of the type $[\text{Os}(\text{bpy})_2\text{LCl}]^+$ where $\text{bpy} = 2,2'$ bipyridine and $\text{L} = 4,4'$ -dipyridyl, 1,2-bis(4-pyridyl)ethane, or 4,4'-trimethylenedipyridine was examined in Chapter 4. The voltammetry obtained was consistent with that from an Os^{2+} to Os^{3+} species. Peak to peak splitting was considerably higher than expected, i.e., 73 mV, whereas under ideal conditions a zero peak to peak splitting is expected. For monolayers of this type not only can interactions occur between redox-active head groups but also may occur when switching of the redox state of the monolayer is induced. This switching introduces electrostatic interactions and may account for the larger splitting experienced over monolayers where electrostatics do not apply. Monolayers of $[\text{Os}(\text{bpy})_2\text{P3PCl}]^+$ were also shown to exhibit strong ion-pairing with a number hydrophobic and hydrophilic anions. This was witnessed by a progressive negative shift in the formal potential resulting in making oxidation more facile with increasing electrolyte concentration. Temperature effects on $[\text{Os}(\text{bpy})_2\text{P2PCl}]^+$ monolayers showed increased FWHM values at the elevated temperatures. However, the increase was not significantly large enough to conclude that temperature caused an increase in interactions. The differences are most possibly due to thermal broadening.

In the initial analysis of lateral interactions amongst spontaneously adsorbed species, 1-amino-2-sulphonic-4-hydroxy-anthraquinone $[\text{AQNH}_2\text{SOH}]$ was analysed. This quinone was shown to exhibit extremely well defined voltammetric responses at concentrations typically in the micromolar range. Splitting between the anodic and cathodic peak potentials was as low as 17 mV for monolayers formed from 1 μm deposition solutions and the full width at half height for the same monolayer was 53 mV. These results are higher

than expected for an immobilised species under ideal conditions, however in comparison to redox-active species containing different charges in different redox states, they would be considered quite low. The electrochemistry observed for [AQNH₂SOH] monolayers at high concentrations, typically 1.5 μ m and greater, proved to be extremely interesting. In the anodic branch of the voltammetric response from [AQNH₂SOH] monolayers, an unusually large sharp spike was witnessed. The spike was never at any time greater than a few millivolts wide and suggests the response is possibly due to some form of surface feature rather than a diffusional process. If the spike is due to a surface effect then interactions between adsorbates may be accountable. Electron and proton transfer are coupled in quinonoid monolayers and therefore, switching between Q and H₂Q does not change the state of charge of the film. Thus, electrostatic effects are unlikely to significantly influence the nature or degree of lateral interactions.

Interactions on electrode surfaces between immobilised species can also result in hydrogen bonding. This is possible because of the diminished inter-site separation between adsorbates. This seems likely as the spike appeared in the voltammetry at concentrations where saturation coverage was approaching and the position where separation of the adsorbates are at their lowest.

Molecular modelling of this quinone shows us that intramolecular hydrogen bonding is possible between certain groups. Although modelling was unable to aid in determining the extent of intermolecular hydrogen bonding due to constraints within the package we have determined through other methods that intermolecular interactions are highly possible. Protonation of the quinone resulted in a significant decrease in the intensity of the spike between the pH of 1.03 and 4.1. Also, when temperature was applied to the system the intensity of the spike decreased. We believe that this quinone orders itself on the mercury surface in a manner in which hydrogen bonding may take effect and when temperature is applied to the system, the ordered monolayer is broken down due to disorder from the temperature increase. This would result in an increase in inter-site separation such that intermolecular hydrogen bonding cannot be supported, with the resultant loss of the spike.

This interaction theme was continued in Chapter 6 whereby binary monolayers of anthraquinone-2,7-disulphonic acid (2,7-AQDS) and 1-chloro-4-hydroxy-anthraquinone (1,4-AQClOH) were adsorbed on mercury electrodes and investigated. Single and binary monolayers exhibited well-defined electrochemistry and the adsorbates interact laterally within both single- and two-component monolayers with the concentration dependence of the surface coverage being adequately described by the Frumkin adsorption isotherm over the concentration range 1 – 30 μM .

The fact that the formal potential, the free energies of adsorption, the saturation coverages and Frumkin interaction parameter all change when the monolayer exists as a binary system suggests that adsorbates are affected by the adsorption of the second quinone. Also, these results suggest dissimilar adsorbates interact laterally most probably through intermolecular hydrogen bonding.

The rate of adsorption of these binary monolayers was also found to differ. After initial adsorption, it was found that 2,7-AQDS desorbed from the electrode surface and 1,4-AQClOH adsorbed to the free area. 2,7-AQDS was found to desorb according to first order kinetics. Desorption is most possibly due to the reduced form of the quinone having a lower adsorption coefficient over the reduced form of 1,4-AQClOH. Results indicate 1,4-AQClOH to freely move around the free surface before adsorption of diffusing 1,4-AQClOH.

Transition metal and quinone compounds offer a novel way to analyse monolayers which may undergo hydrogen bonding through lateral interactions amongst adsorbates since they form unusually ideal and stable films on a variety of electrode surfaces. In conclusion, it is hoped this work may offer an insight into processes, which occur at the electrode / solution interface from these immobilised redox-active.

Major Symbols

Roman Symbols

A	area	cm ²
C	capacitance	F
C _d	differential capacitance of the double layer	μF cm ²
E _f	final potential	V
E _i	initial potential	V
E _{max}	maximum potential	V
E _{min}	minimum potential	V
E _p	peak potential	V
E _{pa}	anodic peak potential	V
E _{pc}	cathodic peak potential	V
ΔE _{p1/2}	E _{pa} – E _{pc} in CV	V
ΔH _f [‡]	standard enthalpy of activation	KJ mol ⁻¹
ΔS _{rc} [*]	reaction entropy	J mol ⁻¹ K ⁻¹
F	the Faraday: charge on one mole of electrons	C
i _{pa}	anodic peak current	A
i _{pc}	cathodic peak current	A
i _{ss}	steady state current	A
k	heterogeneous electron transfer rate constant	s ⁻¹
Q	charge passed in electrolysis	C
r _s	electrode radius	cm
V	scan rate	V

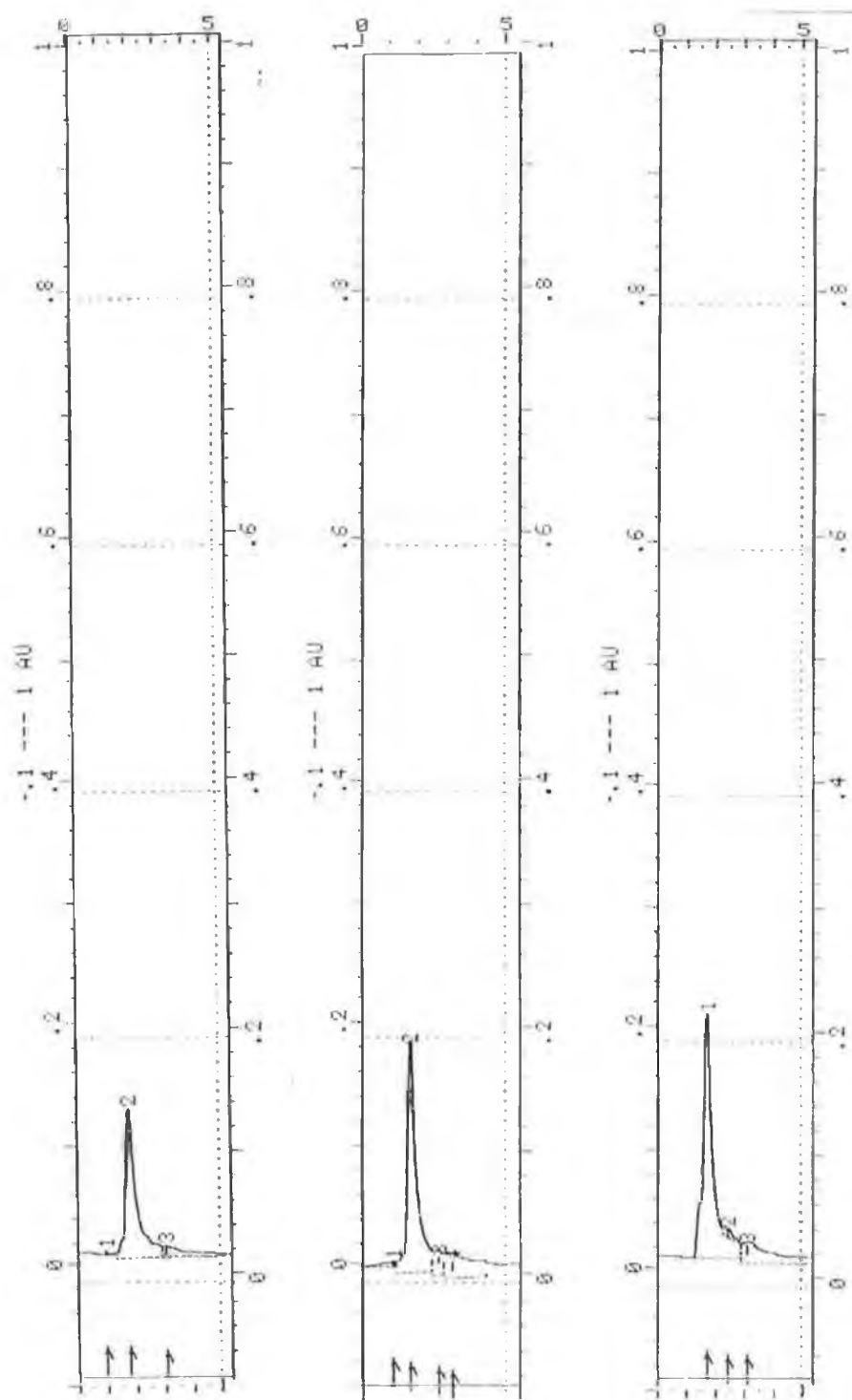
Greek Symbols

β	absorption coefficient	M ⁻¹
η	overpotential, E - E _{eq}	V, mV
Γ	surface coverage	molcm ⁻²
σ ^d	excess charge density in the diffuse layer	
σ ^I	charge density from specifically adsorbed ions in the inner layer	
σ ^m	charge density on the electrode side of the double layer	
σ ^s	total charge density	
C	concentration	M

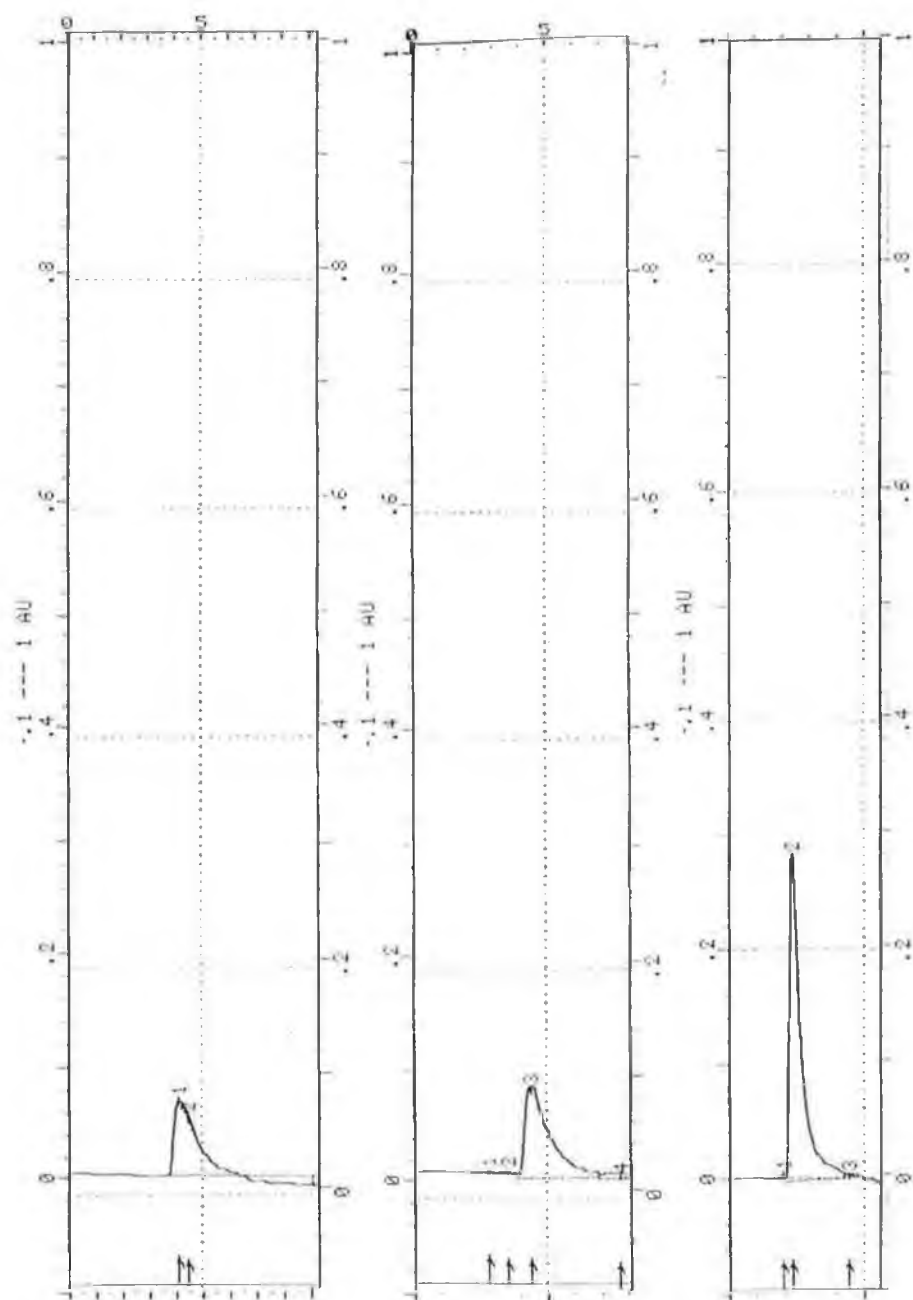
Standard Abbreviations

[1,2,4-AQNH ₂ SOH]	1-amino-2-sulphonic-4-hydroxy-anthraquinone
[1,4-AQClOH]	1-chloro-4-hydroxy-anthraquinone
[2,7-AQDS]	anthraquinone-2-7-disulphonic acid
ACN	acetonitrile
bpy	bipyridine
CV	cyclic voltammetry
DMF	N, N-dimethylformamide
DMSO	dimethylsulfoxide
FWHM	full width at half maximum
LiClO ₄	lithium perchlorate
P0P	4,4' -dipyridyl
P2P	1,2-bis(4-pyridyl)ethane
P3P	4,4' -trimethylenedipyridine
py	pyridine
PZC	potential of zero charge
Q	quinone
QH ₂	hydroquinone
SAM	self assembled monolayer
SFM	scanning force microscopy
STM	scanning tunnelling microscopy
UME	ultramicroelectrode

Appendix 1

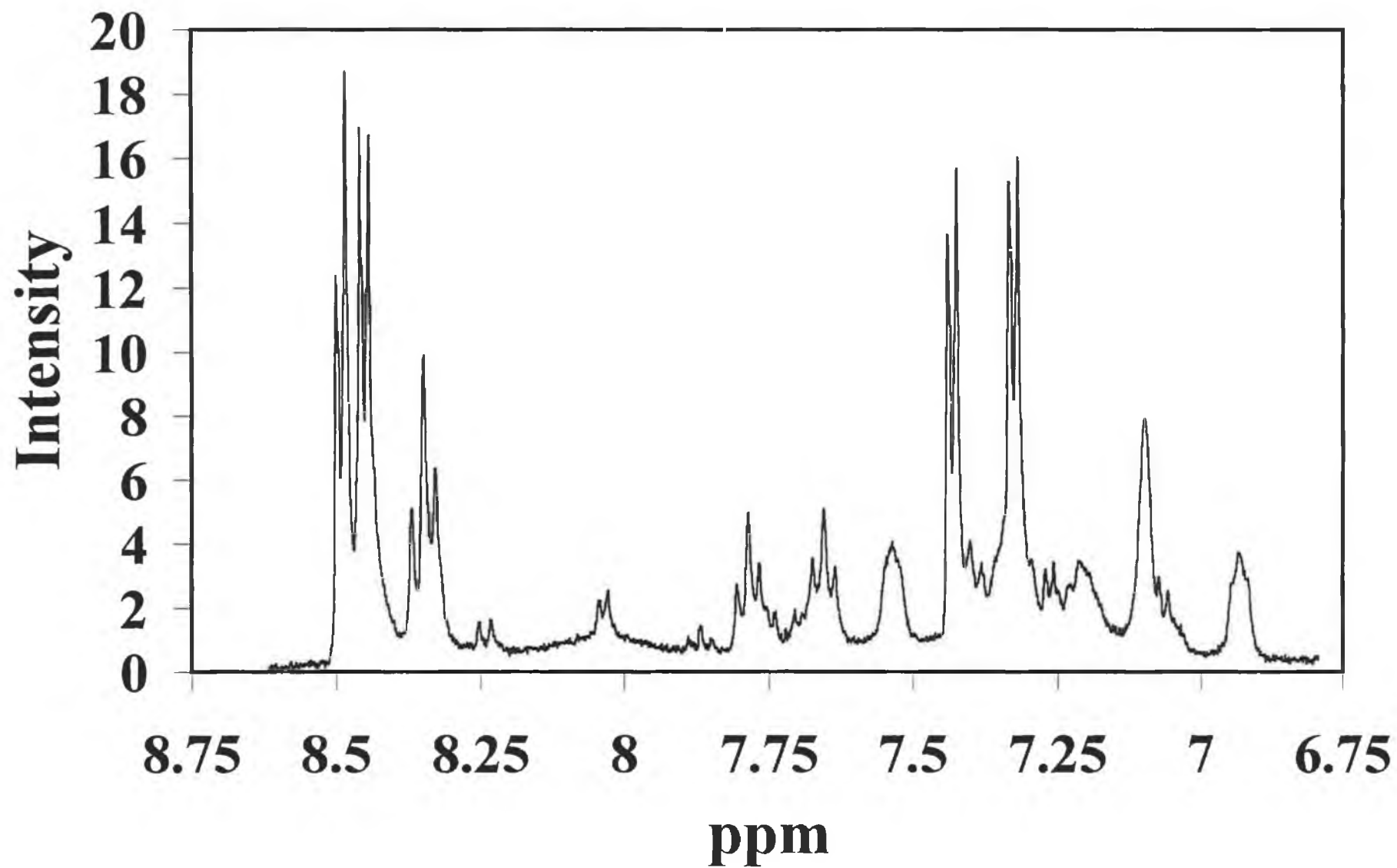


HPLC traces for $N_5 - Cl$ osmium polypyridyl complexes.

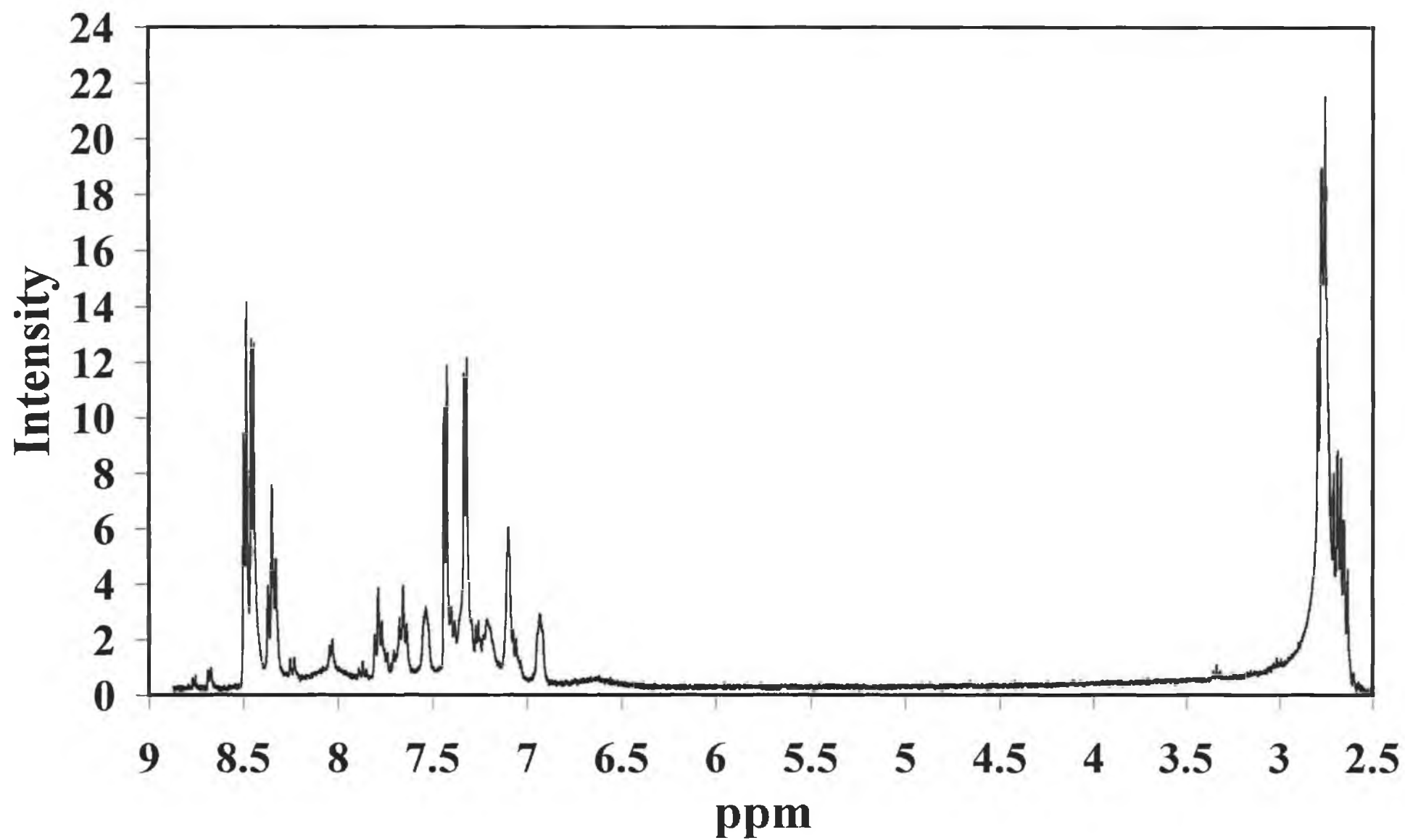


HPLC traces for N_6 osmium polypyridyl complexes.

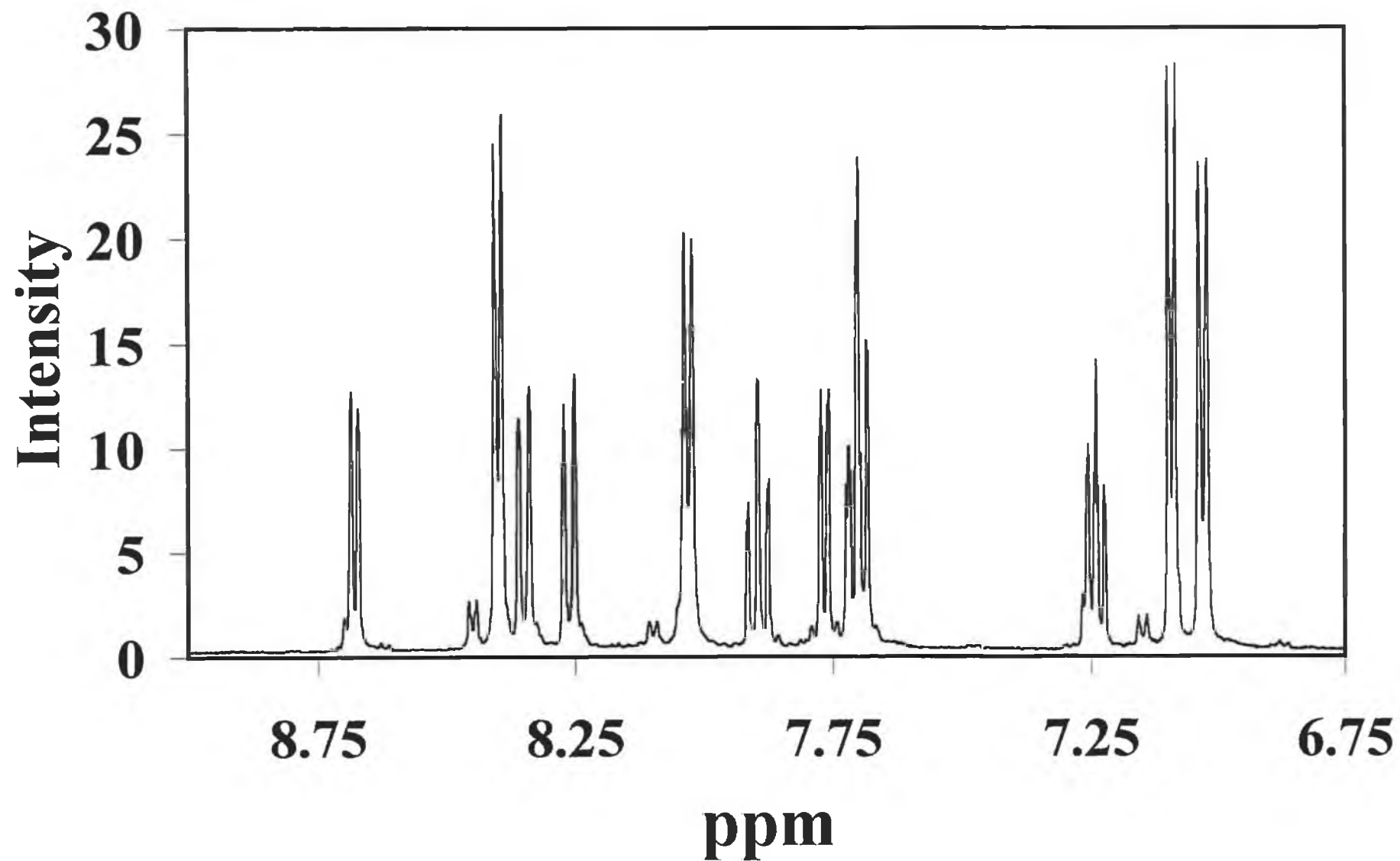
^1H NMR $[\text{Os}(\text{bpy})_2\text{P2P Cl}]^+$, aromatic region in CH_3CN



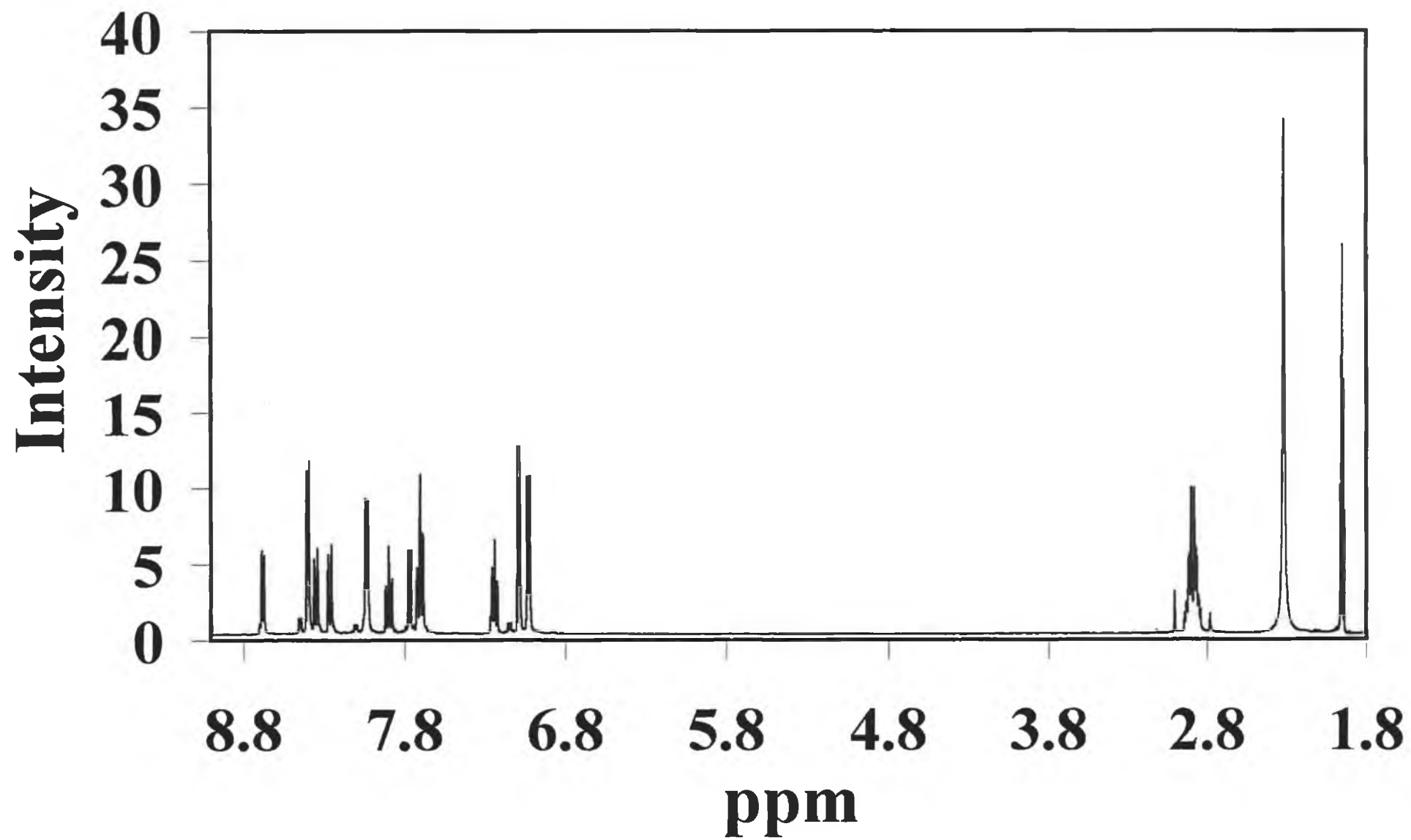
^1H NMR $[\text{Os}(\text{bpy})_2\text{P2P Cl}]^+$ in CH_3CN



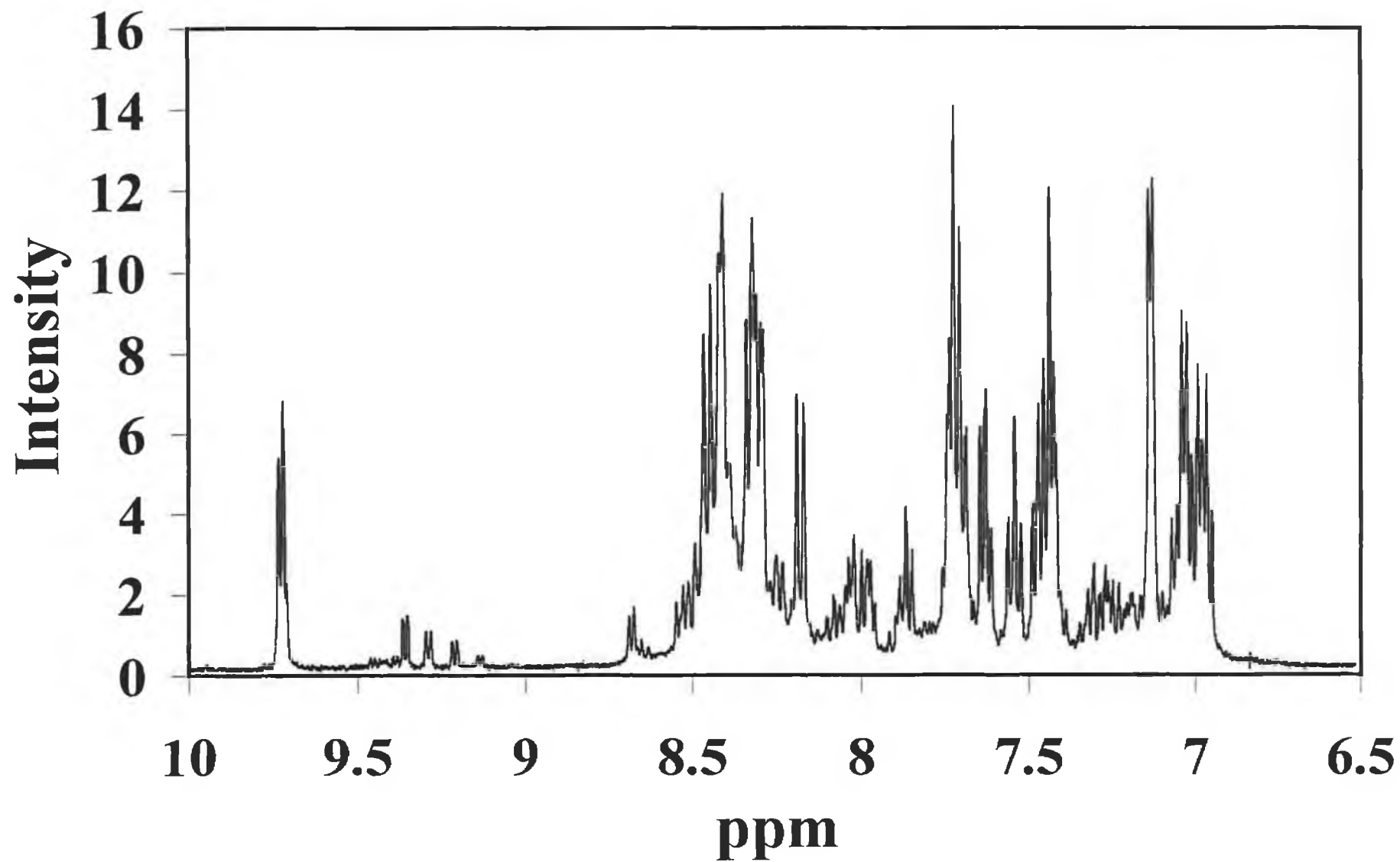
^1H NMR $[\text{Os}(\text{bpy})_2(\text{P2P})_2]^{2+}$, aromatic region, in CH_3CN



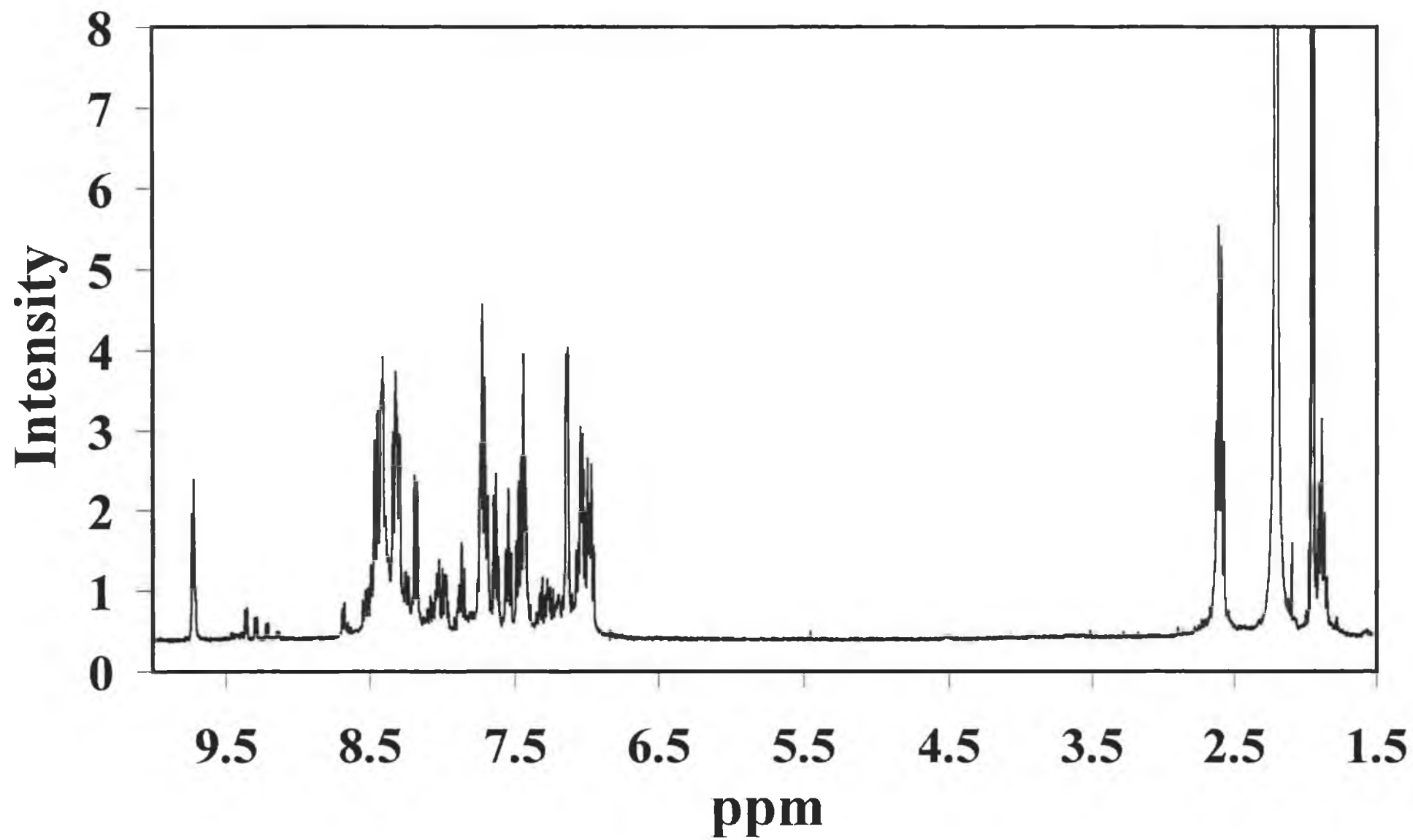
^1H NMR $[\text{Os}(\text{bpy})_2(\text{P2P})_2]^{2+}$ in CH_3CN



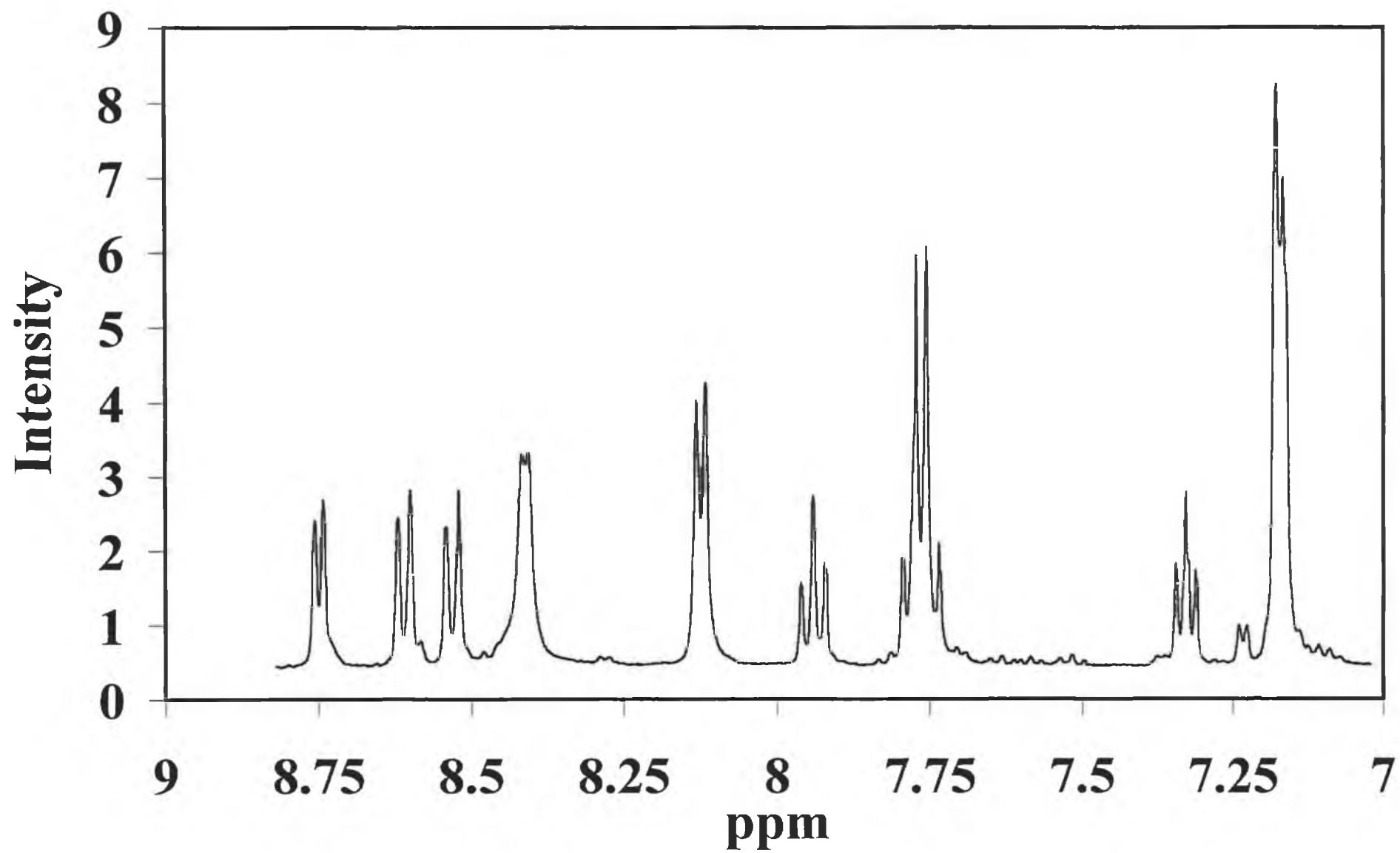
^1H NMR $[\text{Os}(\text{bpy})_2\text{P3P Cl}]^+$, aromatic region in CH_3CN



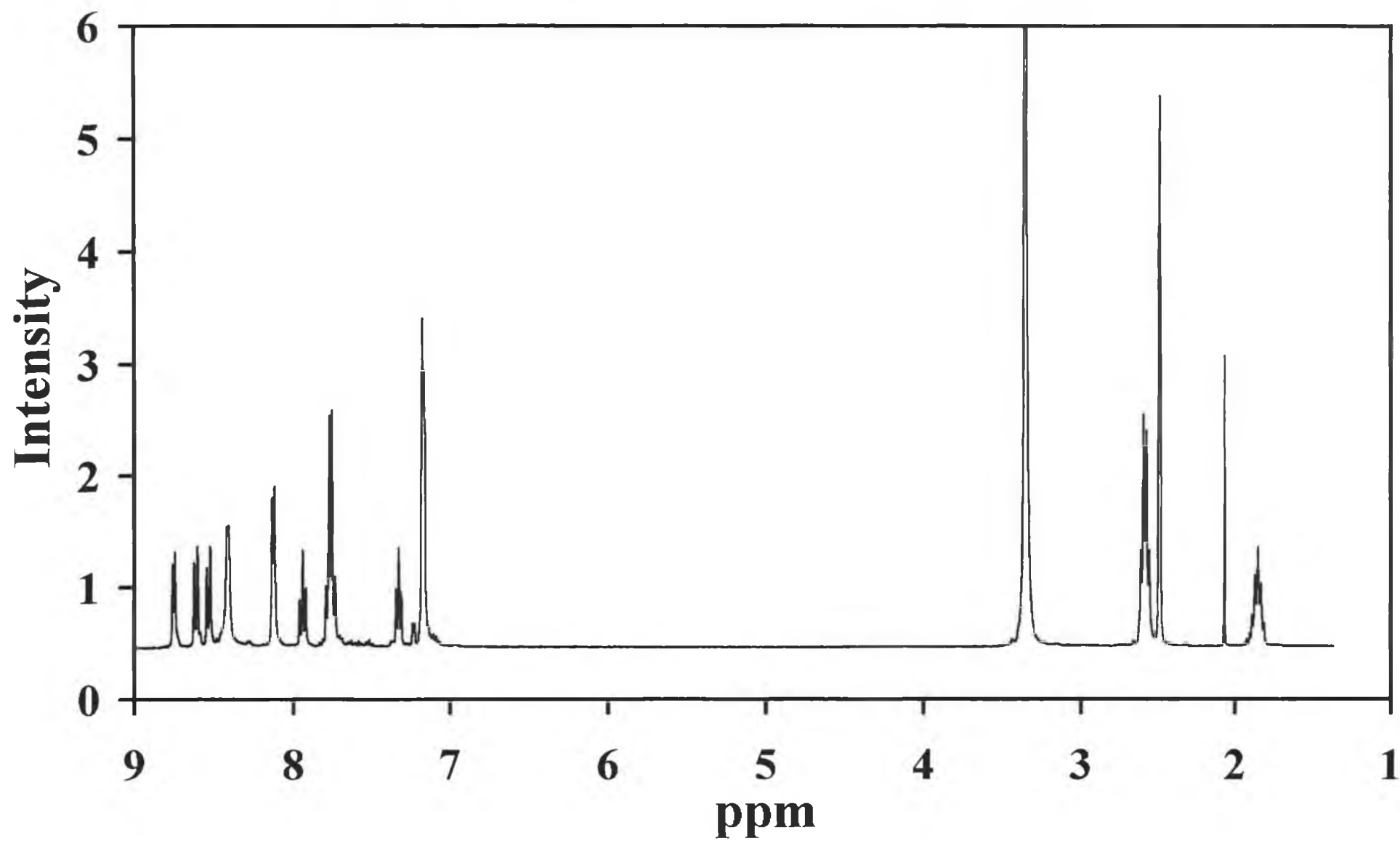
^1H NMR $[\text{Os}(\text{bpy})_2\text{P3P Cl}]^+$ in CH_3CN



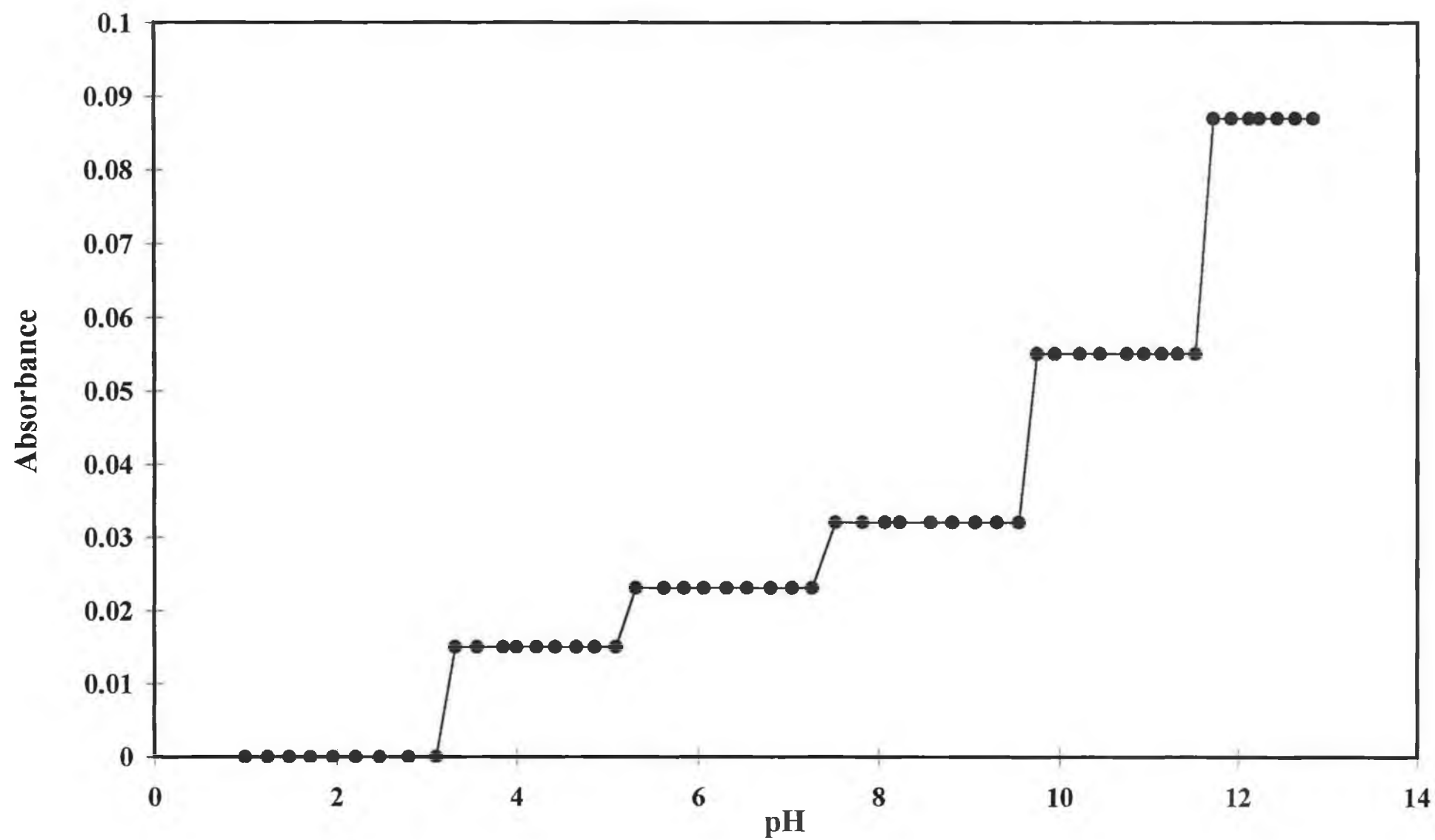
^1H NMR $[\text{Os}(\text{bpy})_2(\text{P3P})_2]^{2+}$, aromatic region in CH_3CN



^1H NMR $[\text{Os}(\text{bpy})_2(\text{P3P})_2]^{2+}$ in CH_3CN

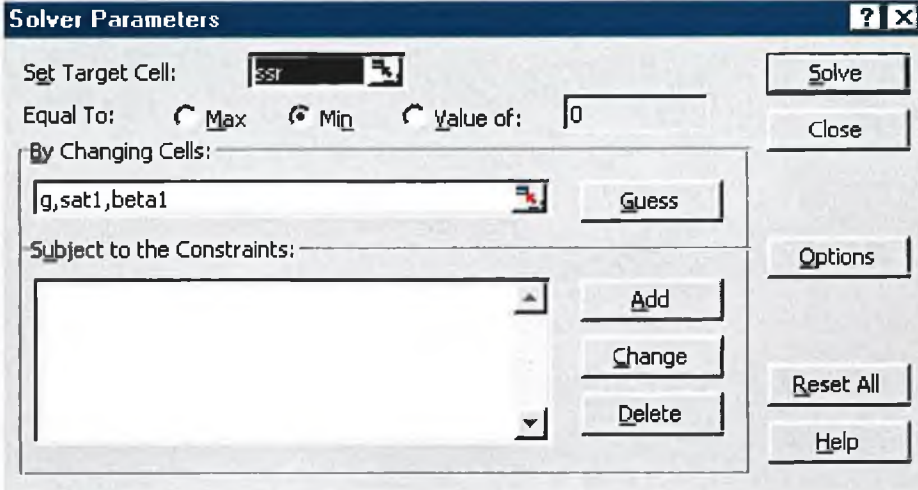


pK_a of $[\text{AQNH}_2\text{SOH}]$



Modelling of Frumkin Adsorption Isotherm.

Conditions used in Excel SOLVER model to fit experimental data to the Frumkin Adsorption Isotherm.



The Solver Parameters dialog box is shown. The 'Set Target Cell' is 'SSR'. The 'Equal To' is set to 'Min'. The 'By Changing Cells' is 'g,sat1,beta1'. The 'Subject to the Constraints' section is empty. The 'Solve' button is highlighted.

Solver Parameters

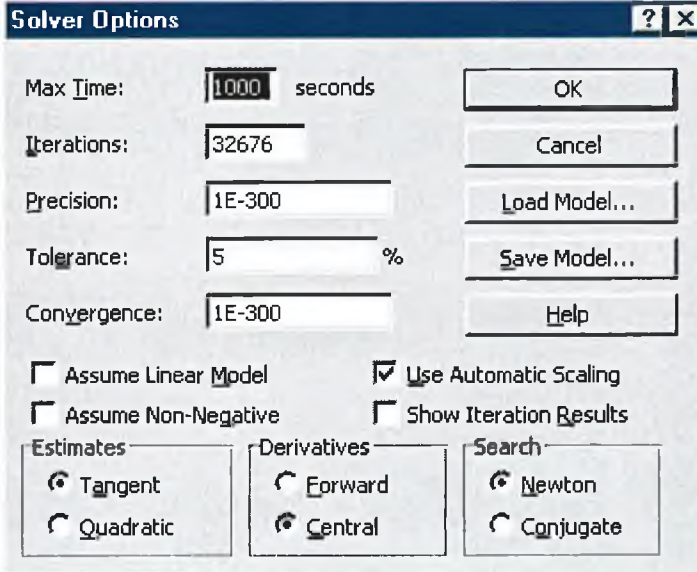
Set Target Cell:

Equal To: ☐ Max ☒ Min ☐ Value of:

By Changing Cells:

Subject to the Constraints:

Buttons: Solve, Close, Options, Reset All, Help



The Solver Options dialog box is shown. The 'Max Time' is '1000' seconds. The 'Iterations' is '32676'. The 'Precision' is '1E-300'. The 'Tolerance' is '5 %'. The 'Convergence' is '1E-300'. The 'Assume Linear Model' checkbox is unchecked. The 'Assume Non-Negative' checkbox is unchecked. The 'Use Automatic Scaling' checkbox is checked. The 'Show Iteration Results' checkbox is unchecked. The 'Estimates' section has 'Tangent' selected. The 'Derivatives' section has 'Central' selected. The 'Search' section has 'Newton' selected.

Solver Options

Max Time: seconds

Iterations:

Precision:

Tolerance: %

Convergence:

Assume Linear Model ☐ Use Automatic Scaling ☒

Assume Non-Negative ☐ Show Iteration Results ☐

Estimates: ☒ Tangent ☐ Quadratic

Derivatives: ☐ Forward ☒ Central

Search: ☒ Newton ☐ Conjugate

Buttons: OK, Cancel, Load Model..., Save Model..., Help